Theses and Dissertations

December 2022

Mechanical Erosion Investigation Through the Solid Rocket Motor's Nozzle

Mohamed Ahmed Abdelazim Abousabae
University of Wisconsin-Milwaukee

Follow this and additional works at: https://dc.uwm.edu/etd

Part of the Mechanical Engineering Commons

MECHANICAL EROSION INVESTIGATION THROUGH THE SOLID ROCKET

MOTOR'S NOZZLE

by

Mohamed A. Abousabae

A Dissertation Submitted in

Partial Fulfillment of the

Requirements for the Degree of

Doctor of Philosophy

in Engineering

at

The University of Wisconsin-Milwaukee

December 2022

ABSTRACT

MECHANICAL EROSION INVESTIGATION THROUGH THE SOLID ROCKET
MOTOR'S NOZZLE

by

Mohamed A. Abousabae

The University of Wisconsin-Milwaukee, 2022
Under the Supervision of Professor Ryoichi S. Amano

The solid rocket motor (SRM) is considered one of the essential engines that facilitates aerospace research; thus, investigating the propellant burning process is vital. One of the challenges facing its growth is the oxidization of the aluminum into aluminum oxide at the exhaust's high pressures and temperatures. The oxidized aluminum forms agglomerates, impinge on the exit nozzle walls, causing severe damage (erosion) to the nozzle material. Thus, the present work attempts to investigate and reduce this erosion. Two different approaches are followed in the current work, the first one aims to better understand the aluminum oxide agglomerates break-up mechanism and the factors affecting it experimentally (subsonic condition due to the safety purposes limitations), while the other establishes a numerical model to predict the nozzle mechanical erosion within the rocket's combustion chamber severe conditions.

The breakup process and some factors affecting it are investigated in three sections. Two-phase air-water flow experimental set-up is used, as a substitute for liquid aluminum agglomerates and exhaust combustion gases, in the three sections. The first section's experimental results show that increasing the exhaust air velocity enhances the droplet's break-up tendency to reduce the average diameter and increase droplet numbers per the testing channel volume. Numerical models

ii

were constructed and validated using the experimental results. The percentage error in the droplets' average diameter and the number is between 6–15% and 8-18%. Furthermore, the effect of reducing the liquid surface tension was studied. The results showed that it facilitates water bodies' separation from the interface surface, because of the reduced bounding forces between surface's molecules, which enhances the break-up process (0.5-17% increase in the droplets' average diameter and 4-100% increase in its number) and reduce the droplets impact on the nozzle walls, hence reduce the SRM nozzle erosion problem.

While the second section investigated the breakup process at different water flow rates and constant air velocity, where the results were used to validate a numerical model. The results revealed an excellent acceptance between the numerical, the experimental data (6-19%), and the effect of increasing the water flow rate on the break-up mechanism. The validated numerical model was further used to study the airflow acceleration impact on the break-up process. It was found that applying acceleration to the airflow subjects the water surface to rapid and sudden changes in the relative velocity between the gas and liquid, thus separating more water fragments from the primary liquid. In other words, it enhances the break-up process by reducing the average diameter with a range from 6.5% to 9% compared to the no-acceleration case and increasing the average droplets' number [8.5-17%].

Finally, the third section investigated the submerged nozzle configuration on the breakup process under different air and water flow rates, in addition compared between the submerged nozzle and the external one. It was found that having a submerged nozzle enhances the droplets breakup in the nozzle convergent section due to the existence of the recirculation zones. However, the separated droplets will have higher velocity to hit the walls with, hence a supersonic model

simulates the actual conditions within the rocket is essential to decisively conclude the submerged nozzle effect on the nozzle mechanical erosion.

Erosion prediction of the solid propellant nozzle is vital for its design process. Thus, the second approach employing a multi-phase numerical model is established based on the Eulerian-Lagrangian approach to model the aluminum particles burning inside the combustion chamber, in addition to simulating the mechanical erosion of the nozzle. The numerical model is validated against numerical and experimental results from the literature. Then the validated model will be further used to investigate the SRM nozzle erosion at different boundary conditions, nozzle configurations, particles, and propellant properties. First the model was used to simulate the agglomerates' break-up, in addition to predicting the mechanical erosion for aluminum particles with lower surface tension. The results showed that applying the Reitz-Diwakar breakup model reduces the erosion rate by 6.2% - 24% depending on the injected droplets. In addition, it was found that a decrease in the erosion rate by 1% to 4.5% can be achieved by reducing the aluminum additive's surface tension by 15%.

Then, an investigation of the effect of increasing the propellant aluminum content and different particles' injection velocity on the nozzle mechanical erosion was conducted and the results showed that having higher aluminum content increases the nozzle erosion by 4-10% compared to the 15% case. Furthermore, the aluminum particles will not fully burn within the combustion chamber and will participate in the nozzle erosion. In the end, having particles with higher initial velocity at the burning surface increases the nozzle mechanical erosion, despite of the incident mass flux decline.

Finally, the submerged nozzle configuration effect on the mechanical erosion was studied at seven particle diameters and was compared against the external nozzle results. And it was

concluded that comparing the external nozzle and submerged nozzle configurations in terms of the predicted mechanical erosion, the external nozzle will perform better than the submerged one as lower mechanical erosion exists in its different sections.

Dedicated to my parents, and my sisters
for their unconditional love, support, and encouragement

TABLE OF CONTENTS

x

LIST OF FIGURES

xiv

LIST OF TABLES

NOMENCLATURE

Symbols

A_f	Area of the face targeted by erosion
A_k	Oxidizing species availability
A_t	Nozzle throat area
A_p	Projected area of a particle
B	Continuous phase body forces' vector
CCD	Charge-coupled device
CMOS	Complementary Metal-Oxide-Semiconductor
C_d	Drag Coefficient
C_p	Specific heat
D_p	Real-time aluminum particle diameter
D_{p_o}	The initial aluminum particle diameter
D_s	Stable droplet diameter
E	Continuous phase total energy per unit mass
E_f	Mechanical erosion rate
e_r	Erosion ratio
F_b	Body forces affecting a particle
F_d	Drag force
F_s	External forces affecting a particle
h	Continuous phase Enthalpy
K	Aluminum burning rate constant

k	Thermal conductivity
LES	Large-eddy simulation
m_{AL}	Aluminum particle mass
m_p	Particle mass
$\dot{m}_p$	Particle evaporation rate
m_{Π}	Particles' mass flow rate in each parcel
Nu_p	Particle Nusselt number
p	Continuous phase pressure
P_C	Combustion chamber average pressure
Pr	Prandtl Number
$\dot{q}''$	Continuous phase heat flux vector
Re_p	Reynolds number for a particle
r	Radius of droplet
Sh	Sherwood number
SGS	Sub-grid scale
S_u	Continuous phase user-specified source term
T_p	Particle temperature
T_v	Continuous phase viscous stress tensor
t	Time from the burning process beginning
U	Particle relative velocity
V	Two-phase velocity difference (relative velocity)
V_{air}	Air velocity

V_{water}	liquid velocity
VOF	Volume of fluid
v	Continuous phase velocity
v_k	Particle cut-off velocity
v_P	Particle velocity
v_s	Particle slip velocity
We	Weber number
We_{cr}	Critical Weber number
x_i	Mole fraction of species i

Greek letters

ρ_{air}	Density of air
σ	Surface tension of a liquid
ρ	Continuous phase density
ρ_{AL}	Aluminum density
μ	Dynamic viscosity
α	Particle incident angle
α_o	Calibrated transition angle
ε_C	Calibrated cutting coefficient
ε_D	Calibrated deformation coefficient
σ	Surface tension of a liquid
τ_b	Characteristic time scale

Abbreviations

ACC_0   Constant air velocity (20 m/s) (No-acceleration case)

ACC_20   Airflow with an acceleration of 20 m/s^2

ACC_30   Airflow with an acceleration of 30 m/s^2

ACC_60   Airflow with an acceleration of 60 m/s^2

AP   Ammonium perchlorate

AL   Aluminum

C-D   Convergent divergent

CEA   Chemical equilibrium analysis

EBU   Standard Eddy-Break-Up model

EXP   Experimental results

EXT_N   External nozzle configuration

fps   Frame per second

HTPB   Hydroxyl-terminated polybutadiene

NASA   National Aeronautics and Space Administration

SIM   Simulation results

SRM   solid rocket motor

SUB_N   Submerged nozzle configuration

SUB_N_T   Submerged nozzle tip

W/O Br   Cases without considering the droplets' breakup model

W Br_NST Cases considering the droplets' breakup model

W Br_LST Cases considering the droplets' breakup model, and droplets' lower surface tension

ACKNOWLEDGMENTS

Chapter 1 : Introduction

1.1 Introduction

Space exploration has been a race only between nations represented by their governmental agencies. But now more with the participation of the private sector, space exploration is becoming a much more accessible industry. Rocket motors play vital role in aviation and aerospace fields by supplying the thrust force required by any vehicle to satisfy its mission. Any rocket motion can be described by Tsiolkovsky Equation (Classic rocket equation) which is detailly discussed in Appendix A. The solid propellant was first used by the Chinese since 800 years ago, however the real evolution of the rocket propulsion systems occurs in the twentieth century [1]. Rocket motors can be classified following different aspects: energy source, system function, vehicle type, propellant type, construction, or number of rocket units. The most common classification is based on the energy source (chemical, solar, or nuclear). Chemical type propulsion system is the current used and most stable technology, where the mixed fuel and oxidizer burn together generating product gases at high pressures and temperatures (2500 – 4100 ^{o}C). These gases travel through the combustion chamber and expand in the rocket's nozzle converting their high stored energy into kinetic energy (1800 - 4300 m/s) and providing the rocket with its designed thrust force. There are different rocket types classified under the chemical propulsion system: solid, liquid, and hybrid rocket motors.

1.2 Solid Rocket Motor

Since this work is concerned with the solid rocket motor, it will be discussed in detail more than the other types. Solid rocket motor has the simplest configuration with no moving parts, leading to easy maintenance and long storage time (5-20 years). However, in some cases, the rocket

1

nozzle is equipped with thrust equipped control actuators, but still the solid rocket motor configuration is simpler than the other types. Its generated thrust can range from milli-newtons (for micro thrusters used in small spacecrafts) to 10 Mega-newtons for space vehicles launch boosters. Figure **1-1** shows the different components within any solid rocket booster.

Solid Fuel Rocket Booster (SRB)

1. Primary parachute
2. Forward separation rockets
3. Flotation system
4. Principal parachutes
5. Platform for electronic equipment
6. Pyrotechnic ignition
7. Fixing harness to external tank
8. Joint between solid fuel segments

9. Solid fuel segment
10. Fixing harness to external tank
11. Solid fuel block
12. Articulated joint for nozzle
13. Rear separation rockets
14. Skirt
15. Thermal insulation
16. Diffuser nozzle
17. Anchor point

Figure 1-1: Solid rocket booster configuration, [2].

1.2.1 Grain Configurations

The propellant grain composes of a polymer binder (also used as a base fuel), oxidizers' crystals, and additional fuel powder (like aluminum). The well mixed blend is then casted, molded, or extruded to fit inside the rocket combustion chamber case with different configurations. A grain configuration can be defined as the shape of the burning surface at the burning process beginning. The grain configuration controls the burning type to be either neutral, progressive, or regressive. Neutral burning means approximately having a constant grain surface area, thrust, and pressure during the burning process, while progressive burning refers to having an increasing surface area, thrust and pressure. On the contrary, a decreased surface area, thrust, and pressure during the

2

burning process indicates a regressive burning. There are several grain configurations such as the internal burning tube (progressive, Figure **1-2** (a)), star (neutral, Figure **1-2** (b)), slots and tubes (neutral), and wagon wheels (neutral).

(a)   (b)
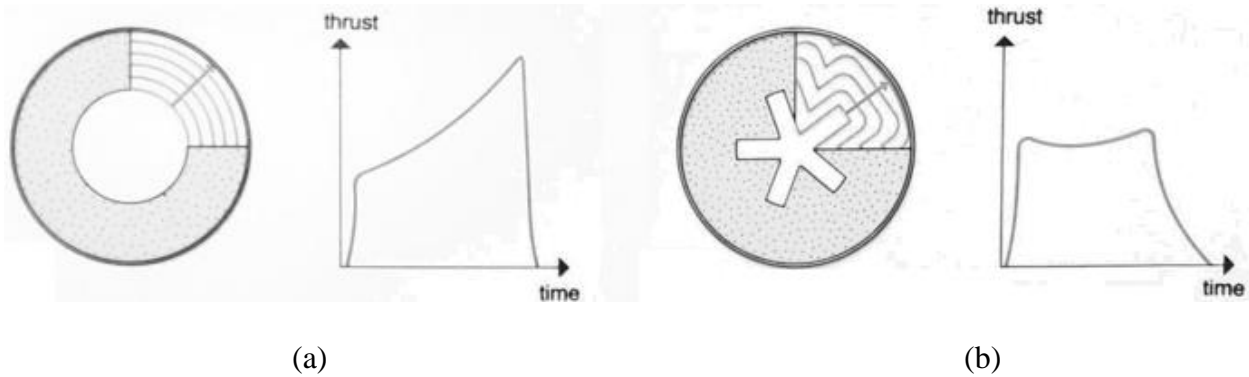
Figure 1-2: Propellant grain cross sections, [2].

1.2.2 Power Process and Rocket Nozzle

A commonly metalized solid propellant (Ammonium perchlorate (AP) / Aluminum (AL) / Hydroxyl-terminated polybutadiene (HTPB)) is used in the current work, and it called metallized, as it includes a percentage of metal (aluminum) to increase the fuel specific impulse. The propellant's compositions react together in the combustion chamber generating exhaust gases (like water vapor (H_2O), carbon dioxide (CO_2), carbon monoxide (CO), hydrogen (H_2), hydrochloric acid (HCL), and nitrogen (N_2)) with high pressure and temperature. The rocket's exhaust nozzle is the part where the exhaust gases' high potential energy is converted into kinetic energy which force the rocket through its mission. Figure **1-3** shows two common rocket nozzle configurations with an illustration for their different components. The external nozzle is the common and classic nozzle as it has a simple design, on the other hand the submerged nozzle is utilized to reduce the rocket length and weight. Despite its advantages, it causes flight instability because of the accumulation of the aluminum oxide particles in the pocket region. Figure **1-4** presents the material selection for each nozzle part and its corresponding function

3

Flow ➔

Throat

Thermal liner

Insulator

Entrance

Structure

Exit

Combustion chamber

(a)

Flow ➔

Throat

Thermal liner

Entrance

Insulator

Structure

Exit

Reentry

Combustion chamber
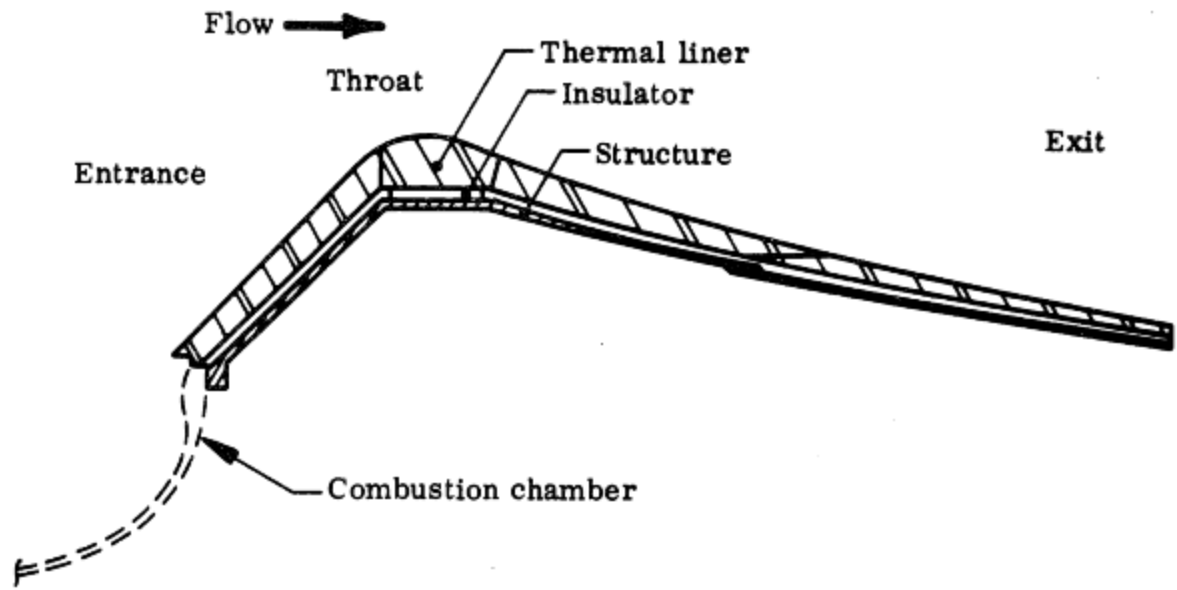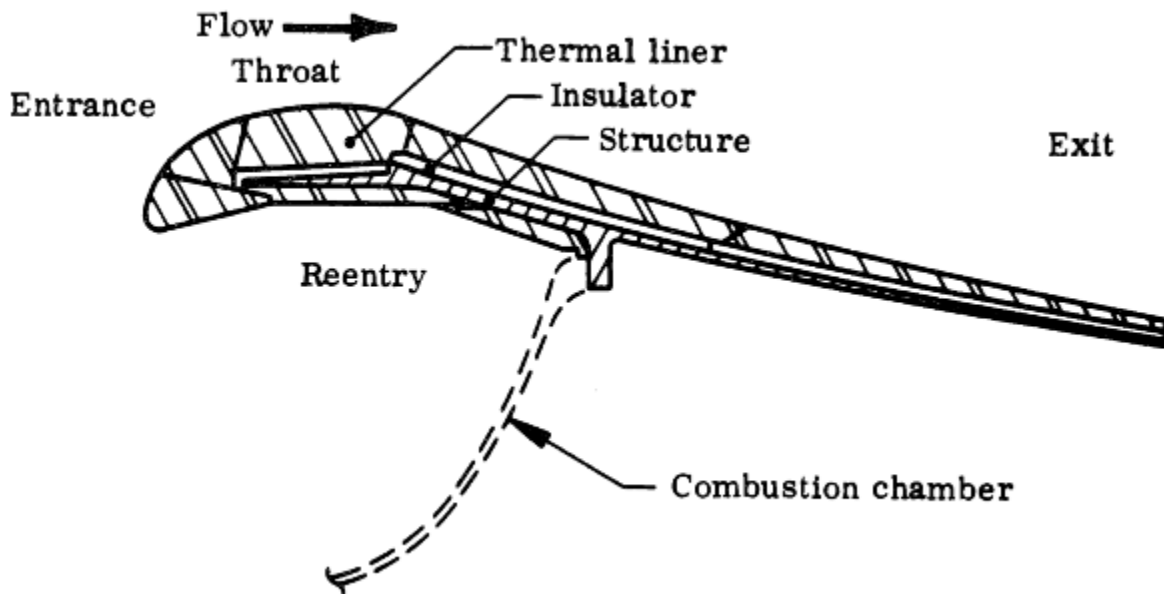
(b)

Figure 1-3: Rocket nozzle configurations, (a) external nozzle. (b) submerged nozzle, [4].
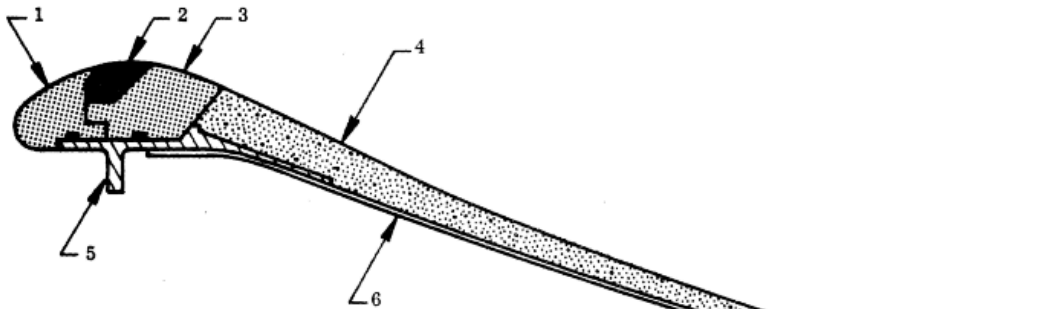
Item	Material	Function
1	Carbon/phenolic die molding	Entrance thermal liner and insulation
2	Tungsten	Throat insert
3	Carbon/phenolic die molding	Throat insulation and throat extension thermal liner
4	Silica/phenolic tape	Exit thermal liner and insulation
5	Aluminum	Attach, entrance, throat, and throat extension structure
6	Glass-cloth/epoxy	Exit structure

(a)
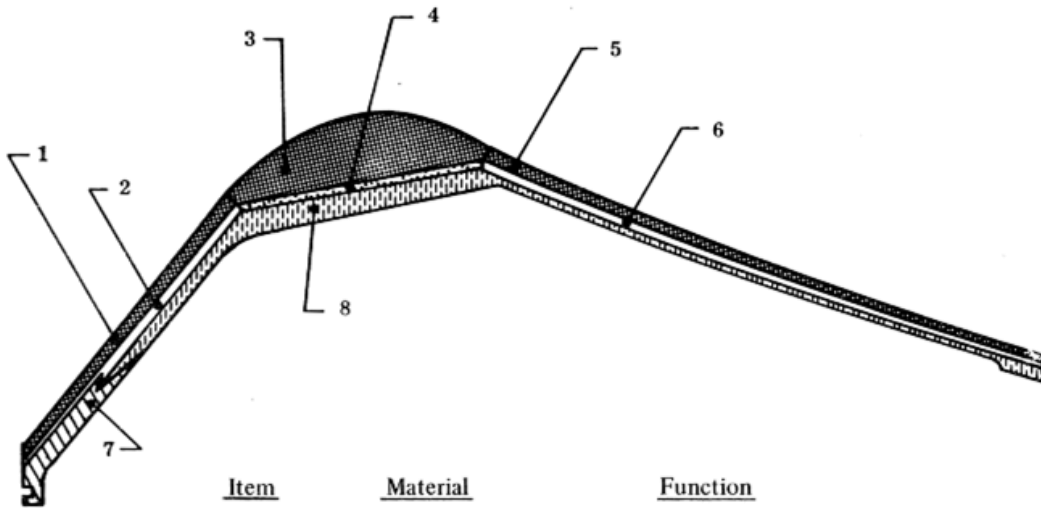
Item	Material	Function
1	Graphite/phenolic tape	Entrance thermal liner
2	Asbestos/phenolic tape	Entrance insulation
3	Polycrystalline graphite	Throat insert
4	Silica/phenolic tape	Throat insulation
5	Graphite/phenolic tape	Exit thermal liner
6	Asbestos/phenolic tape	Exit insulation
7	Steel	Attach structure
8	Glass-cloth/epoxy laminations	Entrance, throat, and exit structure

(b)

Figure 1-4: Rocket nozzle different parts' material, (a) apogee motor, HS-303A satellite, (b) pershing first stage, [4].

5

1.2.3 Nozzle Erosion Problem

The rocket nozzle is subjected to severe erosion in the convergent and throat sections which is very complex and occurs due to several overlapping factors: combustion chamber operating conditions, aluminum content in the solid fuel, operating conditions, aluminum content in the solid fuel, nozzle material and configuration, exhaust gases species type, and mass fraction. The nozzle overall erosion can be divided in two categories, chemical and mechanical erosions. The exhaust gases raise the nozzle material temperature rapidly to an extreme temperature higher than the nozzle material melting point, or sometimes even it is lower than the material melting point but higher than the formed oxides melting point. The melted material is swept by the exhaust gases high momentum causing chemical erosion. While the mechanical erosion occurs because of the two-phase flow through the combustion chamber and nozzle. During the combustion process, a fraction of the aluminum particulates being released from the burning surface unreacted. They are further oxidized to Al2O3 in the rocket core. The formed aluminum oxide agglomerates (liquid droplets), which impinges the nozzle walls, erodes the throat surfaces. The nozzle erosion can be critical as it increases the nozzle's throat diameter and hindering the overall rocket performance and its nozzle reusability chances.

1.3 Liquid Rocket Motor

The liquid rocket motor idea was first discussed by Tsiolkovsky [3], then on March 16, 1926, Robert Goddard successfully launched the first liquid rocket motor. This technology utilizes liquid fuel (has high density and specific impulse, hence small tank) and oxidizer which are injected into the combustion chamber using a turbopump, as the injection pressure should be higher than the combustion chamber pressure. The turbopump are used due to its light weight and high

performance, on the other hand, sometimes a high-pressure inert gas tank is used to push the fuel into the combustion chamber. An ignition system is used to lit the fuel/oxidizer mixture, where hot gases are generated from this reaction at high pressure and temperature, accelerate through the exhaust nozzle, giving the rockets its required thrust force. The liquid rocket motor is preferred due to some advantages: its thrust force can be controlled by controlling the propellant inlet flow rate, also, it can be used for several flights, in addition, it doesn't severely struggle from the two-phase flow nozzle erosion problem. Finally, it can be tested before using it in actual flight. On the contrary, it has several issues associated with its utilization because of its complicated design which raise its components' failure chances. Moreover, the liquid propellant tank represents most of the rocket mass, consuming it during the flight causes a control difficulty due to the center of mass shifting. In addition, the liquid propellant cannot be stored for a long period of time and needs an immediate preparation just before the flight launch.

1.4 Hybrid Rocket Motor

The hybrid rocket motor applies the best of solid and liquid rocket motors, where it uses a pressurized tank filled with liquid oxidizer and a solid propellant packed in the combustion chamber. It has a simpler design compared to the liquid rocket motor, since the liquid propellant tank and turbopump are eliminated. Metal additives also can be added to increase the specific impulse, in addition the solid propellant acts as a shield for the combustion chamber walls from the product gases high temperature, unlike the liquid rocket motor where the liquid propellant is used as a coolant. Finally, its operation is easier in terms of start/stop/throttling compared to the solid rocket motor. Aside from its advantages, its oxidant to fuel ratio is variable over the flight and along the combustion chamber, which shifts the chemical operation performance point from its peak. Since the hybrid rocket motor uses the solid propellant as a fuel, its reuse ability in several

flights is lost. Moreover, in case of large hybrid rocket with high thrust force, a turbopump will be essential to achieve high oxidant injection pressure. This turbopump is usually powered by the liquid propellant in case of liquid rocket motor, but in this case, there is no liquid propellant, so an oxidant, which can be used as a monopropellant, will be used, however these types of propellants are less efficient as oxidants. Or a tank of liquid propellant will be included in the system design making it more complex like the liquid rocket motor.

1.5 Problem Statement

As mentioned before, there are two nozzle erosion types mechanical and chemical, this work focuses on the mechanical one, as the chemical erosion was detaily investigated by several researchers (will be presented in the next chapter). Studying the two-phase flow within the rocket internal environment is essential to reduce the mechanical erosion. The current work is investigating the agglomerates' break-up process experimentally and numerically, and the factors affecting it like reducing the agglomerates surface tension, and the influence of the exhaust gas flow acceleration during the flight as smaller particles are easier to be entrained by the exhaust gases momentum, thus less erosion. All these investigations are conducted under subsonic conditions because of the safety precautions required for the experimental work unlike the real flow nature of a rocket (super-sonic). So, in order to study the effect of these different parameters on a real rocket flow case, a numerical model predicting the mechanical erosion, and reflecting the actual conditions inside a rocket is established. Having this model will provide a detailed information for the near surface thermo-fluid dynamics and particle trajectories, allowing for a high-fidelity investigation of the nozzle material erosion.

Chapter 2 : Literature Review

2.1 Introduction

A solid rocket motor is one of the pillars of the aviation and aerospace applications because of its simplicity and the stationary operation of all its parts, leading to easy maintenance and long storage time. However, due to the hostile environment within its combustion chamber [5,6] (high pressure and temperature and two-phase flow), the materials of the exhaust nozzle experience severe erosion. Such erosion can hinder the rocket performance caused by the increase in the nozzle's cross section areas [7-9]. The metal additives cause the two-phase flow. Commonly, metal powders (aluminum mainly) are added to propellant fuels to increase their specific impulse and combustion stability [10].

2.2 Chemical Erosion

During the propellant combustion process, the exhaust gases with high temperatures rise the nozzle material temperature rapidly, so a heterogeneous chemical reactions take place at the nozzle surface between its material and the oxidizing species existing in the exhaust gases (such as H_2O, CO_2, and OH) causing severe erosion to the nozzle, especially the throat section where the nozzle material has the highest temperature. It was also reported that a percentage of more than a 5% increase in the nozzle throat area is not acceptable [11]. This erosion type is called chemical erosion and was investigated by several researchers experimentally and numerically.

Johnston et al [12] in 1966 investigated the rocket nozzle throat erosion for different nozzle's materials (refractory metals, metal carbides, fiber-reinforced plastics, ceramics, and graphite's). The experiments were conducted using different propellants with 4700, 5600, 6400 ℃ flame temperatures and 1000 psi chamber pressure. They found that the refractory metal nozzle is

better than the other materials in terms of resisting the erosion and cracks due to thermal stresses. While Geisler et al [6] tried to investigate the metal powder (aluminum) mass fraction in the fuel on the motor efficiency by conducting experiments using the BATES (ballistic test and evaluation systems) and different aluminum mass fractions (15, 18, 21, 24, 27, and 30%). Keswani et al [13] developed a correlation to predict the erosion in the nozzle throat based on the oxidizing species diffusion close to the nozzle surface, and operating conditions in terms of pressure and temperature, in addition the correlation was validated by the collected experimental results from two different motors. Thakre et al [10, 14-16] developed numerical frameworks to study the nozzle's throat chemical erosion for different nozzle's materials, operating conditions, and developed erosion controlling techniques. They first started by investigating the carbon-carbon/graphite nozzle under different operating conditions and different propellant's' types (metalized and non-metalized) [14], the model considered a flow of multicomponent reacting species, properties of the nozzle material and the heterogeneous reactions occurs at the nozzle surface. It was found that the numerical model can successfully predict the nozzle recession rate compared to a three different experimental data sets and that the erosion rate trend is following the same trend of the heat flux distribution where it has the maximum value at the nozzle throat. From the oxidizing species, it was proven that the water vapor has the most significance effect on the nozzle erosion rate followed by the hydroxide and carbon dioxide. Moreover, they reported that the erosion rate increases linearly with increasing the operating chamber pressure due to the increased heat transfer and heterogeneous reactions rates. Additionally, it was proved that increasing the aluminum mass fraction in the fuel leads to a reduction in the throat nozzle erosion because of the decrease in the oxidizing species concentrations. Then, they expanded their investigations to cover the refractory-metal nozzles [15] (rhenium, tungsten, and molybdenum)

following the same numerical framework mentioned before. The erosion rate behavior followed the same behavior of the carbon-carbon/graphite nozzle; however, it was found that the graphite nozzle exhibits a slower erosion rate compared to the tungsten one. Furthermore, they analyzed the effect of applying a nozzle boundary layer control system (NBLCS) on the nozzle erosion for a solid rocket motor using non-metalized propellant. Where it was found that the NBLCS can reduce the chemical nozzle erosion to negligible values for the vertical injection arrangement which can be explained by the reduction in the oxidizing species near the nozzle surface [10]. Finally, they investigated the nozzle material roughness and radiation effects on the nozzle erosion rate, where it was found that applying the material surface roughness increases the nozzle erosion as a result for the near wall turbulence increase. On the other hand, they found that including the radiation heat transfer reduces the erosion rate, in addition to not having the same effect on the as the surface roughness [16].

2.3 Mechanical Erosion

Aluminum particle at room temperature is covered by an oxide layer. The initial thickness of the oxide layer for different micron-sized aluminum particles varies from 10 to 20 nm. Due to the elevated temperature at the fuel combustion surface, the aluminum particles melt, forming tiny liquid droplets which remain unreacted (a large portion of it). These droplets coalesce together, forming large agglomerates (usually $100 - 200$ μm), which slowly burn during their travel within the combustion chamber. The burning process generates aluminum gas, where at the flame sheet, aluminum vapor reacts instantaneously with CO_2 and H_2O (oxidizing species coming from the outer regions) to form a mixture of aluminum monoxide (AlO) and dialuminum dioxide (Al_2O_2). The mixture travels toward the condensation sheet where the suboxides react with additional carbon dioxide and water vapor to produce $Al_2O_3(l)$ (aluminum oxide smoke). A fraction from

the aluminum monoxide (AlO) diffuses back to the agglomerate surface from the primary flame sheet undergoes collision-limited reaction with the surface to form AL2O3(l) which is added to the cap.
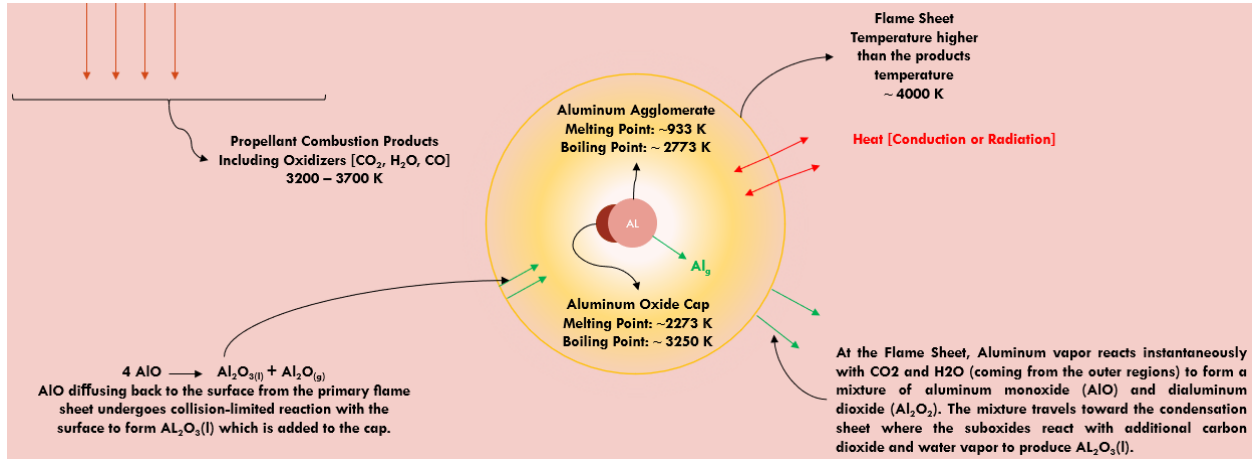
Figure 2-1: Aluminum agglomerate burning process.

The aluminum agglomerates with oxide shells have a slow combustion rate compared to the pure aluminum droplets. Thus, the aluminum combustion produces a bimodal distribution of smoke (aluminum oxide with 1.5 μm mean diameter and can be simulated as a part of the continuous phase), and aluminum agglomerates with aluminum oxide caps (20-300 μm) [17,18]. The agglomerates' size depends on the aluminum particles' amount, diameter, physical properties, and operating combustion chamber conditions. The unburnt multi-component agglomerates travel through the motor and impinge on the nozzle walls causing a mechanical erosion.

Several researchers attempted to investigate mechanical erosion by either studying the combustion process and its products' properties or the two-phase flow field, especially the formed agglomerates' trajectories.

Predicting the agglomerates' size, distribution, and mass fraction of each component is very important for modeling the two-phase complex flow field and calculating its effect on the rocket performance either by enhancing the combustion instabilities or by eroding the nozzle surface.

12

Thus, the aluminum combustion process and its agglomeration life cycle were investigated and recorded using different techniques such as high-speed cameras [19-21], shadowgraph images [22], and holography [23]. Liu et al [24] presented the latest developments and lab results for the aluminum particles' combustion process. They reported a particles' size distribution based on their case study and suggested adding an organic fluoride compound to reduce the particles' size as proved by their experiments. Also, they reported that using the laser diffraction technique proved to be effective in studying the combustion process, moreover, the recorded videos by high-speed charge-coupled (CCD) device showed the aluminum particles' burning process: Exposure – accumulation – sintering – detachment – agglomeration/combustion.

The flow field inside the rocket chamber is overly complex due to the existence of agglomerates, so studying their distribution, size, trajectories, and breakup is vital for predicting the rocket performance during its flight and the mechanical erosion, specifically in this study. Several studies were conducted to predict the agglomerates' trajectories. Hwang et al [25] proposed a numerical solution for the gas-particle flow field using MacCormack scheme to solve the governing equations for the particles. Amano et al. [26-28] conducted research to ease the two-phase flow modeling process in the rocket combustion chamber by identifying the agglomerates initial velocity at the burning surface. The developed new technique is using the x-ray real-time radiography (RTR) to measure the particles' initial velocity and their trajectories within the chamber (by a developed image processing code), then the experimental results were further used to validate a numerical simulation. Majdalani et al. [29] and Simoes et al. [30] tracked the change in pressure fluctuations and agglomerates' trajectories within the motor core because of using different agglomerates' diameter and initial velocity. They found that varying the agglomerate's diameter critically influences its trajectory. Moreover, Li et al. [31,32] investigated the two-phase

flow influence on the solid rocket motor performance with respect to the particles' size. 2-D numerical simulation was developed and was validated by lab-scale experimental tests. The results showed that gases velocity field around the particles decays where the decay increases with larger particles' sizes till 10 μm, then it decreases again, in addition they found that the two-phase flow loss decreases with larger particles' sizes.

Another crucial factor to be considered in the prediction of the two-phase flow inside the motor is the breakup of the agglomerates into smaller particles due to the nature of the flow field (high Weber number). So, the breakup process of these agglomerates and the factors affecting it were studied numerically and experimentally. Amano et al [33-35] studied a two-phase flow (water-air) behavior within a straight channel experimentally, then modeled the same case using a computational fluid dynamics (CFD) software considering the large-eddy simulation turbulence model. The breakup process was recorded within the straight channel using a high-speed camera followed by post processing the data using MATLAB codes. Finally, the authors compared the post-processed data by welch frequency transform from both experiments and simulations to validate the CFD model and proves its ability to predict the breakup process. Also, It was proven that breaking up large agglomerates into smaller ones helps in reducing erosion as smaller particles will be entrained by the exhaust gases' flow momentum.

Chen et al. [36,37] studied the break-up mechanism in vertical and horizontal convergent divergent nozzle arrangements experimentally and numerically, compared between them where it was found that the break-up process is higher in the vertical arrangement compared to the horizontal one, in terms of smaller droplets' diameter and a higher number of droplets. It is worth mentioning that all these studies were for subsonic flows (air-water) in horizontal and vertical set-ups due to the difficulty and safety precautions in experimentation on supersonic flows.

2.4 Research Objectives and Thesis Outline

The present study objectives can be summarized into two sections (will be discussed in detail in the next sections). The first section is studying the factors affecting liquid droplets' breakup pattern in a gas flow field under subsonic conditions experimentally and numerically due to the harsh environment associated with supersonic experiments, while the last section introduces a numerical model predicting the nozzle erosion for the rocket's real environment (supersonic flow conditions). Chapters 3 is covering the experimental setup configuration and procedures, while chapters 4, 5, 6, 7 and 8 are introducing the established experimental work and numerical models, in addition discussing the results, conclusions from the study objectives.

2.4.1 Liquid Droplet Flow Behavior in a Vertical Nozzle Chamber

2.4.1.1 Liquid Surface Tension Reduction Effect on Water Droplet Flow Behavior

As previously demonstrated, studying the agglomerates' break-up mechanism through the rocket nozzle is essential to limit mechanical erosion and to improve the rocket performance. However, the previously conducted research did not cover all the factors affecting the break-up process in the rocket nozzle, like reducing the pure aluminum surface tension by 10%-15%, which can be achieved by adding strontium and magnesium (aluminum alloys) [38]. Consequently, the influence of varying the liquid surface tension on the break-up phenomena, in terms of the droplets' size and numbers per different sections of the nozzle, has been investigated in this study, both experimentally and numerically, like the research done by Chen et al. [36,37]. In addition, a modified post-processing algorithm code, better in capturing more details during the break-up process, is introduced in this study. SRM combustion process takes place in high pressure and temperature, which are obstacles to be conducted in a laboratory for safety reasons. The two-phase

air-water flow will be used as a substitute for liquid aluminum agglomerates and exhaust combustion gases. Numerical simulations will be conducted, and their results will be compared with the experimental results. After validation, more numerical cases will be developed to study the surface tension reduction effect. Chapter 4 will cover the results, and conclusions of this section.

2.4.1.2 Air Flow Acceleration Effect on Water Droplet Flow Behavior

Reducing the agglomerates size by breaking up the larger formed agglomerates before reaching the rocket exit nozzle is essential to avoid or lessen the mechanical erosion in the nozzle throat. One factor that may affect the break-up mechanism is the acceleration of the exhaust gases before entering the exit nozzle due to the increase in the fuel combustion area with the flight time.

Usually, the solid rocket boosters have a hollow central core, and the combustion process occurs on the internal surface of the propellant. The formed thrust force is variable during flight and depends mainly on the propellant surface area exposed to the combustion process. During the flight, the internal surface of the propellant is regressing, and the combustion surface area increase, which will instantaneously increase the thrust force [39,40]. The instantaneous higher thrust force is a result of the increase in the exhaust gas volume flow rate and, subsequently, its velocity (acceleration over time).

Consequently, the present work attempts to numerically investigate the exhaust gases acceleration effect on the break-up process before and through the motor exit nozzle. This section will utilize the same adjusted post-processing code (boosting the details capturing ability through the break-up process) developed in the first section. SRM combustion process occurs in a severe operation environment due to high temperature and high pressure, which are barriers to conduct experimentally for safety purposes. So, a two-phase air-water flow is utilized as an alternative for

liquid Al agglomerates and exhaust gases. The experimental results are collected and compared with a numerical simulation model with the same boundary conditions to validate the numerical models. After validation, more numerical simulation cases are built to study the exhaust gas' acceleration effect. Chapter 4 will cover the results, and conclusions of this section.

2.4.1.3 Submerged Nozzle Configuration Influence on Water Droplet Flow Behavior

The submerged nozzle is used to reduce the rocket length and weight, in addition, it is built to ease the directional control by utilizing the nozzle inclination. Despite its advantages, it was reported that using this nozzle may cause flight instability because of the accumulation of the aluminum oxide particles in the pocket region which have several effects on the rocket performance. Slag is another definition for the aluminum oxide droplets captured in the nozzle cavity either by hitting the nozzle back-face or getting trapped by the recirculation zone. Several studies were conducted to study the effect of the submerged nozzle on the rocket performance parameters, however there is a scarcity in the published work studying the effect of this nozzle on the break-up process of the aluminum oxide agglomerates. The effect of changing the exhaust air velocity, and formed aluminum oxide mass flow rate, since they are changing with the combustion of the solid propellant, is studied in this nozzle configuration experimentally and compared with the external one.

2.4.2 Mechanical Erosion Investigation in Solid Rocket Motor Nozzle Through Droplet Breakup and Surface Tension Influence

Mechanical erosion due to agglomerates impingement on the nozzle walls can be predicted using developed models for cases with identical conditions. These models were developed either for solid rocket motor erosion, slurries in pipes, or turbo machinery. The mechanical erosion depends on several factors such as eroded surface material, agglomerates' hardness, relative

velocity, and impingement angle. The mechanical erosion of the solid rocket motor was simulated numerically by Thakre et al. [41], and Tarey et al. [42].

Sabnis [17] established a Eulerian – Lagrangian numerical framework to model the internal flow field of the rocket combustion chamber, where the Eulerian approach was used to simulate the multicomponent gases inside the chamber, and the Lagrangian approach was used to describe the discrete phase motion through the multicomponent gas. The results showed that an extended combustion zone exists due to the aluminum slow combustion rate. The extended zone causes nonuniformity in the combustion chamber chemical composition and temperature distribution.

Thakre et al [41] introduced a numerical model to study the rocket nozzle mechanical erosion where the Eulerian – Lagrangian approach was used to model the continuous and discrete phases respectively. The aluminum combustion process was considered in their study, in addition to employing an empirical correlation to determine the nozzle mechanical erosion. The results showed that the mechanical erosion is severe and only concentrated in the convergent section of the nozzle. Moreover, Tarey et al [42] introduced a new model to predict the agglomerates' size and distribution, then the results of the new established model were incorporated in a numerical framework (CFD) to calculate the mechanical erosion of the nozzle surface. they found that reducing the initial aluminum particle size, reduces the mechanical erosion rate.

As discussed before, several researchers modeled the mechanical erosion on the nozzle surface numerically, however they did not include the agglomerates' secondary breakup within their models. So, the current study attempts to develop a more accurate numerical model predicting the mechanical erosion considering the secondary agglomerates' breakup, then it is expanded to study the effect of reducing the aluminum additives' surface tension [10%-15%] by adding

magnesium or strontium [38] for different agglomerates' diameters. Chapter 5 will cover the results, and conclusions of this section.

2.4.3 Propellant Aluminum Content and Alumina agglomerates Initial Velocity Impacts on the Mechanical Erosion in Solid Rocket Motor Nozzle

The existing validated numerical model for the SRM internal environment under supersonic flow conditions will be used to further predict the mechanical erosion for different aluminum content and discrete phase injection velocity, while considering the agglomerates' breakup. Comparing between these cases and the external nozzle erosion rates will provide essential information for proper design process.

In the current numerical model, the aluminum content in the propellant is 15%, however this percentage is variable. So, the effect of having different aluminum content on the mechanical erosion will be further investigated in this section. Five aluminum contents (15%, 18%, 21%, 24%, and 27%) will be studied.

Additionally, the particles injection velocity in the radial direction was assumed to be approximately 4% of the continuous phase velocity at the burning surface [41]; using the reported data by Madabhushi et al. [74] that the particles' injection velocity (1-25% of the continuous phase velocity) does not affect the system performance. However, it was found that there is not available research addressing the effect of the alumina particles injection velocity on the nozzle's mechanical erosion. So, in this section this factor will be investigated by modeling 24 cases for different droplet's diameter, injection velocity while considering two conditions: Simple model without applying the breakup model (W/O BR), and more complicated model include the droplet's breakup effect (W BR).

2.4.4 Numerical Investigation of the Mechanical Erosion Within a Submerged Nozzle Configuration

As mentioned earlier in Section 2.4.1.3, there is a scarcity in the published work studying the effect of having the pocket region on the rocket nozzle mechanical erosion. So, this section will concentrate on predicting the submerged nozzle mechanical erosion and addressing the effect of particles' diameter on the mechanical erosion, while comparing the results with the external nozzle predicted values.

Chapter 3 : Experimental Set-up and Procedures

3.1 Introduction

The current experimental set-up is prepared and assembled in the University of Wisconsin Milwaukee to study the breakup process and factors enhancing it. Two-phase (gas-liquid) flow behavior is investigated through a vertical convergent divergent nozzle, where the breakup phenomena is recorded and studied in detail, while changing the two-phase flow conditions and properties. Since the break-up process happens in a very short period, milliseconds, or less, a high-speed camera (Photron Fastcam Mini UX) is used in the experimental work to collect data. Two main challenges are encountered using a high-speed camera. The first one is that any behavior with a higher frequency than the high-speed camera's frame speed limit will not be recorded. The second challenge is that any droplet with a size less than a Complementary Metal – Oxide - Semiconductor (CMOS) pixel will not be recorded.

3.2 Experimental Set-up Configuration

The environmental operating conditions inside the rocket combustion chamber are enormously severe (very high pressure and temperature). Thus, numerical simulations are usually used to study the two-phase flow inside the rocket. However, experimental work should be conducted first to validate the numerical simulation model. Therefore, two-phase air-water flow inside a channel is used to study the break-up mechanism experimentally. The experimental set-up consists of a water tank, pump, blower, testing channel, flow meters, hoses, and ducts, as shown in Figure 3-1. Two different testing channels' configurations are used; external nozzle and submerged nozzle, both of them will be explained in the next paragraphs.
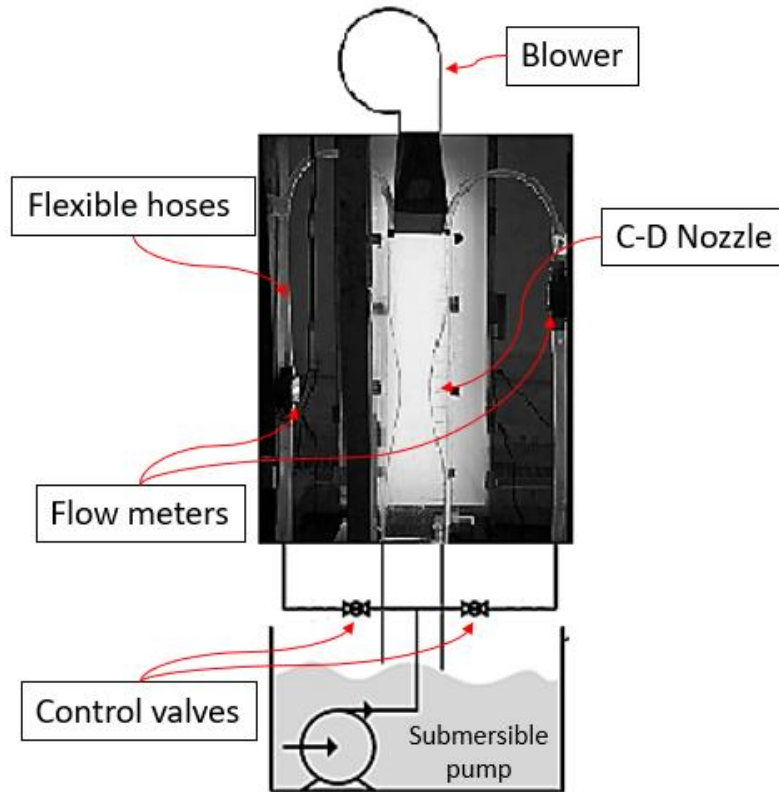
Figure 3-1: Experimental setup schematic

The testing channels is made of clear acrylic plates machined by a CNC machine located

in UWM architecture building (Figure 3-2). The machined parts are shown in Figure 3-3.

Figure 3-2: Machining the set-up covers using UWM CNC machine
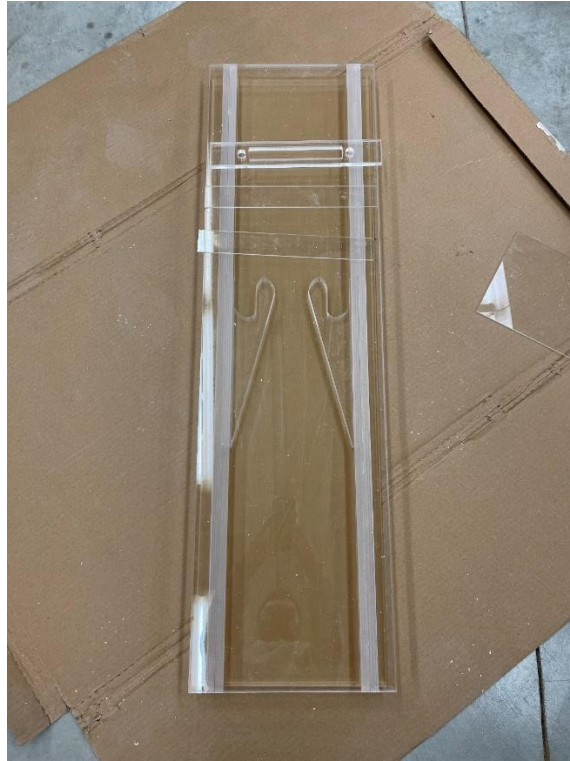
Figure 3-3: Submerged nozzle manufactured parts

The inlet manifolds for water and air are 3-D printed as shown in Figure 3-4. In addition, several

connecting parts are used to assemble the whole setup together such as: PVC ball valves, connector

adapters, tee connectors, flow meters, PVC hoses, and aluminum foil tape.

Figure 3-4: Air and water inlet manifolds 3-D printed parts

External Nozzle: The testing channel comprises three partitions: a 0.2 m straight partition followed by a convergent-divergent nozzle with 0.6 m, then an end with another 0.2 m straight partitions; each partition has 0.2 m width and 0.02 m depth. Water and air are pumped from the upper edge. The blower is used to push the air through 0.16 m of the channel width with adjustable variable flow rates. In contrast, the water is pumped over the channel's two side edges with adjustable variable flow rates. To determine the break-up mechanism properties in terms of the average droplets' diameter and their number, three sections were carefully chosen with approximately the same volume and represent a certain part of the channel geometry. Figure 3-5 introduces these three sections: inlet [from 0.23 to 0.28 m], throat [from 0.46 to 0.54 m], and exit [from 0.73 to 0.78 m] sections.
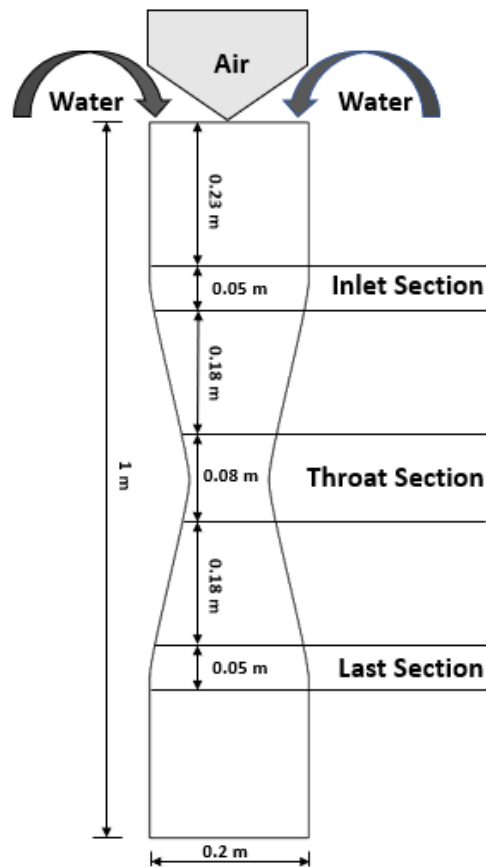
Figure 3-5: C-D Nozzle Configuration

24

Submerged Nozzle: The nozzle design is shown in Figure 3-6 (built using SolidWorks, please see Appendix D for the detailed engineering drawings) which is a reproduction of the cavity of P230 SRM of Ariane V as reported by Stella et al [76]. The new channel set-up was designed and finished as shown in Figure 3-7, to avoid the inclination in the water inlet ports and the preliminary method used before to fix the air and water manifolds with the channel (tape). Also, a flexible duct is used to connect the blower outlet with the new channel set-up. The testing channel comprises three partitions: a 0.4 m straight partition followed by the submerged nozzle insert with its cavity with 0.3 m, then an end with another 0.35 m straight partitions; each partition has 0.2 m width and 0.02 m depth. Water and air are pumped from the upper edge. The blower is used to push the air through 0.16 m of the channel width with adjustable variable flow rates. In contrast, the water is pumped over the channel's two side edges with adjustable variable flow rates. And as before to capture the break-up phenomena in terms of the average droplets' diameter and their number, three sections were selected to represent different certain parts of the channel geometry: inlet [from 0.23 to 0.29 m], throat [from 0.375 to 0.5 m], and exit [from 0.73 to 0.79 m] sections.
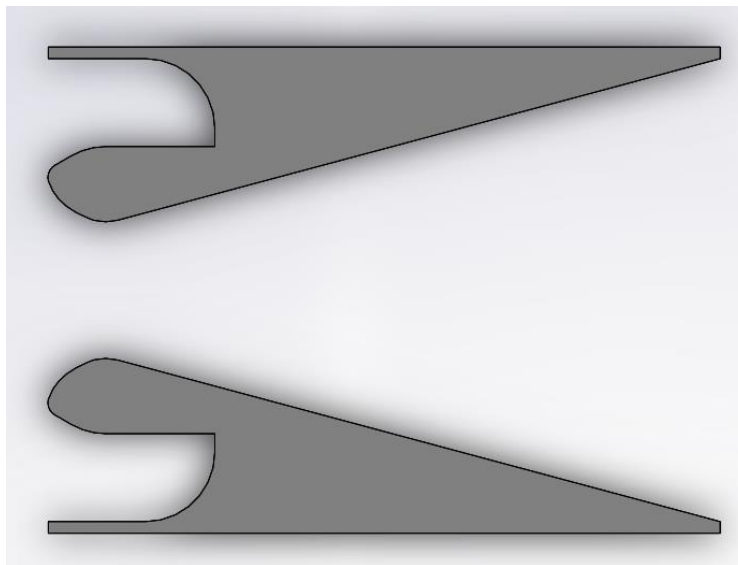
Figure 3-6: Submerged nozzle 2-D sketch
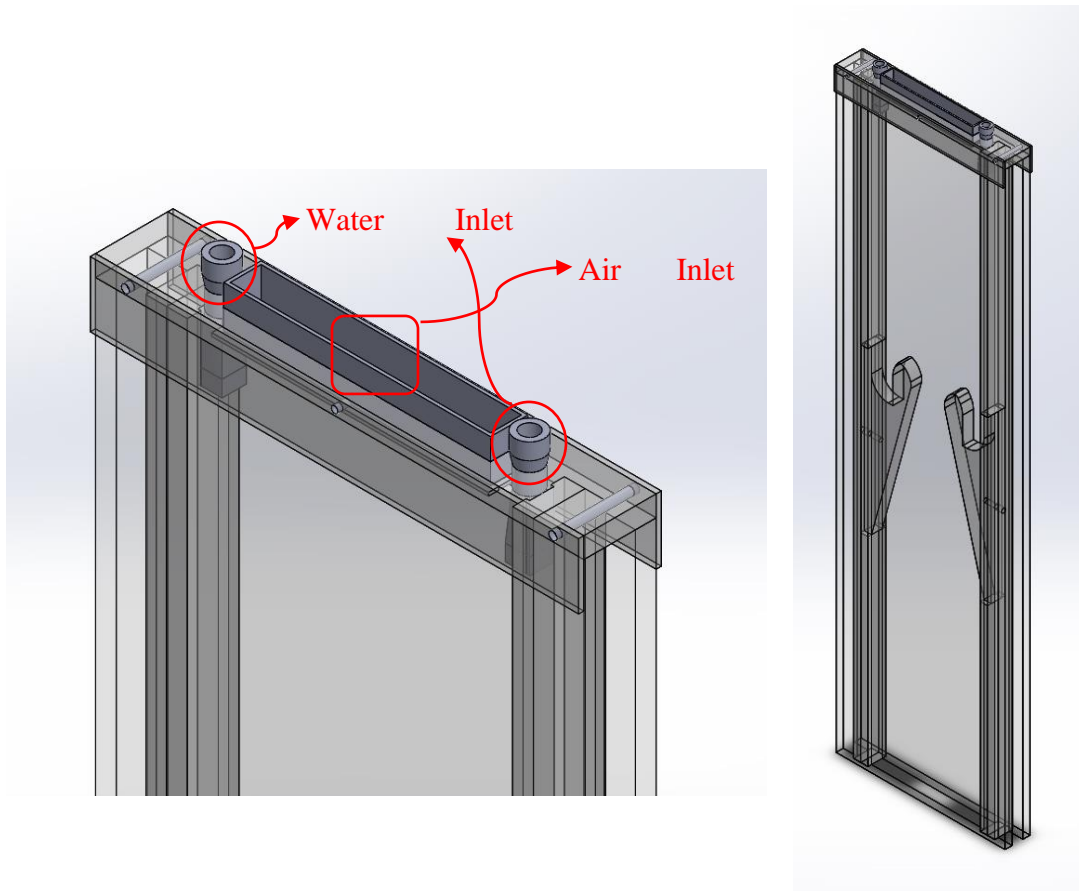
Figure 3-7: New experimental set-up with the submerged nozzle configuration

Recording the break-up mechanism or extracting data from it is not an easy process, primarily because of its concise period (milliseconds or less). And as discussed in the literature, high-speed cameras can be used to capture the break-up mechanism. So, Photron Fastcam Mini UX (Figure 3-8) was utilized to record the event. There are three main parameters to be considered for any high-speed camera: record duration, resolution, and frame rate. Generally speaking, increasing the number of the captured frames per second (frame rate) besides using images with high-resolution results in a decrease of the recorded time, as shown in the high-speed camera specification in Table **3-1**; it is a tradeoff process. Therefore, 2000 fps was selected to ensure acceptable resolution (1280 x 1024 pixels) and suitable recording time (1.09 sec). Also, it is worth mentioning that two challenges were faced while experimenting: the high-speed camera is not

recording any event with a frequency higher than its capturing frame speed threshold, and any

droplet with a size smaller than the Complementary Metal-Oxide-Semiconductor (CMOS) pixel.

Table 3-1: Photron Fastcam Mini UX specifications.

Frame Rate (fps)	Horizontal	Vertical	Recording Duration (sec)	Frames
1000	1280	1024	2.18	2180
2000	1280	1024	1.09	2180
4000	1280	512	1.09	4361
5000	1280	488	0.92	4575
8000	1280	296	0.94	7543
10000	640	240	1.86	18607
20000	1280	120	0.93	18607
40000	1280	56	1	39872
80000	1280	48	0.58	46518
100000	1280	24	0.93	93036
160000	1280	8	1.74	279108

Figure 3-8: Photron Fastcam Mini UX high-speed camera

A pitot tube is used with the experimental set up to calibrate the velocity at the testing channel's

entry. The velocity can be read by using Fluke device, Figure 3-9.
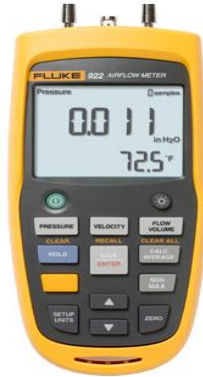
Figure 3-9: Fluke handheld micro-manometer

Vectra L2 DC Centrifugal Pump (submerged) is used to deliver the water from the water tank to the channel inlet, it has a maximum flow of 3100 gph (11,500 lpm) which can be adjusted using the pump driver. The water flow pumped in each branch before entering the testing channel is measured using a flow meter (RESTMO water flow meter)

3.3 Image Processing

As previously mentioned, the break-up process details cannot be captured with the naked eye as it occurs very fast, and to overcome that, a high-speed camera is used to capture the process. But still, although we can differentiate and may be determined, with the captured images' visible observation, if the applied factors enhance the break-up process or not, a post-processing tool is required to acquire precise data such as droplets average diameter and number. And since any case has more than 3000 frames for the break-up process, MATLAB algorithms are used to process all these data.

After revising the experimental images, it was found that a brightness fluctuation exists in them, so an algorithm (Appendix B) was built to scale the images' contrast and to create a video for the captured process. Another algorithm (Appendix C) was developed to process each image

separately, extract the droplets, calculate the average diameter, and count their number, then average all these data for all the captured images. Figure 3-10 depicts the followed procedures to process the captured images and collect the droplets' number and diameters.
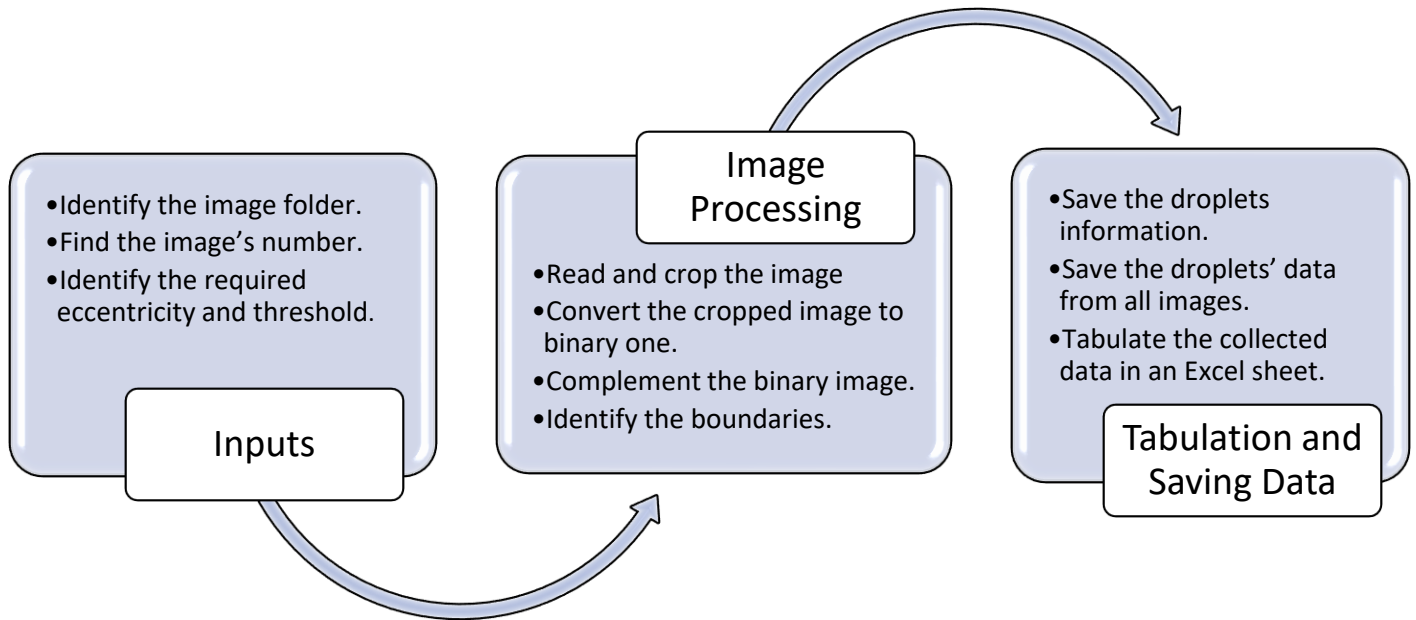
Figure 3-10: Image processing (Enabling algorithm) workflow

Several attempts were conducted to find the threshold for each experimental images set. The threshold value is controlled by capturing all the image details without magnification or reduction of the captured boundaries. Since the inlet water free surface edge is known (12 mm), the threshold was validated by determining its length using the current algorithm (12-pixel length or 13 mm) as shown in Figure 3-11.
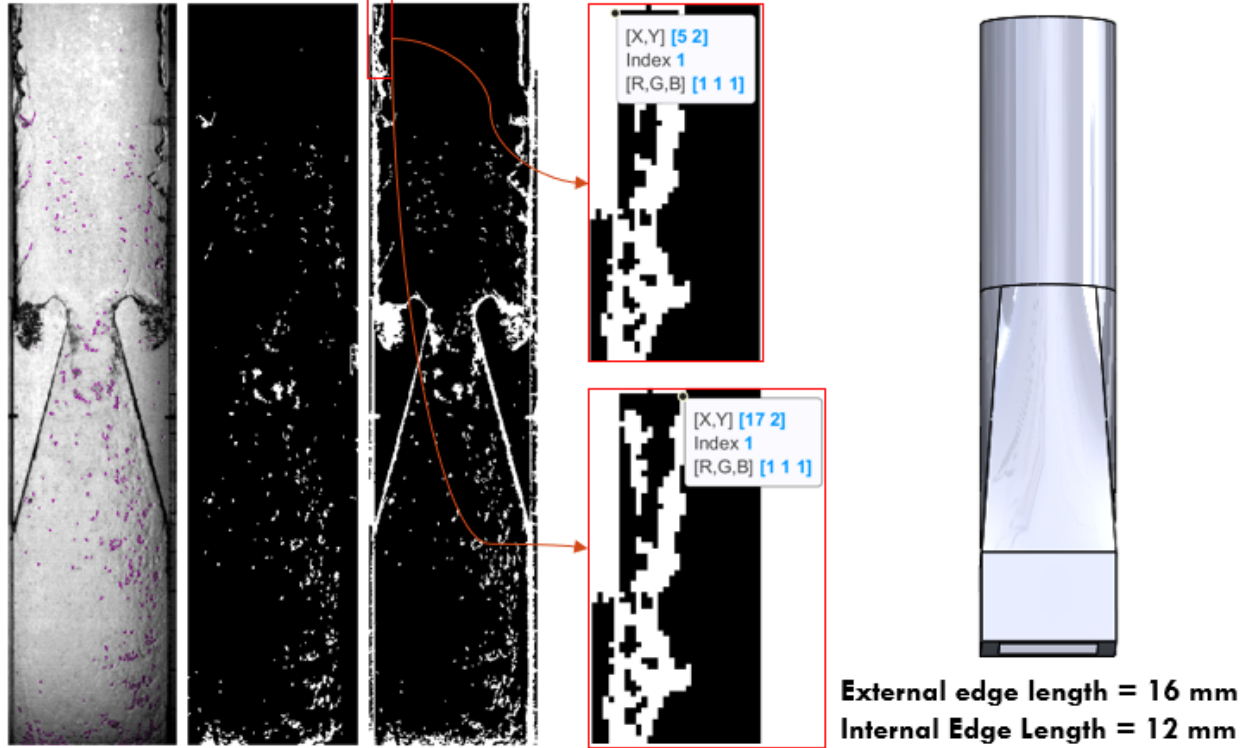
Figure 3-11: Threshold selection process

3.4 Experimental Work Error Analysis

The results obtained from the experiments will be associated with some errors due to the measurement devices accuracy and the high-speed camera capturing process. The water flow rate is measured using flow meters with accuracy of ±5%, while the air flow velocity at the testing channel inlet is measured using Fluke handheld micro-manometer with ±2.5%. The error in the breakup capturing process can be attributed to four sources. The high-speed camera has a resolution of (1280 x 1024 pixels), the 1024 pixel in the vertical direction captures 1000 mm (testing channel length), in other means each pixel represent 0.977 mm. So, the first error source is the camera resolution and is measurable with ±0.977 mm. The second error source is the droplets elongation (blurring) due to the camera exposure time. The camera has a Megapixel CMOS Sensor and a shutter speed of 3.9 microsecond. So, the elongation in the droplet's diameter can be

determined by multiplying the droplet velocity by the shutter speed, however, the individual droplets' velocity can't be calculated using the current experimental set-up. The maximum water droplets velocity will be less than the adjacent air velocity, and since the air velocity within the testing channel ranges from 20 m/s to 85 m/s (at throat for the 40 m/s case), the elongation error ranges from 0 mm to 0.3 mm (worst case scenario). The last two error sources are not measurable, one is due to the 3-D testing channel configuration while recording a 2-D images. The droplets can overlap each other and affect the captures number of droplets and diameters. While the other can occur when two droplets or more with diameters smaller than 1 mm are in two adjacent pixels, so they will appear as one droplet with larger diameter. All the previous mentioned error measures are related to the droplet itself, however since the droplets number are in the range of 0.5 – 1 million, the average error in the experimental results is not exactly determinable and it will range from 1.3×10^{-6} to 1 mm.

Chapter 4 : Investigation of Liquid Droplet Flow Behavior in a Vertical Nozzle Chamber

4.1 Numerical Model

STAR CCM+ software package software was used to simulate the two-phase subsonic break-up process in the C-D nozzle. twelve cases were simulated; six of them were used for comparison with the experimental results to validate the numerical model, while the other six were used to discuss the surface tension and air flow acceleration effects. The computational domain is shown in Figure 4-1 and is discretized with the trimmer model. In addition, the meshes near walls were refined by adding ten prism layers to solve the fluid details near walls and account for the boundary layer effect (y+~1, as demonstrated in Figure 4-1). Four different cell sizes were used to create a mesh independence study, as shown in Table 4-1. The study objective compares the separated droplets' average diameter and number for the whole nozzle volume at each cell size.

Table 4-1: Independent study for several mesh base sizes

Mesh base size (m)	Mesh count (Millions)	Average Diameter Error (%)	No of Droplets per Frame volume Error (%)
0.000955	4.6	8.71	41.096
0.0008	7.6	11.41	27.38
0.0007	11	13.92	-18.39
0.0006	17.2	14.42	-19.64

It was found from Table 4-1that a cell size with 0.0007 m achieves an acceptable error percentage (~18-19%) and maintains a good tradeoff between accuracy and simulations time cost. Since our cases includes a two-phase flow field, the LES model was used because it can predict turbulence behavior better [43-45]. The CFD physics was resolved using Navier-Stokes equations and Large Eddy Simulation (LES) as a turbulence model. The LES transient model solves the large-scale turbulence eddies directly similar to the direct numerical solution (DNS), while models

the small-scale turbulence eddies [46-52]. This model is following the Kolmogorov hypophysis where at sufficiently high Reynolds number, a range of scales, at which the energy is neither produced nor dissipated but simply transferred from larger scales to smaller ones, exist. In other words, these small scales simply transfer any energy passed to them. So simply if we cut this energy flux at intermediate point and provided a proper dustbin for the energy flux, perhaps the larger scales will not notice the absence of the smaller scales. The LES model has the closest accuracy compared to the direct numerical solution; however, it is very computationally expensive due to its complicity and fine mesh requirements. The solved equations for the LES model are based on spatial filtering not on averaging process as per the Reynolds averaging Navier Stokes equation (RANS). Each solution physics quantity is divided into a filtered value $\tilde{\phi}$ and a sub grid value ϕ'

$$\phi = \tilde{\phi} + \phi' \tag{1}$$

The filtered values are plugged in the Navier Stokes equation which is arranged in a form similar to the RANS equation. Where the turbulent stress tensor represents the sub-grid scale stresses. These stresses are modeled using Boussinesq approximation as per the following:

$$T_{SGS} = 2\mu_t S - \frac{2}{3}(\mu_t \nabla.\tilde{v})I \tag{2}$$

Where S is the mean strain rate tensor and computed from the resolved velocity field, I is the identity tensor, and $\tilde{v}$ is the filtered velocity.

The sub-grid scale model is used to dissipate the right correct amount of energy from the large scales by describing the sub-grid scale turbulent viscosity μ_t. In this study, the WALE (Wall-

33

adapting local eddy viscosity) sub-grid scale model is used. It is similar to the Smagorinsky sub-grid scale model but with less sensitivity to the model coefficient and gives accurate scaling at walls.

$$\mu_t = \rho \Delta^2 s_w \tag{3}$$

where the Δ, and s_w are the length scale or grid filtered width, and deformation parameter, respectively. The length scale is described based on the cell volume as:

$$\Delta = \begin{cases} C_w V^{\frac{1}{3}} & if\ length\ scale\ limit\ is\ not\ applied \\ \min\left(\kappa d, C_w V^{\frac{1}{3}}\right) & if\ length\ scale\ limit\ is\ \ applied \end{cases} \tag{4}$$

C_w is a model coefficient and equals to 0.544 as a default value (based on the literature) which works well for the flow inside channels and the isotropic homogeneous decaying turbulence. While the deformation parameter is calculated from the resolved velocity field.

The two-phase flow field is solved using the Eulerian multi-phase approach. The Eulerian multiphase model is simulating each distinct phase with its own set of conservation equations. The pressure is considered constant in all phases, while the volume fraction represents the share occupied by each phase in the fluid domain. And since we are concerned with the break-up process and having a sharp interface between the two fluids (immiscible) [53-57], the volume of fluid (VOF) model was used and coupled with the implicit unsteady solver to capture the break-up process. The VOF model is usually used for simulating the sharp interface between two immiscible fluids [53-57]. The distribution of different phases in the fluid domain using the VOF model is defined by each phase volume fraction within each cell,

$$\alpha_i = \frac{V_i}{V} \tag{5}$$

where, V_i is the phase volume within the cell, while the summation of different phases volume fractions must equals one.

$$\sum_{i=1}^{N} \alpha_i = 1 \tag{6}$$

where N is the number of all phases existing in the fluid domain. The cell may include only one phase from the available phases or multi-phases based on the α_i value. Each cell with two or several phases includes interface between them, and its properties can be calculated as a mixture as follows:

$$\rho = \sum_i \rho_i \alpha_i \tag{7}$$

$$\mu = \sum_i \mu_i \alpha_i \tag{8}$$

$$C_p = \sum_i \frac{(C_p)_i \rho_i}{\rho} \alpha_i \tag{9}$$

Each phase i distribution is calculated using the phase mass conservation equation, however in the case where only two phases exist in the fluid domain (our case), the phase mass conservation is solved only for the first phase in each cell, then the second phase volume fraction is calculated to keep a volume fraction summation of 1 in the cell.
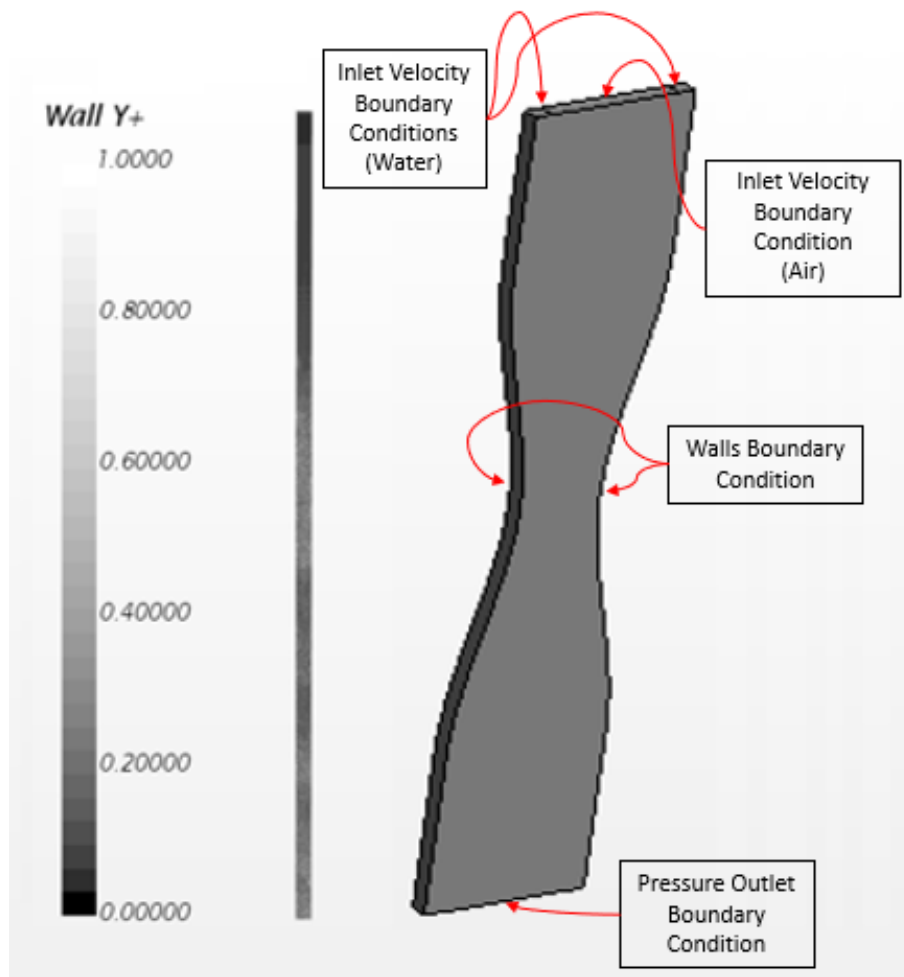
Figure 4-1: The numerical model computational domain (C-D Nozzle) and Y+ distribution over the wall

4.2 Liquid Surface Tension Reduction Effect on Water Droplet Flow Behavior

4.2.1 Study Methodology

In this part, three different air velocities were used in the experimental setup associated with a constant water flow rate (0.000315 m^3/s), where the air velocity effect on the break-up process was studied. Three numerical cases with the same experimental boundary conditions were validated using the experimental data in terms of the separated particle number and average diameter per the nozzle's different sections. Finally, three numerical cases with a 50 % reduction

in the water surface tension were performed to study reducing the surface tension on the break-up process. The numerical simulations with normal water surface tension will be named NWST, while the other cases with a 50% reduction in the surface tension will be mentioned as RWST. Also, the break-up mechanism will be discussed in light of the Weber number definition as shown in Eq. 10.

$$We = \frac{\rho_{air} V^2 r}{\sigma} \tag{10}$$

Where (ρ_{air}) is the air density, (V) is the two-phase velocity difference (relative velocity) between the two fluids (V_{air} - V_{water}), (r) is the droplet radius, and (σ) is the liquid surface tension.

The numerical model settings are as per the pervious section, also Table 4-2 gives a summary of the used simulation parameters.

Table 4-2: The numerical simulation setup parameters

Parameter	Value
Mesh count	11 M (Approximately)
Air inlet velocity	20, 30 and 40 (m/s)
Water inlet velocity	0.788 (m/s)
Water flow rate	3.15 x 10^{-4} (m^3/s), 5 gpm (each side)
Outlet pressure	101.325 (kPa)
Time step	1 x 10^{-5} (sec)
Enabled models	- Three-dimensional - Gravity, Constant density / Gas - Implicit unsteady, segregated flow - Turbulence, LES - Eulerian multiphase, Multiphase interaction, volume of fluid

4.2.2 Results and Discussion

Image Post Processing Outcomes. The images (2180 and 5000 for each experimental and numerical case, respectively) of the break-up process associated with each velocity were post-processed using two algorithms, as indicated before.

Figure 4-2 shows the first code results, while Figure 4-3 presents two sets of pictures for the numerical and experimental results. Each set introduces three different images. The first image on the left represents the original image after adjusting the contrast to scale. The second image shows only the captured droplets in white, and the last image shows the original image combined with the captured droplets drawn in purple color.

(a)   (b)
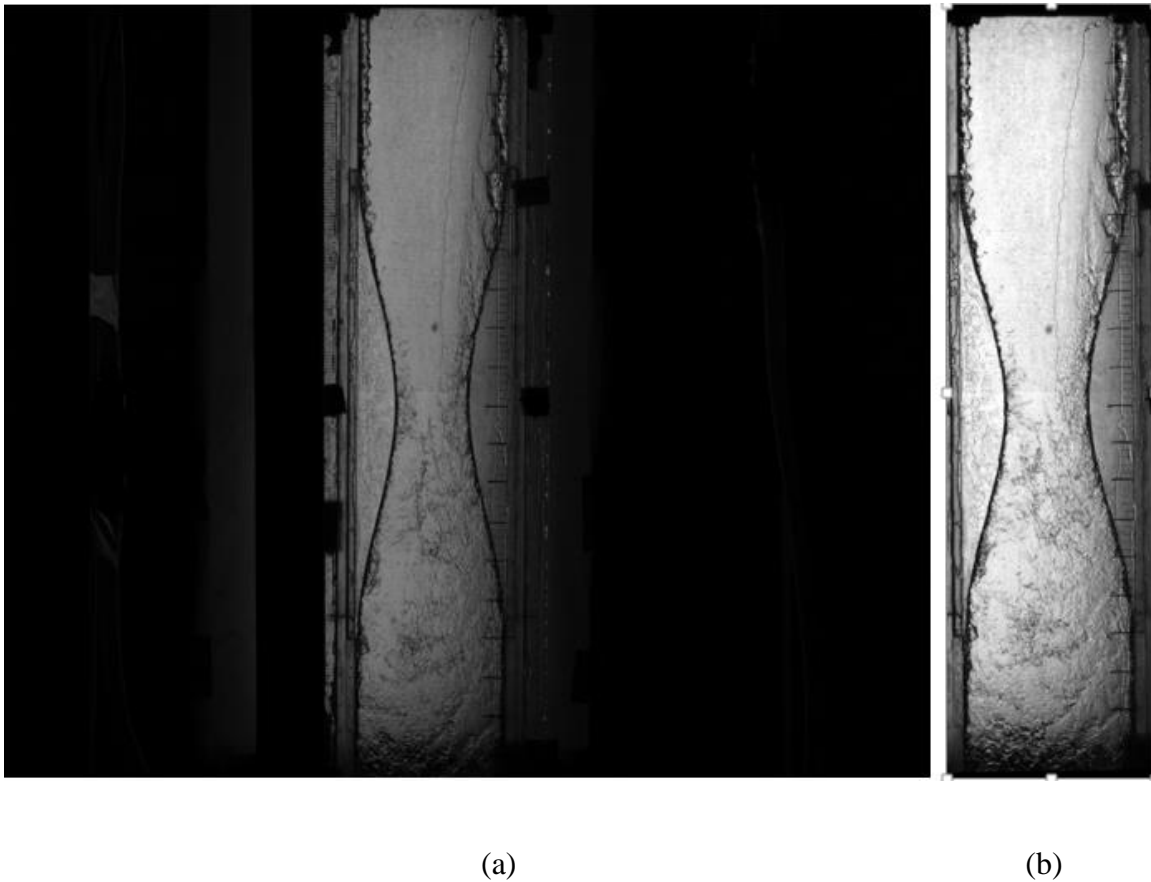
Figure 4-2: The original (a) and the adjusted (b) images using the post processing algorithm
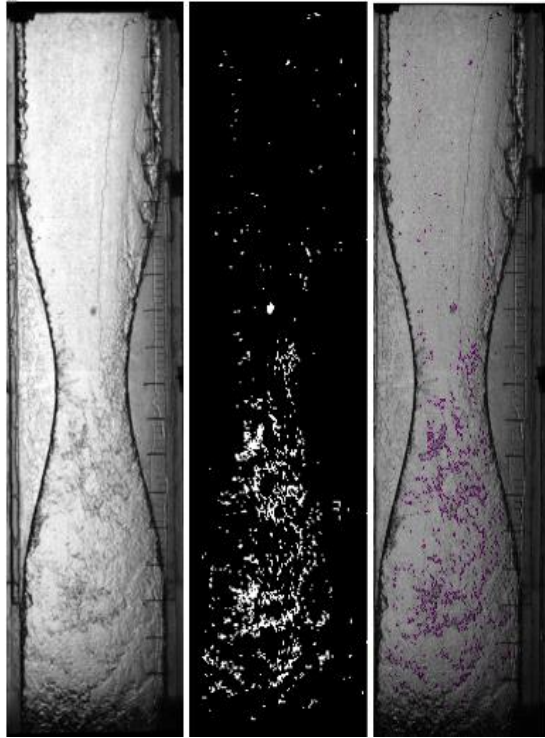
(a) Experimental
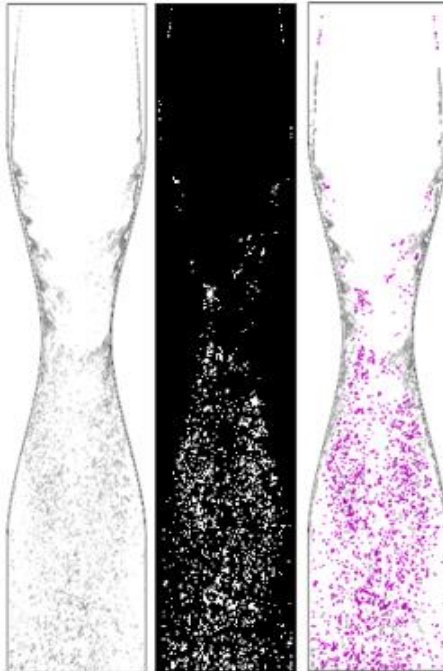
(b) Numerical

Figure 4-3: Image processing sample results

Experimental Outcomes. Three experimental cases were tested at different air velocities 20, 30, and 40 m/s. Figure 4-4, 4-5, 4-6 represent a visualization of the C-D nozzle's break-up phenomena at the different air velocities. It can be observed that as the air velocity increases, the water surface starts to move faster, deform, and major water bodies are separated. Then these major water bodies break up into smaller droplets. Moreover, it is noticed that the break-up process evolution moves up toward the liquid inlet section with increasing the inlet air velocity, 280 – 230 – 130 mm from the inlet section, causing an increase in the droplet travel length and a higher chance for a successive break up to smaller droplets.

Overall, the liquid break-up process in terms of the number of the observed droplets is magnified by increasing the air velocity. However, to get accurate details about the separated particle number and average diameter, the image processing tool was used as indicated before. Also, some figures were created from the obtained data, as discussed below.

t (msec)	0	10	20	30	40	50	60
Images							
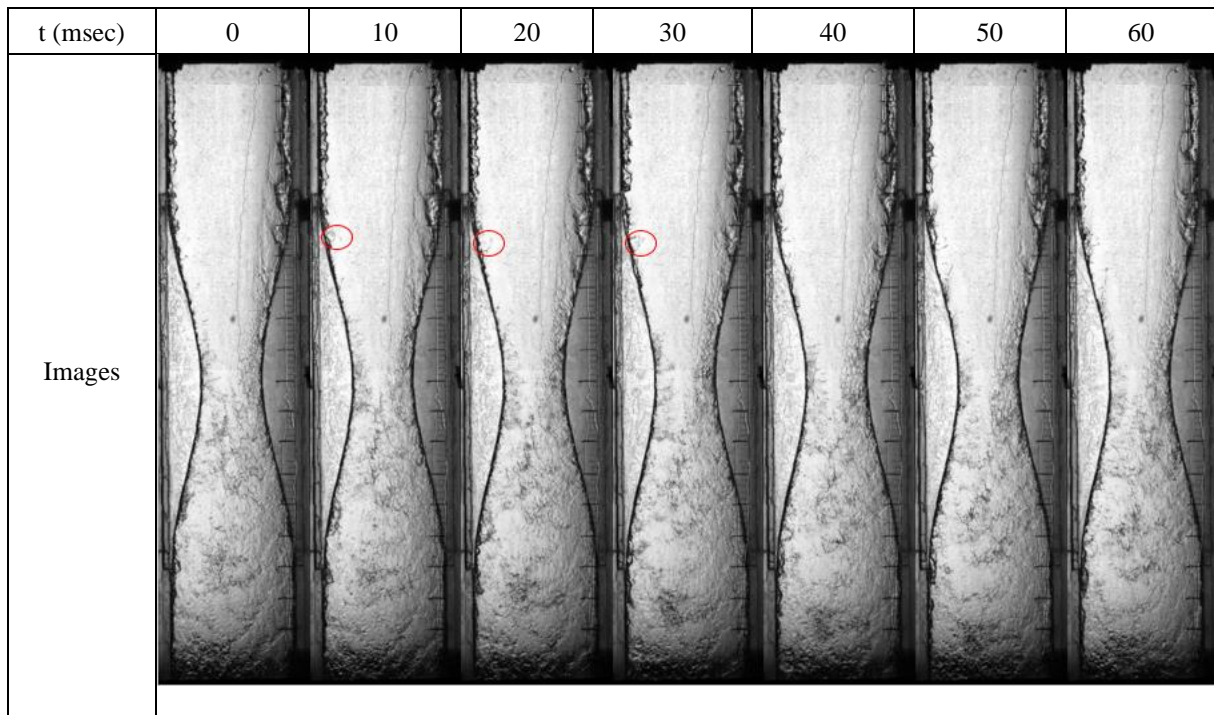
Figure 4-4: Experimental results for air velocity, 20 m/s and normal water (surface tension 0.072 N/m)

t (msec)	0	10	20	30	40	50	60
Images							
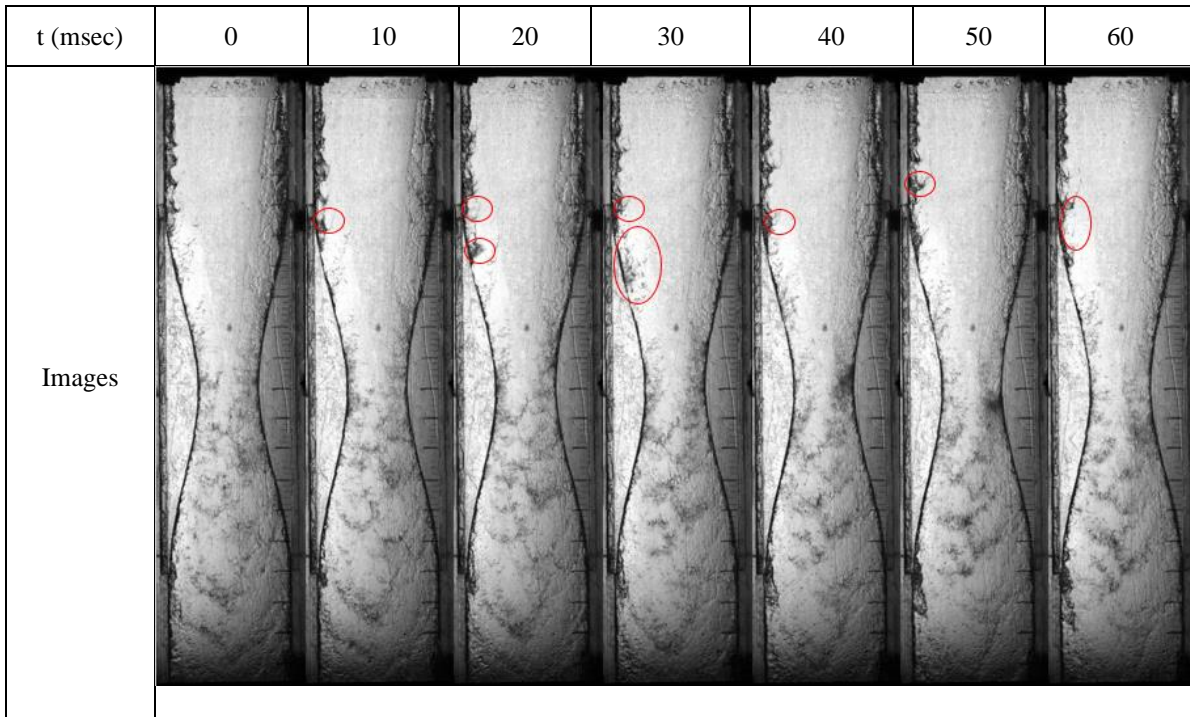
Figure 4-5: Experimental results for air velocity, 30 m/s and normal water (surface tension 0.072 N/m)

t (msec)	0	10	20	30	40	50	60
Images							
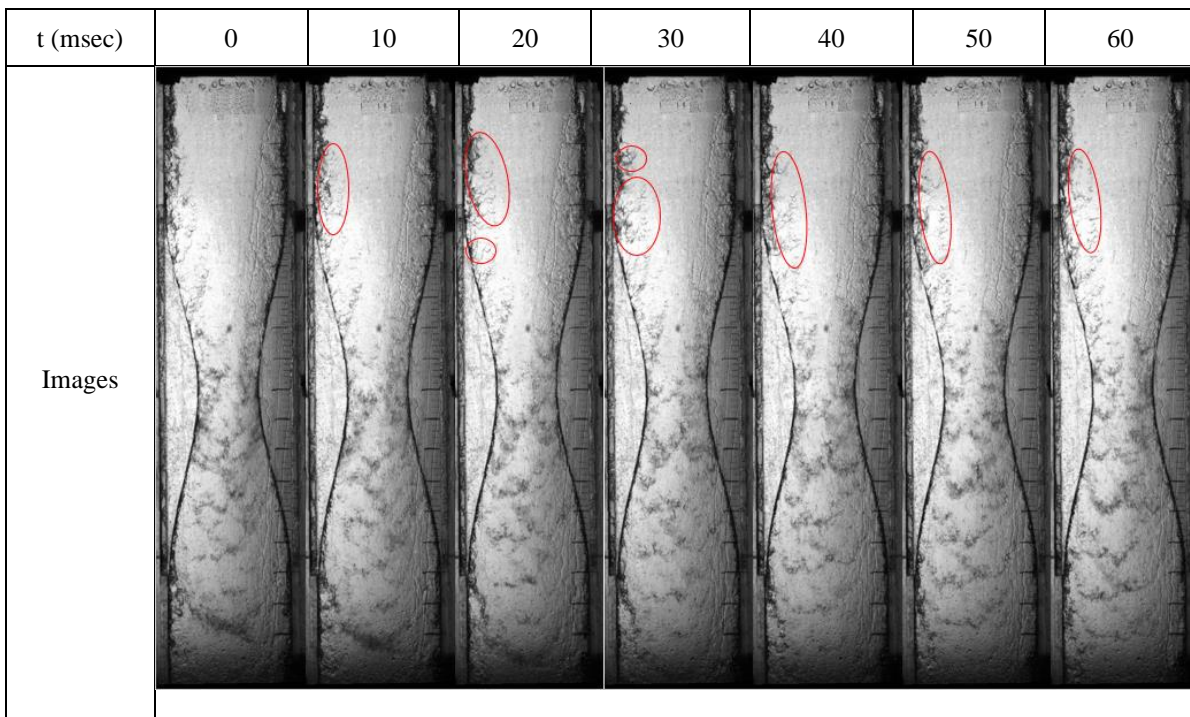
Figure 4-6: Experimental results for air velocity, 40 m/s and normal water (surface tension 0.072 N/m)

Two different analysis schemes were used. The first one compares the droplet's average diameter and number per the total volume of the C-D nozzle (frame) for the different air velocities. The other is comparing the same parameters but for different sections (inlet, throat, and exit) inside the C-D nozzle.

Using the first approach, it is found that increasing the air velocity causes a higher number of separated droplets. On the other hand, the average diameter of droplets decreases, as shown in Figure 4-7 & 4-8. A plausible reason is when the air velocity increases, the liquid body's surface is speeding up, causing more break-up of major separated liquid bodies—these liquid bodies break-up into smaller droplets with high air velocities.
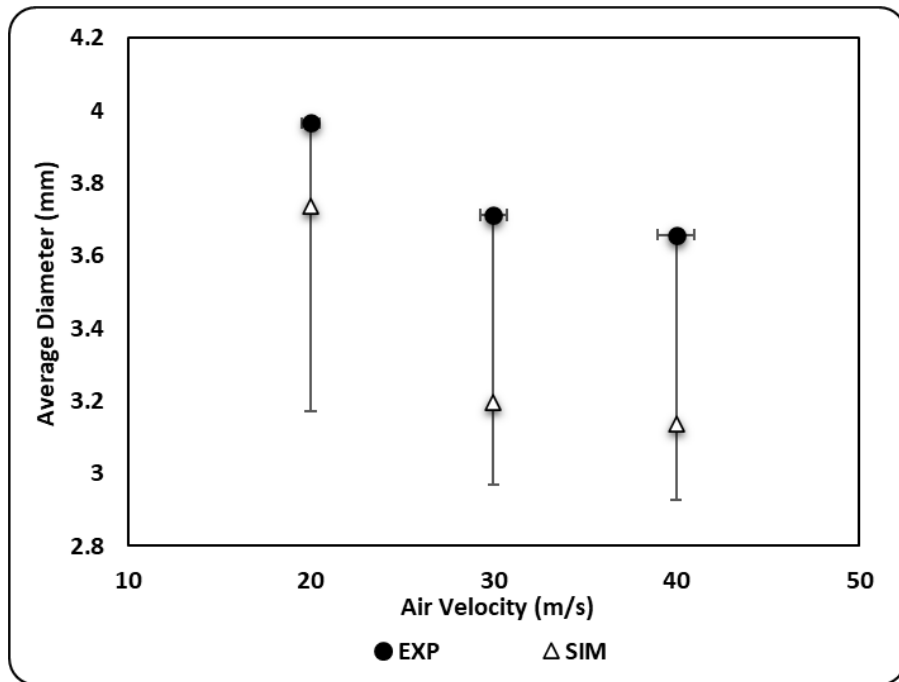
Figure 4-7: Experimental and numerical average droplet diameter throughout the entire testing channel at different air velocities
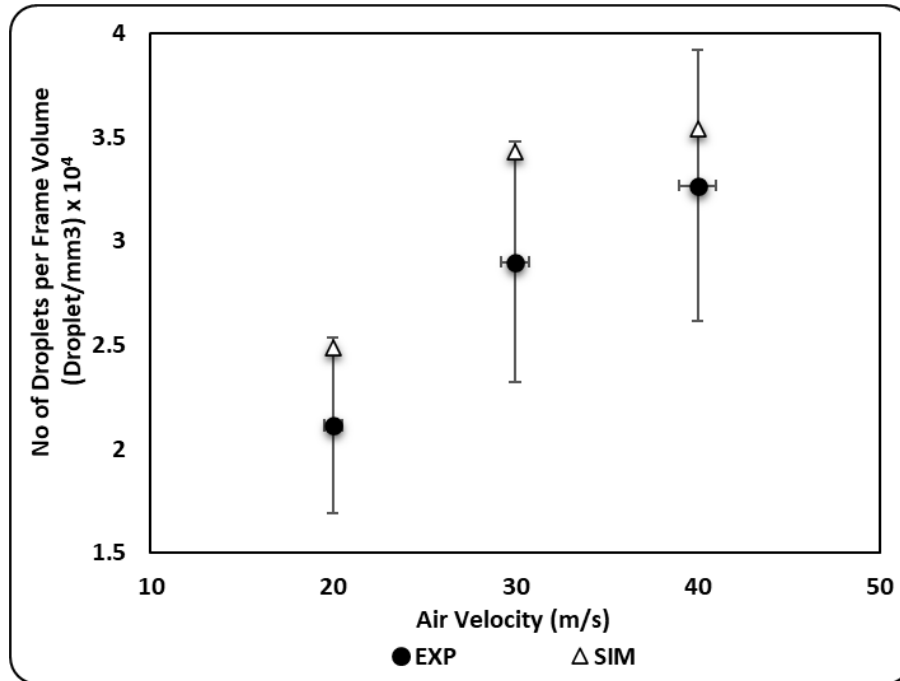
Figure 4-8: Experimental and numerical number of droplets throughout the entire testing channel per its volume at different air velocities

For the other approach, Figure 4-9 & 4-10 & 4-11 & 4-12 show the average diameter and the number of droplets in the inlet, throat, and exit sections. Hence the following can be observed for each section:

Inlet section: the number of droplets separated from the main liquid body increases with increasing the air velocity. On the contrary, the average diameter decreases, which can be explained with the Weber number definition. Higher air velocity means a higher weber number and higher liquid tendency to break up into smaller droplets. This confirms that the break-up phenomenon moves up toward the liquid inlet section with increasing inlet air velocity, as mentioned before.

Throat section: the air velocity increases more in this section because of the convergent part of the nozzle, which leads to more droplet's separation, in other words, bigger average diameter and higher droplets' number compared with the inlet section. The number of droplets increases with increasing the inlet air velocity as the break-up process starts earlier with high air velocities, and

43

weber number rises in the throat leading to more separated water bodies. As evidence, it can be observed that the average diameter is less with higher air velocities compared to the inlet section. Also, it can be noticed that most of the break-up process takes place in this section.

Exit section: in this section, further break-up of the separated droplets from the throat section into smaller droplets, and as the air velocity increase, the tendency of the big droplets to break-up is greater. It was expected that the smallest average diameter is detected at the highest air velocity (40 m/s). One of the significant results obtained is that the number of droplets in 30 m/s air velocity is higher than that one obtained from 40 m/s. With this high velocity (40 m/s), two main reasons are responsible for reducing the total number of droplets. The first one is with this high velocity; the merging chances are higher compared to the 30 m/s case. The second one, with the increase of air velocity, the momentum is increasing. This increase in momentum is responsible for dragging the separated water bodies from the previous section at high velocity without enough time to accumulate at the low-velocity section downstream the throat, as shown in Figure 4-13 & 4-14. However, the break-up process intensity is better in 40 m/s, as the break-up process starts earlier and higher in the previous sections.
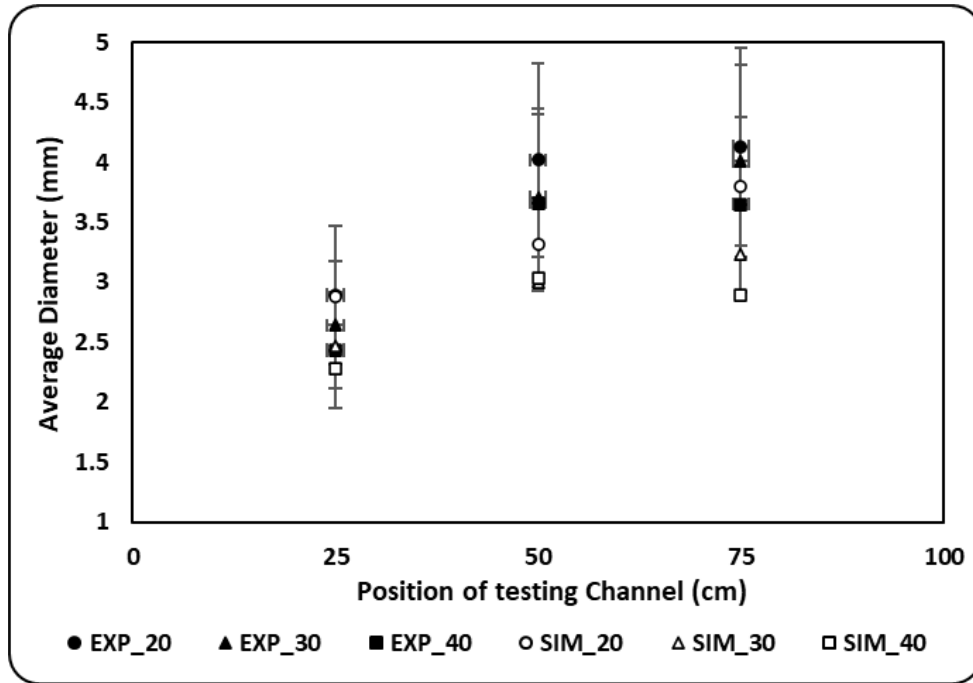
Figure 4-9: Experimental and numerical average droplet diameter at different sections of the testing channel and different air velocities
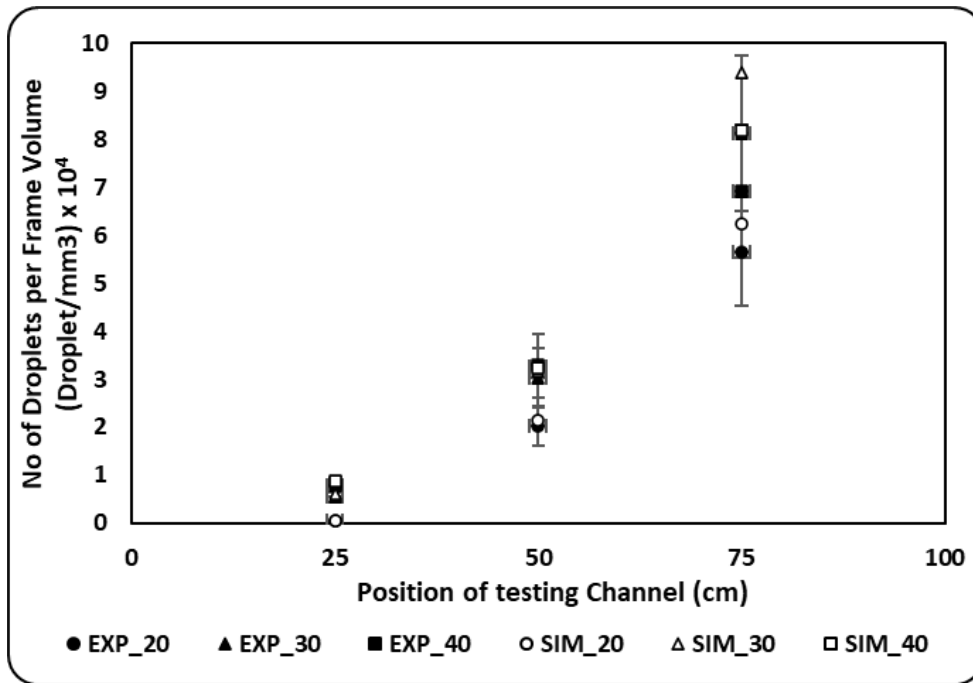
Figure 4-10: Experimental and numerical number of droplets at different sections of the testing channel and different air velocities.

45
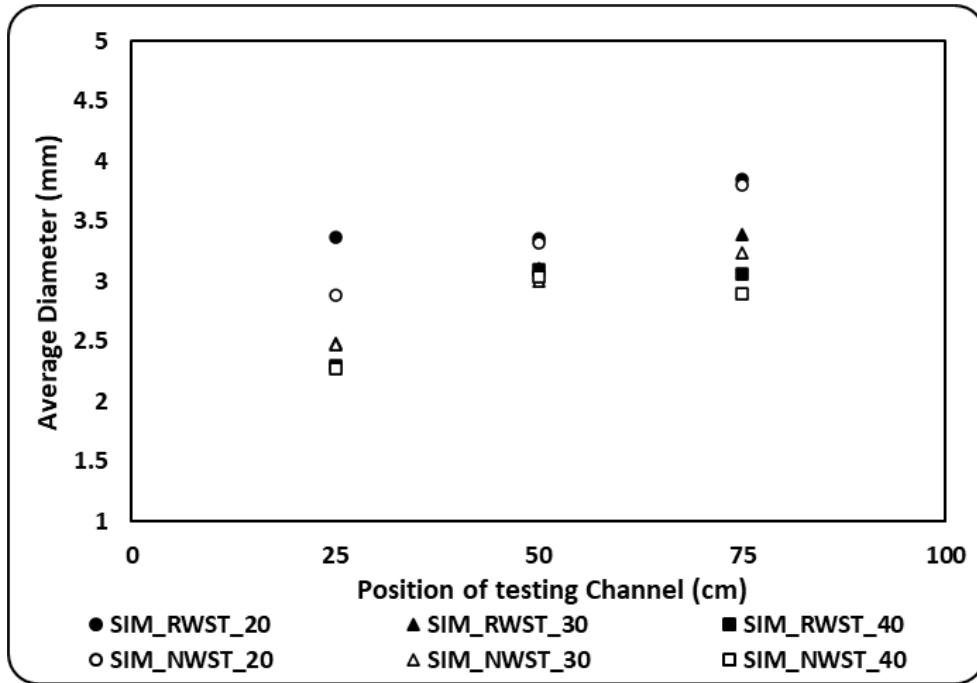
Figure 4-11: Average droplet diameter at different sections of the testing channel, different air velocities and different water surface tension.
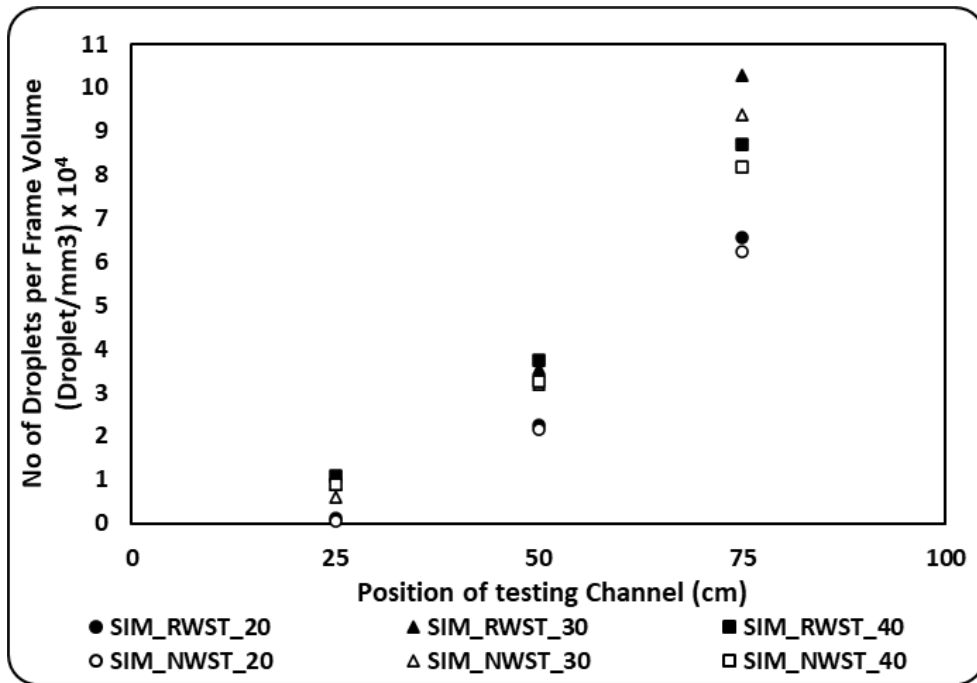
Figure 4-12: Number of droplets at different sections of the testing channel, different air velocities and different water surface tension.

46
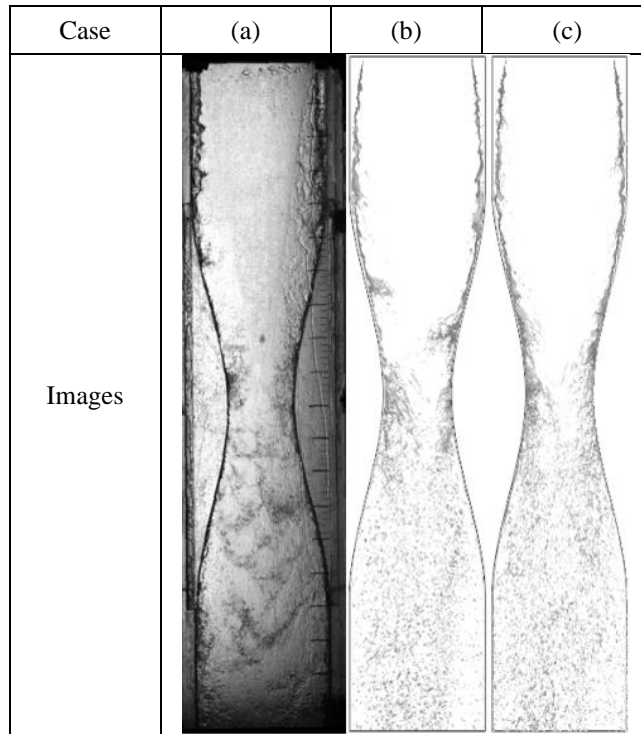
Figure 4-13: The breakup shape pattern at air velocity of 30 m/s, (a) Experiment with NWST, (b) Simulation with NWST and (c) Simulation with RWST
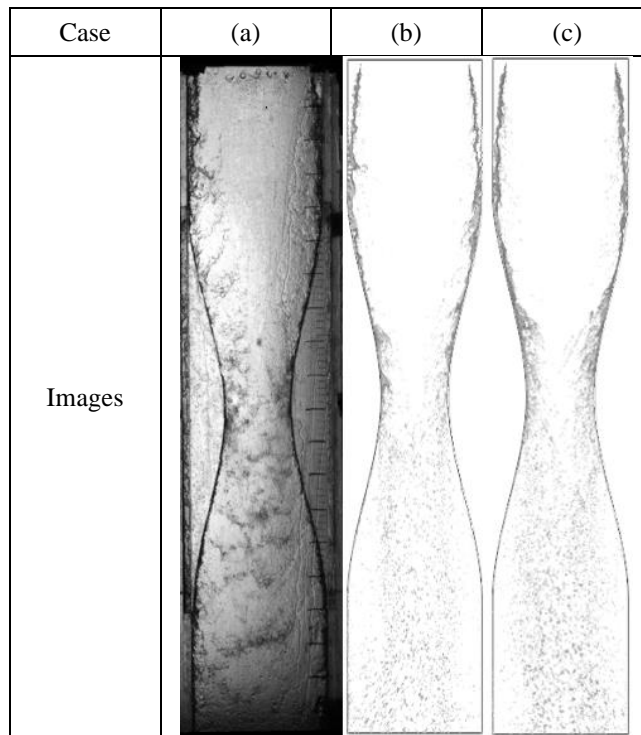
Figure 4-14: The breakup shape pattern at air velocity of 40 m/s, (a) Experiment with NWST, (b) Simulation with NWST and (c) Simulation with RWST

Numerical Simulation and Validation. The numerical model results were validated using the obtained data from the previously discussed experimental cases. Two parameters were used in the validation process: the average droplets diameter and the droplets' number in the whole testing channel and different sections through the channel. Figure 4-15 provides visual images of the break-up shape pattern at an air velocity of 20 m/s; experimentally, numerically for NWST, and numerically for RWST, while Figure 4-13 & 4-14 show the same visual images at air velocities of 30 and 40 m/s. These figures show good agreement between the experimental and the numerical results. However, it can be noticed that the break-up evolution starts later in numerical cases compared with the experimental cases. Comparing the values of the aforementioned parameters above shows that the numerical average diameters for the different air velocities are less than the experimental ones with 6% to 15 %, and the numerical droplets' numbers are higher with 8% to 18%. However, it can be observed from Figure 4-14 that the distribution of the droplet, after the nozzle throat section at an air velocity of 40 m/s, is wider in the experimental case compared to the numerical one. As the numerical simulation over predicts the effect of the air momentum in drawing all the separated water bodies in the flow direction. As a result, more separated bodies accumulated near walls after the throat. Also, the error in the average diameters and the droplets' numbers through the different C-D nozzle sections is from 1% to 18%. Accordingly, this numerical model is used in further cases to study the effect of reducing water surface tension on the break-up process.

48

Case	(a)	(b)	(c)
Images			
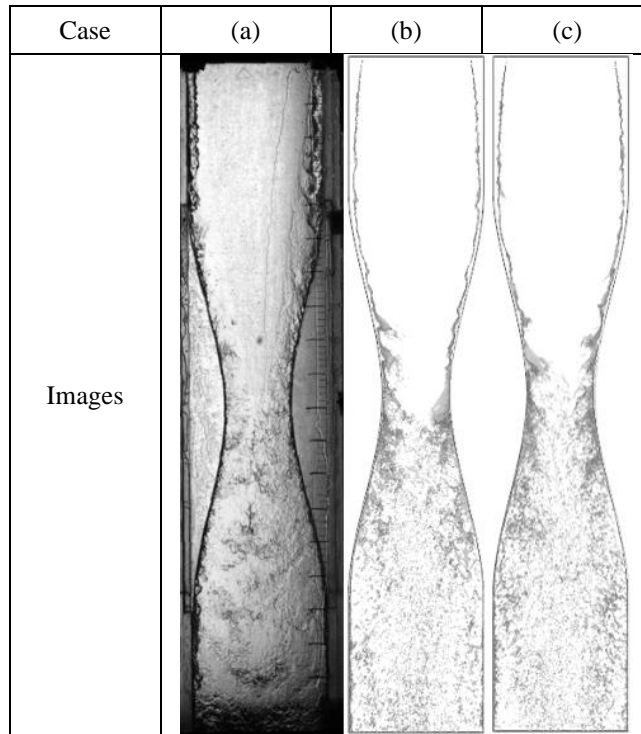
Figure 4-15: The breakup shape pattern at air velocity of 20 m/s, (a) Experiment with NWST, (b) Simulation with NWST and (c) Simulation with RWST

Water Surface Tension Reduction Effect Outcomes. Three cases with 50 % reduction in water surface tension at 20, 30, and 40 m/s were simulated, and the results were compared with the NWST cases. It can be observed from the break-up shape patterns in Figure 4-13 & 4-14 & 4-15 that the RWST cases have higher droplet volume distribution per the C-D nozzle volume compared to the NWST cases. The post-processed data from the algorithms obtained the same results. Decreasing the surface tension means reducing the cohesive forces between water surface molecules, facilitating the break-up process. The Weber number definition can also explain the increase in the break-up process. Weber number is inversely proportional to the liquid surface tension, consequently reducing the water surface tension by 50% doubles Weber number for the same case as shown in Figure 4-16. The break-up process behavior, at different air velocities and different nozzle sections, is the same as discussed before in the experimental and numerical results. Figure 4-17 shows that the average droplets' diameter increase is between 2% to 9%, while the

49

droplets' number increases are only from 1-2% as shown in Figure 4-18. The droplets' characteristics parameters at different nozzle sections, different air velocities, and two water surface tension are presented in Figure 4-11 & 4-12. Compared to the NWST cases, the increase in the average diameter ranges from 0.5% to 17% and from 4 to 100% for the droplets' number for each section volume. Because of the small values for the average droplets' diameter and the number of droplets in the inlet section, it can be observed that the use of percentage change in this section is miss leading as most of the break-up process takes place in the throat and exit sections. The main reason behind this is the high air velocities, which means high Weber number.
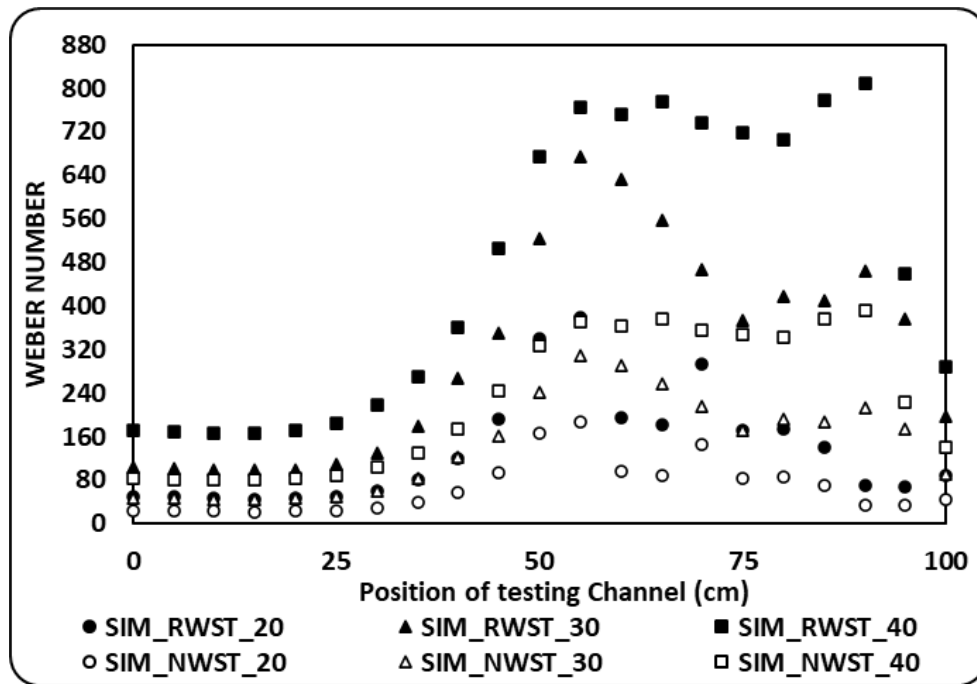
Figure 4-16: Weber Number through the testing channel at different air velocities and different water surface tension
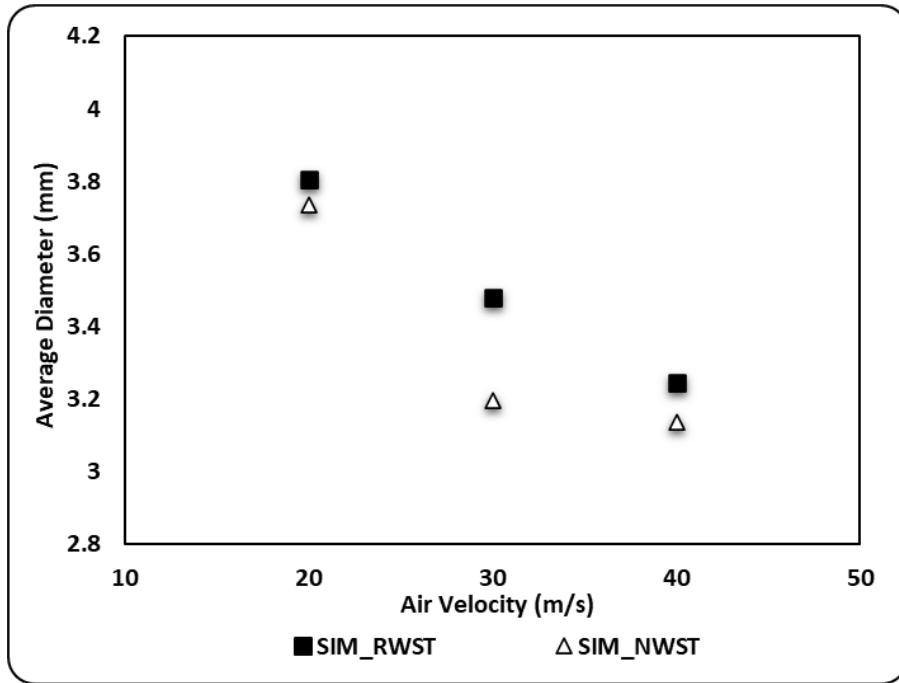
Figure 4-17: Average droplet diameter throughout the entire testing channel at different air velocities and different water surface tension
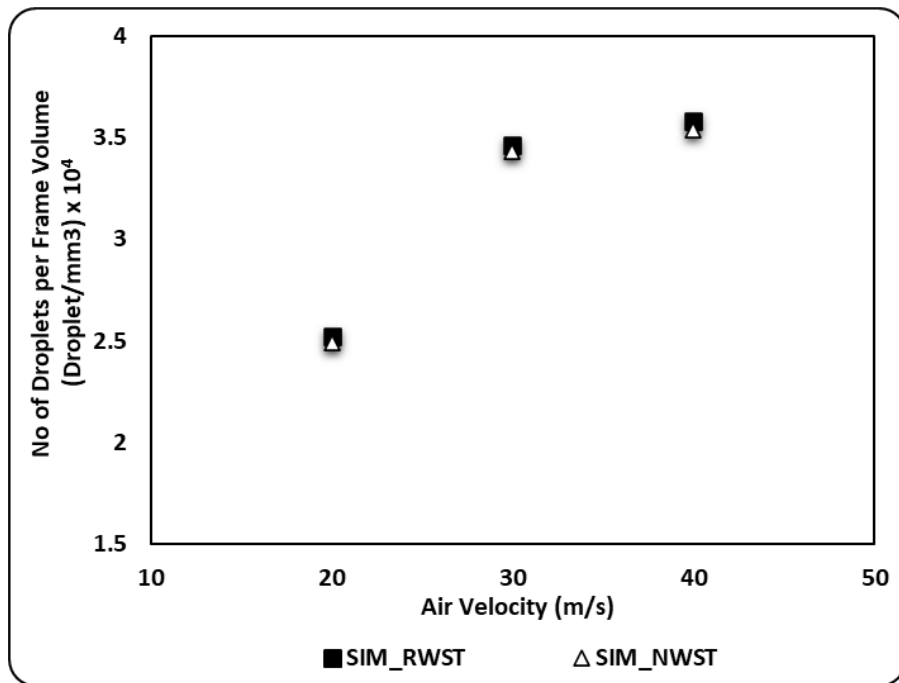
Figure 4-18: Number of droplets throughout the entire testing channel per its volume at different air velocities and different water surface tension

Viscosity Effect Outcomes. Two extra cases were simulated numerically to investigate the viscosity effect on the breakup process. Both cases were at an air velocity of 20 m/s, the first case viscosity is the normal water surface viscosity of 8.9 E-4 Pa.s, while the other case's viscosity is reduced by 50% (4.4 E-4 Pa.s). The Ohnesorge number is a dimensionless number representing the ratio between the fluid viscous, inertia, surface tension forces.

$$Oh = \frac{\mu}{\sqrt{\rho\, \sigma\, D}}$$

Having high Ohnesorge number translates in more dominant fluid internal viscous dissipation, in other words, any provided energy will be used to overcome the fluid internal molecular resistance, and droplet formation will be critical or even impossible. On the other hand, having a lower Ohnesorge number causes lower friction losses due to viscosity forces. Which can be translated in facilitation in droplets separation from the fluid surface, as most of the provided energy used to overcome the surface tension force. Applying the pervious explanation on the current investigated case, reducing the viscosity will reduce the Ohnesorge number, and will cause an increase in the water bodies separation from the fluid main surface. These water bodies will breakup to smaller droplets in the C-D nozzle sections as shown in Figure 4-19. The previous explanations can be interpreted as increasing the Ohnesorge number increases the critical Weber number, in addition to shifting the secondary breakup modes toward higher Weber number regions.

Case	(a)	(b)
Images		

Figure 4-19: The breakup shape pattern at air velocity of 20 m/s, (a) Simulation with normal water viscosity, (b) Simulation with 50% lower water viscosity.

4.3 Air Flow Acceleration Effect on Water Droplet Flow Behavior

4.3.1 Study Methodology

Investigating the exhaust gas's acceleration effect on the break-up process of the aluminum agglomerates before and after entering the exit nozzle is conducted numerically. Still, validation for the numerical model is required before accepting its results. So, three experiments were performed using a constant air velocity (20 m/s) associated with three different water flow rates (1.9, 2.5, and 3.15 * 10^{-4} m^3/s), where the effect of variable water flow rates was studied. The collected data were post-processed and compared with the processed data from numerical models with the same input parameters and boundary conditions for validation. Finally, three additional numerical models were created with the same configuration but with different airflow accelerations. The airflow velocity changes from 20 to 40 m/s. as shown in Figure 4-20, The break-up process duration is 1.333, 1.667, and 2 sec, which means that the flow acceleration decreases from 60 (ACC_60) to 30 (ACC_30) to 20 (ACC_20) m/s^2, respectively. The results of these numerical models were analyzed and compared against the no-acceleration case (Air flows with constant velocity 20 m/s (ACC_0). Also, the break-up mechanism is explained considering the definition of Weber number, as explained before. Weber number represents the ratio between the gas inertia force and droplets surface tension. The numerical model settings are as per section 4.1, also Table 4-3 gives a summary of the used simulation parameters.

Table 4-3: The numerical model used parameters

Parameter	Value
Mesh count	11 M (Approximately)
Air inlet velocity	20 (m/s)

Air flow acceleration	0, 20, 30, and 60 m/s^2
Water flow rate	1.9, 2.5 and 3.15 * 10-4 m3/s
Outlet pressure	101.325 (kPa)
Time step	1 x 10^{-5} (sec)
Enabled models	Three-dimensional, gravity, constant density (gas), implicit unsteady, segregated flow, turbulence, LES, Eulerian multi-phase, multi-phase interaction, volume of fluid

Figure 4-20: Air flow velocity profiles over the time

4.3.2 Results and Discussion

Post Processing Algorithms' Results: More than 36000 and 6500 numerical and experimental images, respectively) for the break-up mechanism were processed by MATLAB algorithms. The experimental images' contrast was first adjusted using the first algorithm (Appendix B). Then, the second algorithm (Appendix C) treated all the experimental and

numerical images where the droplets were marked, extracted, and analyzed. Finally, the collected analysis was tabulated, averaged, and normalized per frame for each case.

Numerical Model Validation: The post-processed data extracted from the MATLAB algorithms and the visual observation for the break-up process images for both experimental (Figure 4-21) and numerical (Figure 4-22) cases were compared. The post-processed data include the droplets' average diameter and number either through the C-D nozzle volume or through certain parts from the nozzle (inlet, throat, and exit).

Case	(a)	(b)	(c)
Images			
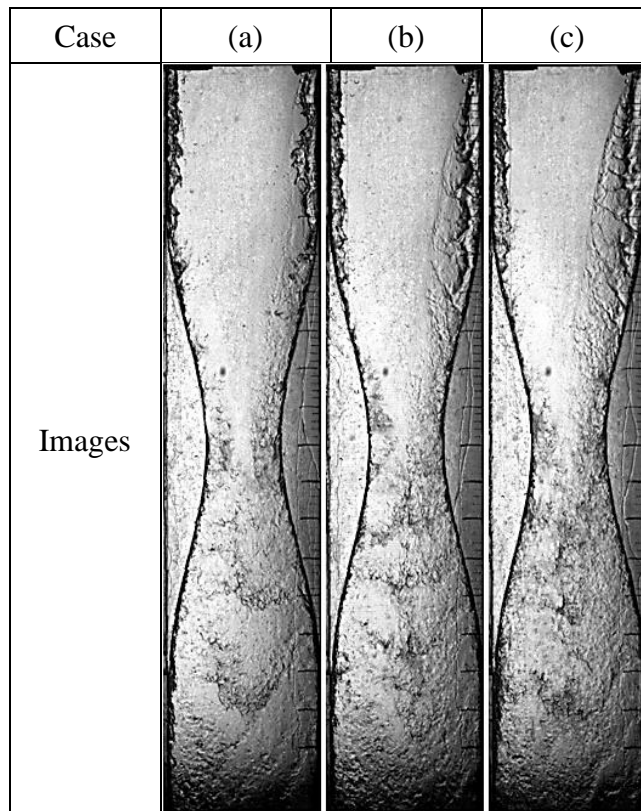
Figure 4-21: Experimental break-up pattern shapes at different water flow rates, (a) 1.9 * 10-4 m3/s, (b) 2.5 * 10-4 m3/s, and (c) 3.15 * 10-4 m3/s.

Case	(a)	(b)	(c)
Images			
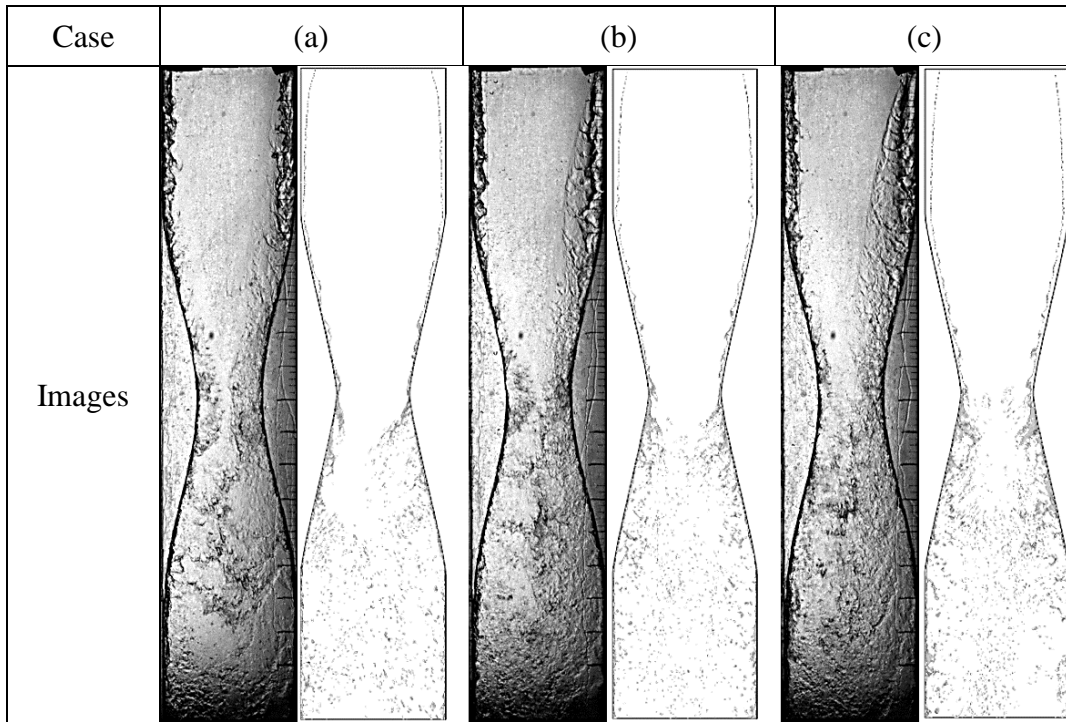
Figure 4-22: Comparison between the experimental (left) and numerical (right) break-up pattern shapes for different water flow rate, (a) 1.9 * 10-4 m3/s, (b) 2.5 * 10-4 m3/s, and (c) 3.15 * 10-4 m3/s

Figure 4-22 presents a comparison between the experimental and numerical break-up pattern shapes for the previously mentioned water flow rates. Visual observation provides an acceptable verification for the numerical results; however, it lacks accuracy. So, the post-processed data were used to create Figure 4-23 & 4-24 & 4-25 to compare the percentile difference in the droplets' average diameter and number.
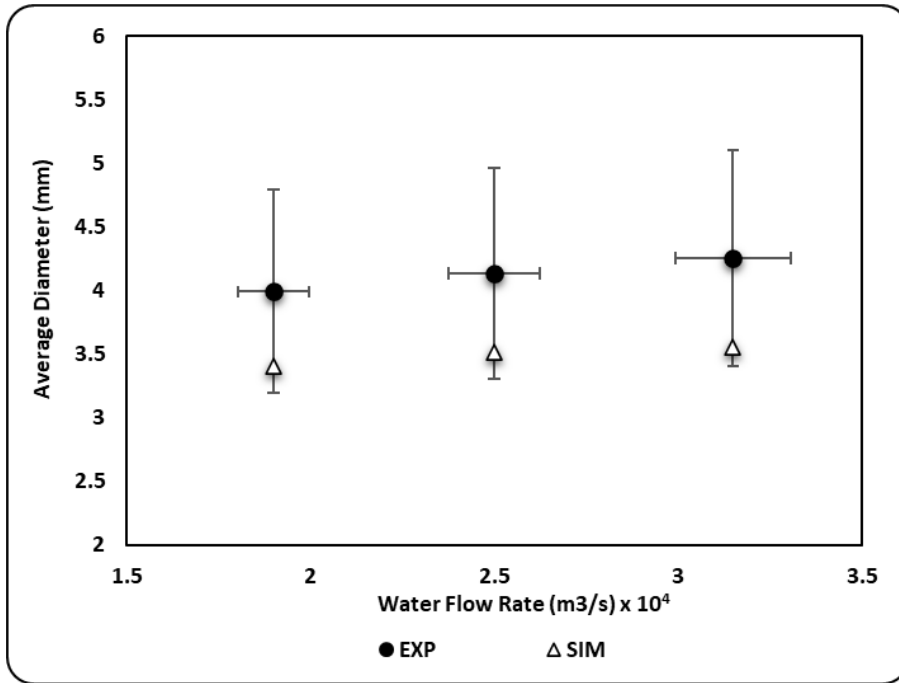
(a)
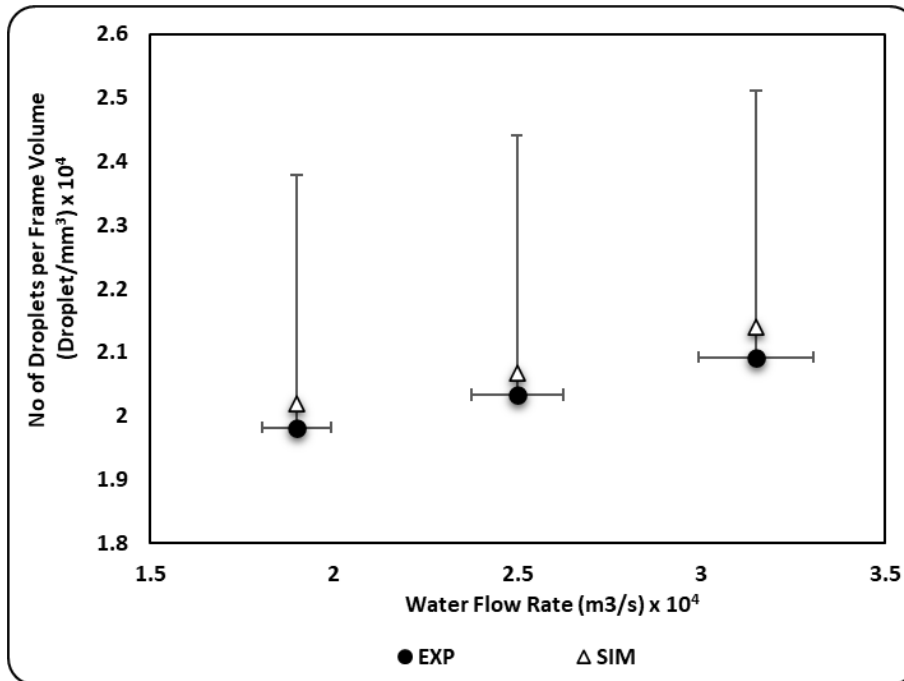
(b)

Figure 4-23: Droplets characteristics at different water flow rates through the whole C-D nozzle volume, (a) Average diameter, and (b) Number of droplets per C-D nozzle frame volume.
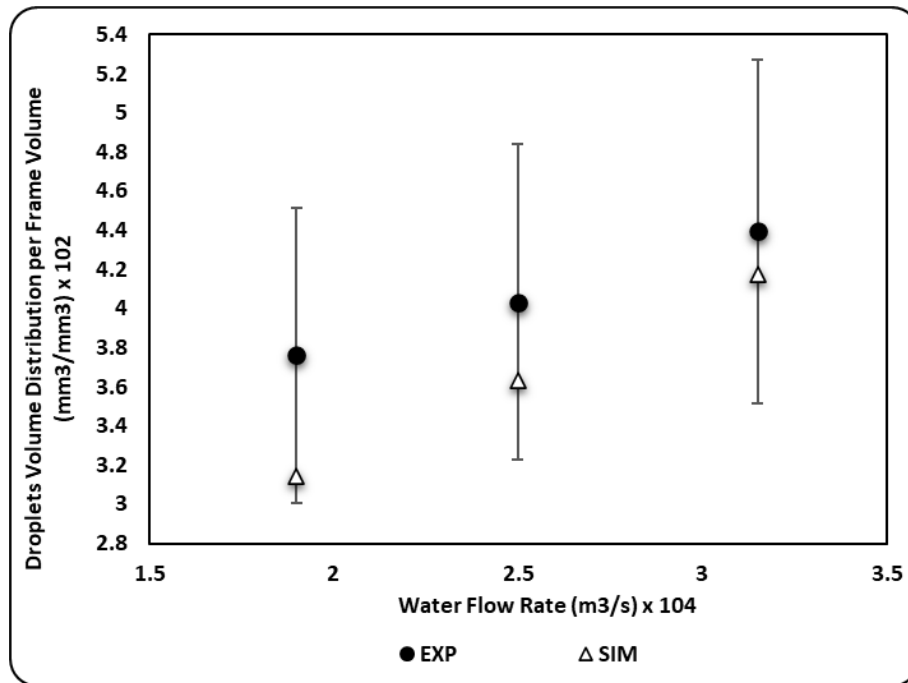
Figure 4-24: Separated droplet's volume at different water flow rates through the whole C-D nozzle volume
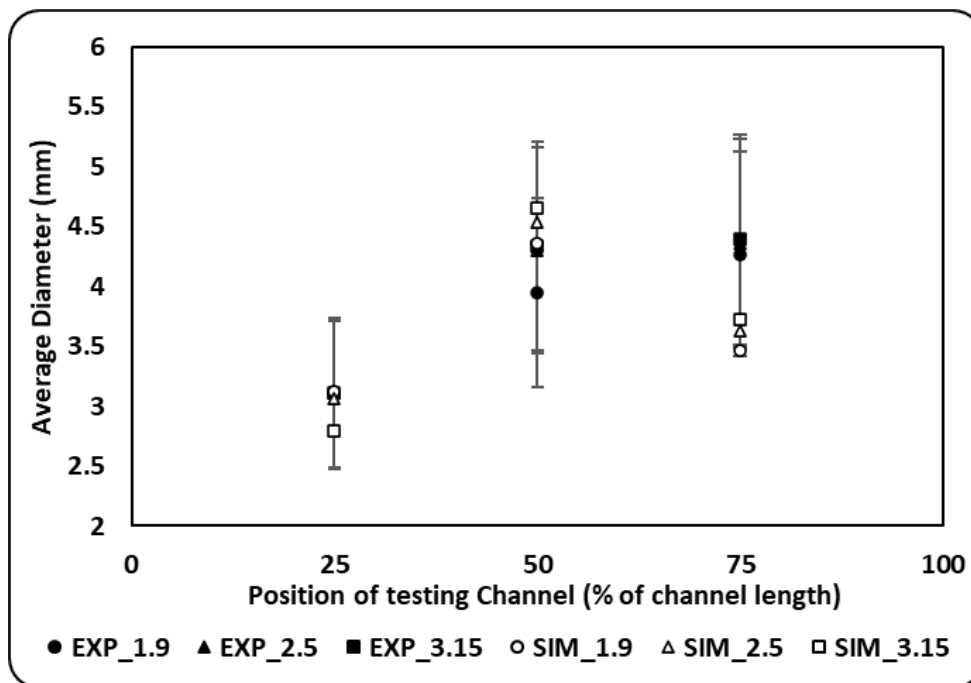
(a)
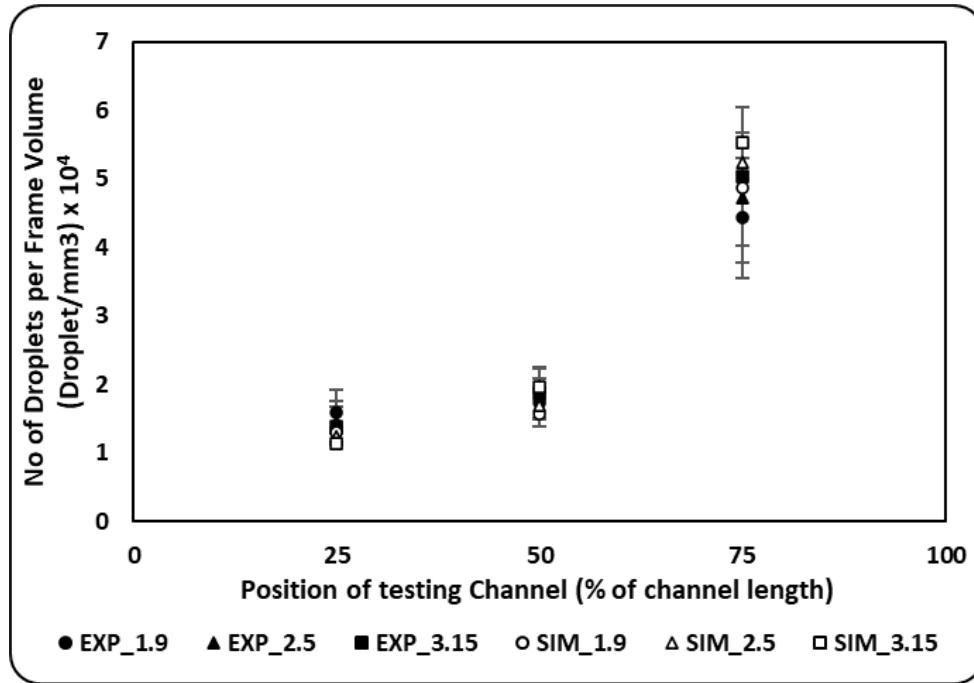
(b)

Figure 4-25: Droplets characteristics at different water flow rates and different sections through the C-D nozzle, (a) Average diameter, and (b) Number of droplets per C-D nozzle section frame volume

It was found from Figure 4-23 (a) that the average diameters through the whole C-D nozzle frame obtained from experiments are greater than the numerical ones with an error range of [14-16%]. While Figure 4-23 (b) shows that the droplets' numbers obtained from experiments are less than the numerical ones with a maximum of 2.5 % [Error bars with only 5%]. At the same time, the percentile difference inferred from Figure 4-25 (a) for the droplets' average diameters ranges from 1% to 19%.and from Figure 4-25 (b) for the droplets' numbers ranges from 7% to 18%. These percentile differences are in the acceptable ranges. Therefore, the numerical model results are verified and validated, and this numerical model can be used for further simulations. More explanation for the reasons behind these differences is provided in the next section.

Experimental and validation Outcomes: As previously mentioned, the experiments and the numerical validation models were performed at three different water flow rates 1.9, 2.5, and 3.15 * 10-4 m3/s and constant air velocity 20 m/s. The experimental and numerical break-up pattern shapes are shown at different water flow rates in Figure 4-21 & 4-22.

It can be inferred from Figure 4-21 & 4-22, that increasing the water flow rate will magnify the break-up rate, including the observed droplets' number. However, the visual observation is not enough to accurately study the break-up mechanism. So, the analyzed data from the algorithms' results are used. The analyzed data are represented by the droplets' average diameter and number at each case study.

An analysis of the droplets' average number, diameter, and volume per the whole nozzle frame volume is analyzed to investigate the effect of a particular specific factor on the break-up mechanism. However, to infer the reasons behind the previous conclusions, another detailed analysis for the droplets' average number and diameter is conducted for three sections (shown in Figure 3-5) with approximately the same volume inside the nozzle.

Overall, using the whole nozzle frame volume averaged data, increasing the water velocity causes a higher number and volume of separated droplets and increases the average diameter of droplets, as shown in Figure 4-23 & 4-24. But according to Weber number definition, Increasing the water flow rate increases the water velocity decreases the multi-phase relative velocity, and reduces the Weber number & the break-up occurrence. The explanation for the previous contradiction is that when the water flow rate increases, water momentum at the inclined surface of the throat region increases, which eases water separation from the nozzle surface—causing more water fragments separation from the liquid surface. These water fragments disintegrate into smaller droplets in the next section of the nozzle.

However, for a more detailed analysis of the break-up process, Figure 4-25 was drawn at different sections of the C-D nozzle where the droplets' characteristics are introduced. Thus, the following observations can be deducted:

Inlet section: the average diameter of droplets separated from the main liquid body is nearly the same in the experimental data. At the same time, it decreases with increasing the water flow rate in the numerical simulation. Also, it is noticed that the number of droplets decreases with a tiny percentage with a higher flow rate in the experimental and numerical data. This is consistent with the Weber number definition (mentioned in equation 10, shown in Figure 4-26) and that it characterizes the liquid break-up tendency as reported by previous studies [58-60], as increasing the water flow rate means less two-phase relative velocity, thus less Weber number and less break-up tendency.
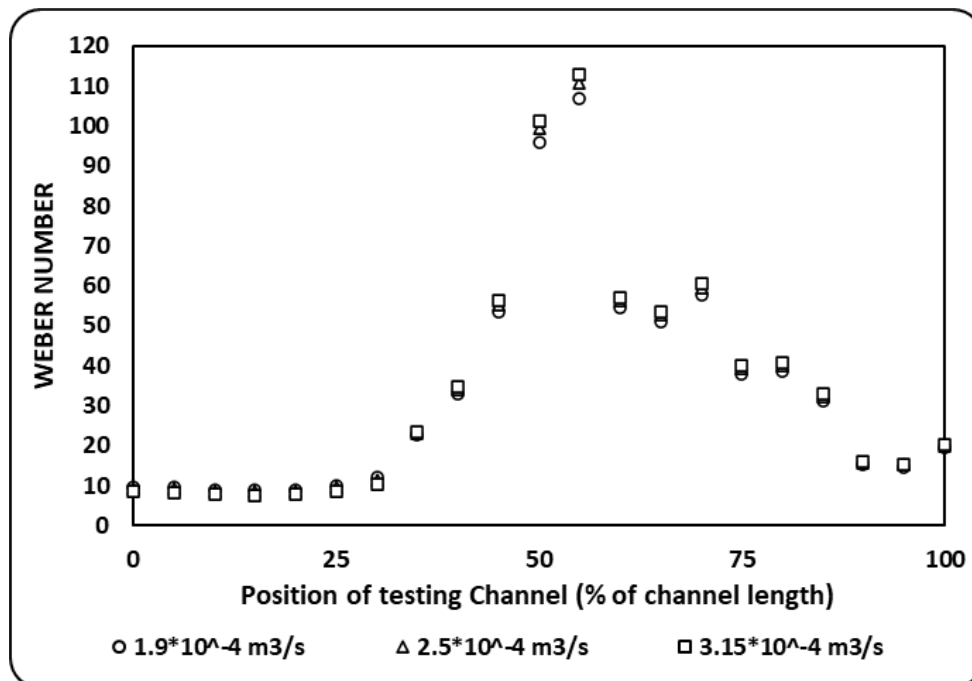
Figure 4-26: Average Weber Number at different water flow rates through the C-D nozzle

62

Throat section: Because of the nozzle configuration, the relative air velocity rises in this section, causing more water fragments separation. Although the relative air velocity decreases with increasing the water flow rate, the break-up process occurs more in this section with increasing the water flow rate. This can be explained by the fact that the water, due to the nozzle wall's inclination, has higher momentum leading to the separation of larger water fragments from the liquid surface. These larger water fragments are subjected to successive break-up events in the following section of the C-D nozzle.

Exit section: the separated droplets from the throat section disintegrate more in this section to smaller droplets as verified by the numerical data for the droplets' average diameters. Therefore, the droplets' number is higher in this section than the throat section and increases with increasing the water flow rate, which is reasonable due to the larger separated water fragments in the throat section. On the contrary, the droplets' average diameters are slightly increasing in the exit section. To understand the reason behind that, an overview of the method used to obtain the break-up process data is needed. A high-speed camera is used to capture the droplets by subjecting them to a light source, where the droplets appear as dark spots in the captured frames. Tiny droplets stick to the front and back covers of the testing channel, merge, forming a larger droplet, or slide on the cover forming dark spots. These dark spots, either from the formed larger droplets or the sliding ones, misleads the post-processing algorithms as the main droplets look much larger than their actual size, and their numbers are less. This reason is also the explanation for obtaining droplets with a greater average diameter and lower number from experiments than a numerical model.

Accelerated Air Flow Effect Outcomes. Three different airflow acceleration cases were computer-simulated (20, 30, and 60 m/s^2) and compared with the no-acceleration case (constant airflow velocity of 20 m/s). Then image processing was conducted using MATLAB, and the results

are shown in Figure 4-27 & 4-28. Applying acceleration to the airflow generally reduces the average diameter with a range from 6.5% to 9% (Figure 4-27 (a)). At the same time, it increases the average droplets' number [8.5-17%] (Figure 4-27 (b)). However, when the airflow acceleration increases, the average diameter, and droplets volume distribution per frame volume increase, while the number of droplets decreases (Figure 4-27 (b)). The break-up process cannot be fully explained using the average analysis for the whole testing channel. Thus, detailed evaluation for the break-up process per different channel sections was introduced in Figure 4-29.
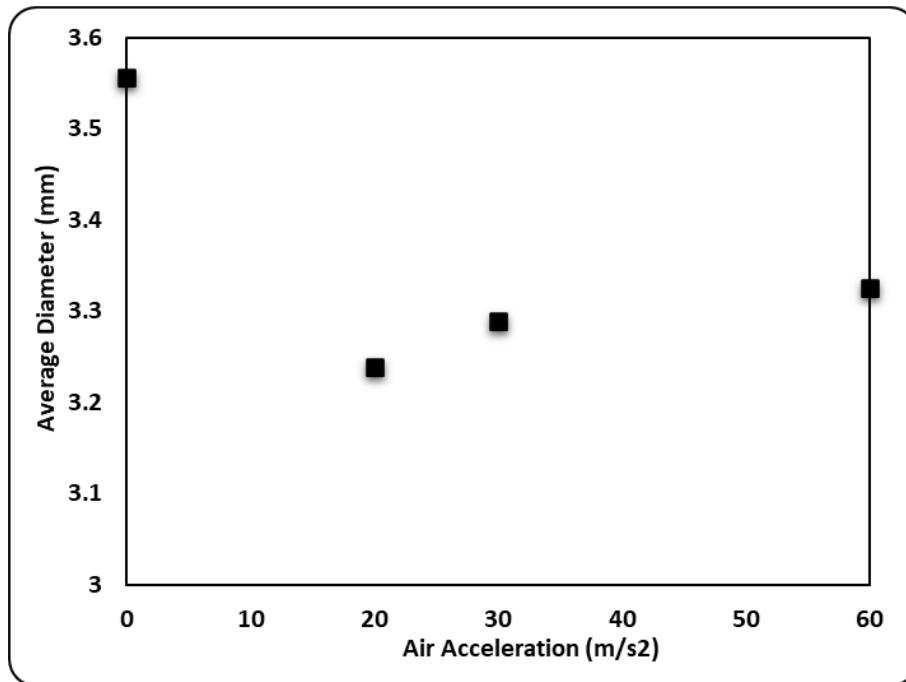
(a)
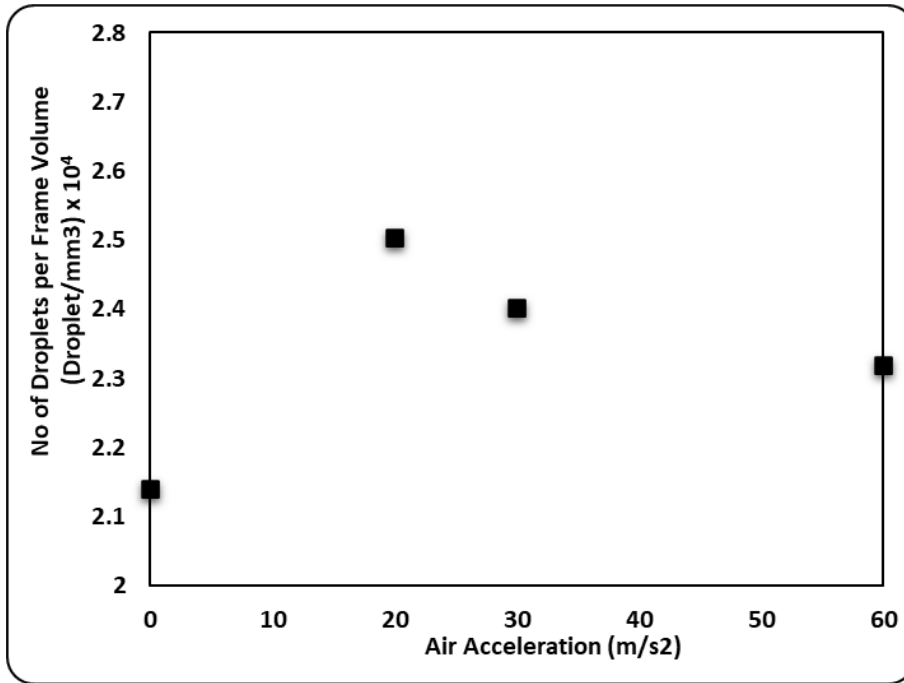
(b)

Figure 4-27: Droplets characteristics at different air acceleration for the total volume of the C-D nozzle, (a) Average diameter, and (b) Number of droplets per C-D nozzle frame volume

Case	(a)	(b)	(c)
Images			
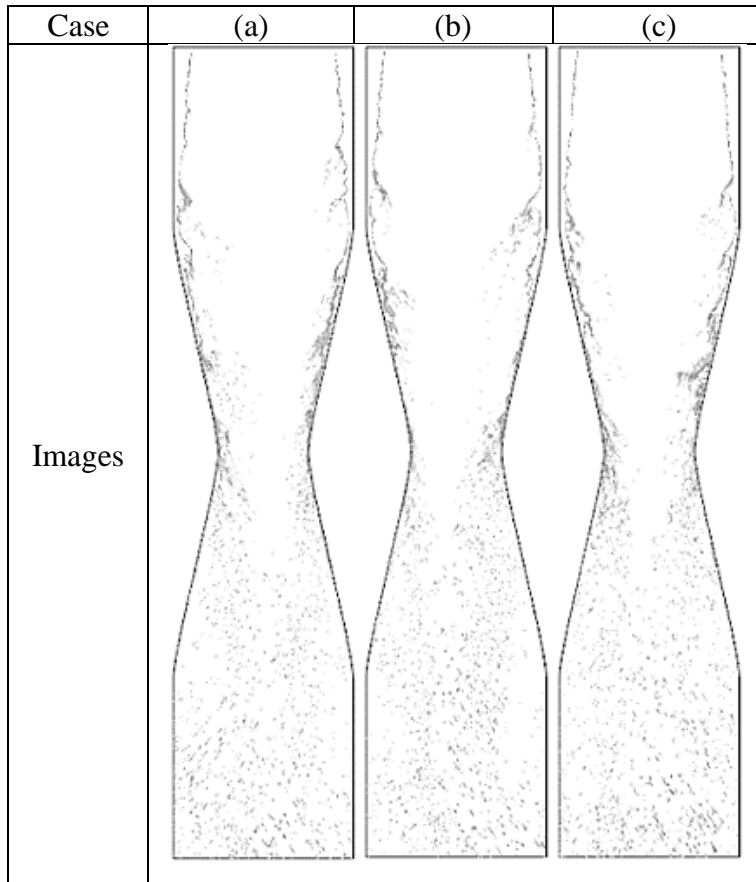
Figure 4-28: Numerical break-up pattern shapes at different air flow acceleration, a) 20 m/s2, b) 30 m/s2, c) 60 m/s2
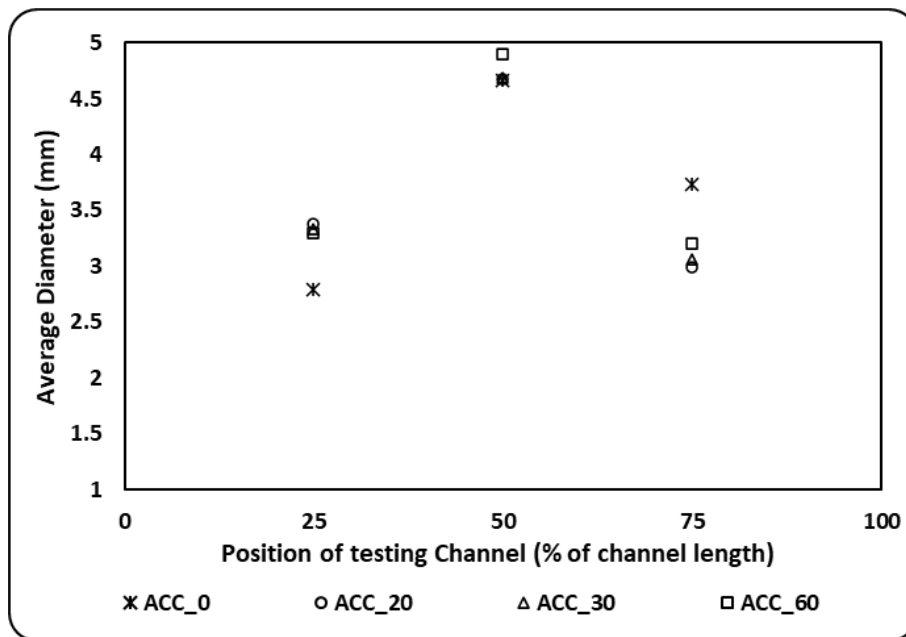
(a)
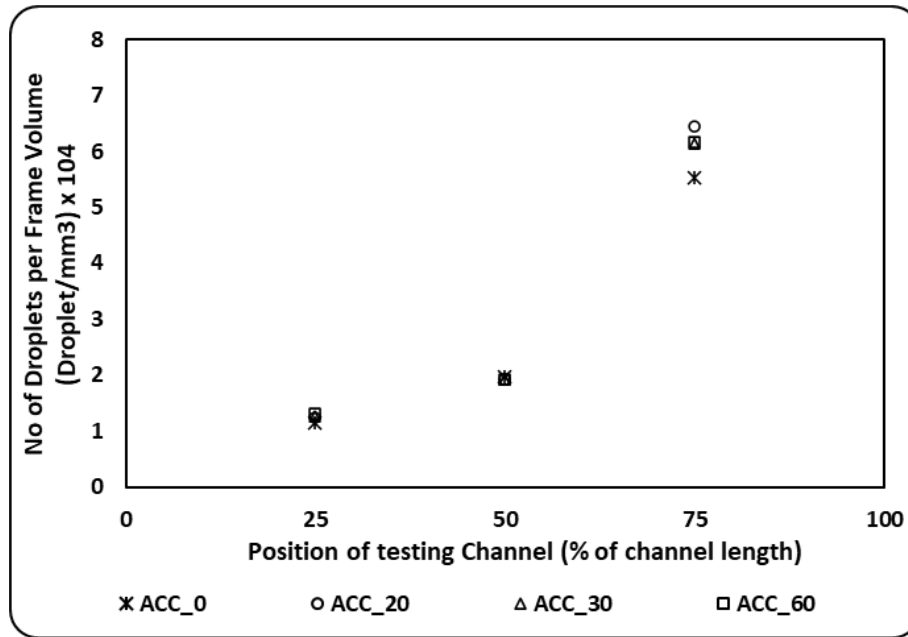
(b)

Figure 4-29: Droplets characteristics at different air acceleration for the C-D nozzle different sections, (a) Average diameter, and (b) Number of droplets per C-D nozzle section frame volume

From a general point of view, it can be inferred that applying acceleration on the airflow enhances the break-up process in means of the reduced average diameter and increased droplets' number. In addition, the increase of the droplets volume distribution per frame volume (shown in Figure 4-28) with increasing the airflow acceleration confirms that the break-up process is enhanced. The average droplets diameter per frame volume also agrees with the previous conclusion. On the other hand, the total number of droplets decreases with increasing the airflow acceleration, which can be explained by the analysis of the break-up process analysis of the testing channel sections.

Inlet section: The highest airflow acceleration has the smallest average diameter, the highest number of droplets, and volume distribution per section compared to the other two cases. Although the differences in the last-mentioned parameters are small, the break-up tendency is slightly higher in the 60 m/s2 acceleration case than in the other two cases in that section. This can be explained

67

that increasing the acceleration of the airflow subjects the water surface to rapid and sudden changes in the relative velocity between the gas and liquid, thus separating more water fragments from the primary liquid.

Throat section: the number of droplets is nearly the same in this section, while the average diameter increases with increasing the air acceleration. Most of the water bodies' separation is happening in this area because of the inclination of the nozzle wall, which eases the separation process. Higher acceleration means higher turbulence and a higher break-up tendency.

Exit Section: in this section, further break-up of the separated fragments from the throat section into smaller droplets, and as the airflow acceleration increases, the tendency of the large droplets to break up is greater. It was expected that the highest droplets' number is detected at the highest air flow acceleration (60 m/s2). On the contrary, it was found that the number of droplets in 20 m/s2 air acceleration is higher than that one obtained from 60 m/s2. With this higher air acceleration (60 m/s2), more significant merging opportunities for the droplets are present, responsible for reducing the total number of droplets.

The droplets' average diameters per the total volume of the C-D nozzle increase by 1.5%, and 2.7% when increasing the acceleration from 20 m/s^2 to 30, and 60 m/s^2, while the droplets' numbers drop by 4%, and 7%. On the C-D nozzle sections level, the average diameters decrease in the inlet section by 1.5%, and 2.5% when increasing the air acceleration from 20 m/s^2 to 30, and 60 m/s^2. At the same time, the droplets' numbers increased by 3%, and 7%. In addition, the average diameters increase in the throat section by 0.4%, and 5%, as the droplets' numbers increase by 1%, and 1%. Finally, the average diameters increase in the exit section by 2%, and 7%, as the droplets' numbers decrease by 4%, and 5%.

On the C-D nozzle sections level, comparing the droplets characteristics of the accelerated airflow cases against the no-acceleration case shows that applying acceleration increases the droplets average diameters and numbers in the inlet section with ranges [18-21.2%], and [7.6-15.1%], respectively. While, in the exit section, it decreases the droplets' average diameter with a range [14.1-19.8%] and increases the droplets' number from 11% to 16.5%. The decrease in the average diameter at the exit section is why the overall average diameter decline per the C-D nozzle total volume, as most of the separated water droplets from the break-up process exist in the exit section.

4.4 Submerged Nozzle Configuration Influence on Water Droplet Flow Behavior

4.4.1 Study Methodology

Investigating the submerged nozzle configuration on the droplet's breakup in the nozzle inlet section and just at the throat tip will be conducted experimentally and will be compared with the external nozzle results to see the effect of the pocket regions (recirculation zones) on the breakup process. So, experiments were performed considering two different scenarios: constant water flow rate ($3.15 * 10^{-4}\,\text{m}^3$/s) and variable inlet air velocities (20, 30, 40 m/s), while the other one is considering constant air velocity (30 m/s) and different water flow rates (1.9, 2.5, and 3.15 $* 10^{-4}\,\text{m}^3$/s). The conducted experiments are shown in the following table. The collected data were post-processed and compared with the processed data from external nozzle experimental results with the same input parameters and boundary conditions. The results of the current nozzle and external nozzle configurations are marked with (SUB_N) and (EXT_N) symbols in figures. Also, the break-up mechanism is explained considering the definition of Weber number, as explained before. Weber number represents the ratio between the gas inertia force and droplets surface tension.

4.4.2 Results and Discussion

Post Processing Algorithms' Results: More than 13000 experimental images were processed by MATLAB algorithms. The experimental images' contrast was first adjusted using the first algorithm (Appendix B) as shown in Figure 4-30. Then, the second algorithm (Appendix C) treated all the images where the droplets were marked, extracted, and analyzed. Finally, the collected analysis was tabulated, averaged, and normalized per frame for each case.
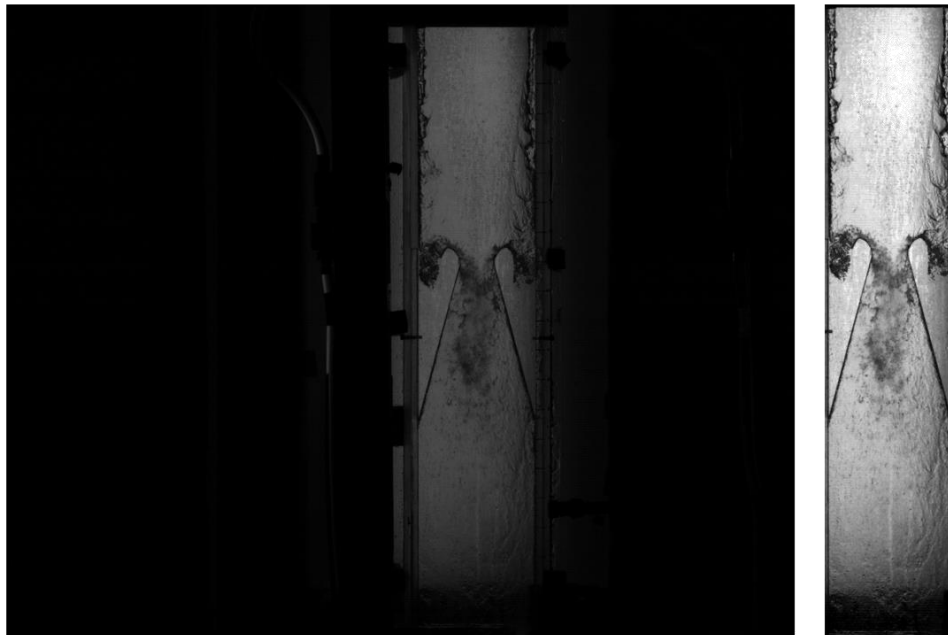
Figure 4-30: Brightness adjustment outcome

Variable Air Velocity Effect: As indicated earlier, three cases were tested at different air velocities 20, 30, and 40 m/s. Figure 4-31 provides a visualization of the C-D nozzle's break-up phenomena at the different air velocities. It can be seen that increasing the air velocity, moving the water surface faster, deforming it, and major water bodies are separated. Then these major water bodies break up into smaller droplets. Moreover, it is noticed that the break-up process evolution moves up toward the liquid inlet section with increasing the inlet air velocity, 230 – 180 – 160 mm from the inlet section, causing an increase in the droplet travel length and a higher chance for a

successive break up to smaller droplets. Comparing the breakup process evolution with the results from Section 4.2.2, the breakup process starts earlier in the submerged nozzle than the external one, because of the nozzle cavity. It can be also noticed that the recirculation zone volume increases with lower air velocities. The air velocity transforms to a high pressure acting on the water surface in the pocket region. Having higher air velocities will increase the applied pressure, causing the water to escape the pocket region, hence less water volume as shown in Figure 4-31.

Overall, the liquid break-up process in terms of the number of the observed droplets is magnified by increasing the air velocity. However, to get accurate details about the separated particle number and average diameter, the image processing tool was used as indicated before. Also, some figures were created from the obtained data, as discussed below.

The same two different analysis schemes explained before are used. Using the first approach, it is found that increasing the air velocity causes a higher number of separated droplet and average diameter, as shown in Figure 4-32 & 4-33. The submerged nozzle pocket region is collecting the water flow, then the water overflow from its side open to the nozzle throat is subjected to the tearing forces by the air flow causing water breakup, however the available area for breakup is small. So, higher air velocities force more water overflow in the throat area, but due to the small available area, the separated droplets have larger diameter. These figures also compare the breakup process in the submerged nozzle with the external nozzle. The number of droplets in the external nozzle is around three times the submerged nozzle due to the same reason mentioned before. The available area for breakup in the throat region is larger, in addition, the divergent section inclination angle is smaller, so the large droplets separated in the throat region are continuously subjected to air momentum till leaving the testing channel. However, with greater inclination

angle, it can be seen that the separated water bodies from the throat region are escaping the air high momentum flow to the divergent section sides where lower air velocities exist.
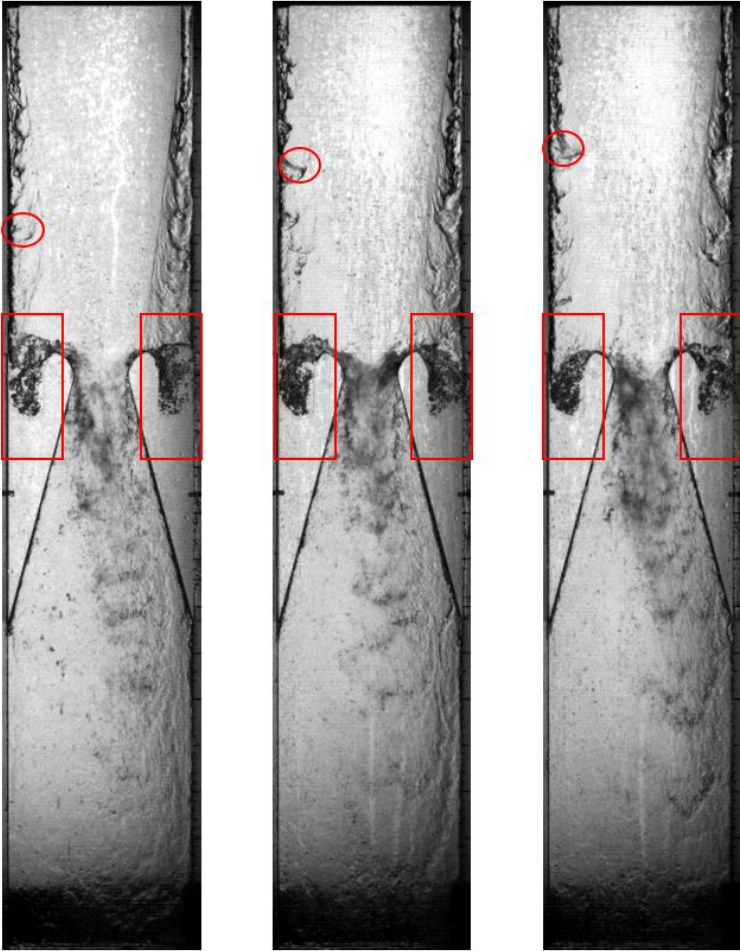
Figure 4-31: Experimental results for air velocity 20, 30, and 40 m/s, respectively
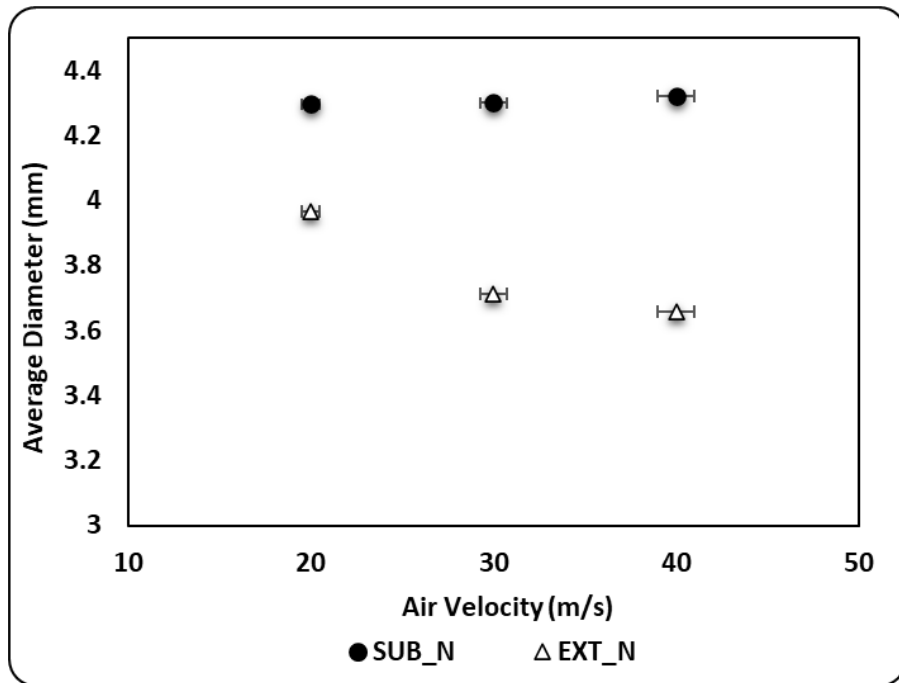
Figure 4-32: Experimental average droplet diameter throughout the entire testing channel for the submerged and external nozzles at different air velocities
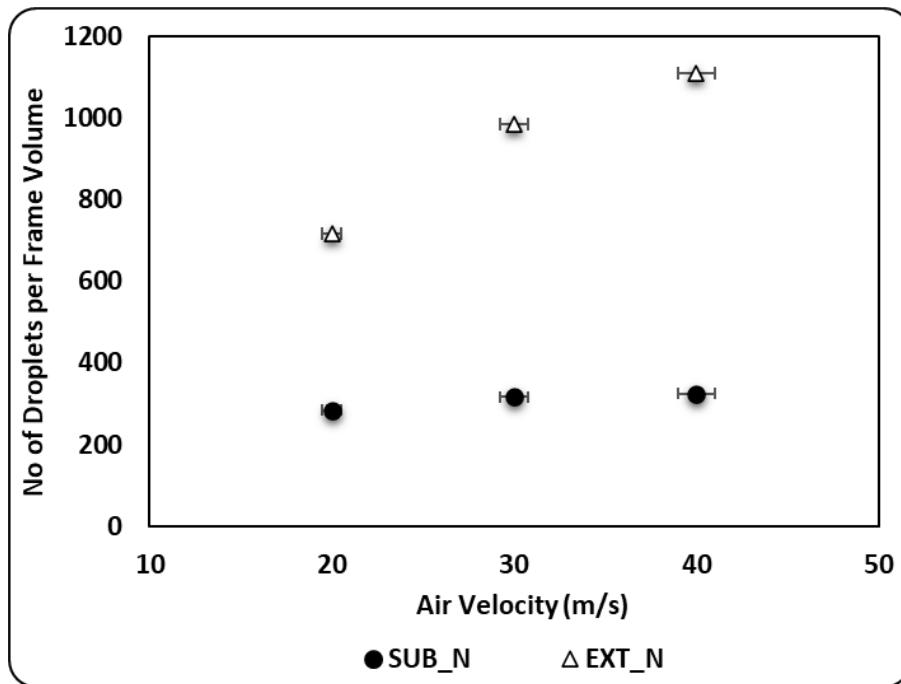
Figure 4-33: Experimental number of droplets throughout the entire testing channel for the submerged and external nozzles at different air velocities

Using the second approach, Figure 4-34 & 4-35 show the average diameter and the number of droplets in the inlet, throat, and exit sections. Hence the following can be observed for each section:

Inlet section: the number of droplets separated from the main liquid body increases with increasing the air velocity. On the contrary, the average diameter decreases, which can be explained with the Weber number definition. Higher air velocity means a higher weber number and higher liquid tendency to break up into smaller droplets. Same trend as the external nozzle results, however the parameters values are higher. The external nozzle testing channel surface moves toward its center, subjecting the water to be squeezed by the air flow towards the wall and delays the breakup evolution process. However, the recirculation zone in the submerged nozzle configuration is helping the water early separation with the air flow, causing an increase in the liquid breakup in this section.

Throat section: the air velocity increases more in this section, while the water piles up in the pocket region, overflows in the throat section, where it will be subjected to more droplet's separation, in other words, bigger average diameter compared with the inlet section. The number of droplets increases with increasing the inlet air velocity, as the Weber number rises in the throat leading to more separated water bodies. However, the number of droplets decreases compared to the previous section due to the small available breakup area as explained before. It can be noticed that most of the break-up process takes place in this section. The larger average diameter and lower number of droplets of the submerged nozzle configuration compared to the external one in the throat and exit sections were explained before by the first approach.

Exit section: in this section, further break-up of the separated droplets from the throat section into smaller droplets, and as the air velocity increase, the tendency of the big droplets to break-up is greater which can be inferred from the higher droplets number with increasing the air velocity.
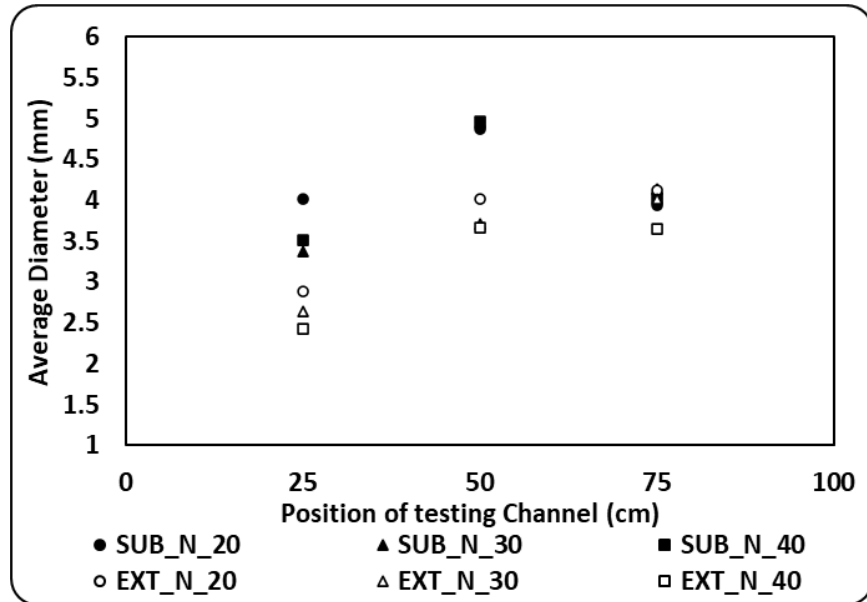
Figure 4-34: Experimental average droplet diameter at different sections of the testing channel and different air velocities
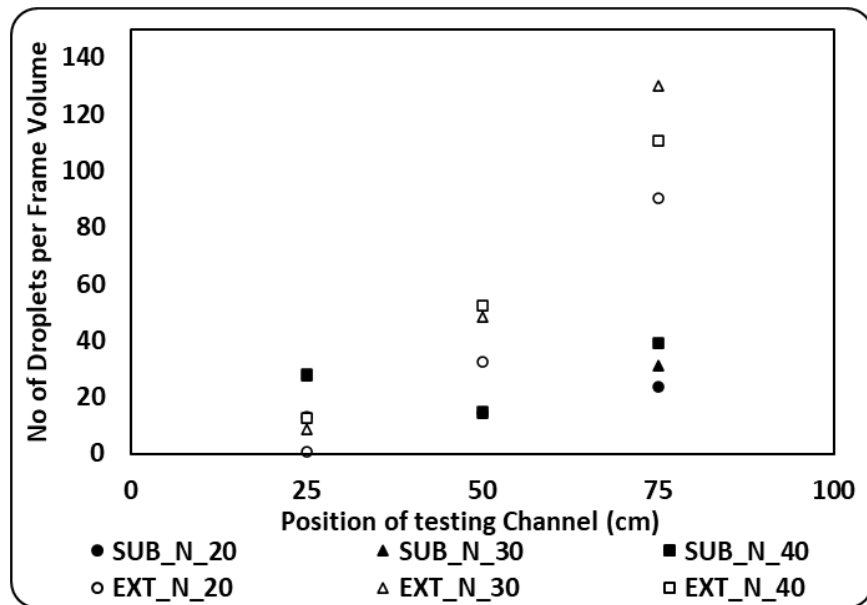
Figure 4-35: Experimental number of droplets at different sections of the testing channel and different air velocities

Variable Water Flow Rate Effect: Three cases were conducted at three different water flow rates 1.9, 2.5, and 3.15 * 10-4 m3/s and constant air velocity 30 m/s. Figure 4-36 provides a visualization of break-up process at these three cases. Higher water flow rate causes more water accumulation in the nozzle pocket region, as the water volume pushed to the throat area is less than the water inlet to the pocket zone as shown in the figure. Also, it can be seen that because of the air recirculation zone, more water is pushed away from the nozzle walls in the inlet section, promoting the breakup process in this section.

The visual observation is not enough to accurately investigate the break-up process. So, the second MATLAB code (Appendix C) is used to extract the droplets' average diameter and number at each case study.

It can be inferred from Figure 4-37 & 4-38, that increasing the water flow rate will magnify the break-up rate, including the observed droplets' number. Comparing the external nozzle and submerged nozzle results, the results are following the same trend with overall decrease in the observed droplets' number for the same region explained in the previous section. Generally, increasing the water velocity causes a higher number and volume of separated droplets and increases the average diameter of droplets.
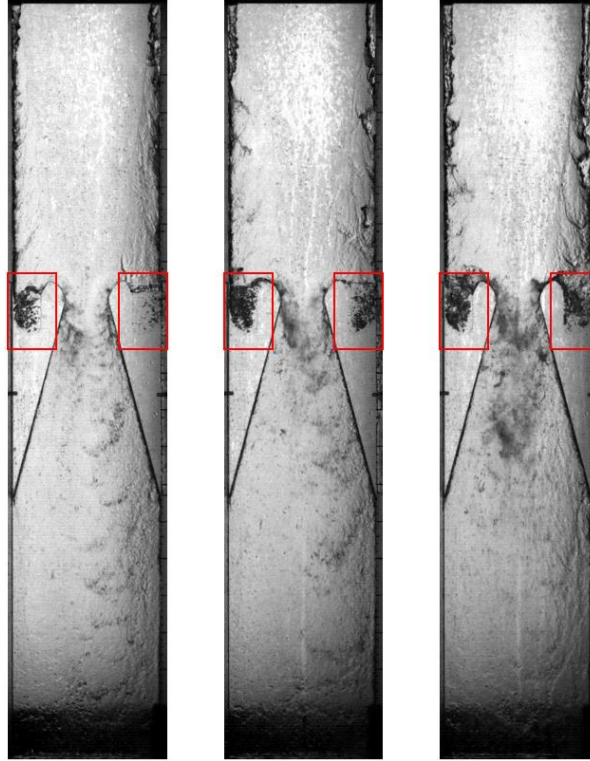
Figure 4-36: Experimental results for different water flow rates 1.9, 2.5, 3.15 x 10^{-4} m^3/s, respectively
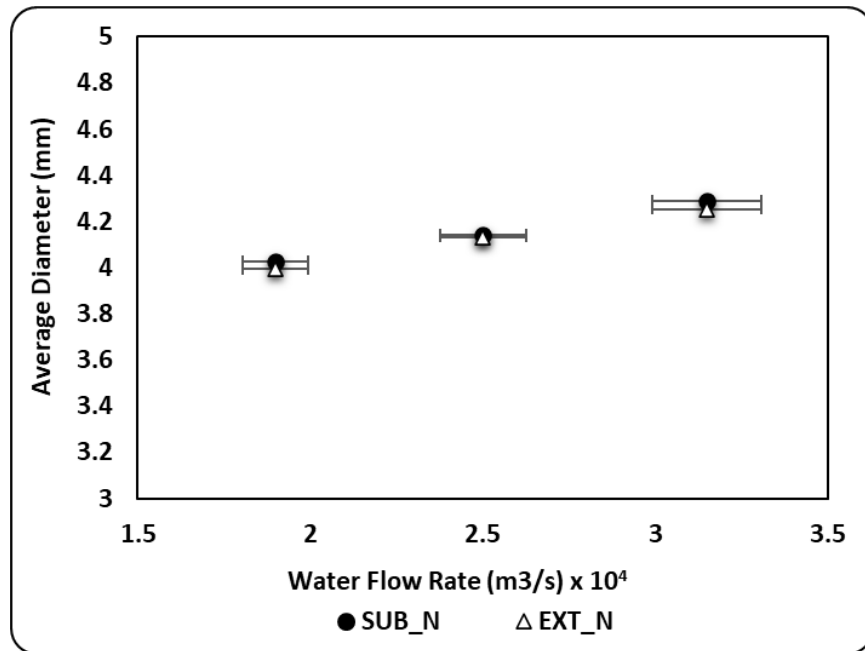
Figure 4-37: Droplets' average diameter at different water flow rates through the whole testing channel volume
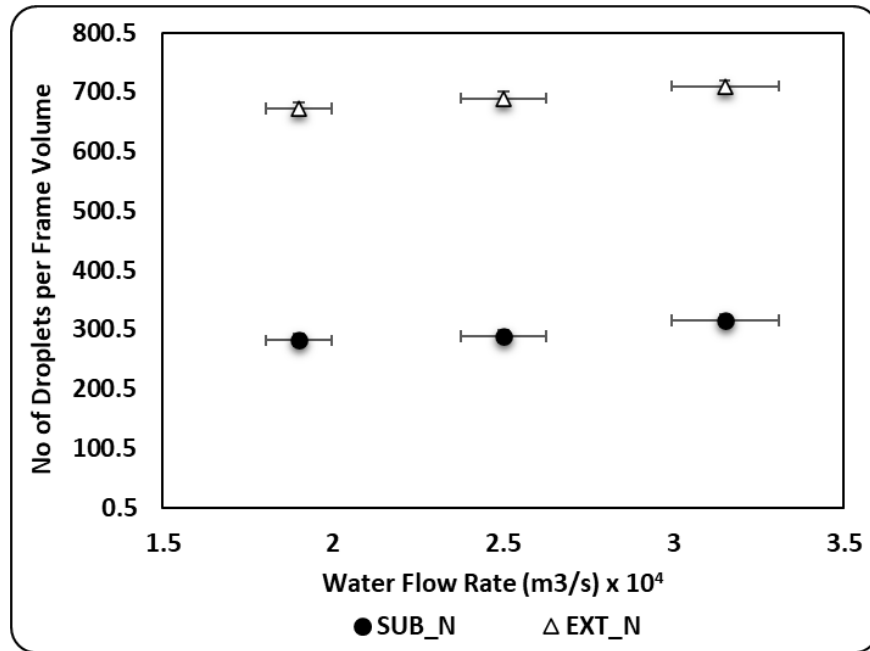
Figure 4-38: Droplets' number at different water flow rates through the whole testing channel volume

For more detailed analysis of the break-up process, Figure 4-39 & 4-40 was drawn at different sections of the testing channel where the droplets' characteristics are introduced.

Inlet section: the average diameter of droplets separated from the main liquid body is very close to each other (tiny increase). Also, it is noticed that the number of droplets increases with a with a higher flow rate. Referring to Weber number definition, Increasing the water flow rate increases the water velocity, decreases the multi-phase relative velocity, and reduces the Weber number & the break-up occurrence. On the other hand, because of the air recirculation zone, more water is pushed away from the nozzle walls in the inlet section, promoting the breakup process in this section. So, by the end, the breakup enhancement, because of the recirculation zone, dominates and the break-up tendency rises in this section. Since, the external nozzle configuration didn't have a recirculation zone, only the Weber number definition controlled the breakup process, and it declines with higher water flow rates.

78

Throat section: Because of the nozzle configuration, the relative air velocity rises in this section, causing more breakup for the water overflow stream. Moreover, more water volume is pushed into the throat section when the water flow rate increases as shown in Figure 4-36, results in more breakup occurrence represented by larger separated droplets' diameter and nearly the same number. The submerged nozzle results are taking the same trend as the external nozzle, but with an increase in the average diameter and decline in the number of droplets for the same mentioned reasons before.

Exit section: the separated droplets from the throat section disintegrate more in this section to smaller droplets. Therefore, the droplets' number is higher in this section than the throat section and increases with increasing the water flow rate, which is reasonable due to the larger separated water fragments in the throat section. On the contrary, the droplets' average diameters are slightly increasing in the exit section. the reason behind that was mentioned in Section 4.3.2.
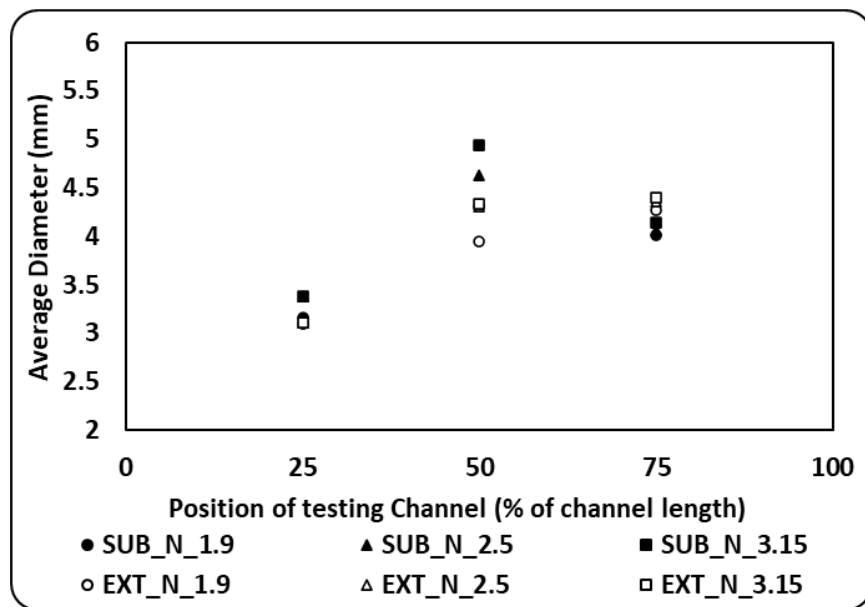
Figure 4-39: Droplets' average diameter at different water flow rates and different sections through the testing channel
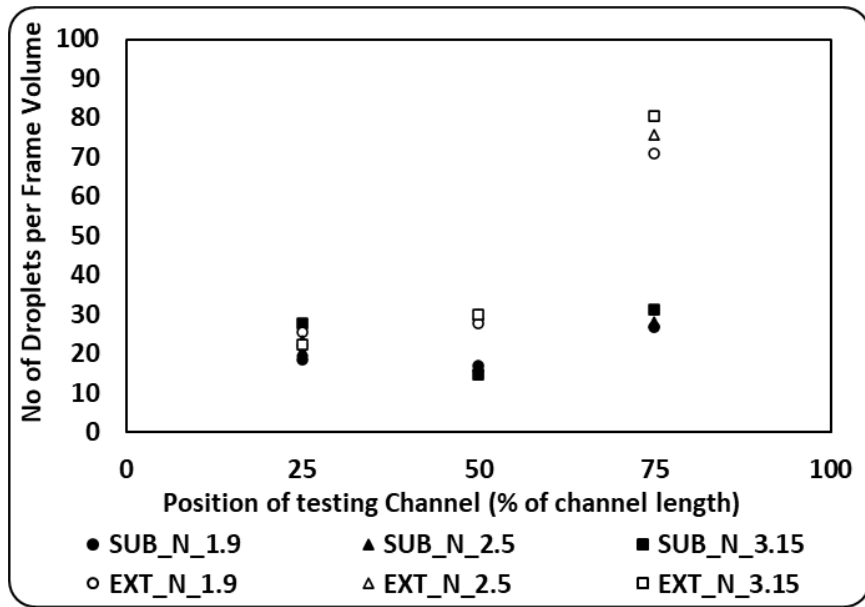
Figure 4-40: Droplets' number at different water flow rates and different sections through the testing channel

Chapter 5 Mechanical Erosion Investigation in Solid Rocket Motor Nozzle Through Droplet Breakup and Surface Tension Influence

All the previous research efforts are conducted using a sub-sonic flow, which is the opposite of the real flow nature of a rocket (super-sonic). So, in order to study the effect of these different parameters on a real rocket flow case, a numerical model predicting the mechanical erosion, and reflecting the actual conditions inside a rocket should be established. Having this model will provide a detailed information for the near surface thermo-fluid dynamics and particle trajectories, allowing for a high-fidelity investigation of the nozzle material erosion. Several researchers modeled the mechanical erosion on the nozzle surface numerically as mentioned in the literature, however they did not include the agglomerates' secondary breakup within their models. So, the current study attempts to develop a more accurate numerical model predicting the mechanical erosion considering the secondary agglomerates' breakup, then it will be expanded to study the effect of reducing the aluminum additives' surface tension [10%-15%] by adding magnesium or strontium for different agglomerates' diameters.

5.1 Theoretical Concept and Governing Equations

The combustion process between the reactants of the metalized solid propellant (Ammonium perchlorate (AP) / Aluminum (AL) / Hydroxyl-terminated polybutadiene (HTPB)) generates multi-species gas products represented by water vapor (H_2O), carbon dioxide (CO_2), carbon monoxide (CO), hydrogen (H_2), hydrochloric acid (HCL), and nitrogen (N_2) [41], in addition to the aluminum combustion products. Burning aluminum produces a bimodal distribution of aluminum/aluminum oxide particles, small and large particles with mean diameters of 1.5 and 100 μm, respectively. The tiny particles can be called smoke as they are exceedingly

small and can follow the multi-species gas momentum. From the aforementioned explanation, the combustion chamber internal flow field numerical simulation shall be treated as a multi-phase environment (multi-species gases and dispersed particulates (aluminum/aluminum oxide agglomerates). There are two approaches to simulate the multi-phase flow: Eulerian-Eulerian approach and Lagrangian-Eulerian approach. Both methods use the Eulerian analysis to model the continuous phase with adding coupling terms to account for the influence of the particles (solid or liquid) on the continuous phase. The Eulerian-Eulerian approach treats the particles or dispersed phase using a continuum model. In contrast, the Lagrangian- Eulerian approach treats the particles as sub-grid from the continuous phase, analyzes them using the Lagrangian description, and models the interaction between phases. Since the aluminum combustion products are not mono-dispersed, simulating them using the Eulerian-Eulerian approach will consume a dramatic computational power that will rapidly increase with increasing the particles number and sizes. The Lagrangian description for dispersed phase treats the discrete phase composition and size as an assigned attribute of each computational particle, so it can account for the change in size and composition due to combustion. Thus, using the Lagrangian- Eulerian approach is more economical and is more practical to be used where the particles' interaction with the chamber walls (boundaries' erosion) is crucial [17].

Multi-Components Gas Flow Field: the combustion gases products are called the continuous phase and are modeled using the mass, momentum, energy, and multi-component (species) conservation equations. Since modeling the combustion chamber internal flow field is extraordinarily complex and includes high-density oscillations because of the supersonic flow, the coupled solver is used to solve the governing equations simultaneously. The cartesian form for the governing equations is as follows:

$$\frac{\partial}{\partial t} \int_V W \, dV + \oint [F - G] \cdot da = \int_V B \, dV \tag{11}$$

$$W = \begin{bmatrix} \rho \\ \rho v \\ \rho E \end{bmatrix} \quad F = \begin{bmatrix} \rho v \\ \rho vv + PI \\ \rho vH \end{bmatrix} \quad G = \begin{bmatrix} 0 \\ T \\ T_v \cdot v + \dot{q}'' \end{bmatrix} \quad B = \begin{bmatrix} S_u \\ f \\ S_u \end{bmatrix}$$

Where ρ, v, p, E, T_v, B, $\dot{q}''$ and S_u are the density, velocity, pressure, total energy per unit mass, viscous stress tensor, body forces' vector, heat flux vector, and user-specified source term. The total energy can also be defined as:

$$E = h + \frac{|v|^2}{2} - \frac{P}{\rho}, \quad h = C_p T \tag{12}$$

The coupled equations are discretized implicitly in time using the Euler scheme accompanied by linearizing all fluxes using the Newton method. The realizable K-Epsilon two-layer turbulence model is used to solve the transport equations to calculate the turbulent eddy viscosity. The K-ε model is selected to be used in the current study after showing a good agreement with results obtained using the Large Eddy Simulation turbulence model [41]. Each gas from the multi-component gas has temperature-dependent thermal and transport properties based on NASA polynomials obtained from the research conducted by Gordan, and McBride [61]. The multi-component gas mixture (continuous phase) specific heat is calculated based on mass-weighted average of the different species' specific heats, while the mixture viscosity and thermal conductivity are calculated using Wilke's and Wassilijewa's approaches [62], respectively.

Aluminum Combustion Process: As explained before in the introduction, part of the unreacted aluminum content agglomerates on the burning surface and burn through its travel in the combustion chamber. Sabnis [17] proposed an approach for the aluminum particle burning process. First, the aluminum particle evaporates into aluminum gas, then the aluminum gas is

oxidized by the oxidizing species of the continuous phase to aluminum oxide. The aluminum particle burning rate is defined by Hermsen [63] as follows:

$$\frac{D_p}{D_{po}} = \left[1 - \frac{K\,t}{D_{po}{}^{1.8}}\right]^{\frac{1}{1.8}} \tag{13}$$

Where D_p and D_{po} are the aluminum particle diameter (variable over time), and the initial aluminum particle diameter (detached from burning surface). K is the burning rate constant, and t is the time elapsed from the beginning of the burning process. From the basic definition of aluminum particle mass, the change of particle mass over the burning time can be written as follows:

$$\frac{d(m_{AL})}{dt} = \frac{d}{dt}\left[\frac{1}{6}\,\pi\,D_p{}^3\rho_{AL}\right] \tag{14}$$

Substituting with the aluminum particle diameter from the previous equation, differentiating the equation, simplifying it, the following equation for aluminum particle mass evaporation rate can be obtained:

$$\frac{d(m_{AL})}{dt} = -\frac{\pi}{2}\rho_{AL}\frac{K}{1.8}D_p^{1.2} \tag{15}$$

where,

$$K = 8.3314 \times 10^{-5}\,A_k^{0.9}\,P_c^{0.27}\,\frac{Sh}{2} \tag{16}$$

The burning rate constant unit is $cm^{1.8}/s$, P_c is the combustion chamber pressure and should be in absolute psi, while the Sh_p is the Sherwood number and its definition as per the following:

$$Sh_p = 2 + 0.6\,Re_p^{0.5}\,Pr^{0.687} \tag{17}$$

A_k is a calculated number representing the oxidizing species availability around each aluminum particle, where the oxidizing species can be CO_2, H_2O, CO, O_2, OH, and O.

$$A_k = 100 \sum_i x_i \qquad (18)$$

After evaporation, the aluminum gas is oxidized to aluminum oxide using the following two reactions:

$$2\,Al + 3\,H_2O \rightarrow Al_2O_3 + 3\,H_2$$

$$2\,Al + 3\,CO_2 \rightarrow Al_2O_3 + 3\,CO$$
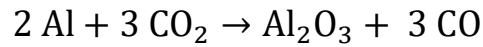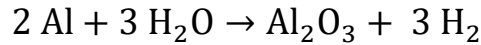
This process is modeled by identifying the multi-component gas as a reacting gas by adding the chemical source term to the conservation equations. The standard Eddy-Break-Up (EBU) model calculates the chemical source term from the mixing time scale.

Aluminum Oxide Particles: Both aluminum and aluminum / aluminum oxide multi-component particles are considered dispersed or discrete phases which are injected into the continuous phase, and they are treated by the Lagrangian approach. The mass flow rates of either single-component particles (Aluminum) or the multi-component particles (Aluminum/aluminum oxide) are calculated based on the continuous mass flow rate and some assumptions regarding the unreacted aluminum fraction based on experimental data. Each particle movement in the continuous phase is governed by the mass, momentum, and energy equation. However, if a large number of particles exist in the studied case, the particles are divided in groups sharing the same properties called parcels. The following equation governs the particle mass change over the time:

$$\frac{dm_p}{dt} = \dot{m_p} \qquad (19)$$

For the single component (Aluminum), the m_p equals the particle evaporation rate, while it will equal zero in the case of multi-component particles (Aluminum oxide). Each particle moves in the continuous phase following the momentum conservation equation in the Lagrangian description:

$$m_p \frac{dv_P}{dt} = F_s + F_b \tag{20}$$

$$F_s = F_p + F_d \tag{21}$$

where v_p is the particle velocity, F_s is the summation of external forces that affects the particle surface (including drag and pressure gradient forces), and F_b is a summation of body forces (including the gravity force). The pressure gradient force is defined as follows:

$$F_p = -v_P \nabla P \tag{22}$$

The particles are affected by drag force from the continuous phase, as indicated before.

$$F_d = \frac{1}{2} C_d \rho A_p |v_s| v_s \tag{23}$$

where ρ, A_p and v_s are continuous phase density, particle's projected area, and particle slip velocity, respectively. The particle slip velocity used in the previous two equations is the difference between the particle and continuous phase velocities and is defined as follow:

$$v_s = v - v_p \tag{24}$$

C_d is the drag coefficient of particles (liquid droplets) following the Schiller-Naumann correlation [64].

$$C_d = \begin{cases} \frac{24}{Re_p}(1 + 0.15Re_P^{0.687}) & Re_p \leq 1000 \\ 0.44 & Re_p > 1000 \end{cases} \tag{25}$$

$$Re_p = \frac{\rho\, v_s\, D_p}{\mu} \tag{26}$$

Each particle is considered to be thermally homogeneous (in other means, with a Biot number less than 0.1). Thus, the energy equation for each particle can follow the following equation:

$$m_p c_p \frac{dT_p}{dt} = Q_t + Q_{rad} + Q_s \tag{27}$$

where c_p is particle material specific heat capacity, and Q_t, Q_{rad}, Q_s are convective, radiative, and other heat transfers from particle to the continuous phase. The particles' convective heat transfer rate is calculated based on the Rans-Marshall correlation [65] as follows:

$$Nu_p = 2\left[1 + 0.3\, Re_p^{0.5}\, Pr^{\frac{1}{3}}\right] \tag{28}$$

$$Nu_p = \frac{h_p\, D_p}{k} \tag{30}$$

Mechanical Erosion Prediction: Till now, and to the best of the authors' knowledge, there is no available data or conducted experiments specifying the mechanical erosion ranges in SRM nozzles. However, there are available experimental data for the overall erosion (chemical and mechanical). On the other hand, mechanical erosion rate can be predicted numerically using the calculated particle mass flow distribution on the nozzle walls. Erosion is modeled by accumulating damage caused by incident particles on the nozzle boundaries. The erosion rate can be calculated as per the following correlation [66]:

$$E_f = \frac{1}{A_f} \sum_{\Pi(f)} m_\Pi\, e_r \tag{31}$$

in which E_f is the mechanical erosion rate in kg (eroded material) / m^2 / s, A_f is the area of targeted face, m_Π is the particles' mass flow rate exists in each parcel affecting the targeted face and e_r is the erosion ratio. The erosion ratio can be calculated based on several correlations. Each correlation is fitted based on experimental data obtained from certain particle material, eroded wall material, and flow conditions. Neilson and Gilchrist [67,68] developed a correlation to calculate the erosion ratio in SRM nozzle based on a conducted experiment. It was found that the correlation depends on the particle velocity, size, material type, and incident angle.

$$e_r = \frac{U^2 (\cos \alpha)^2 \sin\frac{\pi\alpha}{2\alpha_0}}{2\,\varepsilon_C} + \frac{(U \sin \alpha - v_k)^2}{2\,\varepsilon_D} \qquad \alpha < \alpha_o \qquad (32)$$

$$e_r = \frac{U^2 (\cos \alpha)^2}{2\,\varepsilon_C} + \frac{(U \sin \alpha - K)^2}{2\,\varepsilon_D} \qquad \alpha \geq \alpha_o \qquad (33)$$

where U is the relative velocity, α is the particle incident angle, α_o is the calibrated transition angle (20.93°), v_k is the cut-off velocity, ε_C is the calibrated cutting coefficient and ε_D is the calibrated deformation coefficient. The relative velocity is the particle velocity with respect to the wall and is defined as follows:

$$U = v_p - v_{wall} \qquad (34)$$

The conducted experiments include several particles' material impact on different walls' material, from the different studied cases, alumina particles with diameter 297 μm and relative velocity of 110.6 m/s impact on graphite plate is the one concerned in this study. The erosion ratio experimental coefficients were calibrated by Thakre [41] and summarized in Table 5-1.

Table 5-1: Neilson and Gilchrist [41] calibrated parameters

Parameter	Value
ε_c (Cutting Coefficient)	215.7 kJ/kg
ε_D (Deformation Coefficient)	95 kJ/kg
v_k (Cut-off Velocity)	0 m/s

Agglomerates Break-up: Generally, liquid breakups can be categorized as primary and secondary. The primary breakup occurs when a liquid column breaks up into ligaments and large droplets. At the same time, the secondary one describes the further breakup of large droplets caused by the primary breakup to smaller droplets. Since the agglomerates sizes are already small so, the secondary breakup will be considered in the current study. The secondary breakup is driven by the imbalance between the drag force of the continuous phase and the surface tension force of the droplet, which is the definition of the Weber Number.

$$\text{We} = \frac{\rho \, |v_s|^2 \, D_p}{\sigma} \tag{35}$$

The different regimes of breakup process in accelerating flow field were addressed by Stiesch [69] based on the Weber Number: vibrational breakup (at nearly 12 Weber number), bag breakup (< 20), bag / streamer breakup (< 50), stripping breakup (< 100) and catastrophic breakup (> 100). The agglomerates' size varies in the combustion chamber also their velocities along the combustion chamber axis. Thus, the Weber number also varies along the chamber axis. The Weber number of the agglomerates in the nozzle entrance based on the simulated cases, just before hitting the nozzle walls, varies between 10-30. Thus, it can be inferred that the breakup type is either vibrational, bag or bag / streamer bag. The vibrational breakup happens when the droplet oscillates and split into two droplets with the same volume, while the bag and bag /streamer bag breakups occur when the continuous phase momentum deforms the droplet into a bag shape, then breaks it up into a

bimodal size distribution with large droplets at the rim and small droplets at the trailing edge. Since the present study Weber number range is within the bag and bag / streamer breakup, the Reitz-Diwakar breakup model is used. It models the breakup following two mechanisms, bag breakup caused by the variation in the pressure field surrounding the droplet and stripping breakup caused by the shearing and stripping of the droplets' edges. The droplet diameter decreases as per the following:

$$\frac{dD_p}{dt} = \frac{D_s - D_p}{\tau_b} \tag{36}$$

where D_p, D_s are the particle diameter and stable droplet diameter, respectively. τ_b is the characteristic time scale, and its definition depends on the breakup mechanism. The stable droplet diameter can be determined by making the breakup mechanism condition equality.

$$\text{Bag Breakup} \begin{cases} \text{if } We > We_{cr} & , \text{where } We_{cr} = 12 \\ \tau_b = \frac{C_{b2} D_p}{4} \sqrt{\frac{\rho_l D_p}{\sigma}} & , \text{where } C_{b2} = \pi \end{cases} \tag{37}$$

$$\text{Stripping Breakup} \begin{cases} \text{if } We > \max(2C_{s1}Re^{0.5}, We_{cr}) & , \text{where } C_{s1} = 0.5 \\ \tau_b = \frac{C_{s2} D_p}{2 |v_s|} \sqrt{\frac{\rho_l}{\rho}} & , \text{where } C_{s2} = 20 \end{cases} \tag{38}$$

5.2 Numerical Model Description and Boundary Conditions

The computational fluid dynamics software is widely used nowadays to solve complex engineering problems after proving its accuracy compared to the experimental results [48, 49, 51, 52, 70, 71]. Thus, Star CCM+ software package is used in this study to simulate the internal flow field inside the rocket's combustion chamber. A geometry for the motor combustion chamber is used similar to the ballistic test evaluation system (BATES) grain configuration [17]. The

geometry dimensions are as per Figure 5-1. Since the geometry is symmetric in the rotational direction, a small sector (10°) is used in the present study, in addition to employing the periodic boundary conditions (rotational type) on its two sides as shown in Figure 5-2.
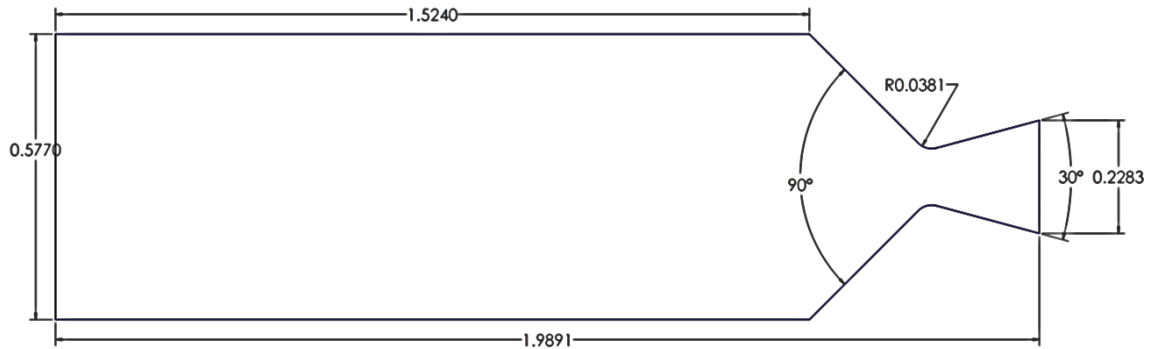
Figure 5-1: BATES geometry schematic
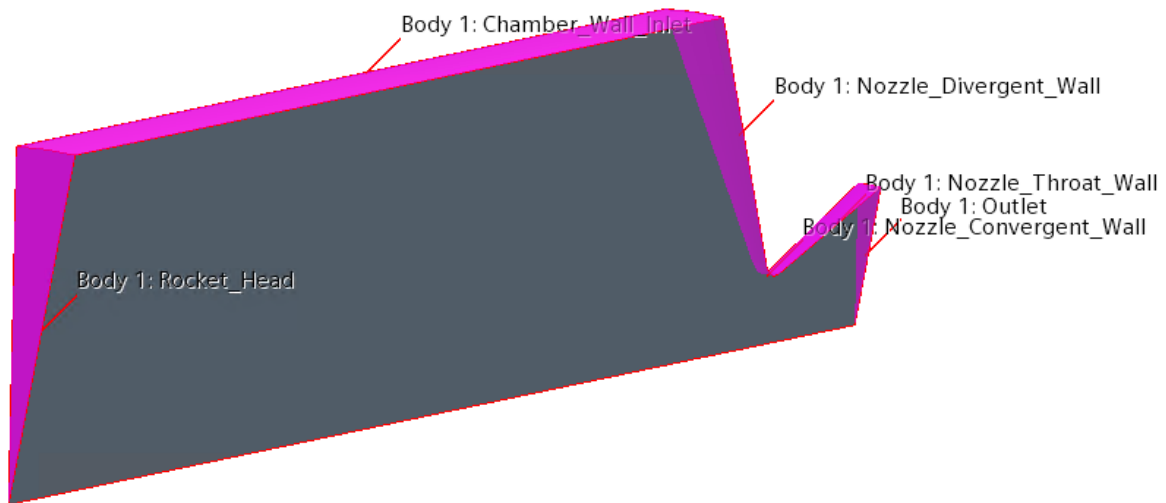
Figure 5-2: Numerical Computational Domain

The mesh is created using a method called directed mesh which create a mesh on the source face and sweep it through all the domain till the target face. This method helps with creating a mesh in the flow direction (shown in Figure 5-3). The mesh is clustered in the nozzle section and at the inlet, nozzle walls with 25 prism layers to ensure low Y+ (<1). The mesh sizes in both radial

91

and axial directions were selected after conducting mesh independence study which will be presented in the results section.
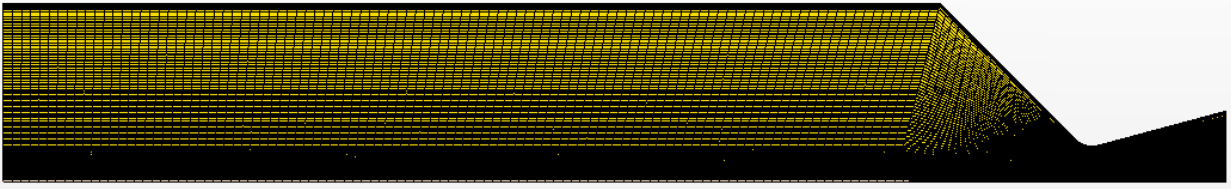
Figure 5-3: Computational domain mesh distribution

The propellent utilized in the current analysis composes of Ammonium perchlorate (AP) / Hydroxyl-terminated polybutadiene (HTPB) / Aluminum (AL) with 71/14/15 mass weight percentages. The propellant has a burning rate of $9.0678 \; x \; 10^{-3}$ m/s and density of 1794.6 kg/m^3 as reported by Sabnis [17]. Based on the propellant properties, the product combustion gases mass flux is 16.273 kg/m^2/s, combustion chamber pressure and temperature are 68 bar and 3327 K [41]. The combustion chamber head is treated as an adiabatic wall, and although the nozzle walls temperature is variable within a range of 2200-2800 K [8], it is assumed as an isothermal wall with 2500 K (average temperature). The numerical model used in the present work is validated on two levels first, the mechanical erosion rate is validated against the numerical results reported by Thakre et al. [41], then the numerical thrust coefficient will be validated with the experimental thrust coefficient obtained from Li et al [32] work. According to the literature, there are several reported values for the unburnt aluminum percentage with a maximum of 30% [18]. However, a conservative assumption of 10% will be followed, as reported by Thakre et al [41]. Thus, 10% (0.15 x 0.1 x 16.273 = 0.244 kg/m^2/s) of the aluminum content in the propellant remains unreacted on the burning surface, while the rest is completely burnt at the propellant burning surface producing aluminum oxide. The propellant burning process products are multi-component gas (as shown in Table 5-2) with mass flux of 15.199 kg/m2/s) with initial mass fraction for each species

obtained from chemical equilibrium analysis (CEA) of (AP (71%) / HTPB (14%) / AL (13.5))
[72].

Table 5-2: Combustion products inlet mass fractions [41]. (Continuous phase)

Gas Species	Mass Fraction
H2O	0.114
CO	0.281
CO2	0.032
H2	0.022
AL	0.000
AL2O3	0.219
HCL	0.232
N2	0.1

It is also assumed that 80% of the formed aluminum oxide is in the form of smoke, while
the rest (20%) is in the form of caps covering the unburnt aluminum. 50% of the unburnt aluminum
$(0.5 \times 0.244 = 0.122$ kg/m^2/s) burns through the combustion chamber following the previously
explained model, and the aluminum oxide covers the other 50% to form alumina agglomerates.
Salita [73] reported that the formed alumina agglomerates of 100 μm (mean diameter) has a log-
normal distribution with $\log_{10}$standard deviation (0.2). A summary for the discrete particles'
injection data is provided in Table 5-3. The particles injection velocity in the radial direction is
assumed to be approximately 3% of the continuous phase velocity at the burning surface [41];
using the reported data by Madabhushi et al. [74] that the particles' injection velocity (1-25% of
the continuous phase velocity) does not affect the particles' dynamics. Applying the former
boundary conditions enables the validation of the current numerical model's mechanical erosion.

Table 5-3: Agglomerates inlet conditions. (Discrete phase)

Liquid Phase	Mass Flux (kg/m^2/s)	Injection Temperature (K)	Droplets' diameter (μm)	Radial Velocity (m/s)
Aluminum droplet	0.122	950	50	0.1
Multi-component droplet (AL/AL$_2$O$_3$)	0.122/0.83	2350	Log-Normal distribution Mean: 100	0.1

Log$_{10}$ standard
deviation: 0.2

Table 5-4: Li et al [32] measured experimental data

No.	P (Mpa)	D10 (μm)	D50 (μm)	D90 (μm)
1	7.157	70.2	105.81	136.18
2	8.114	68.84	103.63	130.84
3	5.674	64.48	98.25	123.13
4	5.96	70.17	104.12	133.36
5	6.059	68.92	104.12	133.36
6	6.22	65.49	99.11	125.85

Then the data shown in Table 5-4 reported by Li et al. [32] are applied as a boundary condition with Rosin-Rammler particle size distribution. The thrust coefficient is calculated as per the following correlations:

$$C_F = \frac{\int_{Nozzle\ Outlet} \rho vv \cdot dA + \int (P_c - P_{atm})\, dA}{P_c\, A_t} \tag{39}$$

As proven by Thakre et al. [41] and the current study validation, the 50% pure aluminum particles, which burn according to the mentioned combustion model, completely evaporate after a short distance from the burning surface, convert to aluminum oxide and other products species. As a result, they do not impact the nozzle walls. Accordingly, a simplified numerical model is established by neglecting the aluminum particles' combustion process and substituting it with their effect on the product's species mass fractions, as modified and shown in Table 5-5.

Table 5-5: Combustion products inlet mass fractions [42]. (Continuous phase)

Gas Species	Mass Fraction
H_2O	0.109111
CO	0.284957
CO_2	0.022013
H_2	0.022267
AL_2O_3	0.232293
HCL	0.230154
N_2	0.099204

The Lagrangian phase injection will be limited to only the multi-component agglomerates, while the continuous phase mass flux is modified to be 15.321 kg/m^2/s. The simplified numerical model will be used to further investigate the effect of varying the droplets (particles) size, incorporating the droplets breakup models, and reducing the agglomerates' surface tension on the nozzle mechanical erosion. The discrete phase mass flow rate will be constant for all cases, the only variables will be droplets' diameters, breakup model status, and droplets' surface tension. Seven different droplets' diameters (60, 100, 140, 180, 220, 260, 300 μm) are used under three different conditions to study the erosion rate. The first one is the base simplified model without applying the droplets breakup model (W/O BR), while the second condition incorporates the droplets' breakup model in the analysis (W BR_NST), and the last condition is reducing the droplets' surface tension by 15% (from 0.791 N/m to 0.672 N/m) (W BR_LST). A total of twenty-one (21) case were studied.

5.3 Results and Discussion

Mesh Independence Study: Ensuring the reliability of the numerical model is essential, so mesh independence studies are conducted. A Directed mesh technique is used to discretize the computational domain where the face in the radial direction is meshed. Then, the face grid is swept all over the computational domain until the exit to have a clustered grid in the nozzle volume where severe conditions exist. Three different sizes are used to mesh the face in the radial direction (0.003, 0.0048, and 0.006 m) and three number of cells in the longitudinal direction (140, 195, 250). The mechanical erosion rate of the nozzle is compared for these cases as shown in Figure 5-4 & 5-5, and it was found that using a face cell size of 0.0048 m and 195 cell in the longitudinal direction give accurate results as the finer cells while maintaining a reasonable computational power.
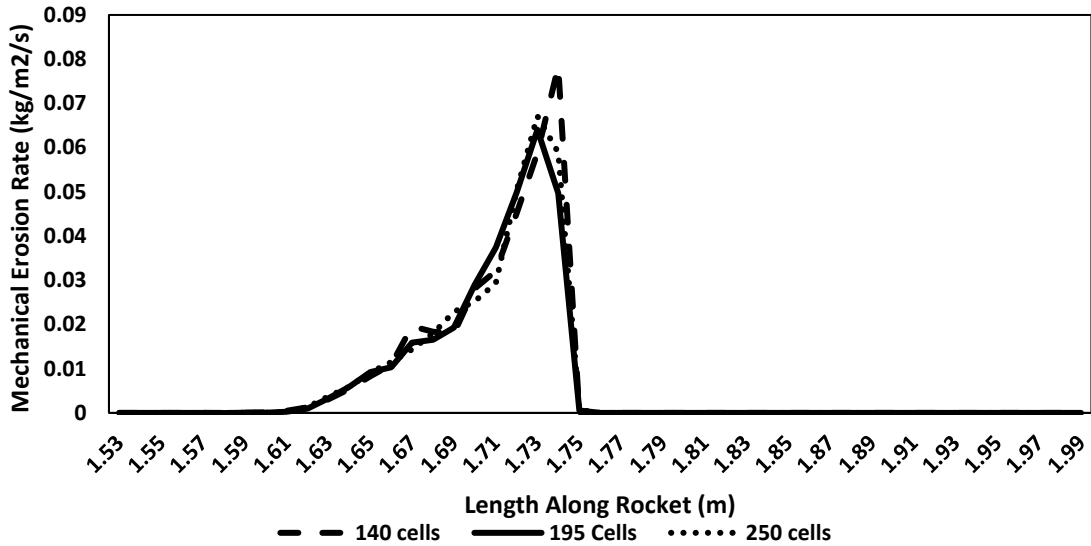
Figure 5-4: Mechanical Erosion Rate Using Neilson Correlation for different cells count in the axial direction
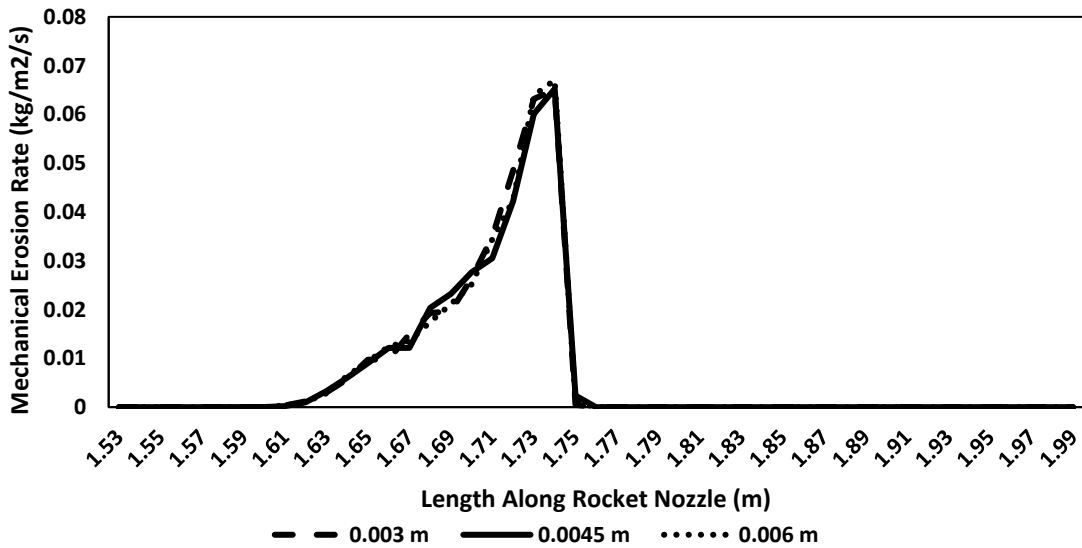
Figure 5-5: Mechanical Erosion Rate Using Neilson Correlation for different cell sizes in the radial direction

Model Validation: Any numerical model should be validated first before being used in any further investigations. The validation could be done against experimental data or numerical data. And since no available experimental data were found for the mechanical erosion rate (the available data is only for the overall erosion rate mechanical and chemical) in the literature, the numerical thrust coefficient is validated using published experimental data by Li et al. [32] as

shown in Figure 5-6. The current study's flow dynamics, thermal analysis, particle trajectories, and erosion rate is compared against numerical published results by Thakre et al. [41]. Although the experimental geometry dimensions and inlet boundary conditions are not clear in the published work, the thrust coefficient results show a good agreement between the experimental and numerical data. All the data lie between two dashed lines (error margins) of 10%.
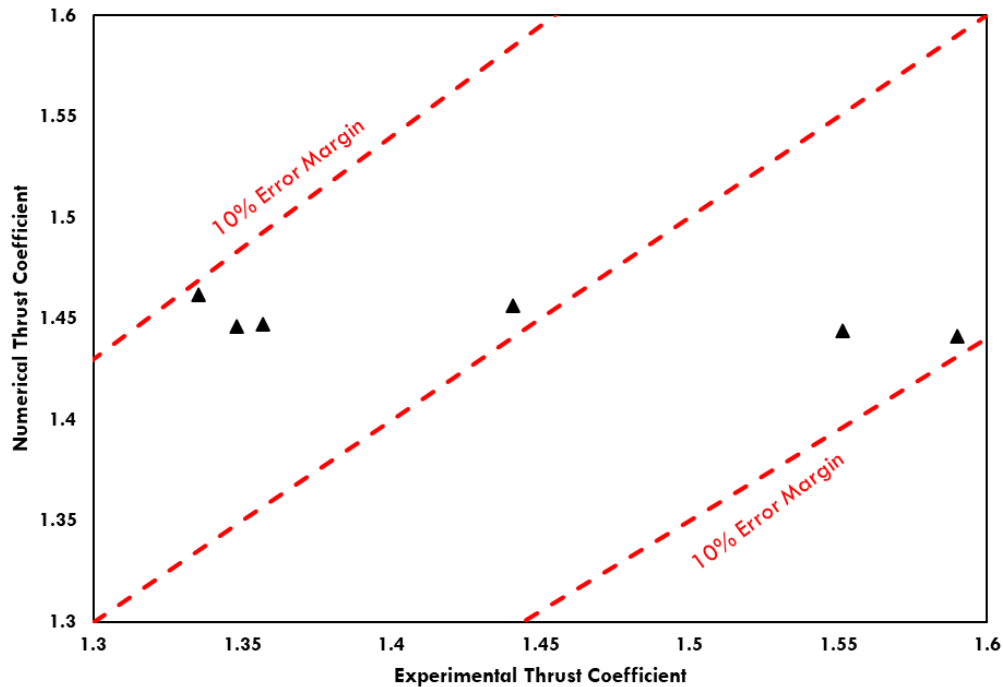
Figure 5-6: Thrust coefficient validation against Li et al [32]

Reviewing the combustion chamber internal flow field characteristics, it was found that the supersonic flow within the nozzle reaches maximum Mach number of 2.65, while the pressure decreases gradually from 68 bar (in the combustion chamber) to 1.7 bar at the nozzle outlet as shown in Figure 5-7. As mentioned before two discrete phases are injected from the combustion chamber circumferential wall: pure aluminum particles and aluminum/aluminum oxide particles. Figure 5-8 shows the pure aluminum particles trajectories within the chamber, and as proved by the figure, the particles completely evaporate after a noticeably short distance from the inlet walls.

While the full evaporation of the aluminum particles is correctly following the aluminum combustion model, but in the rocket actual environment the particles will not fully disappear, The aluminum particle will evaporate till the point where its surface area is so small, the evaporation rate will be minimal, and its size will be around 1 μm (or less). Figure 5-10 presents the increase of the aluminum mass fraction in the near inlet wall due to the evaporation of the aluminum particles to reach a maximum of 0.0072. However, the aluminum concentration disappears due to its reaction with other oxidizing species, converts to aluminum oxide. The results of the oxidization reaction are indicated in Figure 5-11 by the increase in the aluminum oxide mass fraction far from the inlet wall. Modeling the pure aluminum burning process shows that it does not contribute to the erosion of the nozzle walls. So, as indicated before, the burning process will be eliminated in the main model, which will study the effect of including particle breakup and reducing the aluminum droplets' surface tension. On the other hand, the aluminum/aluminum oxide multi-component droplets do not burn within the combustion chamber because of the aluminum oxide outside shell and hit the nozzle walls, causing erosion, as shown in Figure 5-12. The multi-component droplets' velocity increases gradually as they travel in the combustion chamber and reach their maximum 1130 m/s at the nozzle outlet. Figure 5-14 shows the temperature distribution of the multi-component droplets where the temperature increases as the droplets travel through the chamber. The droplets with the highest temperature are the ones that have the highest residence times. Finally, the mechanical erosion is calculated using the correlation of Neilson and Gilchrist [67,68] and mapped on the nozzle walls as shown in Figure 5-15. The nozzle walls are divided into three sections: Convergent section (1.524 to 1.744 m along axial direction), Throat section (1.744 to 1.781 m along axial direction), and Divergent section (1.781to 1.989 m along axial direction). Figure 5-16 provides a comparison between the current study and Thakre et al [41]

98

erosion rates where minor differences are noticed, hence the current study's numerical model is validated and can be used in further investigation. It can also be noted that most of the erosion occurs in the convergent part of the nozzle, while an exceedingly low erosion rate is noticed in the throat area.
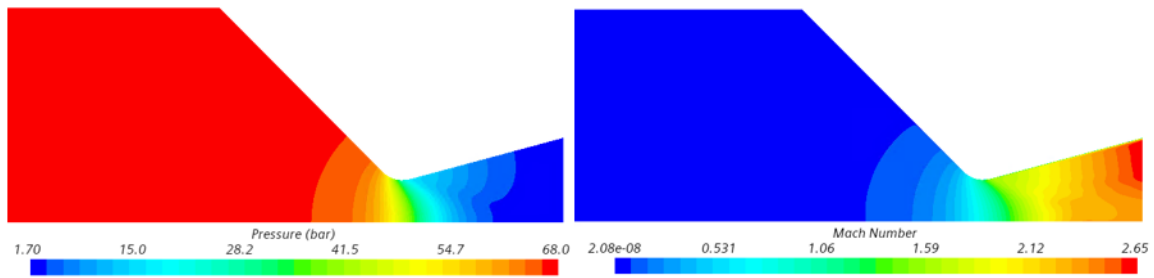
Figure 5-7: Combustion chamber internal flow field contours
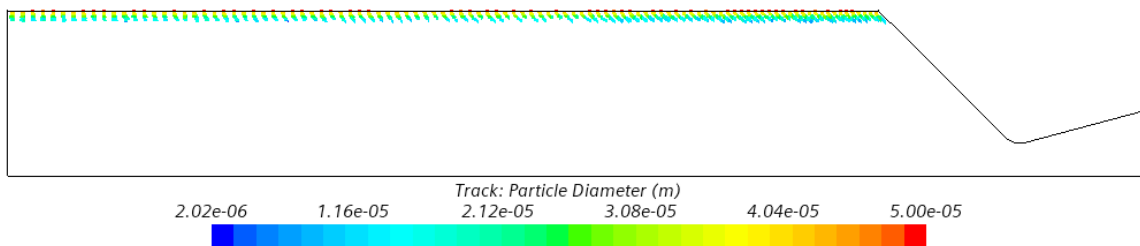
Figure 5-8: Pure aluminum particles trajectories
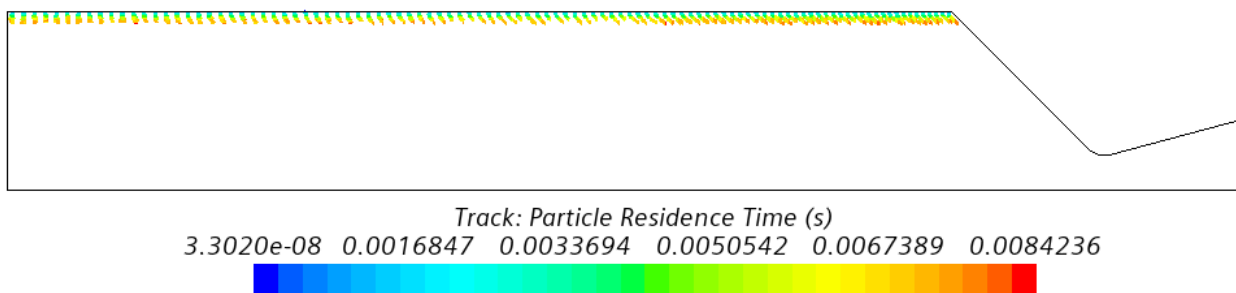
Figure 5-9*:* Pure aluminum particles trajectories colored by its residence time before full evaporation
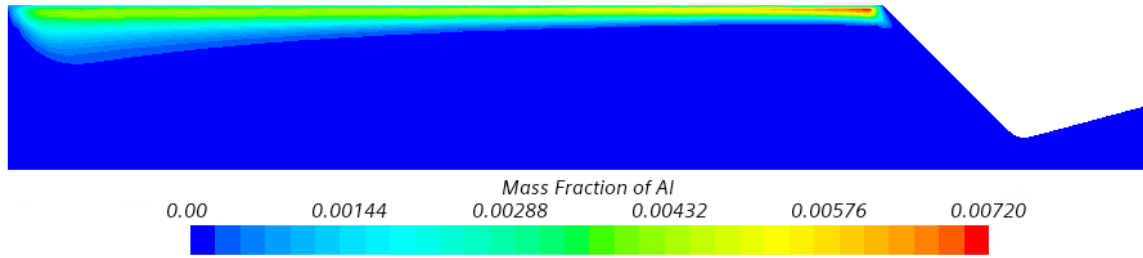
Figure 5-10: Pure aluminum particles mass fraction after burning process
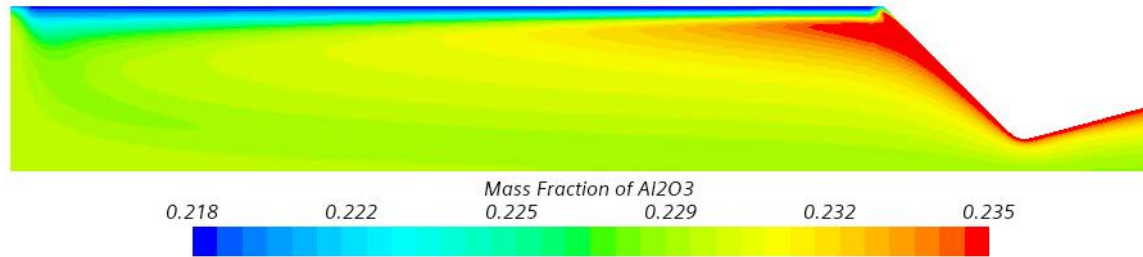
Figure 5-11: Aluminum oxide mass fraction after burning process
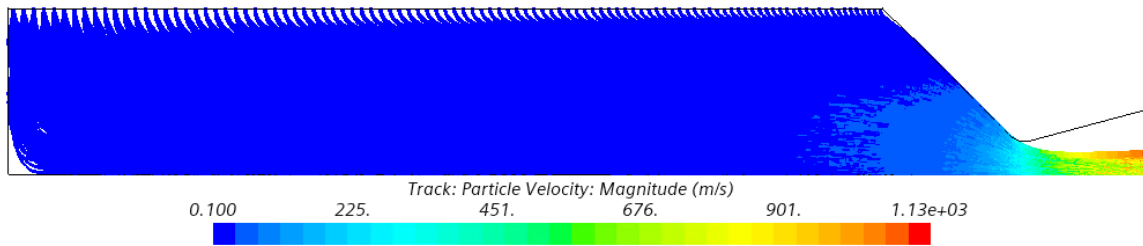
Figure 5-12: Aluminum / aluminum oxide trajectories with velocity distribution
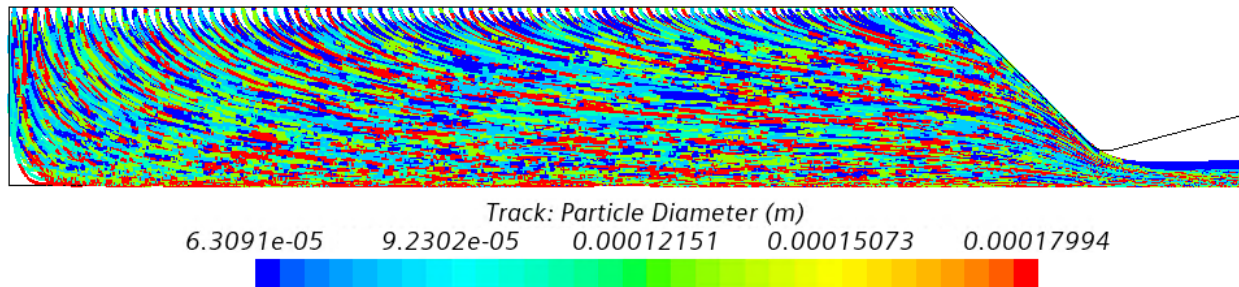
Figure 5-13: multi-component particles' trajectories colored by the particle diameter
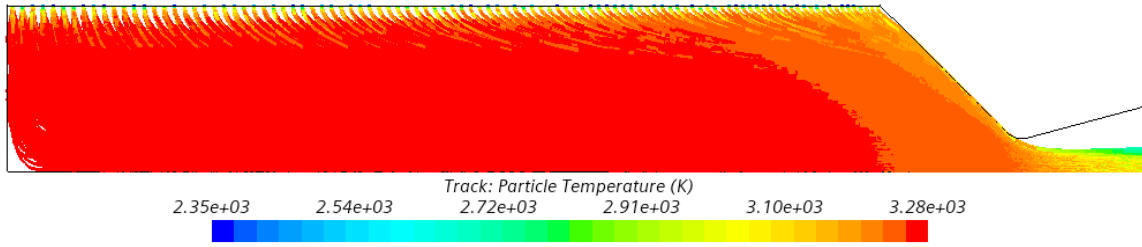
Figure 5-14: Aluminum / aluminum oxide trajectories with temperature distribution
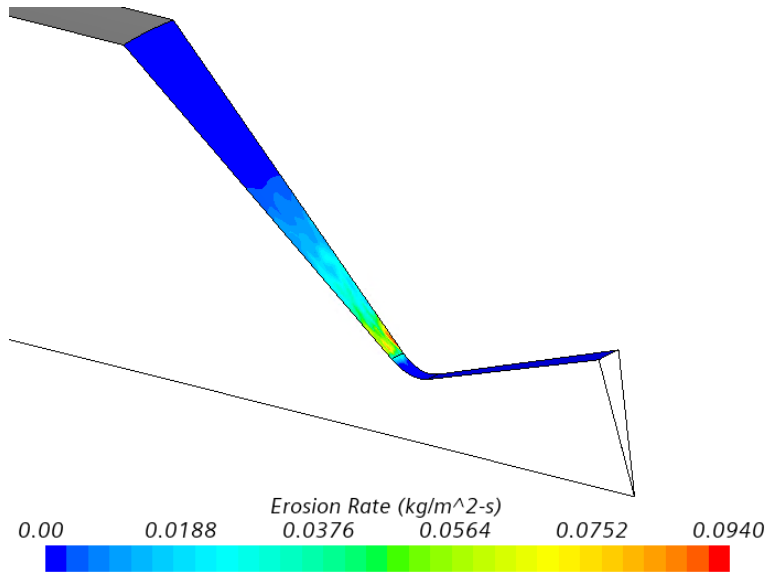
Figure 5-15: Mechanical erosion rate contour over the nozzle walls
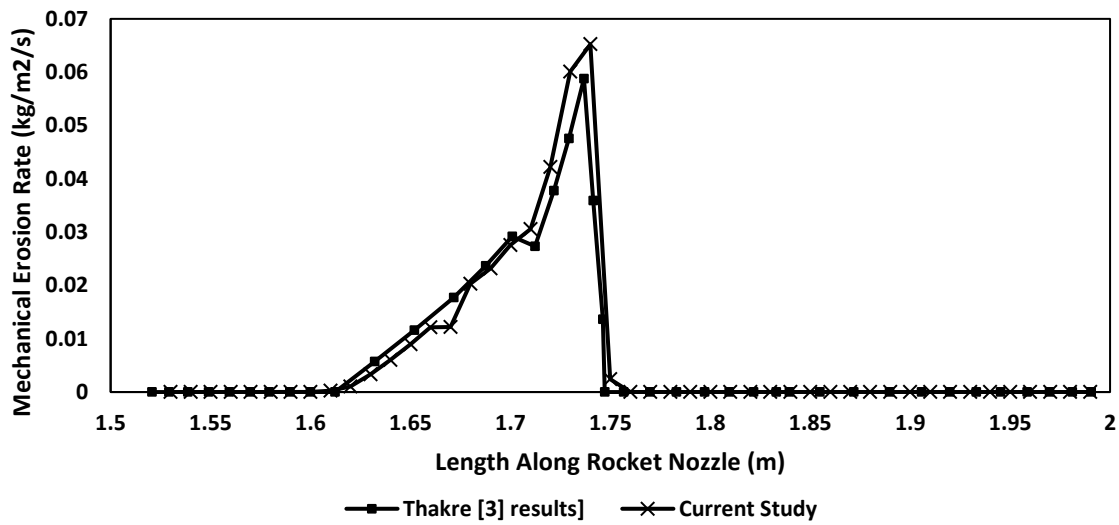
Figure 5-16: Mechanical erosion rate validation against Thakre et al [41].

Droplets' size effect: As indicated before, seven different droplets' diameters (60, 100, 140, 180, 220, 260, 300 μm) are chosen for the upcoming analysis. The droplet's size effect is better be studied on cases where no size change occurs, so the simplified model is used without incorporating the droplets' breakup model. Averaging the erosion rate over the nozzle's three sections gives a better overall representation for each droplet size as shown in Figure 5-17 & 5-16 & 5-17 & 5-18. Figure 5-17 shows that the mechanical erosion occurs in the convergent and throat (only its beginning as will be proved in the next paragraph) sections. It also shows that the throat's erosion rate decreases as the droplets' sizes decrease until it reaches zero for droplets' diameter less than 140 μm. Reviewing the different cases data, it can be inferred that most of the erosion occurs in the convergent section, and that any observed major erosion in the throat section will be caused by the heterogeneous reactions, hence chemical erosion. The erosion in the convergent section is presented in Figure 5-19, where the erosion first increases by decreasing the droplet's diameter to 220 μm, then it starts to decrease again. The erosion rate is not only a function of the incident mass flux of droplets, but also the droplet's relative velocity and incidence angle. As evidence, the average incident mass flux decreases with decreasing the droplet's diameter as shown in Figure 5-20, while the erosion rate increases. This can be explained by the rise in the average relative velocity (shown in Figure 5-21) and the decrease in the incident angle. Smaller droplets are easier to be entrained by the exhaust gases, hence higher relative velocity'. This increase compensates for the droplets' incident mass flux and increases the erosion rate, until the decrease in incident mass flux prevails and the erosion rate starts to decrease. Figure 5-22 shows two different parcels (group of droplets) trajectories through the combustion chamber internal flow field for the seven different droplets' diameters. As the droplet's diameter decreases, it follows the gas flow streamlines. All droplets enter the flow field with the same velocity (0.1 m/s). However, as shown

in the figure, smaller droplets are more influenced by the flow field where they gain axial velocity compared to the larger droplets. On the other hand, larger droplets are heavy, have more momentum, and travel more in the radial direction before moving in the axial direction. Figure 5-22 also shows that smaller droplets hit the nozzle walls in a location further than the larger ones. Figure 5-23 presents a detailed map of the nozzle erosion rate at different droplets' diameter. As explained before, the erosion is prevalent in the convergent section and the beginning of the throat section (just before the throat), which starts to increase gradually until it reaches its maximum just before the throat, followed by a severe decrease to zero. It is also shown that the erosion increases as the droplets' diameter decreases from 300 μm to 220 μm, then it decreases with the diameter decrease. And the reason for that (as explained before), Smaller droplets' diameter leads to less incident mass flux, but higher relative velocity, and smaller incidence angle. Over a certain droplet diameter (220 μm), the relative velocity increase dominates, hence the erosion rate increases, however under that limit, the decrease in the incident mass flux and incidence angle dominates, hence the erosion rate decreases. Figure 5-24 provides the average incident droplets' diameter on the nozzle walls, but since the breakup model is not included, the average diameter is the same injected diameter and constant. This figure also shows that as the droplets' diameter decreases, the erosion starts and ends earlier on the nozzle walls, which can be beneficial by moving the erosion far from the nozzle throat. Finally, Figure 5-25 proves that as the droplets' diameter decreases, the incident parcels on the nozzle walls decrease, hence lower incident mass flux. Also, it shows an opposite distribution for the erosion rate as the incident parcels (incident mass flux) is high at the middle of the nozzle convergent part. It starts to decrease moving downward in the nozzle, which can be clarified by the definition of the erosion rate and the droplets' relative velocity increase domination.
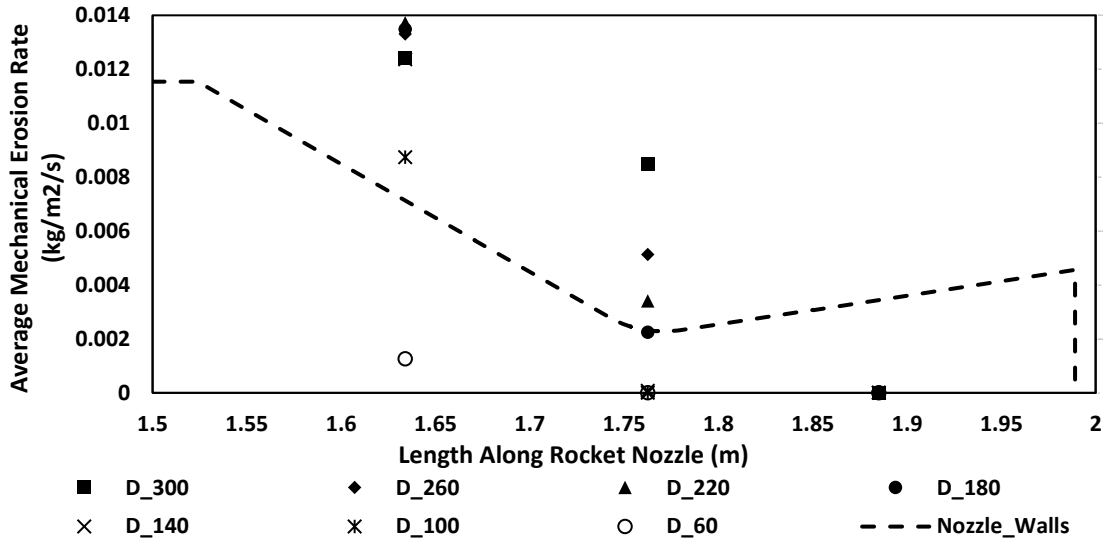
Figure 5-17: Average erosion rate over different sections of the nozzle for different droplets' sizes before applying the breakup model
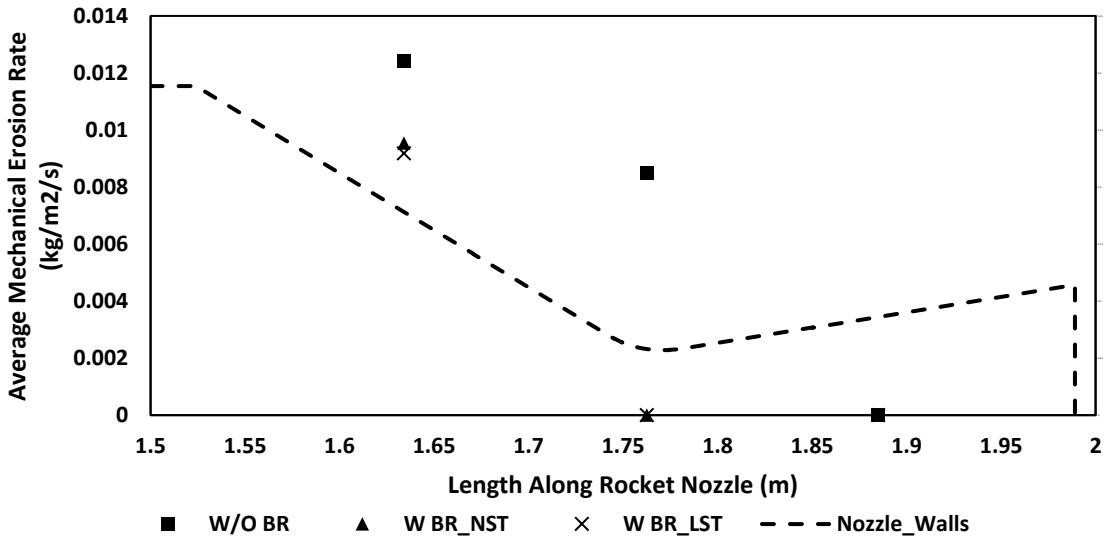
Figure 5-18: Average erosion rate over different sections of the nozzle for 300 μm droplet size
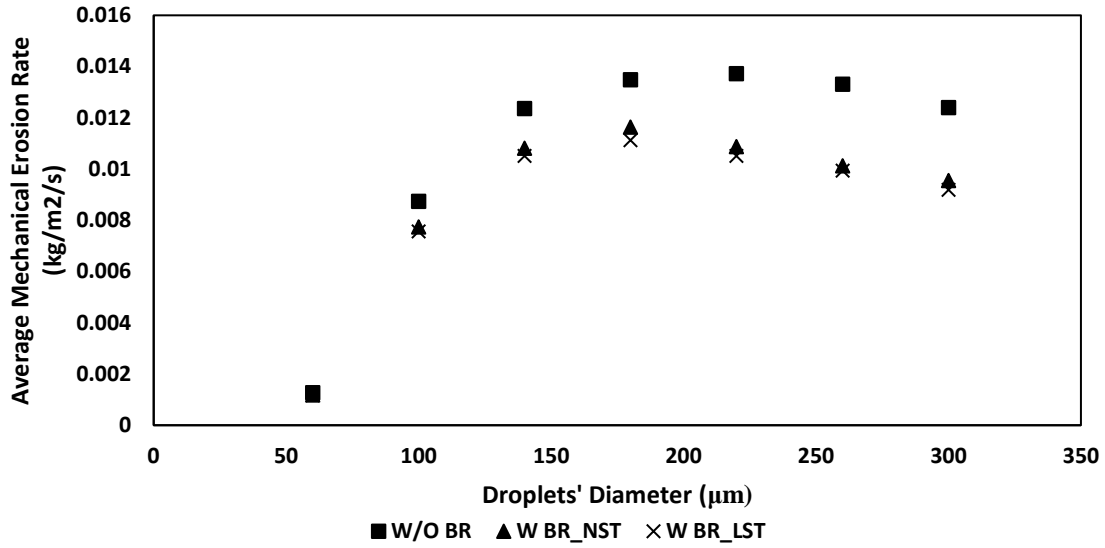
Figure 5-19: Average erosion rate on the nozzle's convergent section at different droplet's sizes
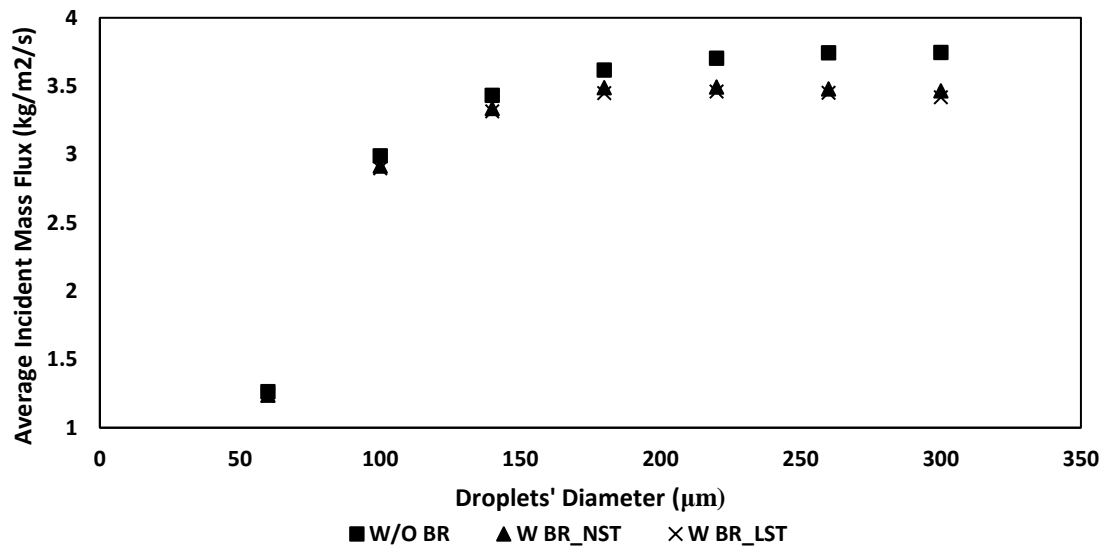
Figure 5-20: Average incident mass flux on the nozzle's convergent section at different droplet's sizes
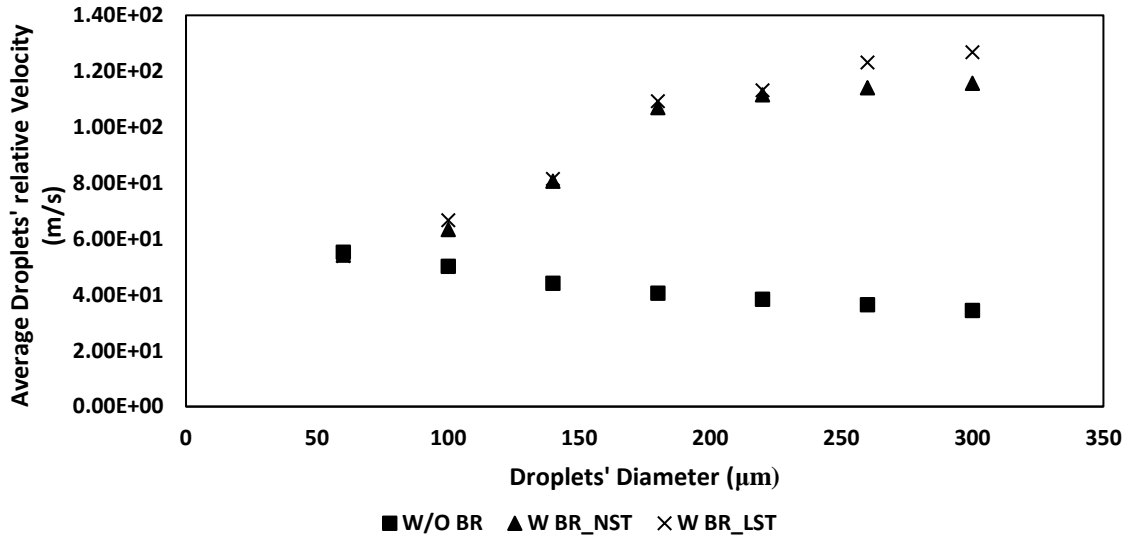
Figure 5-21: Average droplets' relative velocity on the nozzle's convergent section wall at different droplet's sizes
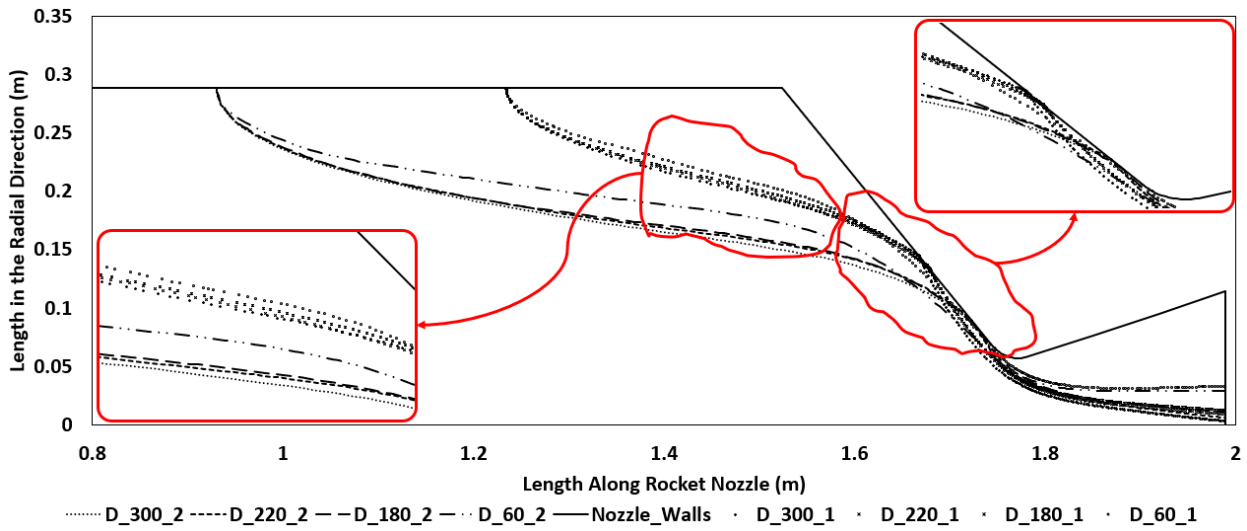
Figure 5-22: Two different parcels trajectories within the chamber at different droplet's sizes.

106
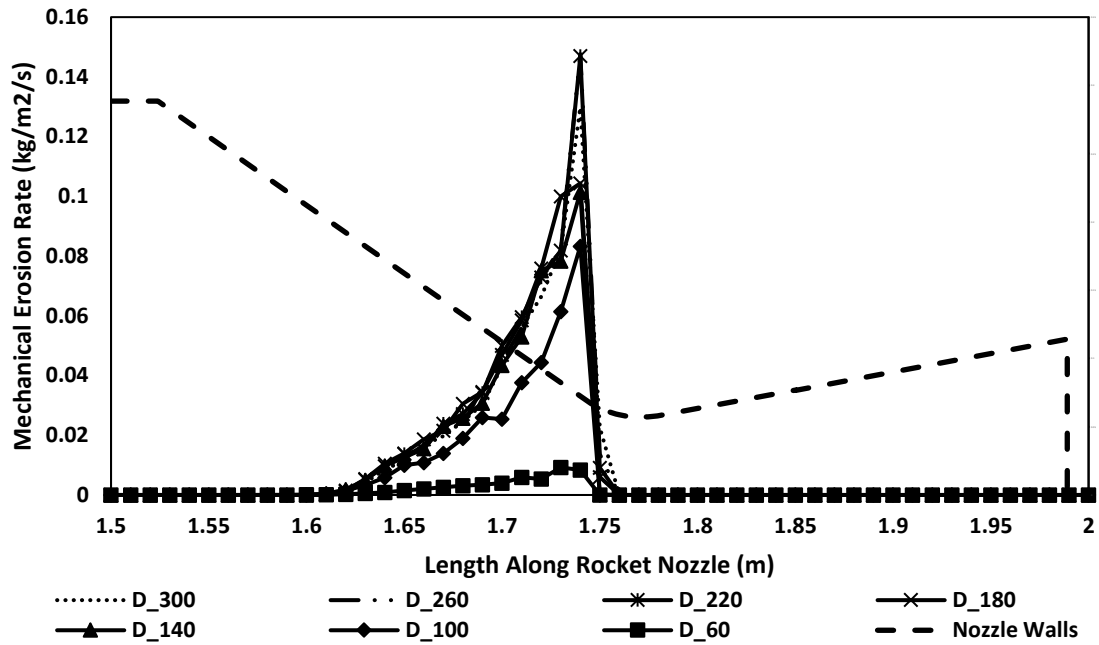
Figure 5-23: Mechanical erosion rate at different droplet's sizes before applying the break-up model
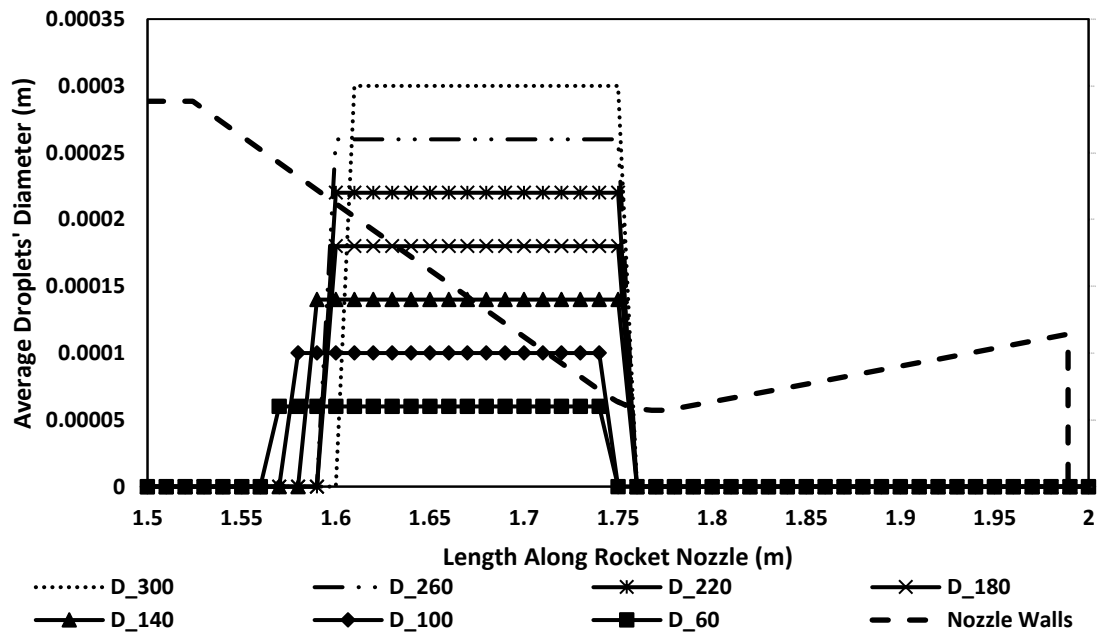
Figure 5-24: Average droplets' diameter at different droplet's sizes before applying the break-up model

107
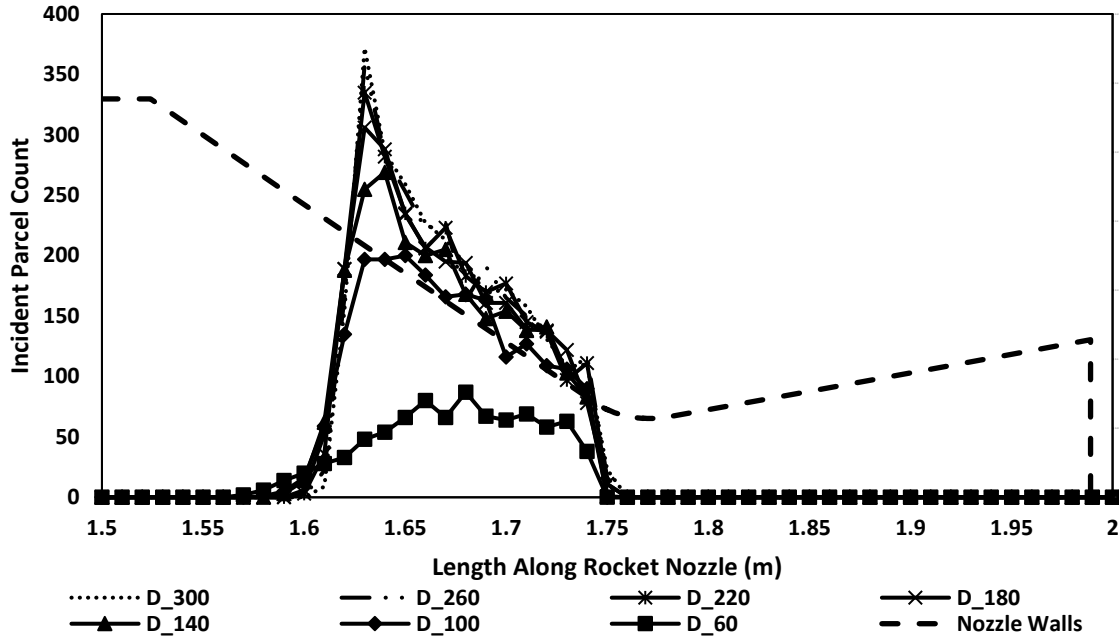
Figure 5-25: Incident parcels count at different droplet's sizes before applying the break-up model

Droplets' breakup effect: The same seven droplets' diameter are modeled, but this time with incorporating the Reitz-Diwakar breakup model. The droplet will breakup into smaller droplets if its weber number passes the critical value (12) which also will determine the breakup form bag or stripping. And now with the incorporation of the breakup model and since the major erosion occurs just before the throat where the droplets' velocity is the highest, smaller droplets will substitute the original ones in this region which are easier to be entrained by the gas flow and not impinge the nozzle walls. Figure 5-18 proves the previous explanation, as it shows that the average erosion rate in the throat section equals zero for the cases where the breakup model is active. The average erosion rate is following the same behavior like the case without including the breakup model, as it increases until a certain droplet's diameter, then it decreases again. However, its value decreases at the same droplet's diameter which can be explained by the breakup of the original droplets to smaller ones. On the other hand, the critical droplet diameter decreased from 220 μm to 180 μm as shown in Figure 5-19. Comparing the erosion rate for the same droplet's

108

diameter, it can be noticed that the erosion reduction percentage decreases from 24% (at 300 μm) to 6.2% (at 60 μm) as the breakup model influence decreases (lower weber number) with the decrease in the droplet's diameter. Unlike the case without applying the breakup model, the incident mass flux increases (shown in Figure 5-20) until droplet's diameter of 180 μm, then it decreases again similar to the erosion rate behavior. Larger droplets have higher breakup chance than average and small ones, in other words smaller average diameter, hence higher average relative velocity as indicated in Figure 5-21. Figure 5-26 presents a detailed map for the nozzle erosion rate at different droplets' diameter, where the erosion rate shows the same trend as before. The maximum erosion rate occurs for a droplet's diameter of 140 μm, however as mentioned before the overall maximum average erosion rate happens at a droplet's diameter of 180 μm. It can be also noticed that although the maximum overall reduction in the erosion rate is approximately 23%, the local erosion rate maximum reduction is significantly higher approximately 53%. Figure 5-27 presents the droplet's diameter change over the nozzle axial length. It begins with the injected diameter, remains constant for a while, then it starts to decrease drastically to around 55 μm. The decrease in the droplets' diameter begins earlier (through the nozzle), as larger diameter means higher Weber number (considering its definition) exceeding the critical one, hence developing droplets' breakup earlier. So, it can be inferred that the critical droplet's diameter for breakup in the current combustion chamber boundary conditions is in the range of 50 to 60 μm. Figure 5-28 shows the incident parcels count which agrees with the explanation provided for Figure 5-25. The detailed map of the erosion rate over the nozzle length is compared for the same droplet's diameter (60, 300 μm) as presented in Figure 5-29 & 5-29. For droplet's diameter of 300 μm, Including the droplets' breakup model significantly reduces the erosion rate due to subjecting the droplets to high Weber number, hence high breakup opportunities which is demonstrated by the average droplets'

diameter data provided in Figure 5-30. Comparing the results of two chosen droplet's diameters (60, 300 μm), the erosion rate reduction is very minimal at 60 μm diameter (Figure 5-31 & 5-30), as the droplets' breakup slightly occurs just before the erosion ends which confirms with the previous conclusion regarding the critical breakup droplet's diameter (50-60 μm). Figure 5-33 & 5-32 show the 300, 60 μm droplets trajectories at the discussed three conditions within the chamber. They highlight a minimal difference in the trajectory where the flow velocity increases, and breakup occurs. However, from these figures, it can be inferred that the droplet's injection diameter has a stronger influence on its trajectory than its breakup existence.
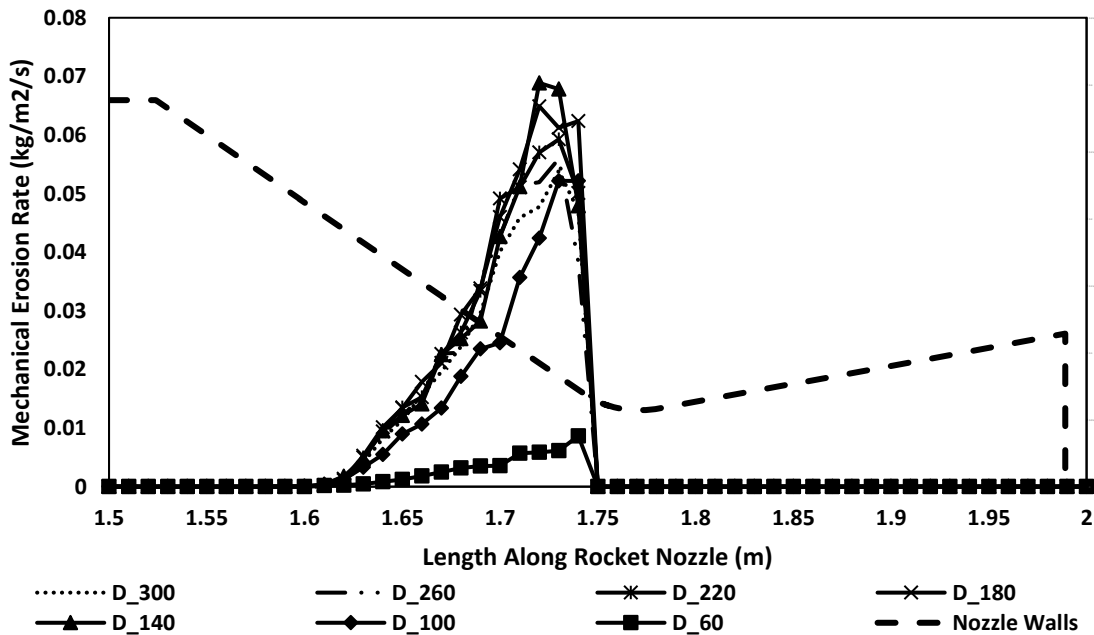
Figure 5-26: Mechanical erosion rate at different droplet's sizes after applying the break-up model
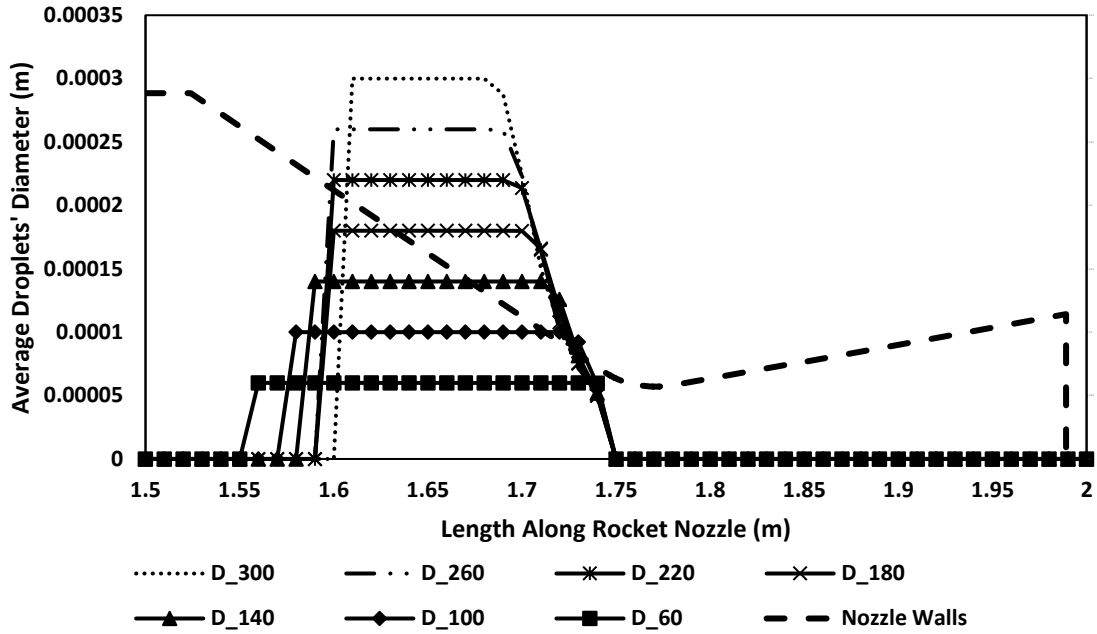
Figure 5-27: Average droplets' diameter at different droplet's sizes after applying the break-up model
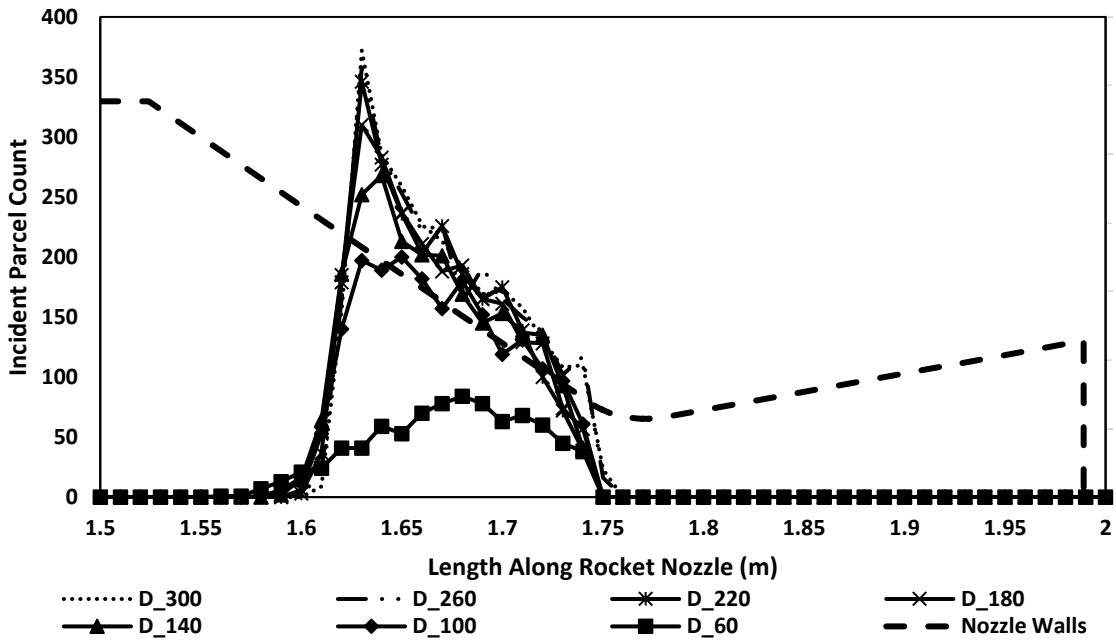
Figure 5-28: Incident parcels count at different droplet's sizes after applying the break-up model
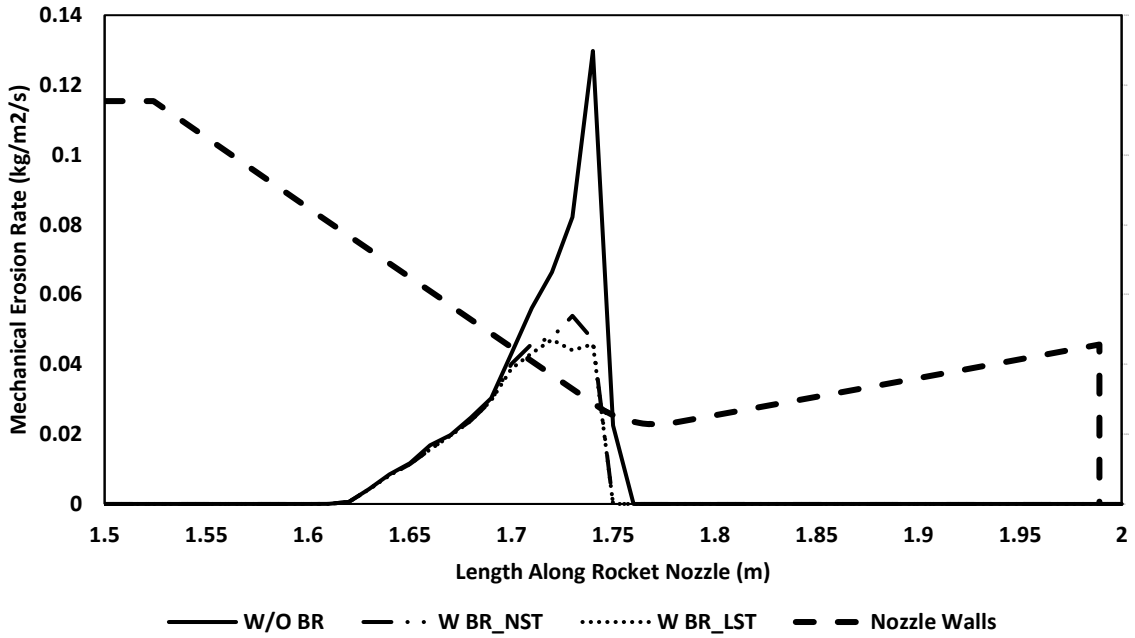
Figure 5-29: Erosion rate at different conditions for 300 μm droplet size
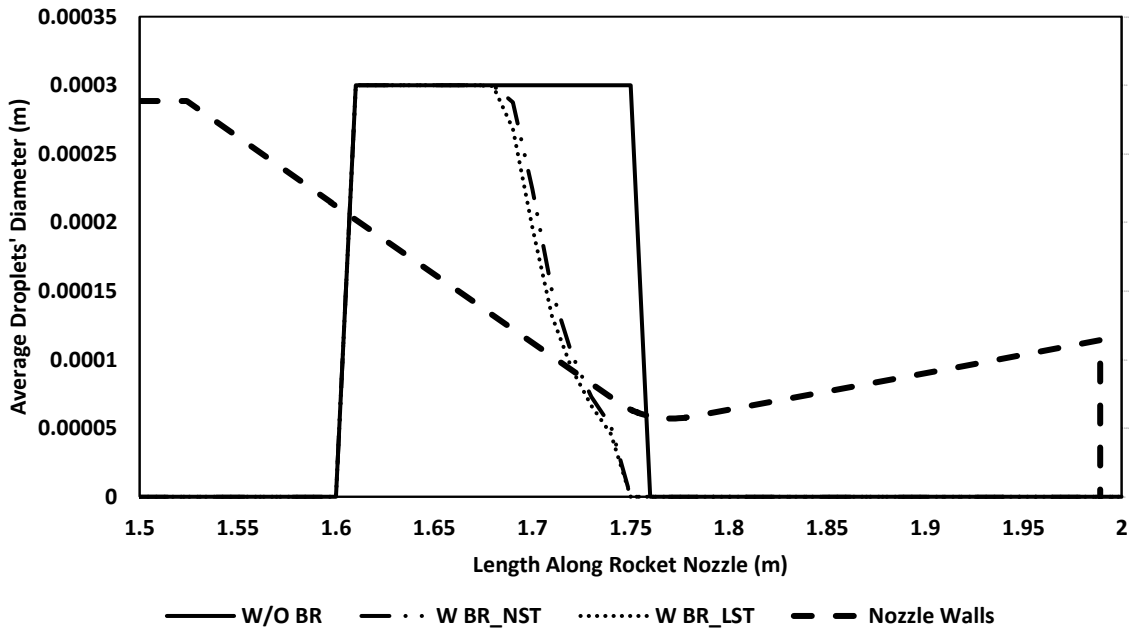
Figure 5-30: Average droplets' diameter at different conditions for 300 μm droplet size
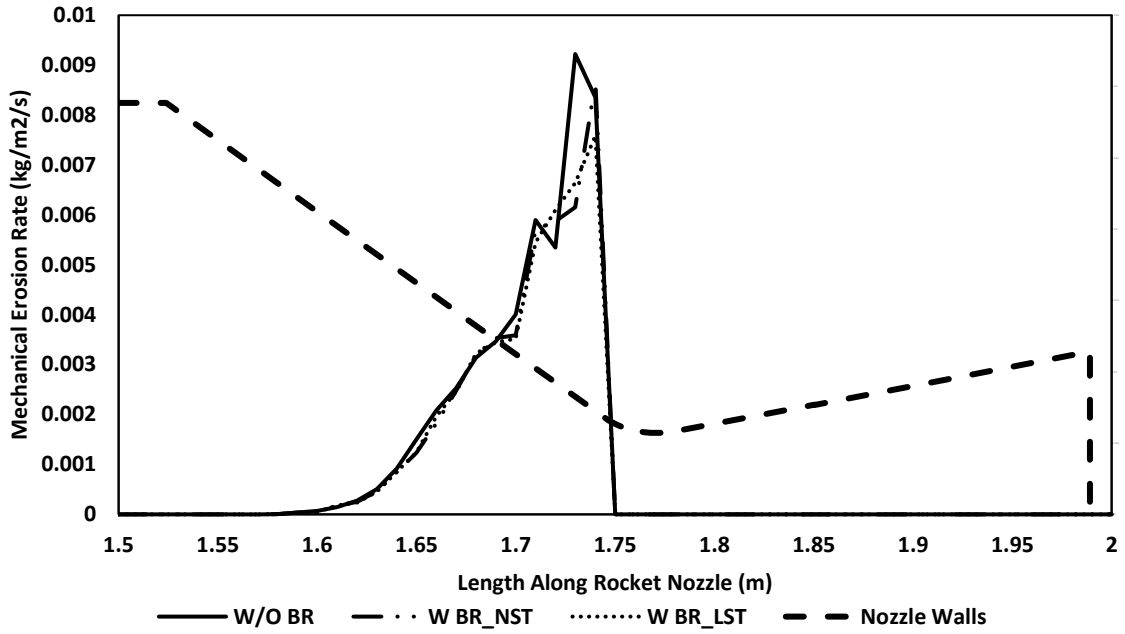
Figure 5-31: Erosion rate at different conditions for 60 μm droplet size
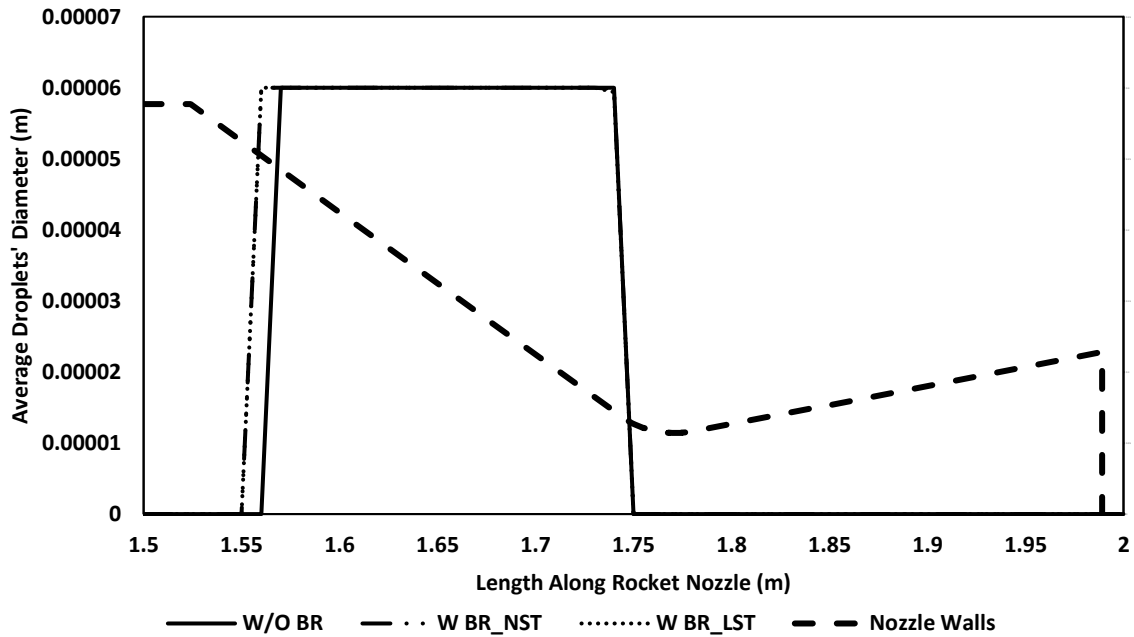
Figure 5-32: Average droplets' diameter at different conditions for 60 μm droplet size
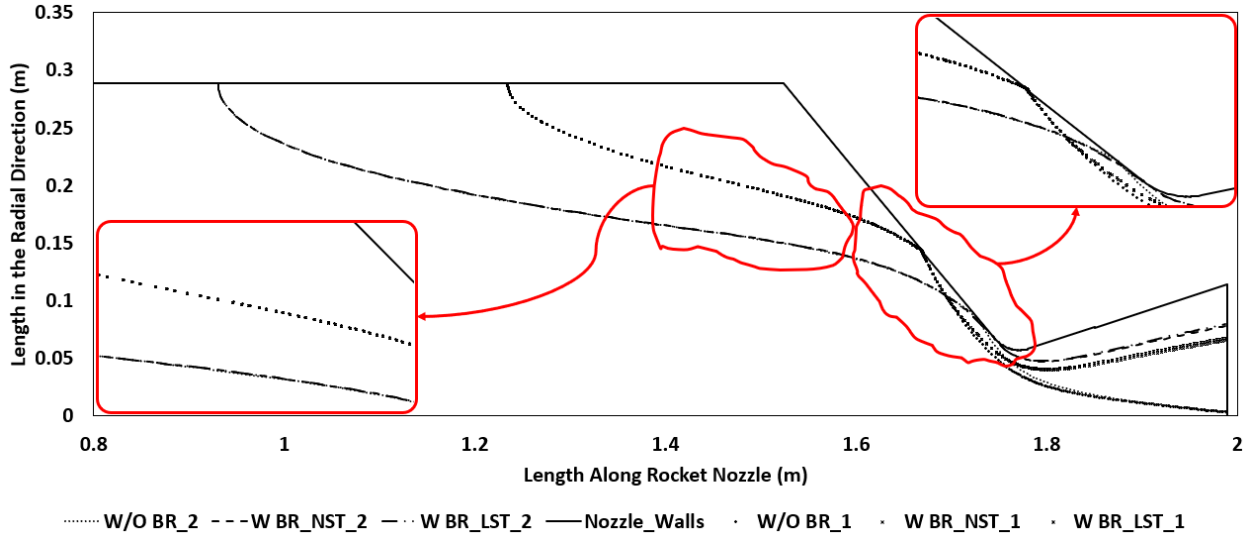
Figure 5-33: Two different parcels trajectories within the chamber for 300 µm droplet size
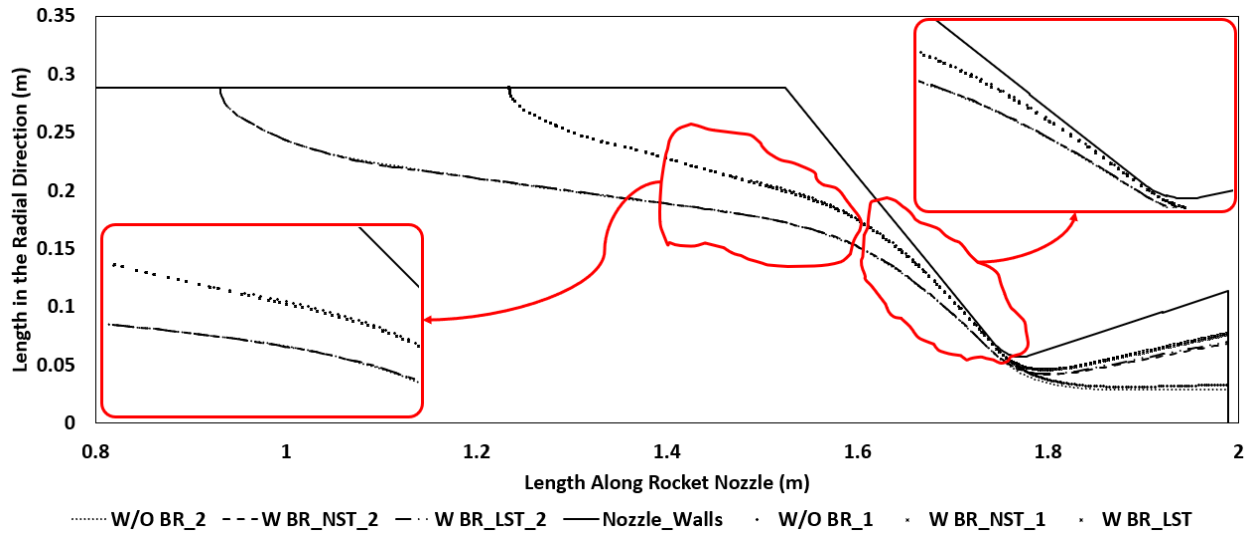
Figure 5-34: Two different parcels trajectories within the chamber for 60 µm droplet size

Reducing surface tension effect: The same seven droplets' diameters were used to model the nozzle's erosion rate but with 15% reduction in the droplets' surface tension (from 0.791 N/m to 0.672 N/m). Figure 5-35 & 5-34 & 5-35 show the erosion rate, average droplets' diameter, and incident parcels distribution over the nozzle surface. They are following the same case trends, including the breakup model effect. Thus, same explanations will apply here. Reducing the droplet's surface tension helps in lowering the average erosion rate by 4.5% to 1%. Moreover, the

114

average incident mass flux decreases by 0.5% to 1.4%. Figure 5-29 shows that reducing surface tension can decrease the maximum local erosion rate by 13%. However, Figure 5-31 assures that the reduction is a function of the droplets' diameter, as it is minimal for the 60 μm droplet's diameter. Reducing the droplets' surface tension increases the Weber number of the same droplet's diameter and velocity, hence increasing the breakup chance. As the droplet's diameter decreases, the breakup opportunities decrease (until it vanishes for droplets with a diameter less than 50 μm). Hence the surface tension reduction influence diminishes.
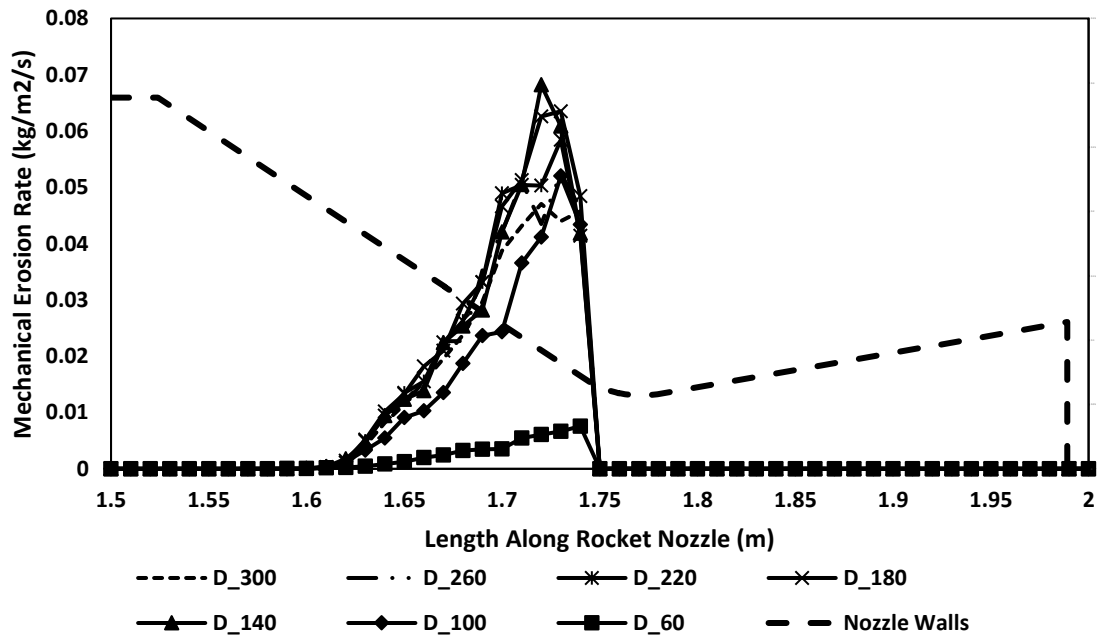
Figure 5-35: Mechanical erosion rate at droplet's different sizes and lower surface tension
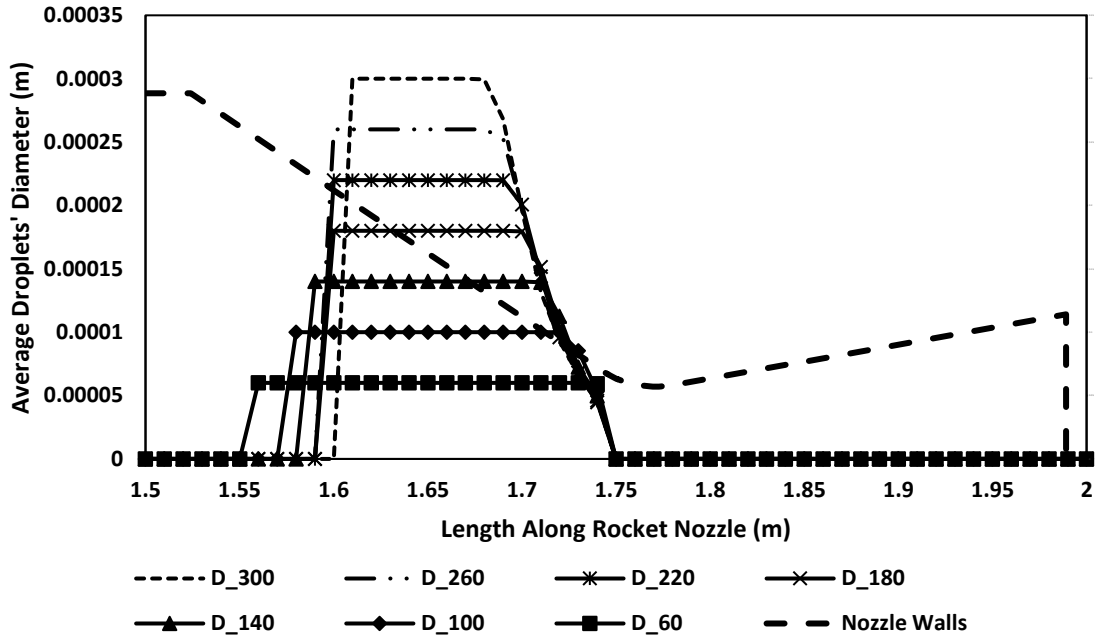
Figure 5-36: Average droplets' diameter at droplet's different sizes and lower surface **tension**
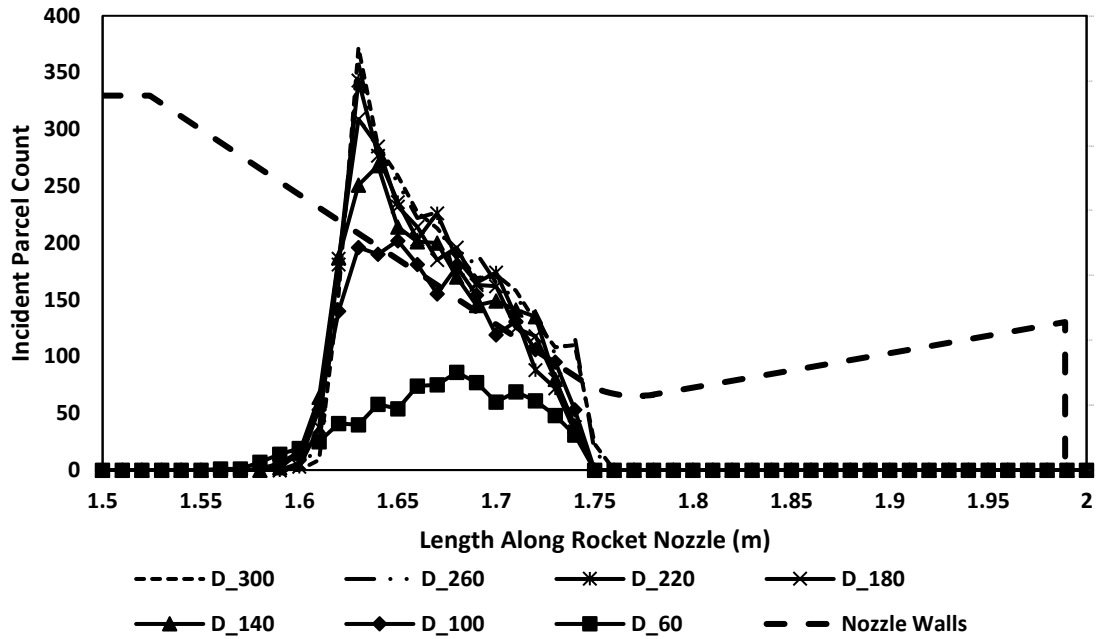
Figure 5-37: Incident mass flux at droplet's different sizes and lower surface tension

Chapter 6 Aluminum Content and Alumina agglomerates Initial Velocity Impacts on the Mechanical Erosion in Solid Rocket Motor Nozzle

Thakre et al. [41], and Tarey et al. [42] numerically studied the mechanical erosion in the solid rocket motor as mentioned earlier. Geisler [6] and Thakre et al. [14] investigated the nozzle recession considering different propellant composition (in terms of the aluminum mass fraction, they had found that having a higher content of aluminum mass fraction reduces the nozzle material recession rate despite of the higher nozzle temperature and they explained that by the decrease in the oxidizing species [CO_2, H_2O] mass fraction when increasing the aluminum content within the propellant. While Madabhushi et al. [74] studied the effect of having different particles' injection velocity (1-25% of the continuous phase velocity) and concluded that increasing the particles injection velocity rises the escaping chance of these particles from the submerged nozzle cavity, however it does not affect the gas flow dynamics.

The mechanical erosion was investigated by several researchers numerically; however, they did not study the effect of having different aluminum mass fraction, different agglomerates' injection velocity while considering agglomerates' secondary breakup in the nozzle convergent section. So, the current section attempts to consider a more accurate numerical framework to predict the mechanical erosion for different propellant composition and injection velocities.

6.1 Theoretical Concept and Governing Equations

Burning metalized propellant (Ammonium perchlorate (AP) / Hydroxyl-terminated polybutadiene (HTPB) / Aluminum (AL) produces high temperature gas mixture of different six species [H_2O, CO_2, CO, H_2, HCL, and N_2], and the burning products of the aluminum combustion process. The Eulerian / Lagrangian approach is used to simulate the continuous phase (product

117

gas) and discrete phases in the computational domain. All the equations describing the continuous phase, discrete phase, aluminum combustion process, mechanical erosion estimation and droplets' breakup were introduced and discussed before in section 5.1.

6.2 Model Description and Input Data

The combustion process occurs between the reactants of the metalized solid propellant A metalized propellant (AP / HTPB / AL) with a density of 1794.6 kg/m3 and burning rate of 9.0678 x 10^{-3} m/s is used [17]. Considering the mentioned propellant properties and the geometry configuration mentioned in chapter 5, the propellant burning rate is 16.273 kg/m2/s, while the motor chamber pressure and temperature are 68 bar and 3327 K, respectively [41]. The nozzle walls' temperature is assumed isothermal (2500 K), while the motor chamber head wall is considered adiabatic [41]. The model used in this section is the same as the previous chapter, so it is already validated against Thakre et al. and Li et al. results.

Having higher aluminum mass fraction in the propellant composition will reduce the nozzle chemical erosion despite of the higher nozzle wall temperature because of the lower available mass fractions of the oxidizing species. The first objective in this section is investigating the effect of having higher aluminum content on the nozzle mechanical erosion. So, five different aluminum mass fractions [15%, 18%, 21%, 24%, 27] are modeled considering two cases: one without applying the agglomerates breakup model (W/O BR), and the other after applying it (W BR). The inlet boundary conditions for each case are based on the data reported by Geisler et al. [6] and shown in the below table.

Table 6-1: Propellant composition and combustion products inlet boundary conditions

Case		1	2	3	4	5
Propellant Composition	AP [%]	75	72	69	66	63
	HTPB [%]	10	10	10	10	10
	AL [%]	15	18	21	24	27
Combustion Products Mass Fractions	CO_2	0.04	0.025	0.015	0.005	0.0015
	H_2O	0.145	0.105	0.07	0.045	0.025
	H_2	2.00E-02	0.02	0.02	0.02	0.02
	CO	0.175	0.18	0.2	0.2	0.2
	HCL	2.40E-01	0.23	0.195	0.19	0.19
	AL_2O_3	0.28	0.34	0.4	0.44	0.4635
	N_2	0.1	0.1	0.1	0.1	0.1
Inlet	[K]	3580	3655	3715	3750	3745

As shown later in the results section, and as indicated in Thakre et al. [41] work, The pure aluminum particles, when using a propellant composition [71/14/15], evaporate fully close to the burning surface. So, the nozzle mechanical erosion depends only on the impingement of the alumina particles, hence a numerical model considering only the injection of the alumina particles is established while the effect of the aluminum particles burning process is considered by updating the multi-species gas mass flux (15.321 kg/m2/s) and mass fractions as shown Table 6-2. The new established numerical model will be utilized further to investigate the effect of having different agglomerates' injection velocity on the mechanical erosion rate. The injection velocity effect is studied at four different alumina particle's diameters (60, 140, 220, 300 μm). Four different injection velocities are considered (4%, 25%, 50%, 75% of the continuous phase inlet velocity), while considering two cases: one without applying the agglomerates breakup model, and the other after applying it.

Table 6-2 Combustion products inlet mass fractions [42]. (Continuous phase)

Gas Species	Mass Fraction
H2O	0.109111
CO	0.284957
CO2	0.022013
H2	0.022267
AL2O3	0.232293
HCL	0.230154
N2	0.099204

6.3 Results and Discussion

Propellant's aluminum content: Having higher aluminum content in the propellant reduces the oxidizing species mass fraction in the multi-species product gas, hence reducing the nozzle chemical erosion, despite of the nozzle higher wall temperature. Five aluminum mass fractions (15%, 18%, 21%, 24%, 27%) were studied to deduct the nozzle mechanical erosion response. The dispersed phases injected mass fluxes increase with increasing the aluminum content. Two cases were investigated for each aluminum content: one without applying the droplets breakup model, while the other after applying the model. The first case is studied to understand the pure effect of the intended factor on the mechanical erosion without overlapping with the droplets' breakup effect. Figure 6-1 & 6-2 show that the erosion occurs mainly in the nozzle convergent section and the tip of the throat section while not applying the droplet breakup model. However, applying the secondary breakup model eliminates the erosion within the throat section and reduces the mechanical erosion rate with more than 50%. The droplets' velocity increases gradually while dragged by the exhaust gases, hence the Weber number increases accordingly till its critical value where the droplets split to smaller droplets. The smaller droplets will be lighter in mass and easier to be entrained by the continuous phase far from hitting the nozzle throat section walls, hence no erosion is noticed in the throat section. Since the mechanical erosion depends on the incident particles mass flux and relative velocity, it decreases significantly due to

the droplets breakup as shown in Figure 6-2. So, it can be deducted that the mechanical erosion is occurring only in the convergent section and has its maximum value just before the throat section. Any other erosion noticed in the throat section is due to the heterogeneous reactions (chemical erosion). Thus, the propellant aluminum content will be investigated only in the convergent section.
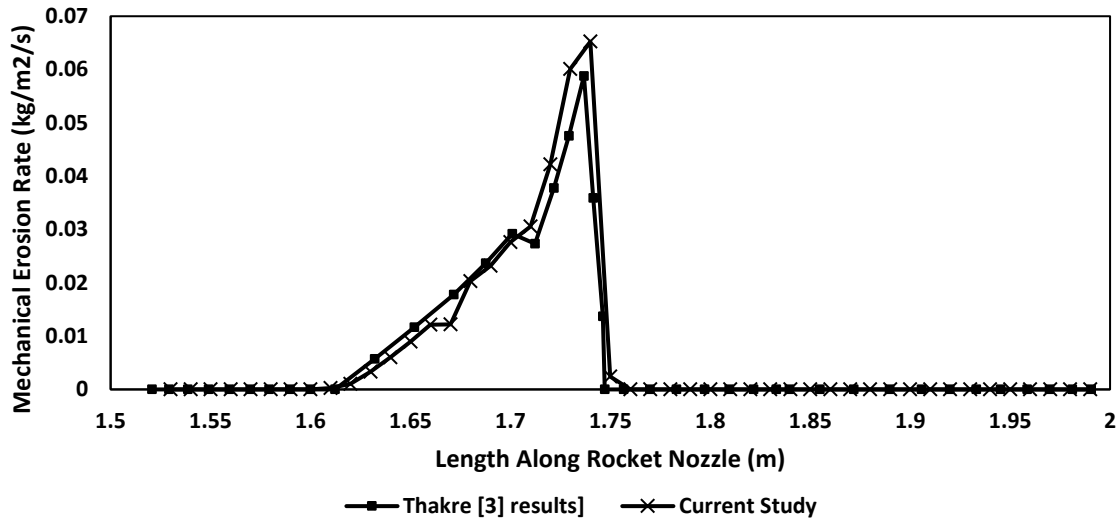
Figure 6-1: Mechanical erosion rate comparison with Thakre et al [41] results.
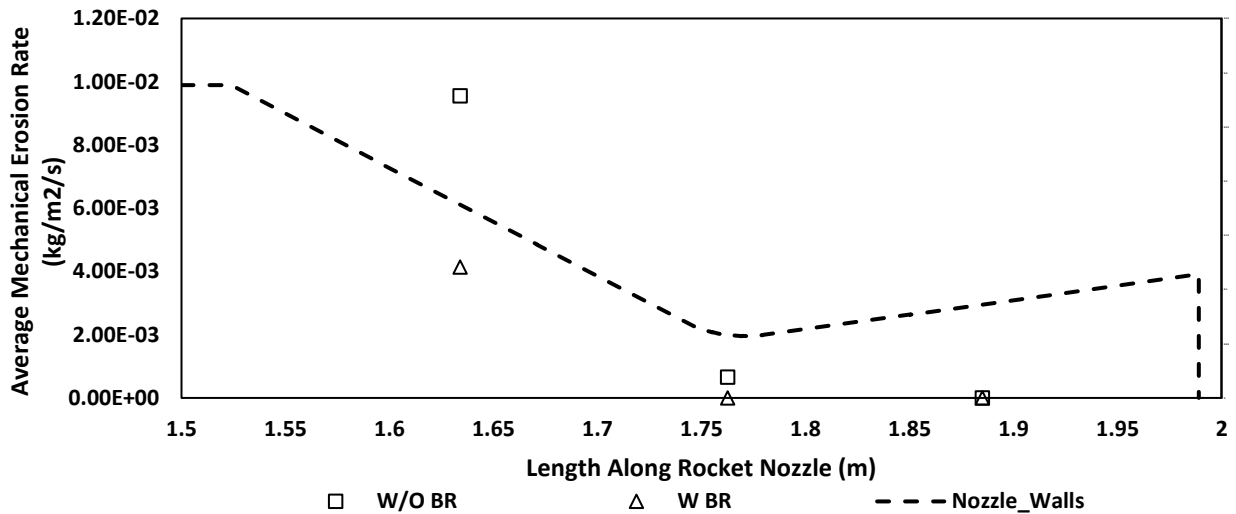
Figure 6-2: Average erosion rate over different nozzle sections for the 15% propellant aluminum content case

121

Figure 6-3 presents the average erosion rate of the whole convergent section at the investigated different aluminum content percentages. Considering the case without applying the droplets breakup model, erosion is increasing with increasing the aluminum content to reach its maximum at 21% aluminum content (9% increase compared to the 15% aluminum content), then it decreases with the aluminum content increase, however the average erosion rate at 27% aluminum content is still higher (4%) compared to the 15% aluminum content erosion. The erosion is following the same trend while applying the breakup model, however the maximum erosion rate (11% higher than the 15% case) is occurring at 24% aluminum content, and the erosion rate at 27% case is 10% higher than the 15% case. Reviewing the particles' incident mass fluxes shown in Figure 6-2 raise doubts about the previous discussed erosion rate trends, as the particles' incident mass fluxes increase with increasing the aluminum content. But, recalling the mechanical erosion definition, it is proportional to the incident mass flux and square of the particles' impingement relative velocity. Increasing the aluminum content reduces the continuous phase mass flux, hence reduces the particles' relative velocity as shown in Figure 6-3. The increase in the incident mass flux balances the particles' relative velocity decrease, and the erosion rate increases till the break point (either 21% or 24% aluminum content), where the velocity reduction dominates, and the erosion rate descends.
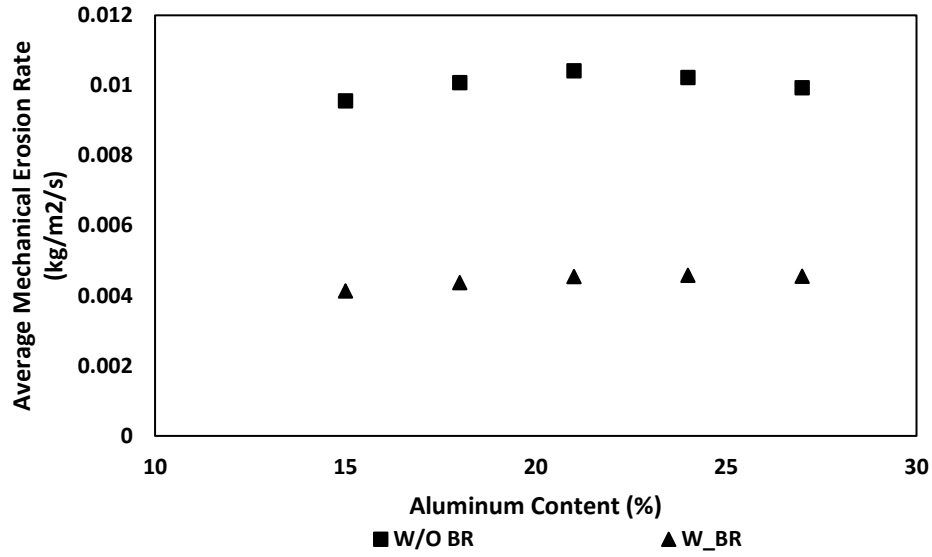
Figure 6-3: Average erosion rate at different propellant aluminum contents
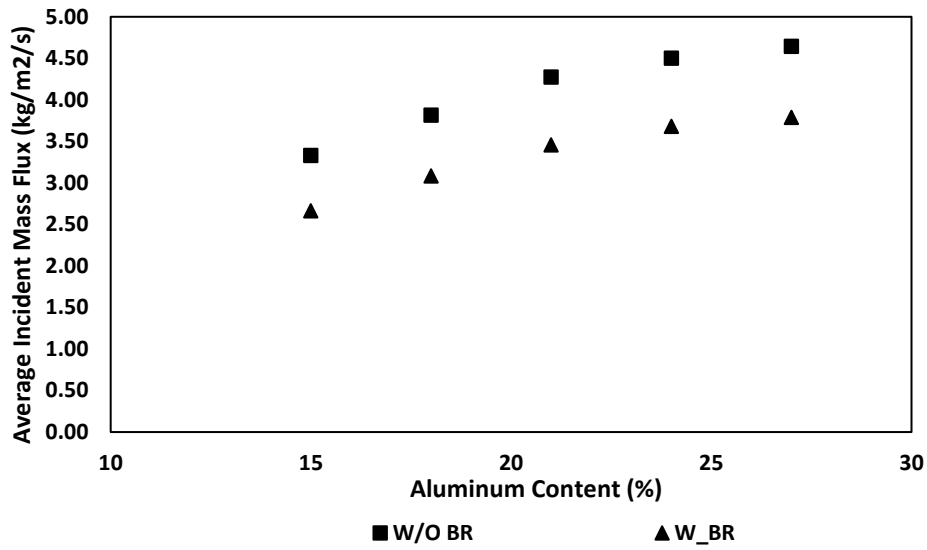
Figure 6-4: Average incident mass flux at different propellant aluminum contents
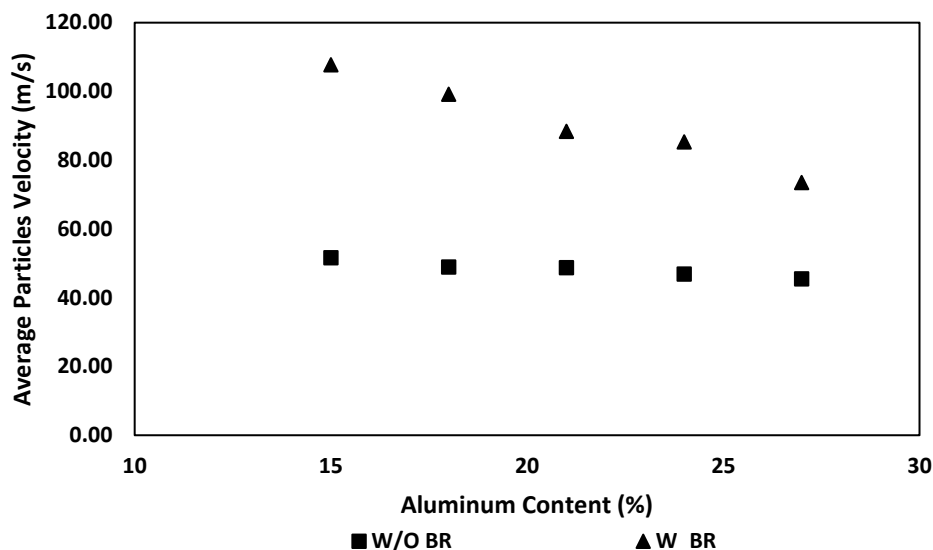
Figure 6-5: Average droplets' relative velocity at different propellant aluminum contents

It was mentioned earlier in the model validation section that at 15% aluminum content, all the injected aluminum particles are burning near the combustion chamber inlet walls and are not participating in the nozzle walls mechanical erosion. But since the aluminum combustion process is controlled by the existence of the oxidizing species around the aluminum particle, the aluminum particle residence time within the combustion chamber will vary at different aluminum content. Three different parcels trajectories traveling through the combustion chamber are shown in Figure 6-6 at different propellant content. Having higher aluminum content reduces the oxidizing species mass fractions within the exhaust gases as shown in Table 6-1, hence lower aluminum evaporation rate and longer aluminum particles path in the combustion chamber. So, Propellants with aluminum content 24% and higher will have a mechanical erosion caused by pure aluminum particles, however the incident aluminum particles mass flux on the convergent nozzle wall is from 0.01% to 0.5% of the multicomponent (aluminum and aluminum oxide) particles mass flux, hence the pure aluminum particles' erosion is minimal.
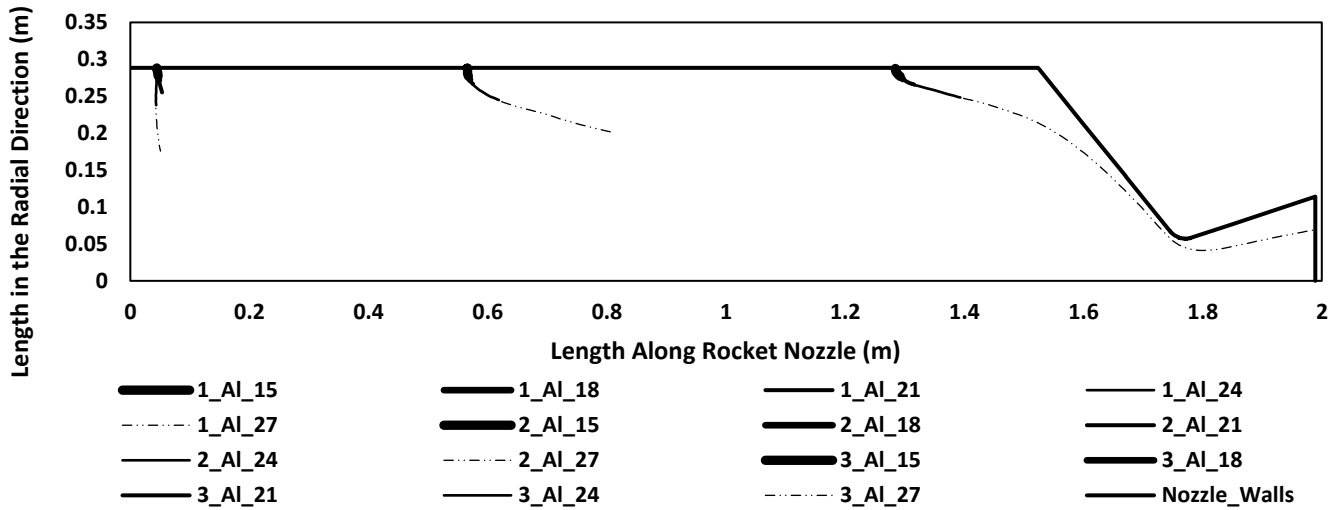
Figure 6-6: Three different parcels trajectories within the chamber at different propellant aluminum contents.

Figure 6-7 & 6-8 provide the nozzle mechanical erosion rate with 1 cm increment for different propellant aluminum contents, before considering and after considering the breakup model. They are presenting a detailed maps for the same discussed results. Figure 6-9 present a comparison between the erosion rate along the nozzle length before and after applying the breakup model at 27% aluminum content and proves the huge impact on the erosion rate due to that consideration.
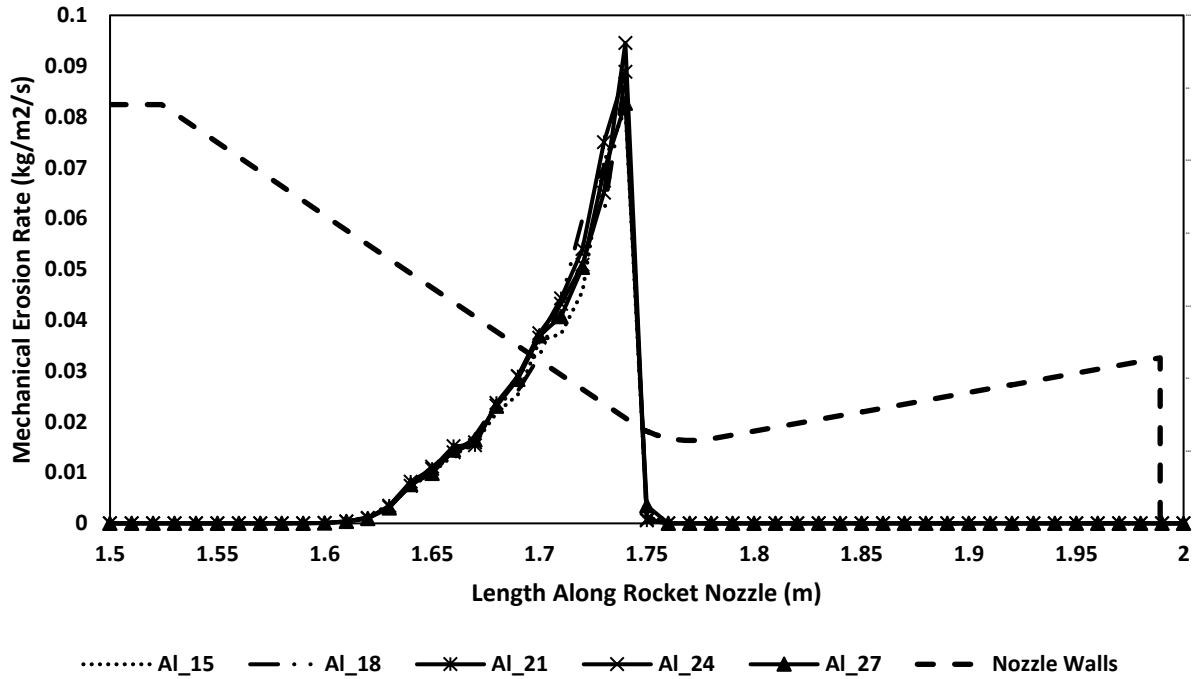
Figure 6-7: Mechanical erosion rate over the nozzle length at different propellant aluminum contents before applying the break-up model
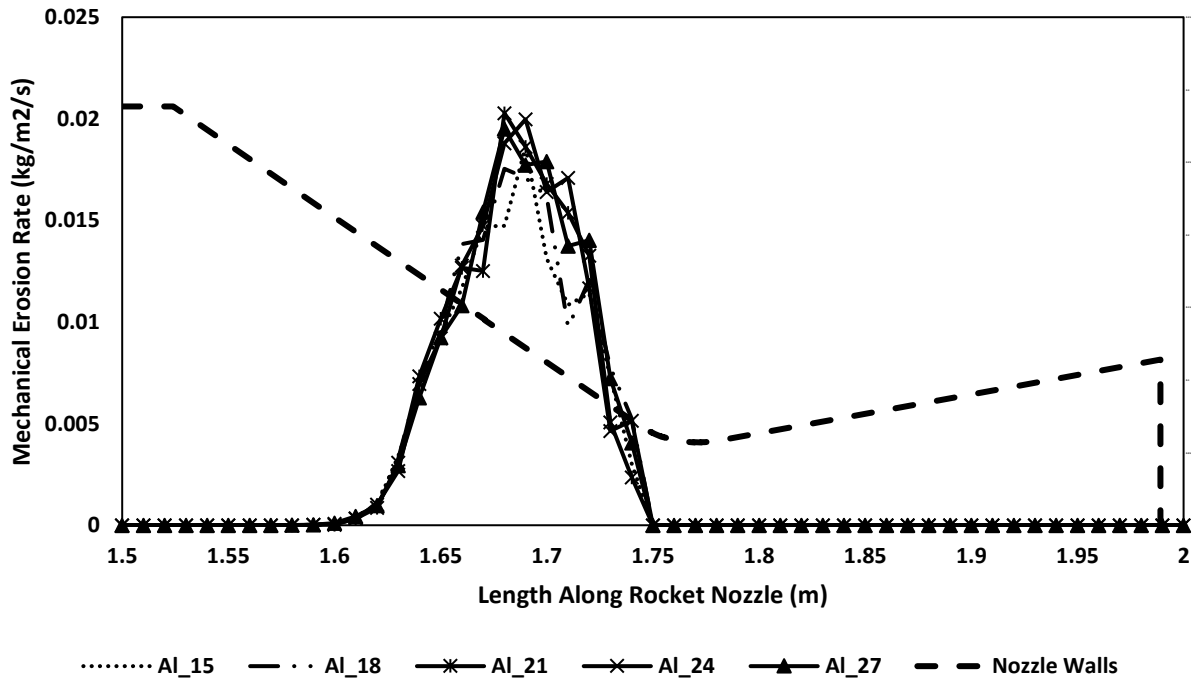
Figure 6-8: Mechanical erosion rate over the nozzle length at different propellant aluminum contents after applying the break-up model
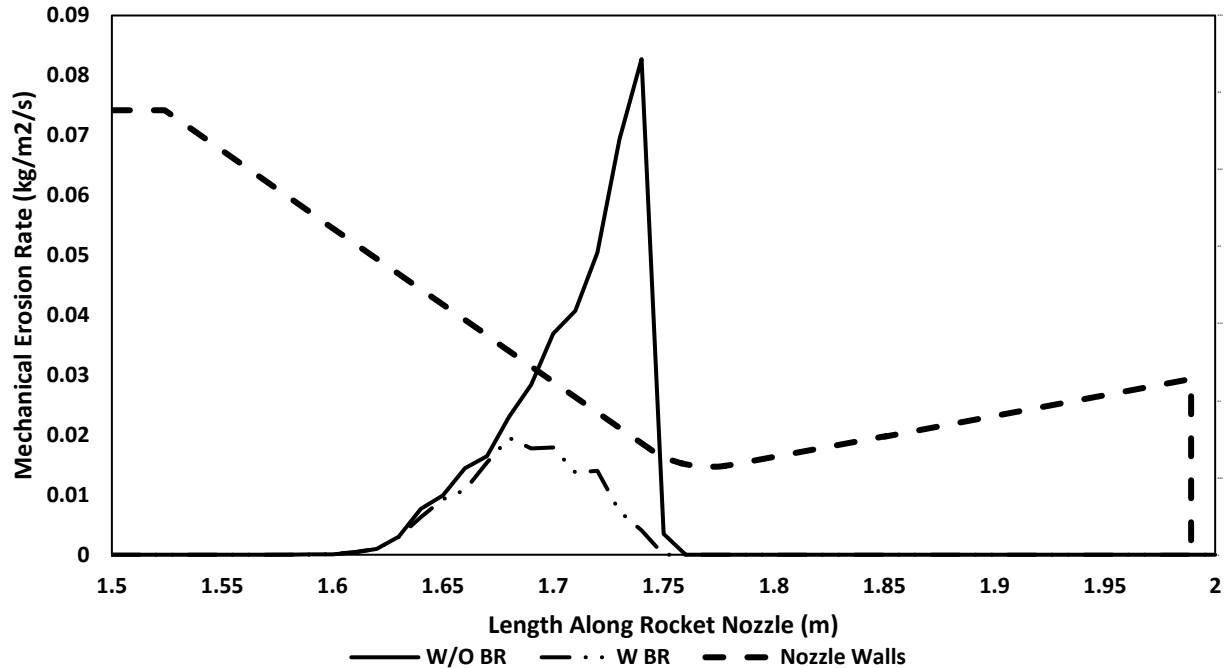
Figure 6-9: Erosion rate over the nozzle length at the 27% propellant aluminum content case

Particles' injection velocity: Having different particles' injection velocity (1-25% of the continuous phase velocity) were investigated earlier [74] and it was found that the higher particles' injection velocity is, the greater chance they have to escape from the submerged nozzle cavity, but it does not affect the gas flow dynamics. The injection velocity influence on the nozzle mechanical erosion was not studied before, so four injection velocities for the multicomponent particles (4%, 25%, 50% and 75%) are considered in the current study. Each injection velocity is investigated using four different particle diameters (60 μm, 140 μm, 220 μm, 300 μm) and on/off breakup model mode. As proved before, most of the mechanical erosion occurs in the nozzle convergent part, so it will be averaged on this section and studied for the current study several cases. Figure 6-10 & 6-11 & 6-12 present the average erosion rates, incident mass fluxes, and particles' average relative velocity variation with different particles' injection velocities, different particle diameters, with and without applying the breakup model. Each factor will have a different impact on the erosion rate, hence each one will be studied separately. Starting with the particle diameter, the erosion rate

127

increases with increasing the particle diameter and reaches its maximum at a particle diameter of 220 μm, then it decreases again. The same behavior is noticed at all the different injection velocities, although of the increase in the incident mass flux. The mechanical erosion correlation is proportional to the incident mass flux, particle's incident angle and the square of particle relative impingement velocity; hence the incident mass flux increase doesn't guarantee a progression of the erosion rate. Reviewing Figure 6-12, it can be noticed that the particles' average relative velocity decreases with the particle diameter increase, which is logical as smaller particles will travel with the exhaust gases faster than larger particles. So, now it is a balancing game between the mass flux increase and the relative velocity decrease. At small particles, the mass flux increase prevails, and the erosion rate increases till a particle diameter of 220 μm, when the particles' relative velocity decrease dominates, and the erosion rate declines. Moving to the incorporation of the breakup model and its effect on the mechanical erosion, generally the mechanical erosion rate decreases significantly at larger droplet diameters than smaller ones, as the droplet ability to breakup declines with its diameter decrease (Less Weber number). Comparing the erosion rate trends before and after applying the breakup model, they are similar, where the erosion rate increases with raising the droplet diameter followed by a decline in its value at 220 μm.

Finally, after understanding the impact of different particles' diameter and breakup model on the erosion rate, it will be easier discussing the injection velocity effect in it. Revising Figure 6-10, It can be concluded that increasing the particles' injection velocity increases the erosion rate. The erosion rate increase percentages between the 4% injection velocity (lowest erosion rate) and 75% injection velocity (highest erosion rate) are between 1-7.5%. On the other hand, Figure 6-11 shows that the incident mass flux declines with increasing the injection velocity for all the cases except for the 60 μm where it goes up and down. But as explained before, the erosion rate is not only a

128

function of the incident mass flux, but also a function of the particles' relative velocity and incident angle. Most cases, the relative velocity is increasing with increasing the injection velocity, but for only two cases, it is going up when increasing the injection velocity from 4% to 25%, decreases about 6% at 50% injection velocity, then increases again. It is noticed that the breakup model is considered in these two cases, which may explain this drop. Figure 6-13 & 6-14 provide the trajectories of two parcels for 60 μm and 300 μm droplet diameters, and the four injection velocities before and after applying the breakup model. It can be deduced from these two figures that applying the breakup model have a very tiny effect on the particles' trajectories, while the particle diameter and injection velocity are extremely affect its trajectory. Particles with small diameters follow the continuous phase streamlines, while larger particles have greater momentum and travel further in the radial direction before following the continuous phase streamlines. Having a higher injection velocity increases the particle momentum in the radial direction, forcing it toward the chamber axis, shifting the impingement locations of the particles closer to the convergent section end, and increasing the escaping chance of particles from hitting the nozzle walls. The previous explanation can clarify the reduction in the incident mass flux with higher injection velocities. The figures show also that the incident angle increase with higher injection velocities causing an increase in the erosion rate. However, the trajectories shifting is very significant at large droplet diameters. Figure 6-15 provides a detailed map for the mechanical erosion along the nozzle length with 1 cm increment for all the previous cases, where it is clearly obvious that the effect of all the discussed factors fades with smaller particle diameters. Figure 6-16 shows the locations where the particles start hitting the nozzle walls, in addition to the breakup events locations and droplets' size after breakup. As discussed earlier, increasing the injection velocity shifts the impingement location towards the nozzle throat, while decreasing the particle diameter shifts the impingement

129

locations toward the combustion chamber walls. Finally, it can be concluded that particles with diameter less than 60 μm will not have the chance to break up in the nozzle convergent section.
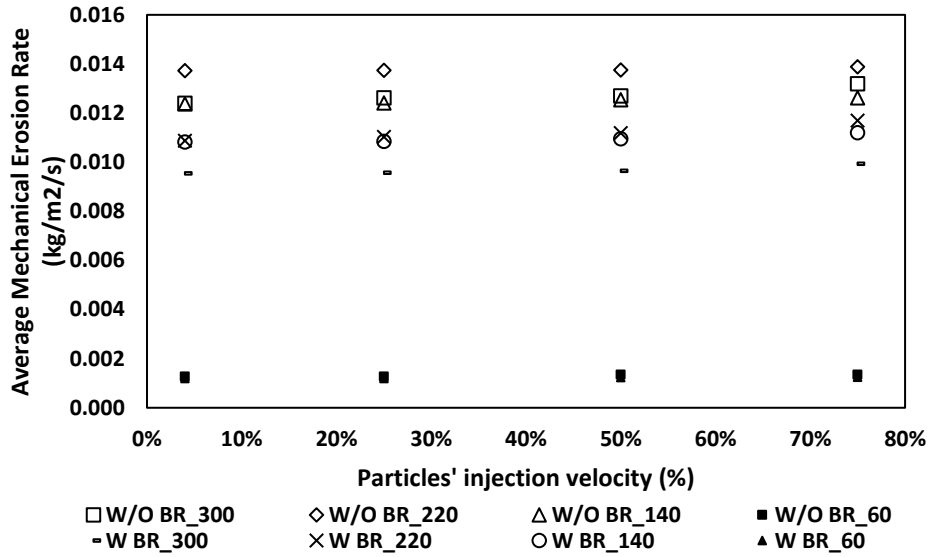
Figure 6-10: Average erosion rate for variable particles' injection velocity
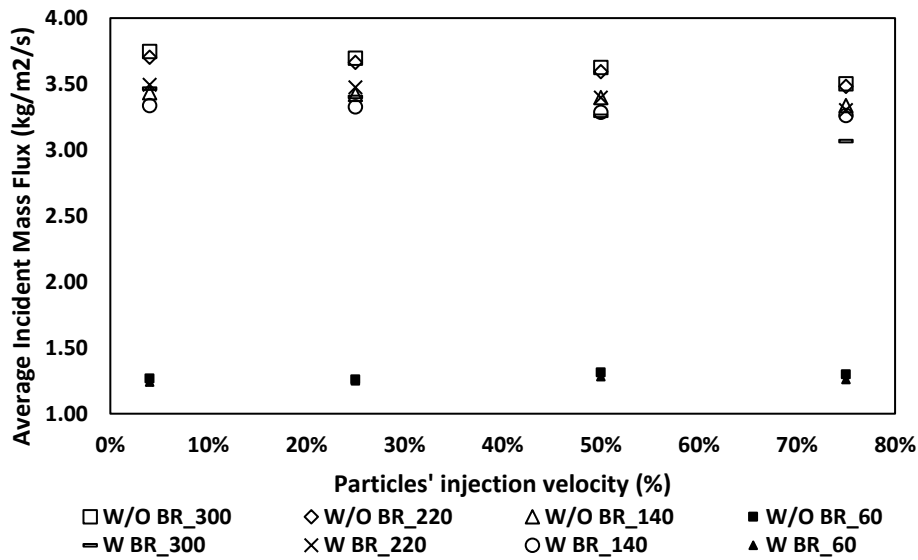
Figure 6-11: Average incident mass flux for variable particles' injection velocity
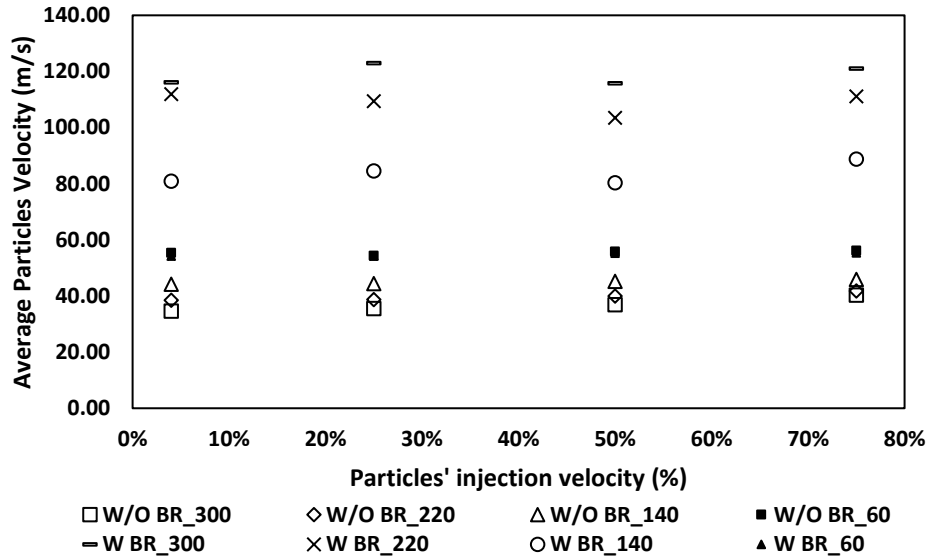
Figure 6-12: Average droplets' relative velocity for variable particles' injection velocity
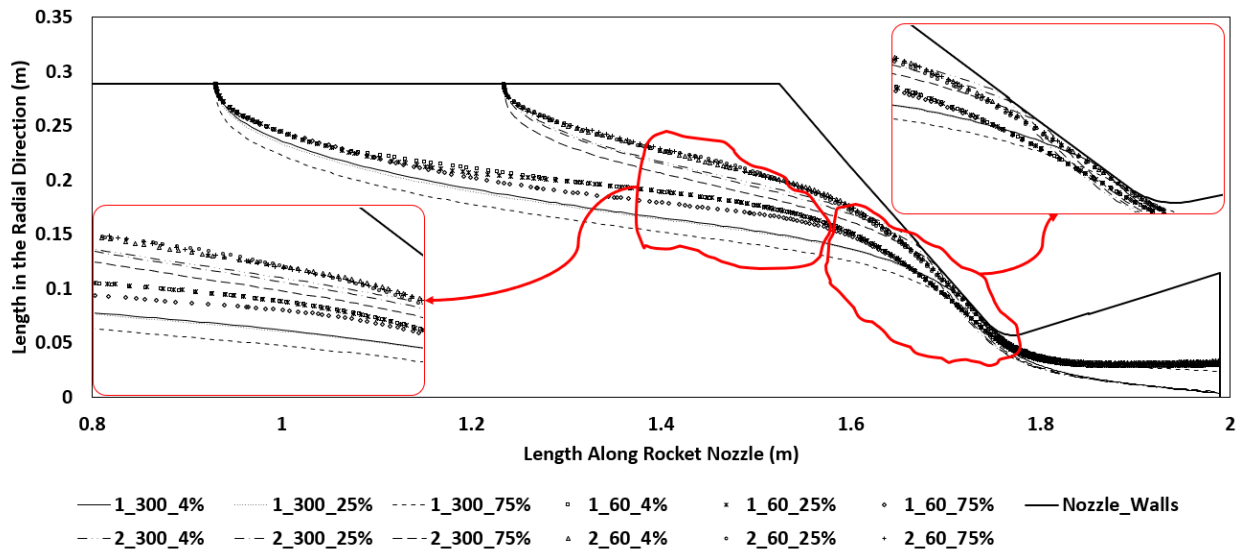
Figure 6-13: Two different parcels trajectories within the chamber for 300 μm, 60 μm droplet sizes and different injection velocities before applying the breakup model.
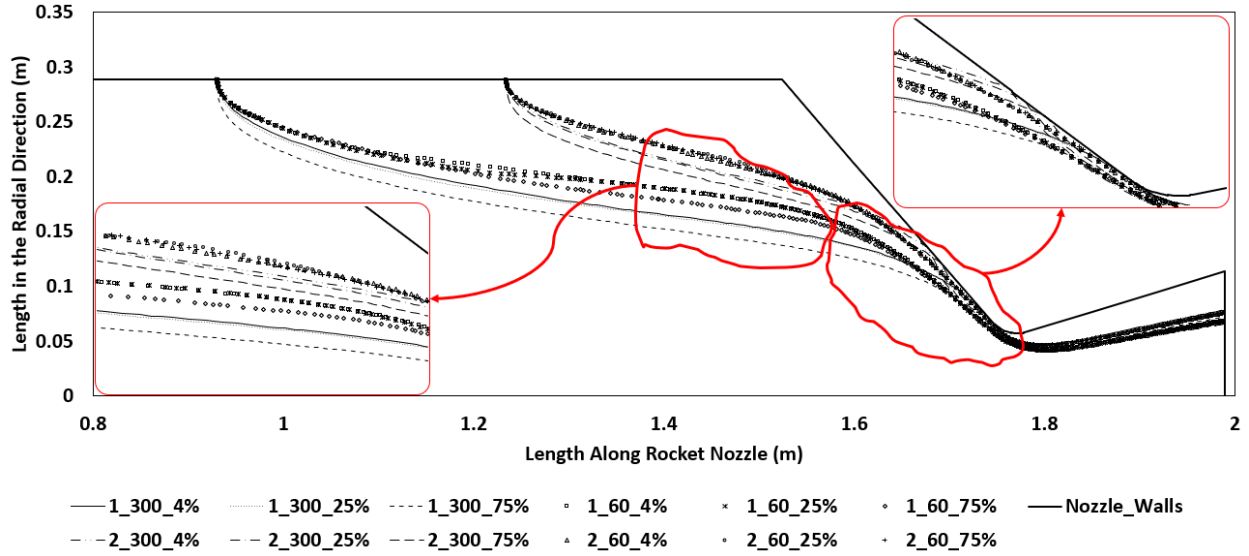
Figure 6-14: Two different parcels trajectories within the chamber for 300 μm, 60 μm droplet sizes and different injection velocities after applying the breakup model.

(a)

(b)

(c)

133
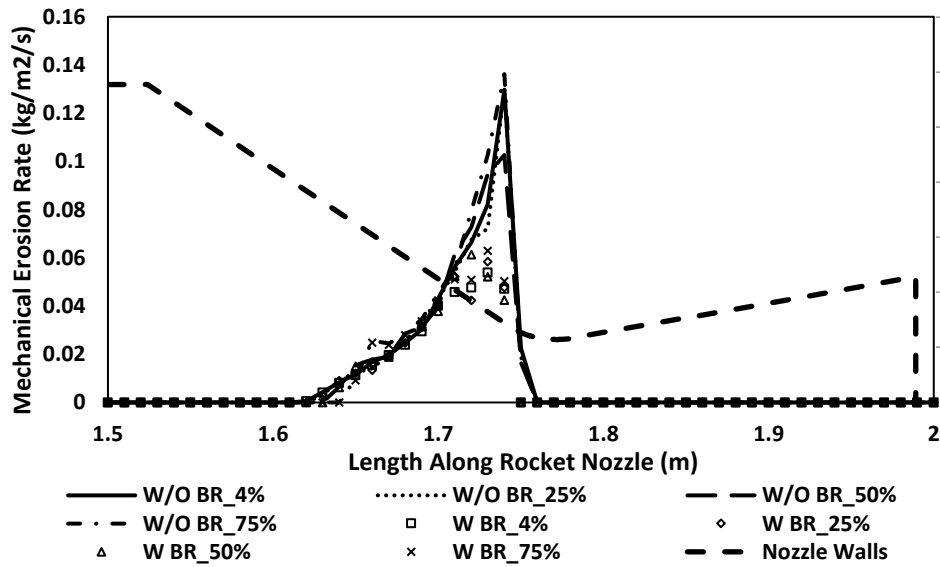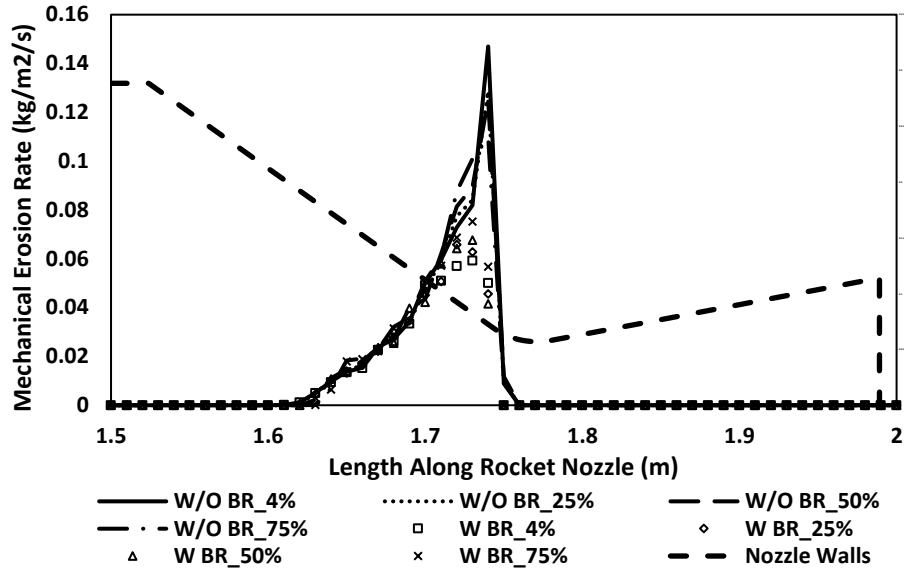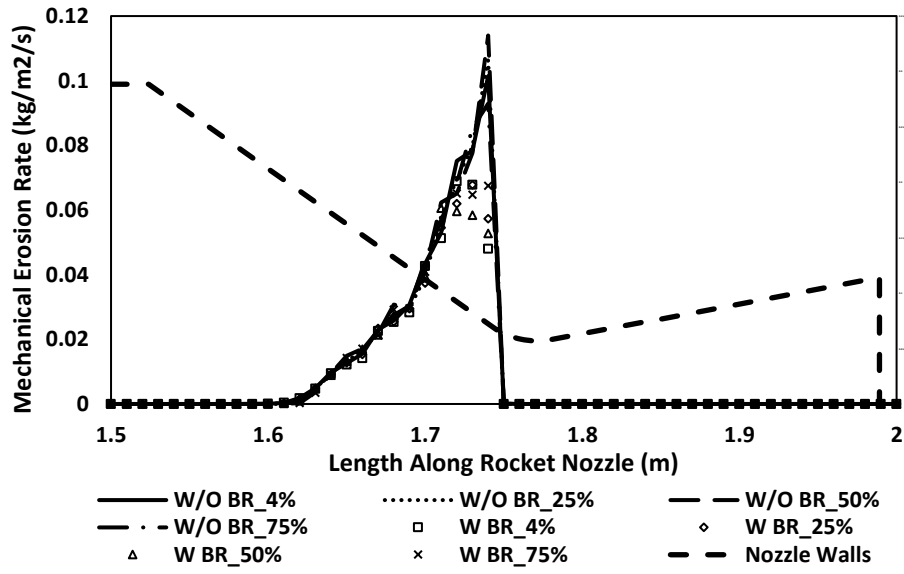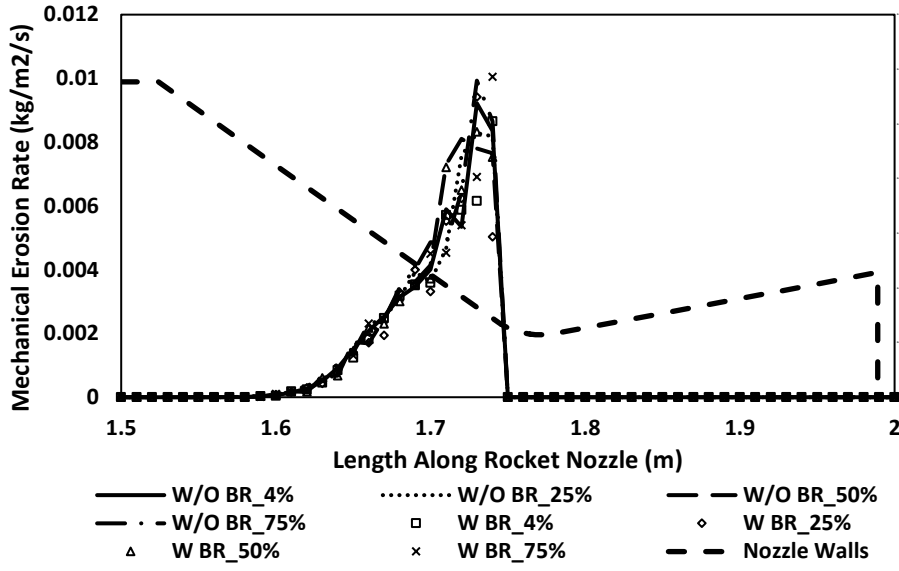
(d)

Figure 6-15: Mechanical erosion rate over the nozzle length with and without applying the breakup model for different particle diameters (a) 300 μm, (b) 220 μm, (c) 140 μm, and (d) 60 μm

(a)

(b)

(c)

135

(d)
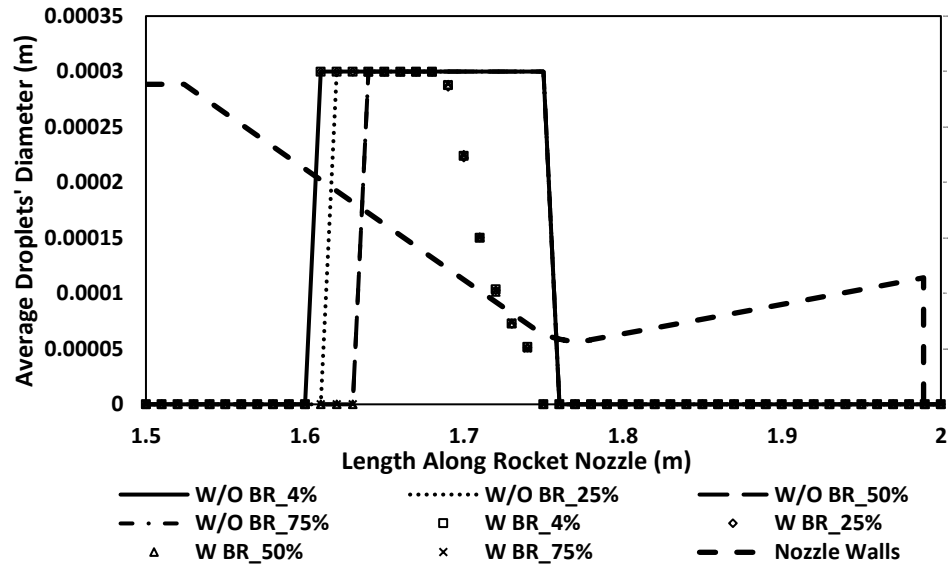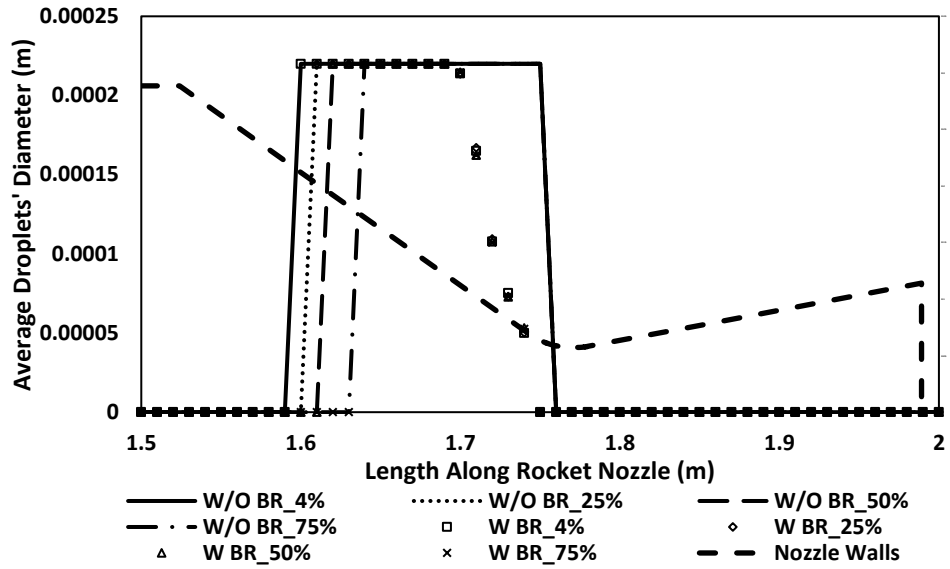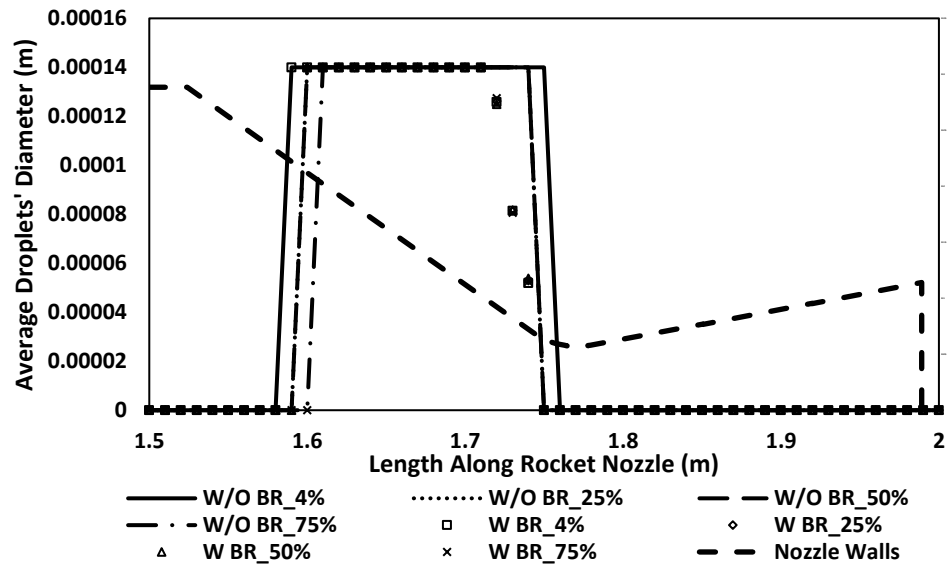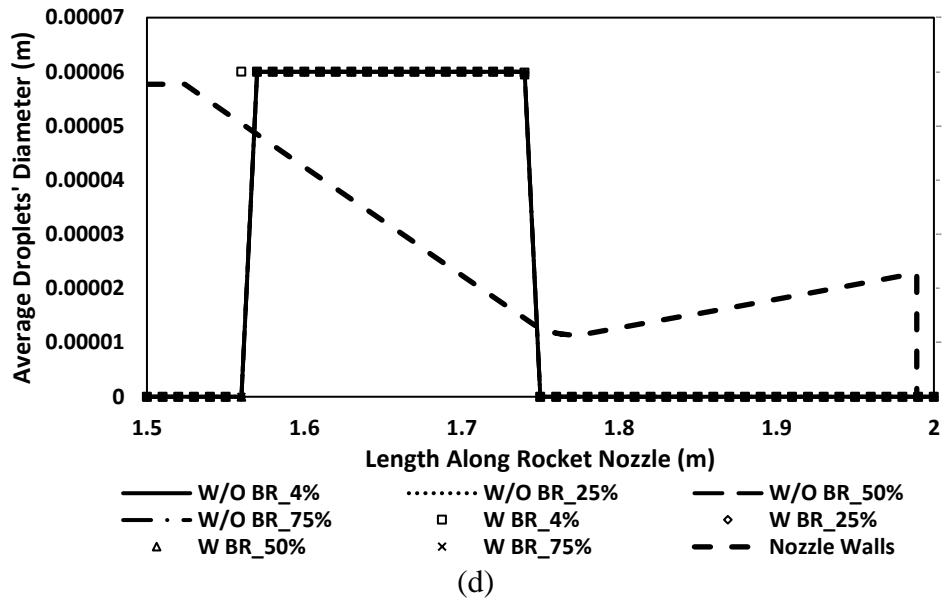
Figure 6-16: Average droplets' diameter over the nozzle length with and without applying the breakup model for different particle diameters (a) 300 μm, (b) 220 μm, (c) 140 μm, and (d) 60 μm

Chapter 7 Numerical Investigation of the Mechanical Erosion Within a Submerged Nozzle Configuration

Another name for the formed aluminum oxide agglomerates is slag and when using a submerged nozzle configuration for its previously mentioned advantages, the slag deposit and accumulate in the pocket zone. Boraas et al. [77] developed analytical procedure to determine certain quantities related to the slag deposition in the submerged nozzle. These quantities are the deposition starting time, the ratio of deposited particles to the total particles, slag pool depth, and slag pooling time. They also found that the flight acceleration does not affect the slag deposition. Madabhushi et al. [78] and Chauvot et al. [79] used the Eulerian-Lagrangian approach to simulate the two-phase flow within the solid rocket motor submerged nozzle. Madabhushi found that with the propellant burning and the grain surface recession, the nozzle cavity flow is affected and starts to recirculate, affecting the particles accumulation and flow. While Chauvot concluded that the particle diameter is a key factor in the slag accumulation weight. Anthoine et al. [80] investigated the nozzle configuration on the SRM aeroacoustics. They conducted numerical simulations using CPS code to study the nozzle pocket region effect on the pressure oscillations and compared the results to Ariane 5 SRM cold flow experimental model. They found that the frequencies are identical, however the pressure levels are overvalued. Bianchi et al. [81] conducted a study to predict the nozzle erosion caused by the heterogenous reactions over a wide range of operating conditions. The numerical model considered the diffusion ablation approach and finite-rate ablation approach for the SRM European Vega launcher submerged nozzle. The model shows close results to the measured data and demonstrates the nozzle shape change importance on the nozzle throat erosion prediction, especially for the long-duration firing.

There is a scarcity in research investigating the mechanical erosion of the SRM submerged nozzle. So, it will be investigated in the current section along with the pocket region and particle size effects on the nozzle mechanical erosion. Also, the predicted mechanical erosion values for the submerged nozzle configuration will be compared with the external nozzle results mentioned in the previous sections.

7.1 Theoretical Concept and Governing Equations

The same metalized propellant (Ammonium perchlorate (AP) / Hydroxyl-terminated polybutadiene (HTPB) / Aluminum (AL) is burned producing high temperature gas mixture of different six species [H2O, CO2, CO, H2, HCL, and N2], and the burning products of the aluminum combustion process. The Eulerian / Lagrangian approach is used to simulate the continuous phase (product gas) and discrete phases in the computational domain. All the equations describing the continuous phase, discrete phase, aluminum combustion process and mechanical erosion estimation were introduced and discussed before in section 5.1.

7.2 Model Description and Input Data

Considering the same earlier mentioned propellant combustion process properties (Section 6.2), the propellant burning rate is 16.273 kg/m2/s, while the motor chamber pressure and temperature are 68 bar and 3327 K, respectively [41]. The nozzle walls' temperature is assumed isothermal (2500 K), while the motor chamber head wall is considered adiabatic [41]. The model used in this section is the same as the previous chapter, so it is already validated against Thakre et al. and Li et al. results. The geometry is modified to consider a reproduction of the cavity of P230 SRM of Ariane V as reported by Stella et al [76] as shown in Figure 7-1. The mesh is created using the directed mesh where is clustered in the nozzle section as shown in Figure 7-2.

Figure 7-1: SRM with submerged nozzle configuration 3-D CAD model.
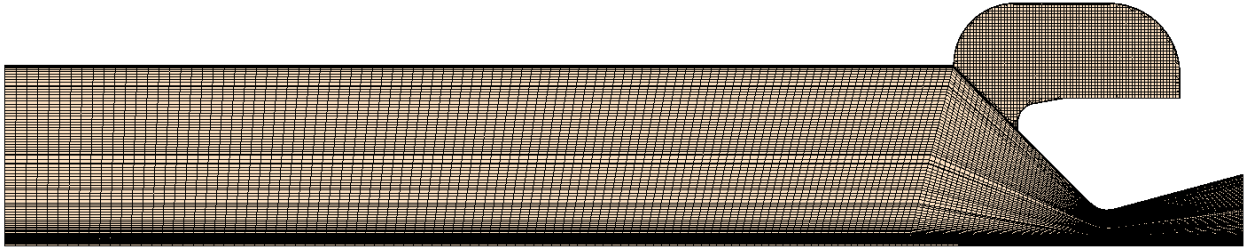
Figure 7-2: Computational domain mesh distribution

As proven by the current study validation, the aluminum particles completely evaporate after a short distance from the burning surface, convert to aluminum oxide and other products species. As a result, they do not impact the nozzle walls. Accordingly, the current numerical model is neglecting the aluminum particles' combustion process, the new modified product's species mass fractions are shown in Table 7-1, and the continuous phase mass flux is modified to be 15.321 kg/m2/s. The Lagrangian phase inlet conditions are as shown in Table 7-2.

Table 7-1: Combustion products inlet mass fractions [42]. (Continuous phase)

Gas Species	Mass Fraction
H2O	0.109111
CO	0.284957
CO2	0.022013
H2	0.022267
AL2O3	0.232293
HCL	0.230154
N2	0.099204

Table 7-2: Alumina particles inlet conditions. (Discrete phase)

Liquid Phase	Mass Flux (kg/m^2/s)	Injection Temperature (K)	Droplets' diameter (µm)	Radial Velocity (m/s)
Multi-component droplet (AL/AL$_2$O$_3$)	0.122/0.83	2350	60, 100, 140, 180, 220, 260, 300	0.1

Having the submerged nozzle cavity will affect the internal flow field within the combustion chamber, hence the alumina particles trajectories and velocities. Thus, the objective of the current section is investigating mechanical erosion change due to the cavity existence. So, seven different particle sizes (60, 100, 140, 180, 220, 260, 300 µm) will be used to investigate the mechanical erosion and compare it with the external nozzle results (Section 5.3).

7.3 Results and Discussion

Reviewing the combustion chamber internal flow field characteristics Figure 7-3 & 7-4 & 7-5, it can be inferred that the supersonic flow within the nozzle reaches maximum Mach number of 2.67, while the pressure decreases gradually from 68 bar to reach its minimum at the nozzle outlet as shown in Figure 7-4. A complex flow structure is generated due to the existence of the pocket region, where it causes vortices within the flow. First a main vortex appears just before the nozzle convergent part tip, then the nozzle tip wall divides the flow with the main vortex to two smaller vortices: the first upper one causes the recirculation zone within the pocket region as shown in Figure 7-6 & 7-7, while the other rotates the flow against the convergent section wall (shown in Figure 7-6). As mentioned before only one discrete phase (Aluminum / Aluminum Oxide particles) is injected from the combustion chamber circumferential wall. The multi-component agglomerates' velocity increases gradually as they travel in the combustion chamber. Figure 7-8 shows the agglomerates trajectories within the combustion chamber, where the slip velocity is increasing while flowing in the nozzle. The slip velocity increases as a result for the increase in

the continuous phase velocity since the slip velocity definition is the difference between the continuous phase and discrete phase velocities. However, the increase in the exhaust gases flow applies more drag forces on the particles causing a rise in their velocities as shown in Figure 7-9 to reach a maximum velocity of 648 m/s at the exit. It is worth mentioned that all the previous flow field characteristics are for particle size of 300 μm. The nozzle walls are divided into four sections: Nozzle tip (1.64 to 1.7 m along axial direction on the pocket region walls, upper side) Convergent section (1.64 to 1.744 m along axial direction on the nozzle walls, lower side), Throat section (1.744 to 1.781 m along axial direction), and Divergent section (1.781to 1.989 m along axial direction).
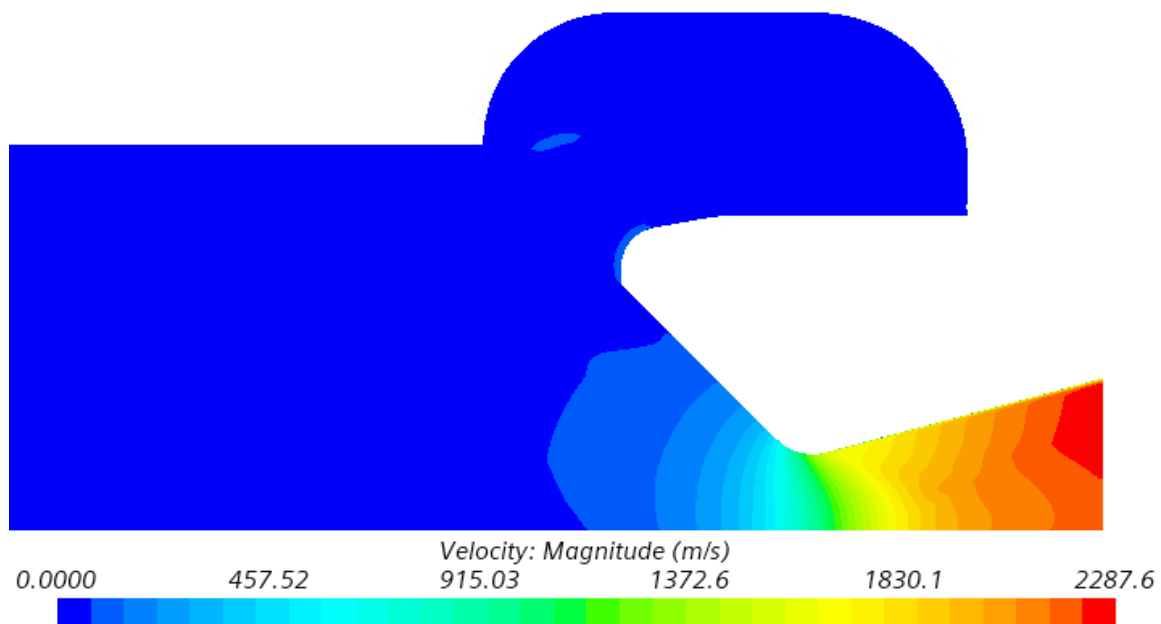
Figure 7-3: Combustion chamber internal velocity flow field contours
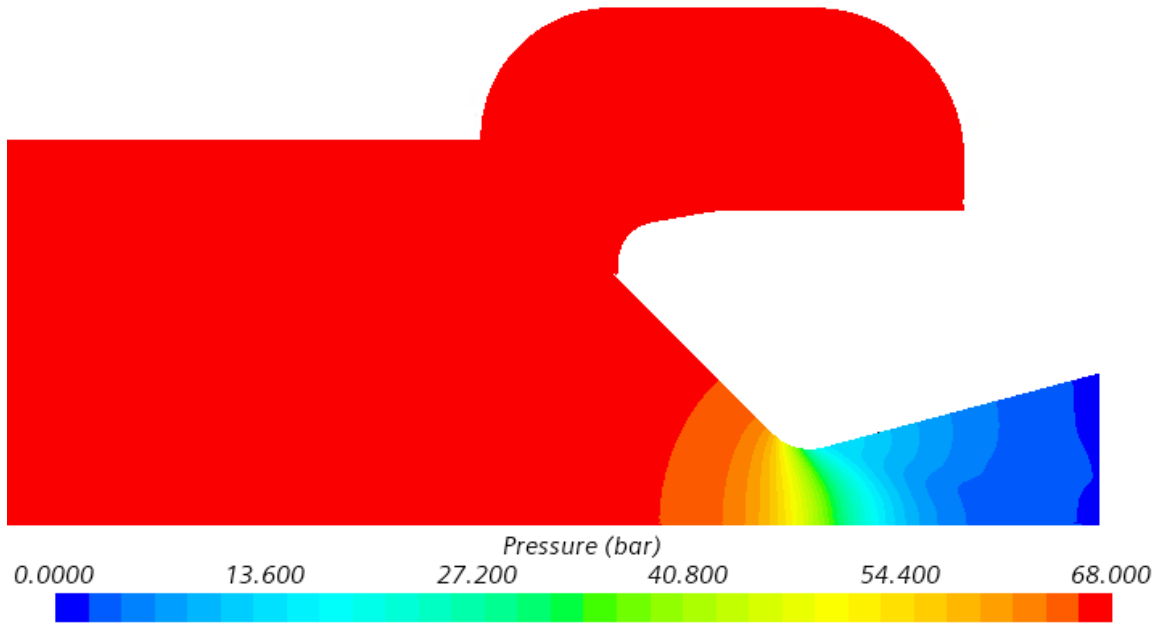
Figure 7-4: Combustion chamber pressure contours
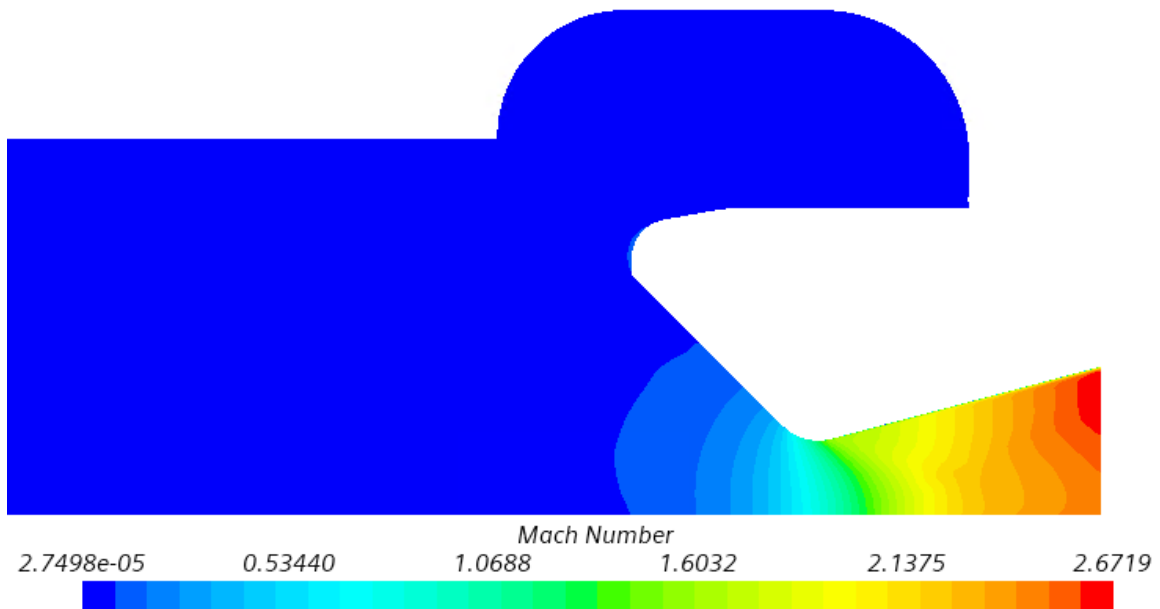
Figure 7-5: Combustion chamber Mach number contours
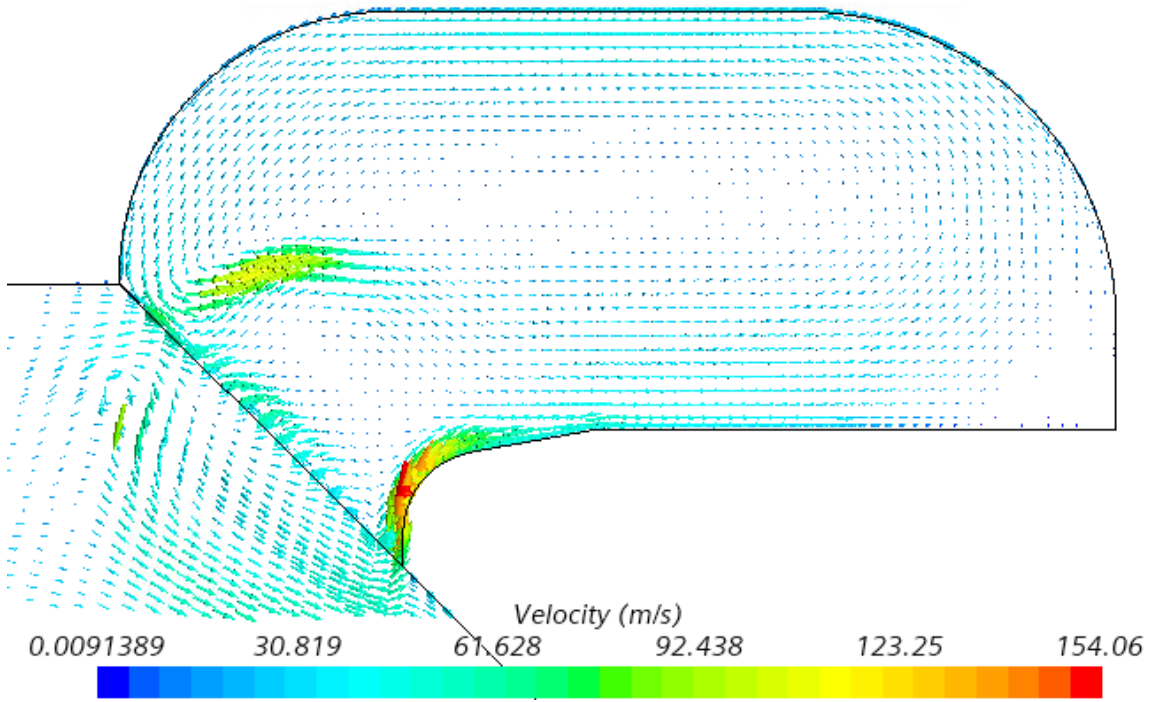
Figure 7-6: Combustion chamber pocket region velocity vectors
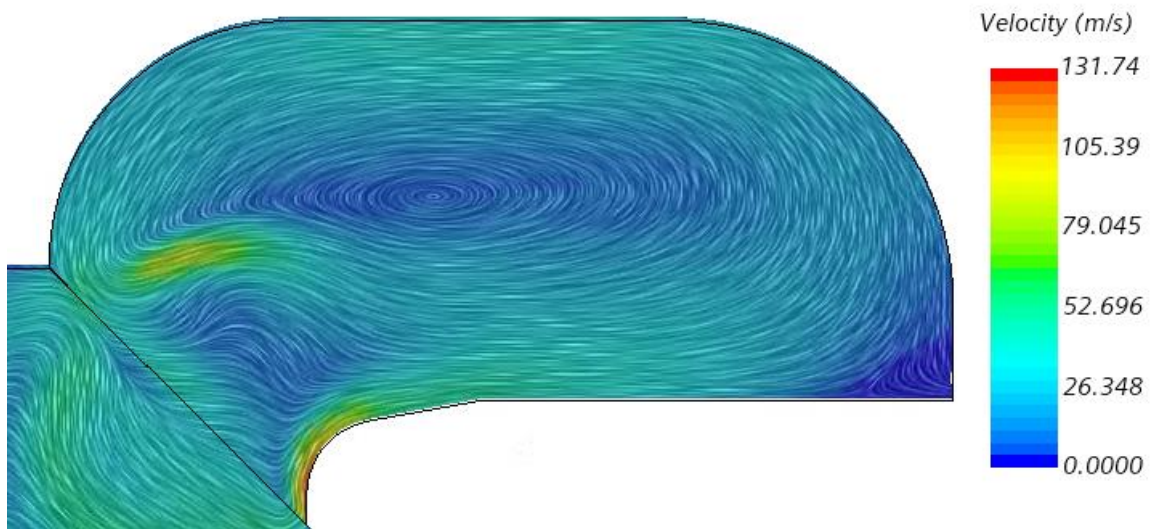
Figure 7-7: Combustion chamber recirculation zone visualization
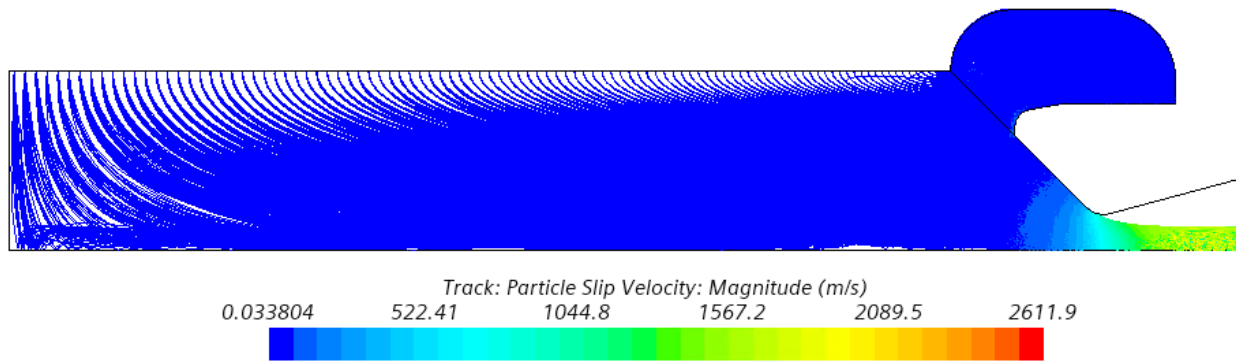
Figure 7-8: Aluminum oxide agglomerates trajectories colored by slip velocity values
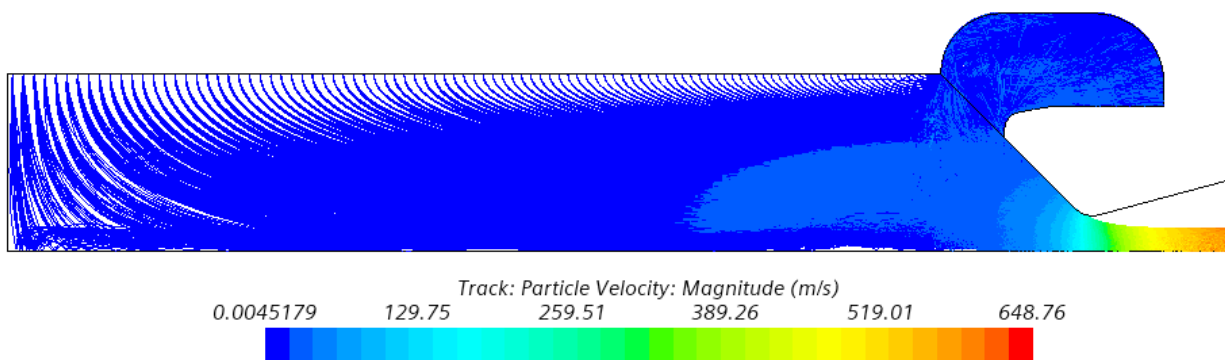
Figure 7-9: Aluminum oxide agglomerates trajectories colored by velocity values

Mechanical erosion and droplets' size effect: As indicated before, the same seven different droplets' diameters (60, 100, 140, 180, 220, 260, 300 μm) used in studying the external nozzle, were utilized for the upcoming analysis. The droplet's size effect is better be studied on cases where no size change occurs, so the simplified model is used without incorporating the droplets' breakup model. As proven before, the mechanical erosion does not affect the nozzle section because of the breakup of the agglomerates to a very small droplets traveling away from the nozzle walls. So, the erosion rate is averaged over the nozzle's convergent and tip sections as shown in Figure 7-10 & 7-11 & 7-12. The erosion in the submerged nozzle convergent and tip sections is presented in Figure 7-10. Reviewing the submerged nozzle convergent section results, the erosion first increases by decreasing the droplet's diameter to 220 μm, (the maximum average erosion rate of 0.035 kg/m^2/s) then it starts to decrease again. As per its definition, the erosion rate

is not only a function of the incident mass flux of droplets, but also the droplet's relative velocity and incidence angle. The average incident mass flux decreases with decreasing the droplet's diameter as shown in Figure 7-11, while the erosion rate increases. This can be explained by the rise in the average relative velocity (shown in Figure 7-12) and the decrease in the incident angle. Smaller droplets are easier to be entrained by the exhaust gases, hence higher relative velocity'. This increase compensates for the droplets' incident mass flux and increases the erosion rate, until the decrease in incident mass flux prevails and the erosion rate starts to decrease. The minimum erosion rate value occurs at particle size of 60 μm with 0.02 kg/m2/s. Moving to the submerged nozzle tip results, the erosion rises as the particle diameter declines, as smaller particles have less radial momentum and will follow the continuous gases streamlines and hit the nozzle walls tip causing more erosion. A better understanding for the erosion increase can be obtained by revisiting the incident mass flux and the particles relative velocity figures, where the incident mass flux slowly decreases. On the other hand, the particles' relative velocity increases rapidly with smaller particles diameter. The rise in the relative velocity dominates the erosion rate trend causing its continuous increase.
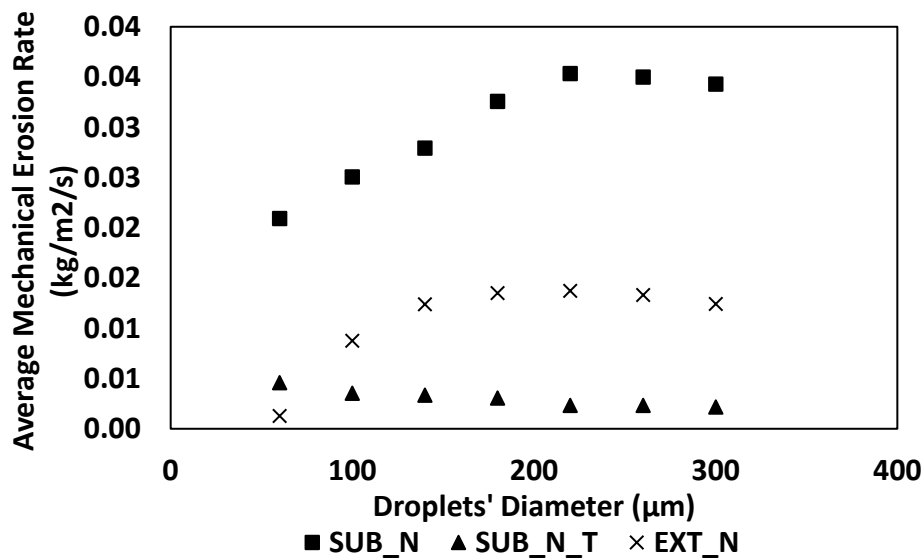
Figure 7-10: Average erosion rate at different droplet's sizes

145
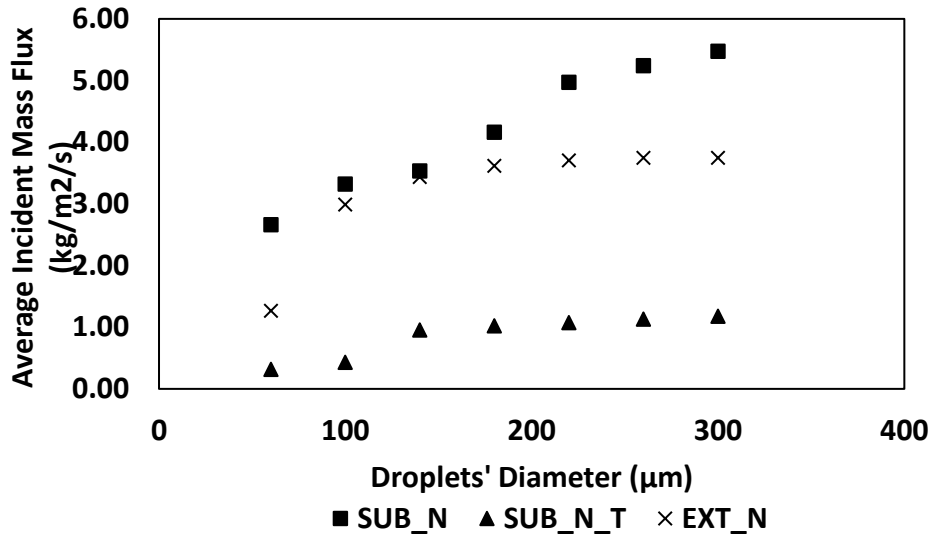
Figure 7-11: Average incident mass flux at different droplet's sizes
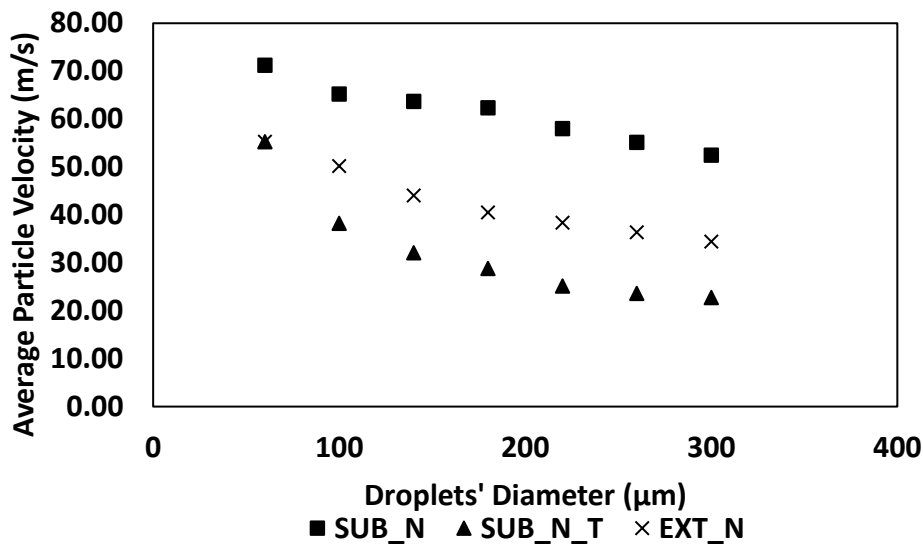
Figure 7-12: Average droplets' relative velocity at different droplet's sizes

Figure 7-13 presents a detailed map of the nozzle erosion rate at different droplets' diameter. As explained before, the erosion is prevalent in the convergent section and the beginning of the throat section (just before the throat). It starts to increase with a spike due to the severe erosion on the nozzle tip, decreases and then gradually increases until it reaches its maximum just before the throat, followed by a severe decrease to zero. It is also shown that the erosion increases as the droplets' diameter decreases from 300 μm to 220 μm, then it decreases with the diameter

146

decrease. And the reason for that (as explained before), Smaller droplets' diameter leads to less incident mass flux, but higher relative velocity, and smaller incidence angle. Over a certain droplet diameter (220 μm), the relative velocity increase dominates, hence the erosion rate increases, however under that limit, the decrease in the incident mass flux and incidence angle dominates, hence the erosion rate decreases. The maximum erosion at the nozzle tip happens at the smallest particle diameter as per earlier discussion. Figure 7-14 provides the average incident droplets' diameter on the nozzle walls, but since the breakup model is not included, the average diameter is the same injected diameter and constant. This figure also shows that as the droplets' diameter decreases, the erosion starts and ends earlier on the nozzle walls, which can be beneficial by moving the erosion far from the nozzle throat. Additionally, Figure 7-15 proves that as the droplets' diameter decreases, the incident parcels on the nozzle walls decrease, hence lower incident mass flux. Also, it shows an opposite distribution for the erosion rate as the incident parcels (incident mass flux) is high at the middle of the nozzle convergent part. It starts to decrease moving downward in the nozzle, which can be clarified by the definition of the erosion rate and the droplets' relative velocity increase domination.

Finally, the trajectories of 5 different parcels are presented in the following figures to show how each particle size is affected by the continuous phase flow dynamics. The five different parcels injection locations are different, they are injected at approximately 1.5, 1.4, 1.3, 1.2, and 0.8 m from the rocket head and Figure 7-16 & 7-17 & 7-18 & 7-19 & 7-20 are representing them, respectively. The droplet trajectory within the chamber is governed by the momentum conservation equation and when the particle diameter decreases, the momentum decreases compared to the external forced, makes it easy for the continuous phase leading the particle path. Figure 7-16 shows the closest injection location to the nozzle where the trajectories of four

droplets' diameters are shown. As just explained, the droplet's diameter decreases, it follows the gas flow streamlines. All droplets enter the flow field with the same velocity (0.1 m/s). However, smaller droplets are more influenced by the flow field and recirculation zones where they gain axial velocity compared to the larger droplets. On the other hand, usually larger droplets are heavy, have more momentum, and travel more in the radial direction before moving in the axial direction as shown in the figures, but once they (the larger droplets) start traveling in the axial direction, they will have higher momentum than smaller droplets and will slowly adjust their trajectories following the continuous phase. Figure 7-16 & 7-17 show the gas flow influence on the 60 μm and how the recirculation zone (shown in Figure 7-7) at the pocket region inlet guided the particles out. Also, the figures show that the injection location greatly affects the particle trajectory and shows that smaller droplets hit the nozzle walls in a location further than the larger ones.
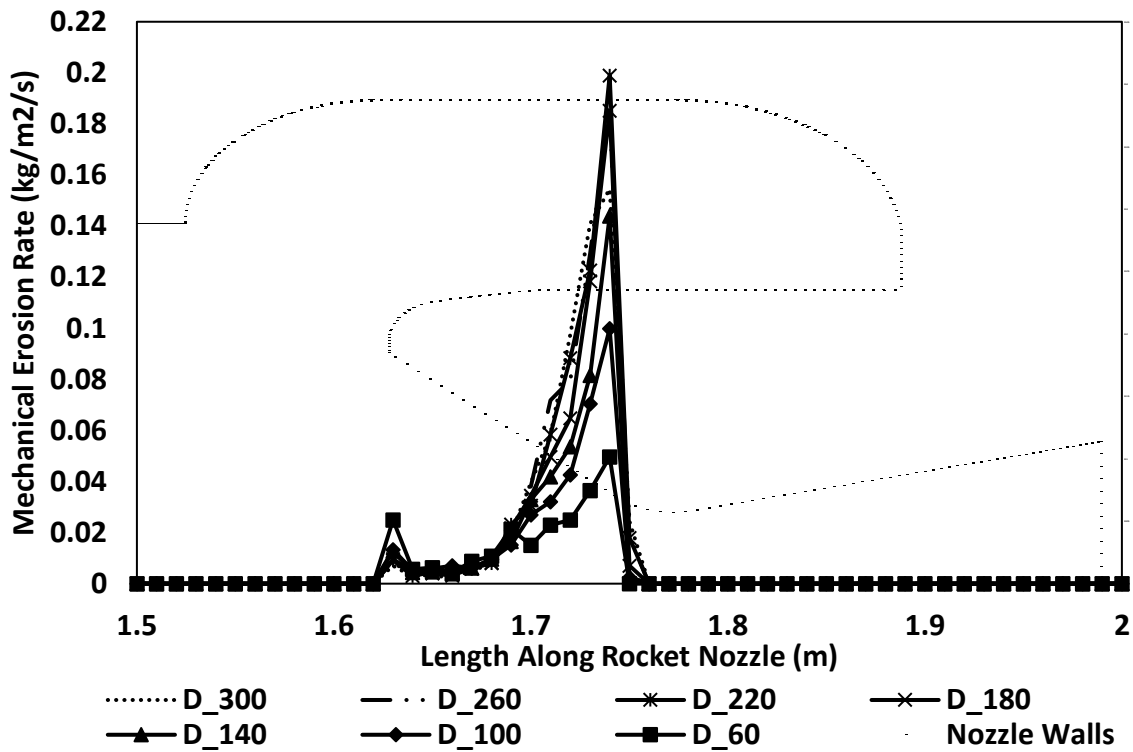
Figure 7-13: Local mechanical erosion rate at different droplet's sizes

148
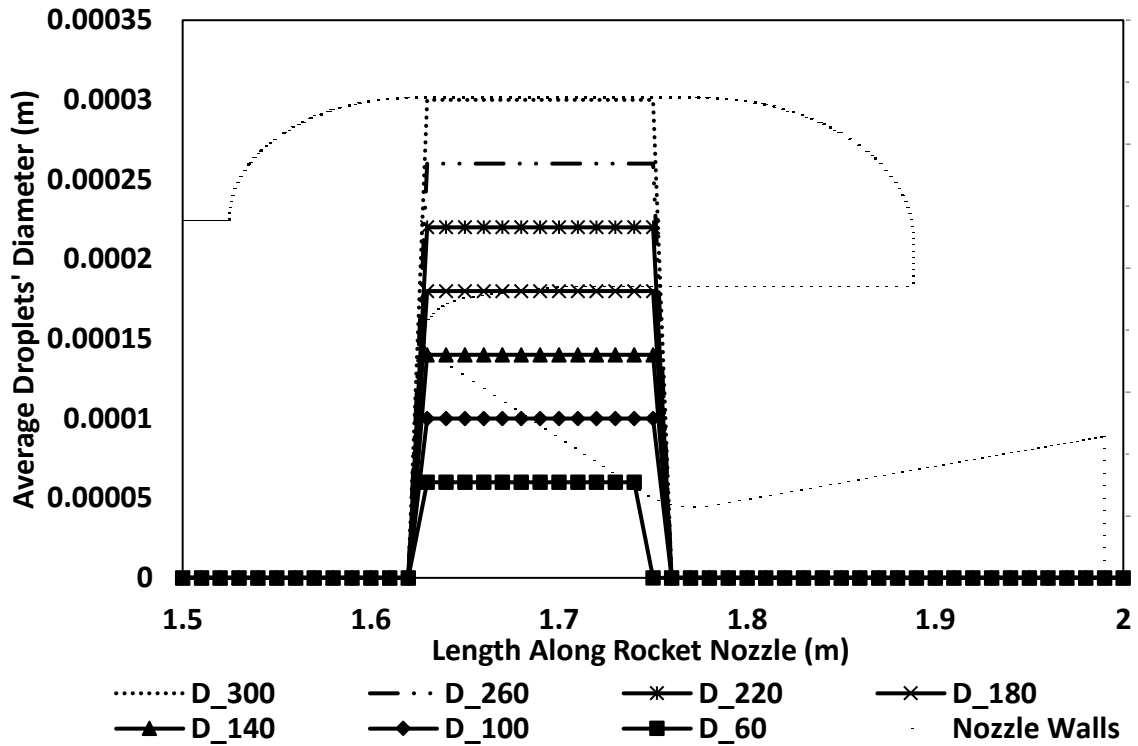
Figure 7-14: Average droplets' diameter at different droplet's sizes
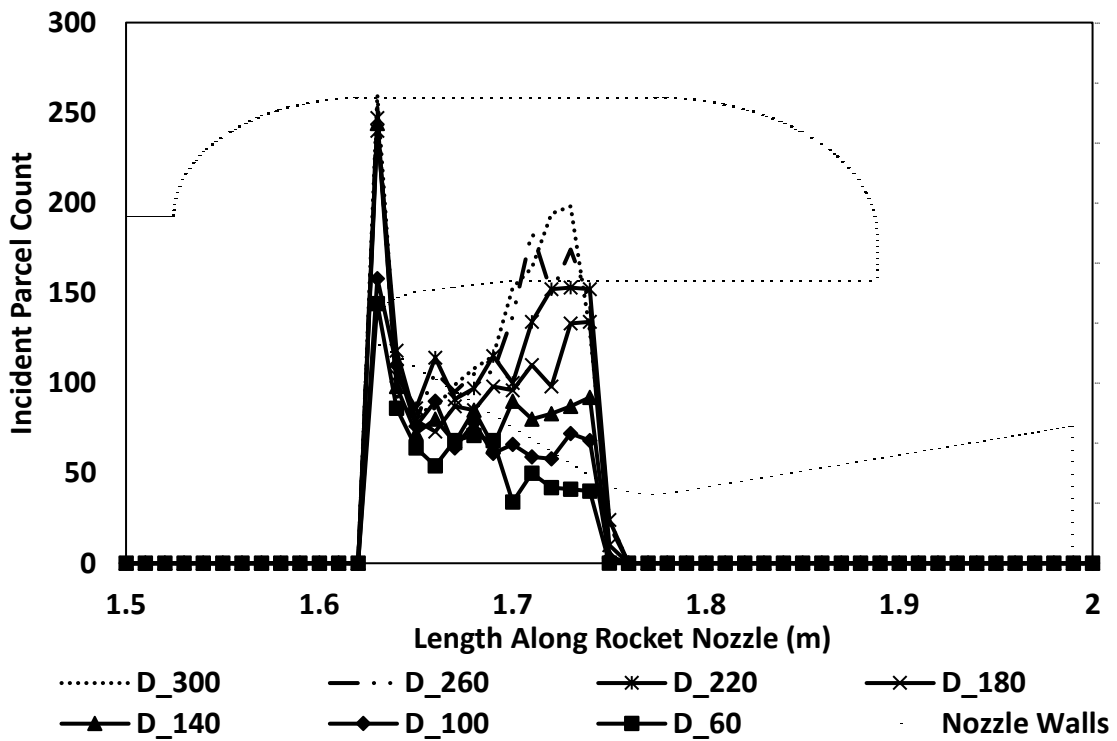
Figure 7-15: Incident parcels count at different droplet's sizes

149
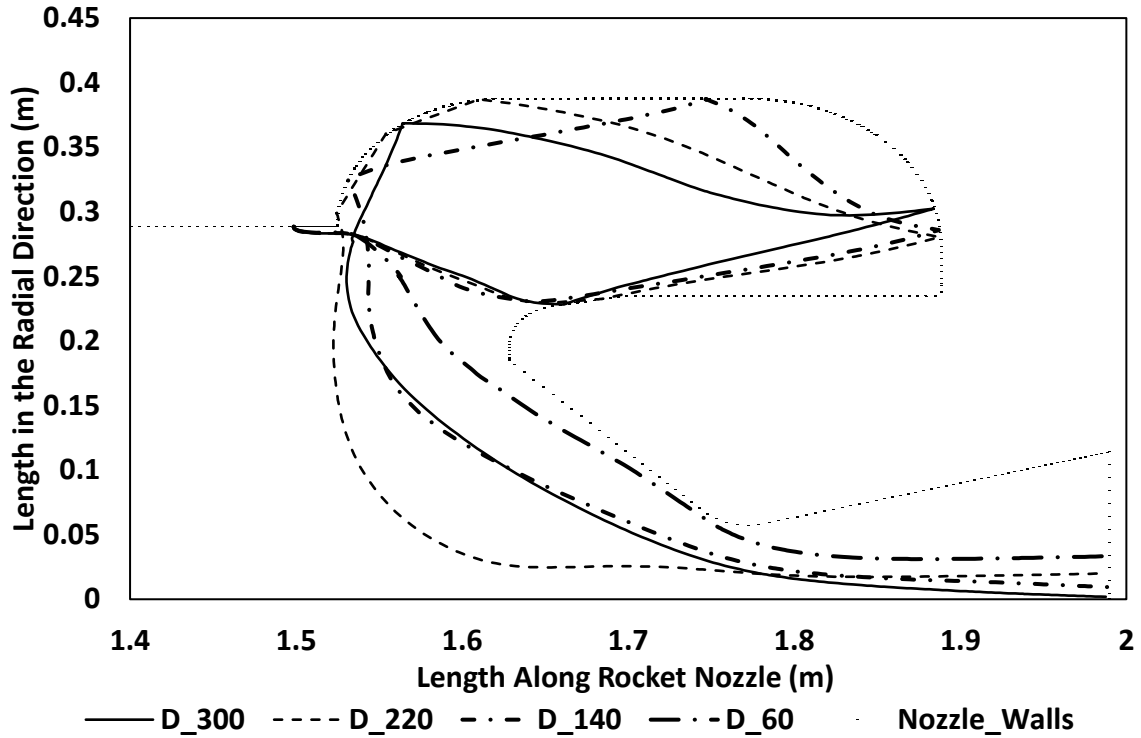
Figure 7-16: Parcel No. 200 trajectories within the chamber at different droplet's sizes.
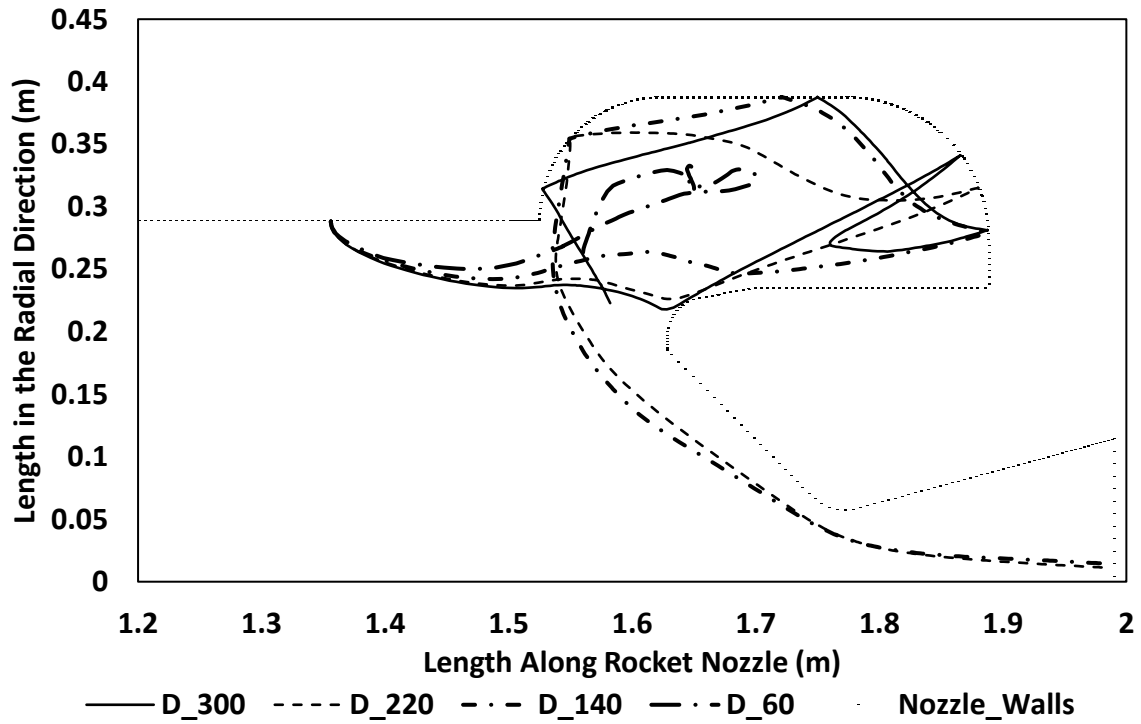
Figure 7-17: Parcel No. 700 trajectories within the chamber at different droplet's sizes.
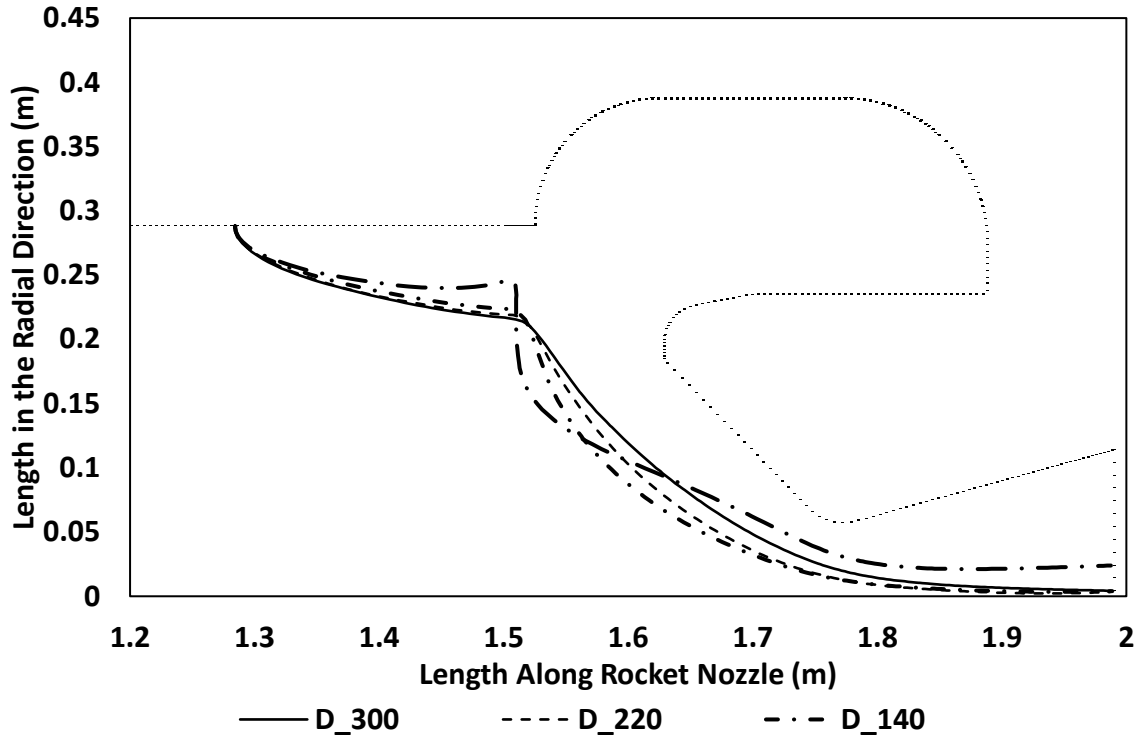
Figure 7-18: Parcel No. 1200 trajectories within the chamber at different droplet's sizes.
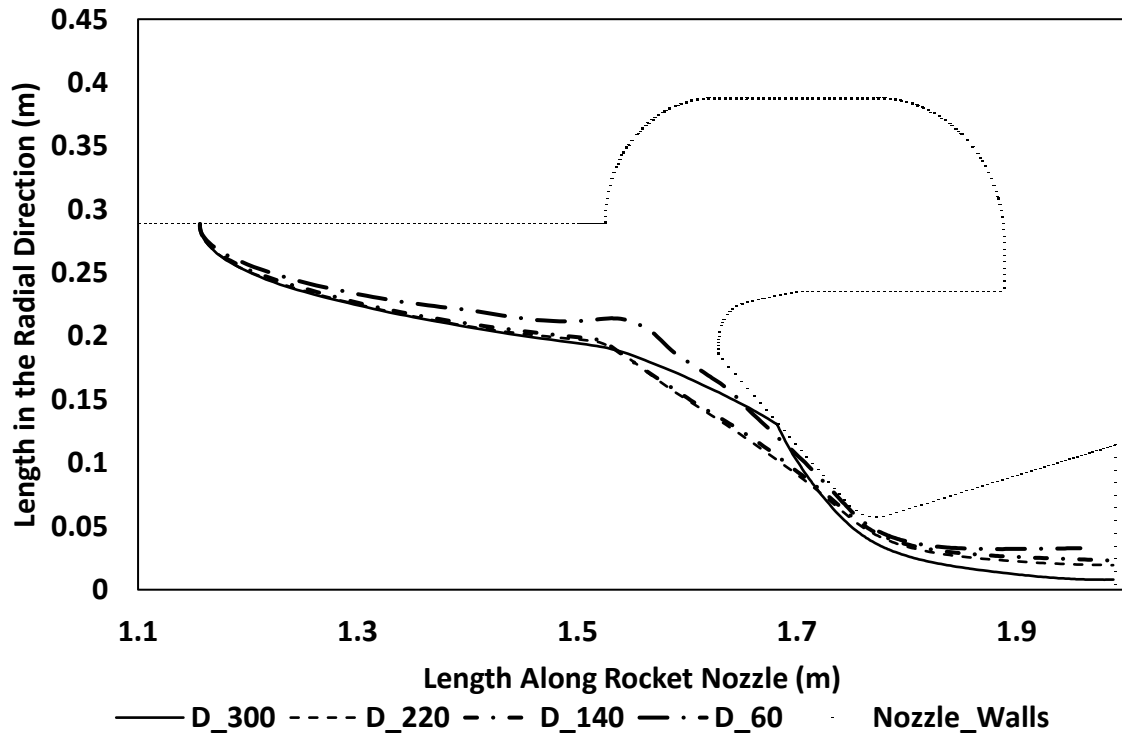
Figure 7-19: Parcel No. 1500 trajectories within the chamber at different droplet's sizes.
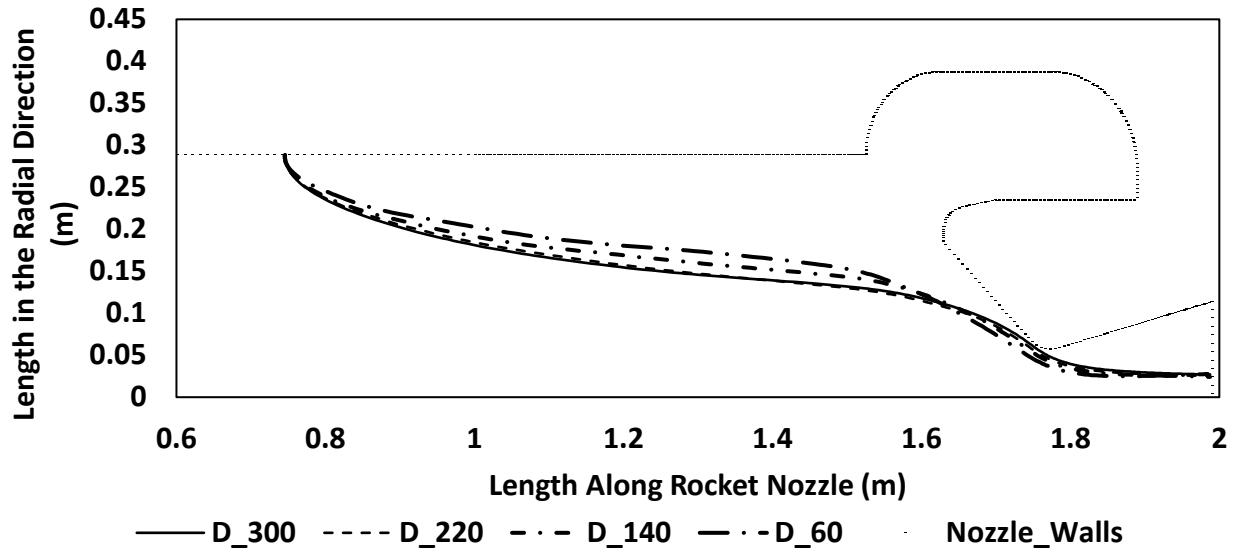
Figure 7-20: Parcel No. 3000 trajectories within the chamber at different droplet's sizes.

External Nozzle VS Submerged Nozzle: The submerged nozzle mechanical erosion results are compared with the external nozzle ones discussed in Chapter 5. Figure 7-10 discusses this comparison, where it can be noticed that the erosion rates in the submerged nozzle case are following the same trend as the external nozzle, but they are way higher than them with percentages range from 126 % (140 μm) to 1550% (60 μm). This increase can be attributed to the rise in the incident mass flux (11-47%) and the particles relative velocity (28-54%). The high particles relative velocity is due to the gained momentum from the recirculation zones. Figure **7-21** & 7-17 & 7-18 represents the local mechanical erosion over the nozzle length for the submerged and external nozzle configurations at three droplet's diameters 300, 140, 60 μm, respectively. The erosion is increasing gradually over the external nozzle surface compared to the submerged nozzle sharp increases and decreases. Also, it can be noticed that huge differences in the erosion rate exist at small droplet diameters as shown in Figure **7-23**. Finally, it is worth mentioning that the current predicted erosion rates for the submerged nozzle is the worst-case scenario where the grain is close to the flight start and the slag pool did not accumulate yet. However, when slag pool forms, some of the droplets will be entrapped in the pocket region, causes a decrease in the mechanical erosion.

152
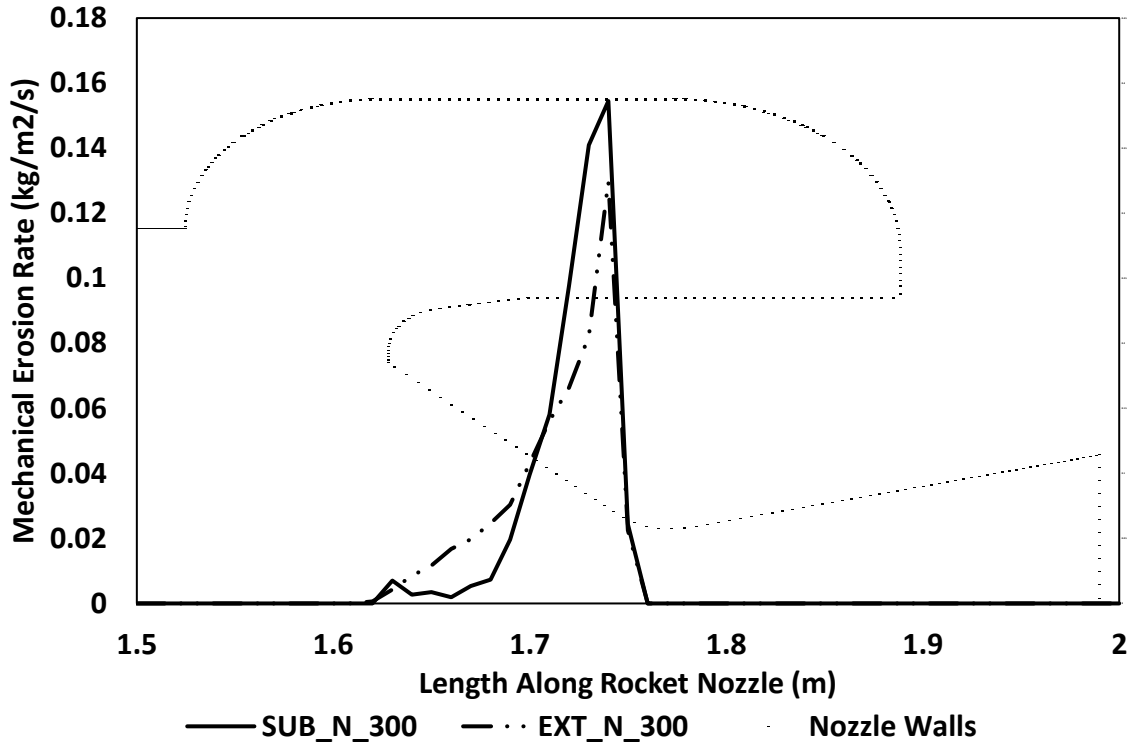
Figure 7-21: Erosion rate at different conditions for 300 μm droplet size
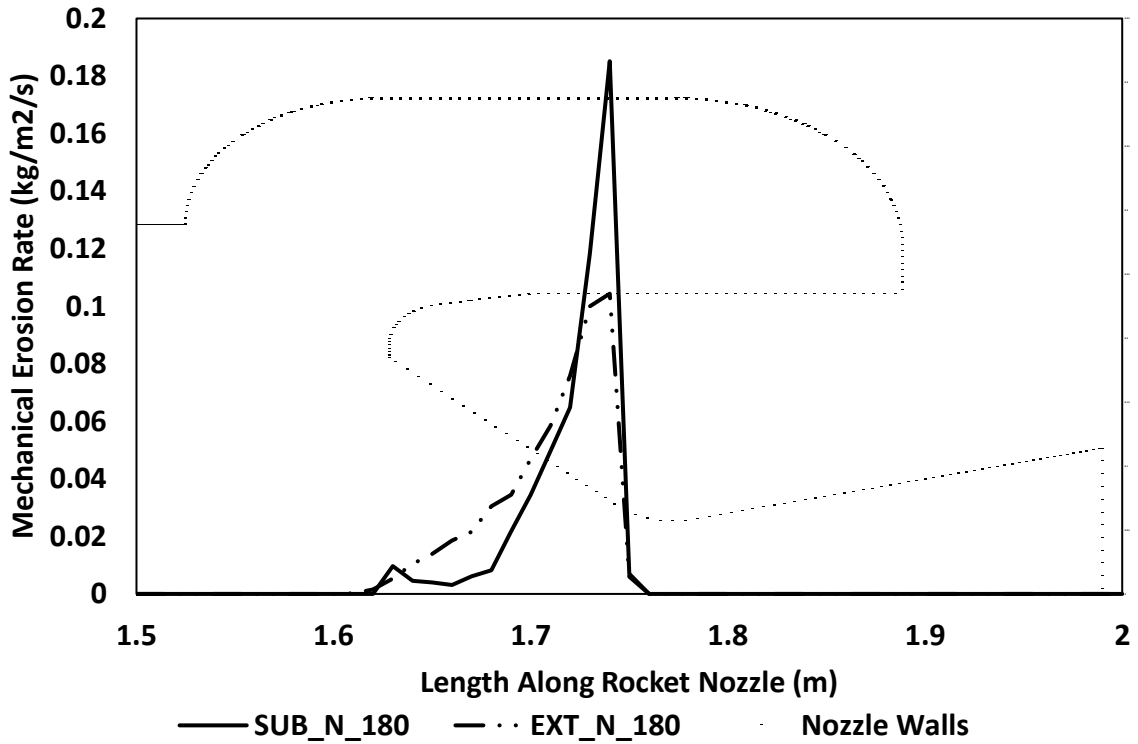
Figure 7-22: Erosion rate at different conditions for 180 μm droplet size

153
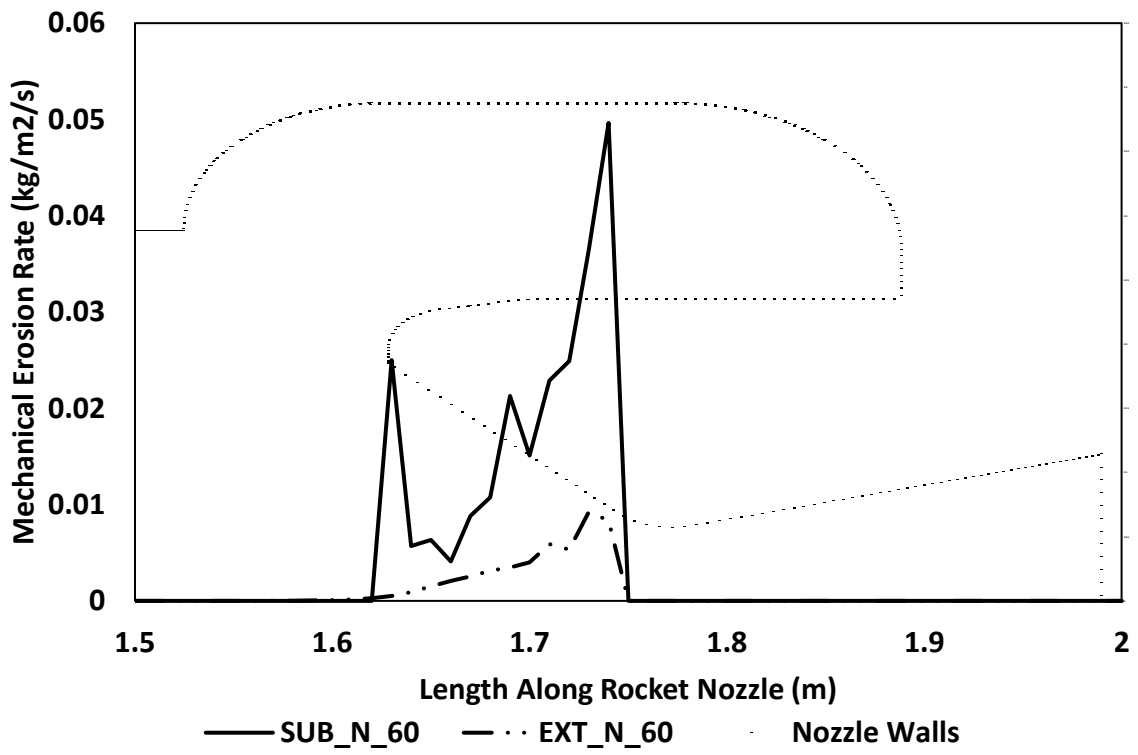
Figure 7-23: Erosion rate at different conditions for 60 μm droplet size

Chapter 8 Conclusions and Future Work

Nozzle erosion problem in the solid rocket motors introduces itself as a pressing matter because of the rocket's ballistic performance reduction, in addition reusable equipment is very vital for space exploration commercialization. Solving the erosion problem will enable us to reuse rockets' nozzle for several trips and resolve the poor performance issue caused by the nozzle erosion. Mechanical erosion is one of two erosion types affecting the nozzle surface and is occurring as a result for the impingement of alumina particles with high velocity on the nozzle surface. Smaller agglomerates are easier to be entrained by the exhaust gases momentum far from the nozzle walls and hence lower erosion rate. So, in the current work (Chapter 4 & 5), the breakup process and the factors affecting it were investigated experimentally and numerically in external and submerged nozzle configurations considering a sub-sonic condition due to the harsh conditions associated with the real rocket conditions and safety purposes which are barriers for lab-scale experiments. However, the computational fluid dynamics software and high-performance computing technology empower the ability of modeling the nozzle erosion considering the severe conditions existing inside the rocket's combustion chamber, and nozzle (supersonic flow). So, Chapters 5, 6, and 7 introduce a numerical model predicting the nozzle erosion for the rocket's real environment while considering the agglomerates' breakup.

8.1 Investigation of Liquid Droplet Flow Behavior in a Vertical Nozzle Chamber Conclusions

8.1.1 Liquid Surface Tension Reduction Effect on Water Droplet Flow Behavior

Experimental and numerical investigation for the break-up mechanism of two-phase flow (water-air) was conducted to study the effect of varying air velocity and liquid surface tension on

155

the break-up process in terms of the droplets' average diameter and number. Through this section, the following conclusions emerged,

- The numerical model results showed an acceptable agreement with available experimental data (6-18% difference in results) to be reliable in predicting the break-up phenomena.

- Increasing the inlet air velocity reduces the average droplet diameter over the entire C-D nozzle volume by breaking up the big water bodies into smaller ones (higher droplets number), enhancing the break-up process.

- With increasing the inlet air velocity, the break-up process evolution moves up toward the liquid inlet section. As a result, droplet travel length will increase, leading to a higher chance of subsequent break-up into smaller droplets.

- At constant inlet air velocity, the droplets' average diameter and number increase while moving through the test channel. However, this is not the same for the exit section's number of droplets in the 40 m/s air velocity case because of the droplets merging and the higher drag driving force even though the break-up process intensity is better in this case, in terms of smaller average droplet size and a higher number of droplets over the entire C-D nozzle volume, as the break-up process starts earlier and is more significant in the previous sections.

- Decreasing the water surface tension does not affect the general behavior (trend) of the break-up process through the nozzle's different sections. However, it weakens the cohesive forces between water surface molecules, which facilitates the separation of voluminous water bodies from the interface surface. So larger droplets' average diameter (0.5% to 17% increase) and higher droplets' number (4 to 100% increase) occurs in the RWST case.

In conclusion, it can be deduced from this study that increasing the exhaust gas velocity and reducing aluminum alloy surface tension by adding strontium and magnesium (aluminum

156

alloys), is very beneficial in lowering mechanical erosion. These two parameters reduce the droplets' average diameter, which will increase the droplets' chance to be entrained by the momentum of the exhaust gases and not hit the nozzle walls.

8.1.2 Air Flow Acceleration Effect on Water Droplet Flow Behavior

The effect of varying the airflow acceleration (substitute of exhaust gases) on the break-up process of water film (substitute of aluminum agglomerates) was investigated experimentally and numerically. At the end of this study, the following can be concluded,

- The numerical model was validated using the experimental data, and the percentile differences were in an acceptable range (6-19%), So it can be used for further simulations and experimentations.
- The combination of increasing the water flow rate and the convergent part of the nozzle results in greater break-up activity in terms of the droplets' average diameters and numbers through the whole nozzle volume. While increasing the water flow rate only causes a decrease in the multi-phase relative velocity and Weber number, diminishing the break-up activity in the inlet section.
- Increasing the exhaust flow acceleration subjects the water surface to rapid and sudden changes in the relative velocity between the gas and liquid, thus separating more water bodies from the primary liquid. Hence increase the liquid break-up tendency, especially in the inlet section.

In conclusion, this study showed that increasing the acceleration of the airflow (substitute for exhaust gas), due to the increase in the fuel combustion area with the flight time, promotes the break-up of the water droplets (substitute for aluminum agglomerates), especially in the nozzle inlet section. Greater break-up activity means more small droplets separation from the nozzle

surface, which has a better chance to be dragged by the exhaust gases' momentum and will not impinge the nozzle walls, reducing the nozzle mechanical erosion.

8.1.3 Submerged Nozzle Configuration Influence on Water Droplet Flow Behavior

The effect of having submerged nozzle configuration on the break-up process of water film (substitute of aluminum agglomerates) is addressed after conducting experimental investigations at different gas velocities and liquid flow rates. The following can be concluded,

- Having higher inlet air velocity causes earlier waterbodies separation and break-up process evolution moves up toward the liquid inlet section. In addition, the breakup process starts earlier in the submerged nozzle than the external one, because of the nozzle cavity.

- The submerged nozzle enhances the water bodies separation from the liquid water surface at higher air velocities in the inlet section because of the recirculation zone, hence larger average diameter, and higher droplets number. Enhancing the breakup tendency in this region helps in reducing the mechanical erosion, however the recirculation zone increases the separated droplets velocity resulting in higher mechanical erosion.

- Overall, the submerged nozzle has larger average diameter and lower number of droplets compared to the external nozzle, because of the less available area for breakup and the divergent section larger inclination angle.

- Higher air velocities results in a reduction in the recirculation zone, on the contrary higher water flow rates expands the recirculation zone.

- The breakup tendency rises in the inlet section when using higher water flow rates because of the recirculation zone effect which supersede the two-phase relative velocity decrease defined by the Weber number.

In conclusion, it can be deduced that the effect of having a submerged nozzle configuration on its mechanical erosion is determinable. It increases the breakup tendency of the liquid compared to the external nozzle, however because of the recirculation zone, the separated droplets will have higher velocity to hit the walls with. So, having a supersonic model simulates the actual conditions within the rocket is essential to decisively conclude its effect on the nozzle mechanical erosion.

8.2 Mechanical Erosion Investigation in Solid Rocket Motor Nozzle Through Droplet Breakup and Surface Tension Influence

The computer simulation model was established to predict the mechanical erosion rate within the solid rocket motor nozzle. The two-phase flow field caused by the propellant combustion process was simulated using the Eulerian-Lagrangian Approach. Model validation was conducted using experimental and numerical published data. Then, the model was used to study the effect of Aluminum / Aluminum oxide multi-component droplets' size, breakup, and lower surface tension on the predicted mechanical erosion rate, where the following was concluded:

- The predicted erosion rates are within limits suggested by Ketner et al. [75] from 0 to 0.16 $kg/m^2/s$ (based on graphite nozzle material density of 1800 kg/m^3), considering that the mentioned range includes both the mechanical and chemical erosion.

- The mechanical erosion mostly occurs in the convergent section of the nozzle and just the head of the throat section. If any erosion is noticed in any actual situation on the nozzle's throat or divergent section, it can be referred to the chemical erosion caused by the heterogeneous reactions.

- The aluminum/aluminum oxide droplets' diameter is the key variable affecting the nozzle erosion rate. It was concluded that there is a critical diameter for each set of conditions where the erosion rate flips its behavior, and the critical diameters are 220 μm, 180 μm, and 180 μm for the base model without incorporating the breakup model, containing the breakup model, and with including the breakup model, in addition to reducing the droplets' surface tension. The average erosion rate increases by decreasing the droplets' diameter, and then it drops again.

- Nozzle's erosion rate is not only a function of the incident droplets' flow rate but also their relative velocity and their incident angle.

- Applying the Reitz-Diwakar breakup model significantly impacts the predicted erosion rate. Moreover, it is more accurate to include it considering the existing flow dynamics within the combustion chamber. The erosion rate is reduced by 6.2% - 24% depending on the injected droplets.

- The critical droplet diameter for breakup in the current combustion chamber boundary conditions ranges from 50 to 60 μm.

- Reducing the aluminum surface tension by 15% promotes a decrease in the average erosion rate by 1% to 4.5%, based on the injected multi-component droplets' diameter. However, the surface tension reduction influence diminishes when the multi-component droplets' diameter is less than 50 μm.

In conclusion, it can be inferred that incorporating the droplet's breakup model is crucial for accurately predicting the nozzle's mechanical erosion rate. In addition, reducing the aluminum surface tension can positively impact the nozzle's erosion rate.

8.3 Propellant Aluminum Content and Alumina agglomerates Initial Velocity Impacts on the Mechanical Erosion in Solid Rocket Motor Nozzle

Numerical framework was adopted to study the mechanical erosion occurring on the SRM nozzle convergent section. The numerical approach includes the modeling of continuous phase (exhaust gases), single component discrete phase (pure aluminum particles) and multicomponent discrete phase (Aluminum/Aluminum Oxide particles). Validation was conducted by comparing the model results against published experimental and numerical data. The propellant aluminum content and the agglomerates' velocity at the burning surface influences on the nozzle mechanical erosion were investigated in the present work. The computed average mechanical erosion rates do not exceed the measured values for overall erosion by Geisler [6] (reported by Thakre [14]) and the suggested limits by Ketner et al. [75]. In conclusion, applying the droplets' breakup model is vital to accurately predict the mechanical erosion, since the mechanical erosion is reduced by 6-50%. In addition, having higher aluminum content exacerbates the mechanical erosion following a polynomial function and increases the single component aluminum particles' residence time within the combustion chamber, even they may erode the nozzle walls. Although, the higher particles' velocity at the burning surface causes a shifting in the impingement locations and enhances the escaping chance of particles from hitting the nozzle walls, the mechanical erosion increases from 1-7.5%. This increase is explained by the mechanical erosion correlation definition, the increase in the particles' axial relative velocity and incident angle.

8.4 Numerical Investigation of the Mechanical Erosion Within a Submerged Nozzle Configuration

The same previously mentioned numerical framework is also used here to study the effect of the pocket region (recirculation zone) and submerged nozzle configuration on the mechanical erosion rates and compare it with the external nozzle configuration. Seven particle diameters are used to address this study. The cavity of P230 SRM of Ariane V is scaled and used in this study. The erosion within the submerged nozzle first spikes on the nozzle tip, then decrease followed by a gradual increase to its maximum value just before the throat. However, when comparing the average erosion rate at different particles diameters, the erosion increases with reducing the particle diameter till 220 μm, then it decreases again till its minimum value at 60 μm. Also, it was found that the injection location affects the particle trajectory, as injected particles near the nozzle cavity will be affected by the vortices generated by the pocket region. Finally, when comparing the external nozzle and submerged nozzle configurations in terms of the predicted mechanical erosion, the external nozzle will perform better than the submerged one as lower mechanical erosion exists in its different sections.

8.5 Recommendations for Future Research

The investigation of the liquid droplet flow behavior in a vertical nozzle chamber (Sub-Sonic flow) can be extended to the following point:

- Experimental and numerical Investigation the viscosity influence on the breakup process.

- Record and analyze the breakup process in a 3-D nozzle configuration to avoid the overlapping errors.

On the other hand, Using the CFD numerical framework showed that it can correctly predict the internal flow field within the rocket internal combustion chamber and the nozzle mechanical erosion considering the actual harsh conditions of the solid rocket motor combustion chamber. So, it can be further used to predict the mechanical erosion at different propellant burn back times to find out the most severe case for design consideration. In addition, modifying the submerged nozzle model to consider the slag accumulation within the recirculation zone will be beneficial for cases close to the flight end. Finally, the model should be expanded to predict the overall nozzle erosion including the mechanical and chemical ones.

References

[1]   Braun, W. V., "History of rocketry & space travel." Thomas Y. Crowell Co, 1974.

[2]   F. Verger, I. Sourbès-Verger, R. Ghirardi, S. Lyle, and P. Reilly, The Cambridge encyclopedia of space : missions, applications, and exploration. Cambridge ; New York: Cambridge University Press, 2003

[3]   K. Tsiolkovsky, in The Exploration of Cosmic Space by Means of Reaction Devices (Исследование мировых пространств реактивными приборами), 1903.

[4]   Anon, "Solid Rocket Motor Nozzles," NASA Space Vehicle Design Criteria Monograph, NASA SP-8115. Washington, D.C, 1975.

[5]   Swope, L. W., and Berard, M. F., "Effects of Solid-Rocket Propellant Formulations and Exhaust-Gas Chemistries on the Erosion of Graphite Nozzles," AIAA Solid Propellant Rocket Conference, Palo Alto, CA, Jan, 1964.

[6]   Geisler, R. L., "The Relationship Between Solid Propellant Formulation Variables and Nozzle Recession Rates," JANNAF Rocket Nozzle Technology Subcommittee Workshop, Lancaster, CA, July 12–13, 1978.

[7]   Borass, S.,"Modeling Slag Deposition in the Space Shuttle Solid Rocket Motor," J. Spacecraft Rockets, 21(1), pp. 47–54, 1984.
Doi: 10.2514/3.8606

[8]   Wong, E., "Solid Rocket Nozzle Design Summary," Proceedings of 4th Propulsion Joint Specialist Conference, Cleveland, OH, June 10–14, 1968.
Doi: 10.2514/6.1968-655

[9]   Amano, R.S., and Yen, Y-H., "Chapter 19: Experimental Investigation of Molten Alumina Breakup in Gas Flows in a Solid Rocket Chamber," 5th International Conference on Chemical Engineering and Applications, IPCBEE, IACSIT Press, Singapore, vol.74, 2014.
Doi: 10.7763/IPCBEE. 2014. V74. 15

[10]   Thakre, P., and Yang, V., "Mitigation of Graphite Nozzle Erosion by Boundary Layer Control in Solid Propellant Rocket Motors," Journal of Propulsion and Power, 25(5), pp. 1079–1085, 2009.
Doi: 10.2514/1.41293

[11]   Sutton, G. P., and Biblarz, O., "Rocket Propulsion Elements, 7th ed., Wiley-Interscience, New York, 2001.

[12]   Johnston, J. R., Signorelli, R. A. and Freche, J. C., "Performance of Rocket Nozzle Materials with Several Solid Propellants," NASA TN D-3428, 1966.

[13]   Keswani, S. T., Andiroglu, E., Campbell, J. D., and Kuo, K. K. (1985) "Recession Behavior of Rocket Nozzles in Simulated Rocket Motors", Journal of Spacecrafts and Rockets, Vol. 22, No. 4, pp. 396-397

[14]   Thakre, P., and Yang, V., "Chemical Erosion of Carbon–Carbon/Graphite Nozzles in Solid Propellant Rocket Motors," Journal of Propulsion and Power, 24(4), pp. 822–833, 2008.
Doi: 10.2514/1.34946

[15]   Thakre, P., and Yang, V., "Chemical Erosion of Refractory Metal Nozzle Inserts in Solid-Propellant Rocket Motors," Journal of Propulsion and Power, 25(1), pp. 40–50, 2009.
Doi: 10.2514/1.37922

[16]   Thakre, P., and Yang, V., "Effect of Surface Roughness and Radiation on Graphite Nozzle Erosion in Solid Rocket Motors," Journal of Propulsion and Power, 28(2), pp. 448–451, 2012.
Doi: 10.2514/1.B34238

[17]   Sabnis, J., "Numerical Simulation of Distributed Combustion in Solid Rocket Motor with Metallized Propellant," Journal of Propulsion and Power, Vol. 19, No. 1, pp. 48–55, 2003.
Doi:10.2514/2.6101

[18]   Jeenu, R.; Pinumalla, K., Deepak, D., "Size Distribution of Particles in Combustion Products of Aluminized Composite Propellant," Journal of Propulsion and Power, Vol. 26, No. 4, pp. 715-723, 2010.

[19]   Grigor'ev, V. G., Zarko, V. E., and Kutsenogii, K. P., "Experimental Investigation of the Agglomeration of Aluminum Particles in Burning Condensed Systems," Combustion, Explosion and Shock Waves, 17(3), pp. 245–251, 1981.
Doi: 10.1007/BF00751292

[20]   Son, S., Sivathanu, Y.R., Moore, J.E., and Lim, J., "Experimental characteristics of particle dynamics within solid rocket motors environments," 56th JANNAF Interagency Joint Propulsion Meeting, FA9300-08-M-3022, Las Vegas, NV, Apr. 14–17, 2009.

[21]   Carlotti, S., Anfossi, J., Bellini, R., Colombo, G., and Maggi, F., "Particulate Phase Evolution Inside Solid Rocket Motors: Preliminary Results," Proceedings of 8th European Conference for Aeronautics and Aerospace Sciences (EUCASS)., Madrid, Spain, July 1–4, 2019.

Doi: <u>10.13009/EUCASS2019-787</u>

[22] Besnerais, G., Nugue, M., Devillers, R. W., and Cesco, N., "Experimental Analysis of Solid-Propellant Surface During Combustion with Shadowgraphy Images: New Tools to Assist Aluminum-Agglomeration Modelling," Proceedings of 7th European Conference for Aeronautics and Aerospace Sciences (EUCASS)., Milan, Italy, July 3–6, 2017.
Doi: <u>10.13009/EUCASS2017-327</u>

[23] Butler, A. G., "Holographic Investigation of Solid Propellant Combustion," Postgraduate thesis, Naval Postgraduate School, Monterey, CA, 1988.

[24] Liu, Z., Li, S., Liu, M., Guan, D., Sui, X.,Wang, N., "Experimental investigation of the combustion products in an aluminised solid propellant," Acta Astronautica, Volume 133, 2017, Pages 136-144, ISSN 0094-5765, https://doi.org/10.1016/j.actaastro.2017.01.025.

[25] Hwang, C., J., and Chang, G., C., "Numerical study of gas-particle flow in a solid rocket nozzle", AIAA Journal, 26(6), pp. 682-689, 1988.

[26] Xiao, Y., Amano, R. S., Cai, T., Li, J., and He, G., "Particle Velocity on Solid-Propellant Surface Using X-ray Real-Time Radiography," AIAA J., 41(9), pp. 1763–1770, 2003.
Doi: 10.2514/2.7294

[27] Xiao, Y., Amano, R. S., Cai, T., and Li, J., "New Method to Determine the Velocities of Particles on a Solid Propellant Surface," ASME J. Heat Trans., 127(9), pp. 1057–1061, 2005.
Doi: <u>10.1115/1.1999652</u>

[28] Xiao, Y., and Amano, R., "Aluminized Composite Solid Propellant Particle Path in the Combustion Chamber of a Solid Rocket Motor," WIT Transactions on Engineering Sciences, 52, pp. 153–164, 2006.
Doi: 10.2495/AFM06016

[29] Majdalani, J., Katta, A., Barber, T., and Maicke, B., "Characterization of Particle Trajectories in Solid Rocket Motors," Proceedings of 49th AIAA/ASME/SAE/ ASEE Joint Propulsion Conference, San Jose, CA, July 14–17, 2013.
Doi: 10.2514/6.2013-3919

[30] Simoes, M., Della Pieta, P., Godfroy, F., and Simonin, O., "Continuum Modeling of the Dispersed Phase in Solid Rocket Motors," Proceedings of 17th AIAA Computational Fluid Dynamics Conference, June, 2005.
Doi: 10.2514/6.2005-4698

[31]   Li, Z., Shi, B., Liu, Z., Liu, M., Liu, X., and Wang, N., "Investigation of Particle Size Effects on Aluminized Solid Rocket Motor Performance", 53rd AIAA/SAE/ASEE Joint Propulsion Conference, Doi: 10.2514/6.2017-5022

[32]   Li, Z., Wang, N., Shi, B., Li, S., and Yang, R., "Effects of Particle Size on Two-Phase Flow Loss in Aluminized Solid Rocket Motors," Acta Astronautica, 159, pp. 33–40, 2019.
Doi: 10.1016/j.actaastro.2019.03.022

[33]   Amano, R.S., "Solid-Fuel Rocket Motor Efficiency Improvement Scheme," Novel Combustion Concepts for Sustainable Energy Development, Springer India, ISBN 978-81-322-2210-1; ISBN 978-81-322-2211-8 (eBook); pp.535-560, 2014. DOI: 10.1007/978-81-322-2211-8_23

[34]   Amano, R. S., and Yen, Y.-H., "Study of Alumina Flow in a Propulsion Chamber," 51st AIAA/SAE/ASEE Joint Propulsion Conference, Orlando, FL, July 27–29, 2015.

[35]   Amano, R.S. and Yen, Y. H., "Investigation of Alumina Flow Breakup Process in Solid Rocket Propulsion Chamber, "AIAA 2016 SciTech, No. 2318567, 2016. Doi: 10.2514/6.2016-0498

[36]   Chen, W., Abbas, A. I., Ott, R. N., and Amano, R. S., "Investigation of Liquid Breakup Process Solid Rocket Motor Part B: Vertical C-D Nozzle." ASME. J. Energy Resour. Technol. September 2020; 142(9): 091301. Doi: 10.1115/1.4046627

[37]   Chen, W., Abbas, A. I., Ott, R. N., and Amano, R. S., "Investigation of Liquid Breakup Process Solid Rocket Motor Part A: Horizontal Converging–Diverging Nozzle." ASME. J. Energy Resour. Technol. May 2020; 142(5): 052102. Doi: 10.1115/1.4046081

[38]   Anson, J., Drew, R., and Gruzleski, J., "The Surface Tension of Molten Aluminum and Aluminum-Silicon-Magnesium Alloy Under Vacuum and Hydrogen Atmospheres," Metallurgical Mater. Transactions B, 30(6), pp. 1027–1032, 1999.

[39]   Greatrix, D.R., 2012, "Powered Flight: The Engineering of Aerospace Propulsion," Springer-Verlag, London Ltd, London (UK), pp. 323-343,426-427.

[40]   Sutton, G.P., 1992, "Rocket Propulsion Elements," 6th ed. John Wiley & Sons, New York, 1992, pp. 446.

[41]   Thakre, P., Rawat, R., Clayton, R., and Yang, V., "Mechanical Erosion of Graphite Nozzle in Solid-Propellant Rocket Motor," Journal of Propulsion and Power, 29(3), pp. 593-601, 2013.
Doi: 10.2514/1.B34630

[42]   Tarey, P., Kim, J., Levitas, V. I., Ha, D., Park, J. H., & Yang, H., "Prediction of the Mechanical Erosion Rate Decrement for Carbon-Composite Nozzle by using the Nano-Size Additive Aluminum Particle." Journal of the Korean Society of Propulsion Engineers. The Korean Society of Propulsion Engineers, Dec. 2015. https://doi.org/10.6108/kspe.2015.19.6.042

[43]   Yen, Y.-H., 2016, "Numerical and Experimental Study of Liquid Break-up Process in Solid Rocket Motor Nozzle," Ph.D. dissertation, The University of Wisconsin-Milwaukee, Milwaukee, WI

[44]   Pei, Y., Hu, B., and Som, S., 2015, "Large Eddy Simulation of an N-Dodecane Spray Flame Under Different Ambient Oxygen Conditions," Proceedings of the ASME 2015 Internal Combustion Engine Division Fall Technical Conference. Volume 2: Emissions Control Systems; Instrumentation, Controls, and Hybrids; Numerical Simulation; Engine Design and Mechanical Development, Houston, TX, Nov. 8–11, p.V002T06A008.
Doi:10.1115/ICEF2015-1034

[45]   Ameen, M. M., Mirzaeian, M., Millo, F., and Som, S., 2018, "Numerical Prediction of Cyclic Variability in a Spark Ignition Engine Using a Parallel Large Eddy Simulation Approach," ASME. J. Energy Resour. Technol., 140(5), p. 052203. Doi: 10.1115/1.4039549

[46]   Plengsaard, C., 2013, "Improved Engine Wall Models for Large Eddy Simulation (LES)," Ph.D. dissertation, University of Wisconsin Madison, Madison, WI. Doi: 10.4271/2013-01-1097

[47]   Hasan, A., Elgammal, T., Jackson, R., and Amano, R., 2020, "Comparative Study of the Inline Configuration Wind Farm," ASME. J. Energy Resour. Technol, 142(6), p. 061302. Doi: 10.1115/1.4045463

[48]   Hasan, A., Abousabae, M., Salem, A., and Amano, R., 2021, "Study of Aerodynamic Performance and Power Output for Residential-Scale Wind Turbines," ASME. J. Energy Resour. Technol., 143(1), p. 011302. Doi: 10.1115/1.4047602

[49]   Selim, O. M., Elgammal, T., and Amano, R. S. 2020, "Experimental and Numerical Study on the Use of Guide Vanes in the Dilution Zone." ASME. J. Energy Resour. Technol. August 2020; 142(8): 083001. Doi: 10.1115/1.4046079

[50]   Alkhafaji, A. A., Selim, O. M., Amano, R. S., Strickler, J. R., Hinow, P., Jiang, H., Sikkel, P. C., and Kohls, N., 2021, "Mass Transfer Performance of a Marine Zooplankton Olfactometer." ASME. J. Energy Resour. Technol. November 2021; 143(11): 112102. Doi:10.1115/1.4049602

[51]   Elgammal, T., Selim, O. M., and Amano, R. S., 2021, "Enhancements of the Thermal Uniformity Inside a Gas Turbine Dilution Section Using Dimensional Optimization." ASME. J. Energy Resour. Technol. October 2021; 143(10): 102102. Doi:10.1115/1.4049284

[52]   Selim, M. O., and Amano, R. S., 2019, "Control Methods to Improve Combustor Exit Temperature Uniformity," AIAASciTech, San Diego, CA, January 7-11. DOI:10.2514/6.2019-1773.

[53]   Senecal, P. K., Pomraning, E., Richards, K. J., and Som, S, 2013, "Grid-Convergent Spray Models for Internal Combustion Engine Computational Fluid Dynamics Simulations." ASME. J. Energy Resour. Technol. March 2014; 136(1): 012204. Doi:10.1115/1.4024861

[54]   Yuan, S., Dabirian, R., Shoham, O., and Mohan, R. S., 2020, "Numerical Simulation of Liquid Droplet Coalescence and Breakup." ASME. J. Energy Resour. Technol. October 2020; 142(10): 102101. Doi: 10.1115/1.4046603

[55]   Carlos Berrio, J., Pereyra, E., and Ratkovich, N., 2018, "Computational Fluid Dynamics Modeling of Gas-Liquid Cylindrical Cyclones, Geometrical Analysis." ASME. J. Energy Resour. Technol. September 2018; 140(9): 092003. Doi:10.1115/1.4039609

[56]   Ballesteros, M., Ratkovich, N., and Pereyra, E., 2020, "Analysis and Modeling of Liquid Holdup in Low Liquid Loading Two-Phase Flow Using Computational Fluid Dynamics and Experimental Data." ASME. J. Energy Resour. Technol. January 2021; 143(1): 012105. Doi:10.1115/1.4047604

[57]   Movahedi, H., Vasheghani Farahani, M., and Masihi, M., 2019, "Development of a Numerical Model for Single- and Two-Phase Flow Simulation in Perforated Porous Media." ASME. J. Energy Resour. Technol. April 2020; 142(4): 042901. Doi:10.1115/1.4044574

[58]   D. D. Joseph, 1999, "Break-up of a liquid drop suddenly exposed to a high-speed airstream," Minneapolis, MN.

[59]   Witherspoon, W., and Parthasarathy, R. N., 1997, "Break-up of Viscous Liquid Sheets Subjected to Symmetric and Asymmetric Gas Flow." ASME. J. Energy Resour. Technol. September 1997; 119(3): 184–192. Doi:10.1115/1.2794988

[60] Barrios, L., and Prado, M. G., 2011, "Modeling Two-Phase Flow Inside an Electrical Submersible Pump Stage." ASME. J. Energy Resour. Technol. December 2011; 133(4): 042902. Doi:10.1115/1.4004967.

[61] McBride, B., and Gordon, S., "Coefficients for calculating thermodynamic and transport properties of individual species," NASA, 1993.

[62] Reid, R. C., Prausnitz, J. M., and Poling, B. E., "The Properties of Gases and Liquids, 4th ed.," McGraw–Hill, New York, 1987.

[63] Hermsen, R., "Aluminum combustion efficiency in solid rocket motors." 19th Aerospace Sciences Meeting, St. Louis, MO, U.S.A. 12-15 Jan. 1981. Doi: 10.2514/6.1981-38

[64] Schiller, L. and Naumann, A., "Ueber die grundlegenden Berechnungen bei der Schwerkraftaufbereitung," VDI Zeits, Vol. 77, No. 12, pp. 318-320, 1933.

[65] Ranz, W.E. and Marshall, W.R., "Evaporation from Drops--Part I and II p. 141," Chemical Engineering Progress, Vol. 48, No. 3, pp. 141, 1952.

[66] STAR-CCM+, Ver 2020.2, CD-adapco Ltd, http://www.cd-adapco.com, April. 2022.

[67] Neilson, J. H., and Gilchrist, A., "Erosion by a Stream of Solid Particles," Wear, Vol. 11, No. 2, pp. 111–122, 1968.

[68] Neilson, J. H., and Gilchrist, A., "An Experimental Investigation into Aspects of Erosion in Rocket Motor Nozzles," Wear, Vol. 11, No. 2, pp. 123–143, 1968.

[69] Stiesch, G. "Modeling Engine Spray and Combustion Processes," Springer (Berlin), Chapter 5, page 154, 2003.

[70] Khalil, E. E., ElHarriri, G., and Abousabaa, M., "Heat Transfer Enhancement in Parabolic Trough Absorption Tube Using Twisted Tape Inserts." 2018 Joint Thermophysics and Heat Transfer Conference. Atlanta, Georgia, June 25-29, 2018. Doi:10.2514/6.2018-3910

[71] Salem, A. R., Nourin, F. N., Abousabae, M., and Amano, R. S., "Experimental and Numerical Study of Jet Impingement Cooling for Improved Gas Turbine Blade Internal Cooling with In-Line and Staggered Nozzle Arrays." ASME. J. Energy Resour. Technol. January 2021; 143(1): 012103. Doi:10.1115/1.4047600

[72] McBride, B., and Gordon, S., "Computer Program for Calculation of Complex Chemical Equilibrium Compositions and Applications II. User's Manual and Program Description," National Aeronautics and space administration, 1996.

[73] Salita, M., "Quench Bomb Investigation of Al$_2$O$_3$ Formation from Solid Rocket Propellants (Part II): Analysis of Data," 25th JANNAF Combustion Meeting, CPIA Publ.498, Vol. I, Chemical Propulsion Information Agency, Laurel. MD. Pp. 185-197.

[74] Madabhushi, R. K., Sabnis, J. S., de Jong, F. J., and Gibeling, H. J., "Calculation of Two-Phase Aft-Dome Flowfield in Solid Rocket Motors," Journal of Propulsion and Power, Vol. 7, No. 2, pp. 178–184, 1991. Doi:10.2514/3.23310

[75] Ketner, D. M., and Hess, H. S., "Particle Impingement Erosion," 15th Joint Propulsion Conference, Las Vegas, NV, USA, AIAA Paper 79-1250, 1979.

[76] F. Stella, F. Paglia," Pressure oscillations in solid rocket motors: Numerical study,"Aerospace Science and Technology, Volume 15, Issue 1, 2011, Pages 53-59.

[77] Boraas, S., "Modeling slag deposition in the Space Shuttle solid rocket motor," Journal of Spacecraft and Rockets, Vol. 21, No. 1, pp. 47-54, 1984. Doi: 10.2514/3.8606

[78] Madabhushi, R., Sabnis, J., De Jong, F., and Gibeling, H., "Navier-Stokes analysis of aft dome flow field in solid rocket motorswith submerged nozzle" 25th Joint Propulsion Conference, Monterey, CA / July 10-12, 1989. Doi: 10.2514/6.1989-2780

[79] Chauvot, J. F., Dumas, L., Schmeisser, K., "Modeling of alumina slag formation in solid rocket motors" 31st AIAA/ASME/SAE/ASEE Joint Propulsion Conference and Exhibit, July 10-12,1995/San Diego, CA. Doi: 10.2514/6.1995-2729

[80] Anthoine, J., and Buchlin, J. M., "Effect of Nozzle Cavity on Resonance in Large SRM: Numerical Simulations", Journal of Propulsion and Power Vol. 19, No. 3, May – June 2003. Doi: 10.2514/2.6141

[81] Bianchi, D., and Nasuti, F., "Carbon-Carbon Nozzle Erosion and Shape-Change Effects in Full-Scale Solid-Rocket Motors" Journal of Propulsion and Power, Vol. 28, No. 4, pp. 820-830, 2012. Doi: 10.2514/1.B34267

APPENDIX A: Tsiolkovsky Rocket Equation

The rocket equation can be derived from newton's third law till the following equation:

$$M\frac{dV}{dt} = -v_e\frac{dM}{dt} - Mg$$

where M is the rocket mass, V is the rocket velocity, v_e is the exhaust gases velocity, and g is the gravity constant. Arranging the previous equation by multiplying it by dt, and dividing by M. It can be written as follows:

$$-v_e\frac{dM}{M} - g\,dt = dV$$

Integrating the previous equation over the rocket's initial and final boundary conditions (At t = 0, V = 0, M = M_i / At t = t_f, V = V_f, M = M_f)

$$-v_e\int_{M_i}^{M_f}\frac{dM}{M} - g\int_0^{t_f}dt = \int_0^{V_f}dV$$

$$V_f = v_e\ln\frac{M_i}{M_f} - g\,t_f$$

The last equation is called Tsiolkovsky rocket equation after Konstantin Tsiolkovsky (Russian Scientist), who introduced and published it on 1903 [3]. It can be concluded that the exhaust gases velocity should be very high to ensure at least a rocket with the escape velocity, moreover the rocket mass initial to final mass ratio should be large and a very short firing duration.

APPENDIX B: Image Preparation Algorithm

```matlab
% Brightness adjust & Video File Builder Script
% Author: Cody Casper
% Author & Revised & Modified: Mohamed Abousabae (abousab2@uwm.edu)
% The purpose of this script is to adjust the photos brightness
% And to create a video file. The steps are:
% 1: Scaling image contrast so there is no fluctuation of brightness
% between images.
% 2: Save processed images in new folder.
% 3: Save images in video format.

tic
clear variables
close all
path = addpath( genpath( 'E:\work\PHD\SRM Project\Exp_Work\40\Far-View' ) );
%adds all subfolders in directory to path
directory = 'E:\work\PHD\SRM Project\Exp_Work\40\Far-View' ;
the_images = dir( strcat( directory , '\*.bmp' ) ); % defines file types to be
used
dest_directory = 'E:\work\PHD\SRM Project\Exp_Work\40\Far-View\example';
mkdir( dest_directory ); % Creates the directory for processed images

for k = 1 : length( the_images ) % creates for loop which goes through each
image in the directory using parallel computing
    image_name( 1 : ( length( the_images ) ) , : , ( k ) ) = transpose( {
the_images( : ).name } );
    base_image_name = the_images( k ).name; % this states that all images
througout the direnew_name_1_lengthctory will be analysed
    analyse_image = imread( base_image_name ); % this defines the image being
worked on throughout the whole directory
    fprintf( 'Working on %s image...\n' , base_image_name ); % this shows where
we are in the script when script is running
    %rotate_image = imrotate( analyse_image , 0.9 ); %for vertical images (far-
View)
    %crop_image = imcrop( rotate_image , [ 480 , 1 , 250 , 1043 ] ); % current
crop is for vertical images (far-View)
    crop_image = imcrop( analyse_image , [ 511 , 1 , 372 , 1023 ] ); % current
crop is for vertical images (close-View)
    adjust_image = imadjust( crop_image ); % Adjusts image contrast to same
scale
%    RGB64 = double( adjust_image )/65535; % needed for horizontal images
    image_contrast( k ) = max( adjust_image( : ) ) - min( adjust_image( : ) );
% Verifies contrast in images are the same (solving brightness fluctuation)

    o_image_contrast( k ) = max( analyse_image( : ) ) - min( analyse_image( :
) );

    new_name_1_length = length( base_image_name );
    new_name_1 = base_image_name( 1 , 1 : ( new_name_1_length - 4 ) ); %Gets
file name without .tif extension
    new_name_2 = { '_p.png' };
    New_Name_2 = char( new_name_2 );
```

```matlab
    new_name( k , : ) = strcat( new_name_1 , New_Name_2 ); % New filename with
_p to distinguish processed files

    imwrite( adjust_image , new_name( k , : ) , 'png'); % Saves processed image
as .png file

end

movefile( '*.png' , dest_directory ); % Moves processed files to new folder

fprintf( 'Image processing complete.\n')

%%
cd example
processed_images = dir( strcat( dest_directory , '\*.png' ) );
writerObj = VideoWriter( 'example2.avi' );
writerObj.FrameRate=1/0.03;
open( writerObj );
for i = 1 : length( processed_images )
    processed_image_name( 1 : ( length( processed_images ) ) , : , ( i ) ) =
transpose( { processed_images( : ).name } );
    proccessed_name = processed_images( i ).name; % this states that all images
througout the directory will be analysed
    processed_image = imread( proccessed_name );
    writeVideo( writerObj , processed_image );
end
close(writerObj);
fprintf( 'Video file created.\n')
```

APPENDIX C: Data Processing and Extraction Algorithm

```matlab
% Video File Builder Script
% Author: YI-Hsin Yen
% Author & Revised & Modified: Mohamed Abousabae (abousab2@uwm.edu)
% The purpose of this script is to capture the number of droplets and thier
% diameter in three different sections in the C-D nozzle
clc
clear variables
spd = 20;            %[20 , 30 , 40]----add all folders here to locate folder
(20,30,40)
m = 1;
Np_t = 0;
plot = 1;%plot yes(1) or no(0),<---------------------[Check Plot]
ecc_filter = 0.96; % <------------------------[Set Eccentric filter]
thresh=0.7;
ttot = cputime;
Total_crop = [ 1 , 1 , 250 , 1020];                         %
Only In Case of Total C-D Nozzle
crop = { Total_crop };                                      %
Only In Case of Total C-D Nozzle
sections = { 'Total'};
%initial_crop = [ 1 , 249 , 250 , 54 ];
%throat_crop = [ 1 , 487 , 250 , 84 ];
%final_crop = [ 1 , 763 , 250 , 54 ];
%crop = { initial_crop , throat_crop , final_crop };
%sections = { 'inlet' , 'throat' , 'last' };
sheet = ( 1 : length( crop ) );
folder = [ 'E:\work\PHD\SRM Project\Exp_Work\',num2str(spd),'\Far-View' ];
folder_imout_01 = [ 'E:\work\PHD\SRM Project\Exp_Work\',num2str(spd),'\Far-
View' ];
figure_name = [ 'Exp_RDST_',num2str(spd),'_' ];
folder_out = [ 'E:\work\PHD\SRM Project\Exp_Work\',num2str(spd),'\Far-View' ];
Files = dir( folder );
filename = { Files.name };
isdir = [ Files.isdir ];
filename( isdir ) = [ ];
s = listdlg( 'ListString' , filename );
filename = filename( s )';
jFL = length( filename );
image_number = j;
    for m = 1 : jFL
        crop_length = length( crop );
        tpic = cputime;
        file = [ folder '\' filename{ m } ];
        image = imread( file );
        Primary_crop_image = imcrop( image , [ 480 , 4 , 250 , 1039 ] );
        adjust_image = imadjust( Primary_crop_image );
        d = imbinarize( adjust_image , 'adaptive' , 'Sensitivity' , thresh );
        a3 = bwareaopen( d , 4 );
        a4 = imcomplement( a3 );
        a5 = bwareaopen( a4 , 4 );
        a6=bwpropfilt(a5, 'Eccentricity', [0, ecc_filter]);
        for ii = 1 : crop_length
            crop_image = imcrop( Primary_crop_image , cell2mat( crop( ii ) ) );
            AD_crop_image = imcrop( a6 , cell2mat( crop( ii ) ) );
```

```matlab
            figure; imshow(AD_crop_image)
            [ B , L , n( jFL ) ] = bwboundaries( AD_crop_image , 'noholes' );
            Status = regionprops( L , 'Area' , 'Eccentricity' , 'EquivDiameter'
);
            numReg = max( L( : ) );
            lenB = length( B );  % total number of particle
            if ii==1                                            %
Only In Case of Total C-D Nozzle from line 51 to line 101
            for j=1:lenB
                clear c
                c=cell2mat(B(j));
                if max(double(c(:,2)<33))>0
                    if max(double(c(:,1)>360))>0
                        if max(double(c(:,1)<690))>0
                            B(j)={0};
                            L(L==j)=0;
                            Status(j).EquivDiameter=0;
                            Status(j).Eccentricity=0;
                            Status(j).Area=0;
                        end
                    end
                elseif max(double(c(:,2)<47))>0
                        if max(double(c(:,1)>422))>0
                        if max(double(c(:,1)<630))>0
                            B(j)={0};
                            L(L==j)=0;
                            Status(j).EquivDiameter=0;
                            Status(j).Eccentricity=0;
                            Status(j).Area=0;
                        end
                        end
                elseif max(double(c(:,2)>197))>0
                        if max(double(c(:,1)>360))>0
                            if max(double(c(:,1)<690))>0
                                B(j)={0};
                                L(L==j)=0;
                                Status(j).EquivDiameter=0;
                                Status(j).Eccentricity=0;
                                Status(j).Area=0;
                            else
                            end
                        else
                        end
                elseif max(double(c(:,2)>180))>0
                        if max(double(c(:,1)>422))>0
                            if max(double(c(:,1)<630))>0
                                B(j)={0};
                                L(L==j)=0;
                                Status(j).EquivDiameter=0;
                                Status(j).Eccentricity=0;
                                Status(j).Area=0;
                            else
                            end
                        else
                        end
                end
```

```matlab
            end                                                    %
Only In Case of Total C-D Nozzle from line 51 to line 101
            end
%               if ii==2
%               for j=1:lenB
%                   clear c
%                   c=cell2mat(B(j));
%                   if max(double(c(:,2)<47))>0
%                       B(j)={0};
%                       L(L==j)=0;
%                       Status(j).EquivDiameter=0;
%                       Status(j).Eccentricity=0;
%                       Status(j).Area=0;
%                   elseif max(double(c(:,2)>180))>0
%                       B(j)={0};
%                       L(L==j)=0;
%                       Status(j).EquivDiameter=0;
%                       Status(j).Eccentricity=0;
%                       Status(j).Area=0;
%                   else
%                   end
%               end
%               else
%               end
            figure; imshow(L)
            Equi_Di=cell2mat({Status(:).EquivDiameter});
            if plot == 1 % if plot =1, plot droplet
                % 07 Plot boundary
                t = cputime;
                clear a7;
                a7 = cat( 3 , crop_image , crop_image , crop_image );
                for j = 1 : lenB
                    if Equi_Di(j)==0
                    else
                        bdl =B{ j };        % find total boundary coordinate
location
                        len = length( bdl );
                        for i = 1 : len % plot boundary loop
                            a7( bdl( i , 1 ) , bdl( i , 2 ) , 2 ) = 0.1;
                        end
                    end
                end
                figure; imshow(a7)
                t = cputime - t;
                sza7 = size( a7 );
                tpic = cputime - tpic;
            else
            end
            Np_t = Np_t + lenB;
            %info_Area(1:lenB,m)=(cell2mat({Status(:).Area}))';
            info_Ecc( 1 : lenB , m , ii ) = cell2mat( {Status(:).Eccentricity}
)';
            info_Dia( 1 : lenB , m , ii ) = cell2mat( {Status(:).EquivDiameter}
)'; % collacting data, frames is in colume
            clear Status;
            tpic = cputime - tpic;
```

```matlab
            fprintf( [ 'process ' , num2str( 100000 + m ) , '.bmp with CPU Time
of ' , num2str( tpic ) , ' sec\n' ] )
%             fprintf( [ 'process ' , num2str( 100000 + m ) , '.bmp' , string(
sections( ii ) ) ] );
        end
    end
%% Tabulate
crop_length = length( crop );
ttot = cputime - ttot;
for k=1:crop_length
    clear info_Dia2 info_Ecc2 sz_info_A info_Dia_v info_Ecc_v tul
    info_Dia2 = single( info_Dia(:,:,k) ); % convert matrix to single precision
    info_Ecc2 = single( info_Ecc(:,:,k) );
    sz_info_A = size( info_Dia(:,:,k) ); % get matrix size
    info_Dia_v = reshape( info_Dia2 , sz_info_A( 1 ) * sz_info_A ( 2 ) , 1 );
% reshpe matrix to single colume
    info_Ecc_v = reshape( info_Ecc2 , sz_info_A( 1 ) * sz_info_A( 2 ) , 1 );
    % --------
    tul = tabulate( info_Dia_v ); % Tabulate info_Dia for the inlet section
    % --------
    pxl = 1.05; %1.05pxl=1mm %% -----> for our images the scale was measured at
1021 pixels / 970 mm
    tul( : , 4 ) = tul( : , 1  ) / pxl;    % convert Diameter to mm
    tul( : , 5  ) = ( ( tul( : , 4  ) / 2 ) .^3 ) * ( 4 * pi / 3 ); % Volume of
droplet
    tul( : , 6  ) = tul( : , 5  ) .* tul( : , 2  ) / jFL;  % total volume
carried by droplet by particular size
    % add image process information log
    tul( 2 , 8  ) = ecc_filter; % Eccentricity filter
    tul( 3 , 8  ) = Np_t; % Total number of detected particles
    %tul( 1 , 2 , k ) = 0; % # of 0 particle is 0
    %tul( 1 , 3 , k ) = 0; % # of 0 particle is 0
    tul( 4 , 8  ) = sum( tul( : , 2  ) ); %calculate total particle # to compare
with filted #
    tul( 5 , 8  ) = 100 * tul( 4 , 8  ) / tul( 3 , 8  ); % percentage of particle
in analyse
    tul( 6 , 8  ) = jFL;     %number of image analyse
    tul( 7 , 8  ) = thresh; %thresh; %image contrast threshold
    tul( 8 , 8  ) = ttot; % total time used
    % size (pxl)|| count ||  %   ||  Dia (mm)  ||  acumulate Vol ||  mass
distribution per frame
    col_header = { 'size (pxl)' , 'count' , '%' , 'Dia (mm)' , 'acumulate Vol'
, 'mass distribution per frame' };
    side_header = transpose( { 'ecc_filter' , 'Total # Detected Particles' ,
'Total vs calculated particles' , '% particle in analyse' , '# of images' ,
'thresh' , 'CPU time' } );
    File_name = [ 'Data_',num2str(spd),'.xlsx' ];
    xlswrite( File_name , col_header , sheet( k ) , 'A1' );
    xlswrite( File_name , side_header , sheet( k ) , 'I3' );
    xlswrite( File_name , tul , sheet( k ) , 'A2' );
end

fprintf( [ 'Total CPU Time of ', num2str( ttot ) , ' sec\n' ] )
```

APPENDIX D: Submerged Nozzle Detailed Engineering

Drawings

6.693

0.250

0.079

41.339

7.874

9.874

11.811

0.250

0.969   0.969

0.250   0.500

1.969   1.969

	NAME	SIGNATURE	DATE
DRAWN			
CHK'D			
APPV'D			
MFG			
Q.A			

UNLESS OTHERWISE SPECIFIED:
DIMENSIONS ARE IN MILLIMETERS
SURFACE FINISH:
TOLERANCES:
  LINEAR:
  ANGULAR:

FINISH:

DEBURR AND
BREAK SHARP
EDGES

DO NOT SCALE DRAWING

REVISION

TITLE:

MATERIAL:

DWG NO.

WEIGHT:

SCALE:1:10

SHEET 1 OF 1

Covers

A4

41.339

Ø0.295

1.250

0.50

0.500

	NAME	SIGNATURE	DATE
DRAWN			
CHK'D			
APPV'D			
MFG			
Q.A			

TITLE:

MATERIAL:

DWG NO.

Long_Side

A4

WEIGHT:

SCALE:1:10

SHEET 1 OF 1

181

13.968

1.250

0.500

1.250

0.500

0.846
5.060
Ø0.157
Ø0.197
0.623
0.500
Ø0.197
1.575
11.811
Ø0.591
0.907

6.457
Ø0.591
0.125
0.190
Ø0.591
0.125
0.907
1.750
0.125
11.811

	UNLESS OTHERWISE SPECIFIED: DIMENSIONS ARE IN MILLIMETERS SURFACE FINISH: TOLERANCES: LINEAR: ANGULAR:	FINISH:		DEBURR AND BREAK SHARP EDGES	DO NOT SCALE DRAWING	REVISION
	NAME	SIGNATURE	DATE		TITLE:	
DRAWN						
CHK'D						
APPV'D						
MFG						
Q.A			MATERIAL:			
			WEIGHT:		DWG NO. Top_cover	A4
				SCALE:1:5		SHEET 1 OF 1

0.591
1.575
1.250

0.079
15.936
0.500

1.250
0.500

	NAME	SIGNATURE	DATE				TITLE:
DRAWN							
CHK'D							
APPV'D							
MFG							
Q.A			MATERIAL:				

DWG NO.
Upper_Short_Side   A4

WEIGHT:

SCALE:1:5   SHEET 1 OF 1

Curriculum Vitae

Mohamed Abousabae

WORKING EXPERIENCE

Harley-Davidson Motor Company, Wauwatosa, WI, USA
Systems Engineer, Sep. 2022 – Present
- Retrieving, preparing and cleanup of CAD parts for CFD volume meshing.
- Develop 3-D thermal models of heat conduction, convection, and radiation to enable thermal design directions and their impact on vehicle components/rider/passenger and power electronic unit.

Harley-Davidson Motor Company, Wauwatosa, WI, USA
CFD Methodology Engineer, Jan. 2021 – Aug. 2022
Internship through the University of Wisconsin Milwaukee working as a research assistant to help with
- Air Intake and exhaust systems CFD analysis development and optimization by using different software packages including (Star CCM+, Sculptor, and modeFRONTIER)
- Revising and developing the tumble calculation methodology used in CFD analysis.
- Study the incorporation of the topology optimization technology developed by Star CCM+ in the company workflow to design new parts.
- Different parts cooling analysis (flow distribution optimization and pressure loss reduction)
- Boiling Prediction (simulation) in the engine cooling circuit.
- Developing an existing JAVA code to generate a power point presentation with the company template from Star CCM+.
- Creating reports to document each completed project, in addition to updating old tutorials.

University Of Wisconsin Milwaukee, WI, USA.
Research Assistant, Aug. 2019 – Aug. 2022
- Experimental and numerical investigation of the factors affecting the liquid break-up phenomena in the solid rocket motor c-d nozzle. (Experimental, Multi-phase, Image processing using MATLAB, Numerical using Star-CCM+, Implicit unsteady, Steady, Eulerian and Lagrangian Approaches, VOF, LES, Particle evaporation, Erosion models)
- Experimental and Numerical Study of Jet Impingement Cooling for Gas Turbine Internal Cooling with In-line and Staggered Nozzle Arrays. (Numerical using Star-CCM+, Steady, Implicit unsteady, RST turbulence model, Heat transfer)
- Optimization Procedure for Residential-Scale Wind Turbines. (Numerical investigation to popularize the use of residential-scale wind turbines using Star-CCM+, Steady, Implicit unsteady, k-ω SST and LES turbulence models, Stationary and Rotational parts)

Industrial Assessment Center, UW-Milwaukee, Wisconsin, USA.
Energy Audit Engineer, Aug. 2019 – Aug. 2022
Participated in a total of 23 energy audits and was the lead student for three of them.
- Inspect and analyze building structures, heating systems, ventilation, air conditioning, water, and industrial processes to ensure energy use is optimal.
- Plan, schedule audit procedures, and present audit findings to clients.
- Prepare cost estimates for potential recommendations.
- Prepare the final report to be reviewed and approved by the DOE.

Power Generation Engineering & Services Company (PGESCO), Egypt.
Mechanical Engineer in Water, Wastewater and Desalination Group, Mar. 2016 – Jul. 2019
- Successfully completed conceptual, detailed engineering, technical evaluation of offers, design review and construction support phases of the desalination, water, and wastewater systems in three (3) power plants projects. The contracts had an average value of 15 million USD.
- Prepared conceptual engineering, P&IDs, PFDs and system description for 2 huge proposals, El-Tahrir Petrochemical Complex El-Sokhna and 8 water treatment plants (25,000 – 51,000 m3/day).
- Good understating of power plant chemistry standards and guidelines of EPRI, IAPWS.
- Good understanding of piping codes and standards such as ASME B31.1, B36.10, B36.19, B16.5.

Institute of Aviation Engineering and Technology, Egypt.
Teaching Assistant, Sep. 2015 – Feb. 2016
- Gave tutorial sections to undergraduate students on topics such as; thermodynamics, heat and mass transfer, theory of Fine Measurements and laboratories.

Cairo University Faculty of Engineering, Egypt.
Teaching and Research Assistant, Sep. 2014 – Aug. 2015
- Wrote and contributed to heat transfer research group publications.
- Gave tutorial sections to undergraduate students on topics such as; numerical methods in engineering and power plants.

Engineering House of Expertise (EGEC), Egypt.
Part Time HVAC Design Engineer, Mar. 2015 – Feb. 2016
- Prepared a detailed designed of central HVAC systems for Resala Hospital (Egypt), Ajyal Villas (Saudi Arabia) and Egypt foods Factory (Egypt).
- Prepared BOQs for the above-mentioned projects.

Institute of dynamics and vibration, Leibniz Universität Hannover, Germany.
Internship, Research Assistant for the rotating machinery workgroup, Jul. 2013 – Sep. 2013
- Worked on linear / nonlinear forced response analysis oscillator under harmonic motion.
- Built up a linear single degree of freedom system and the Newmark time step integration method in MATLAB and check its numerical accuracy and stability in the linear and nonlinear cases.

EDUCATION

University of Wisconsin Milwaukee, Wisconsin, USA
PhD-Mechanical Engineering Candidate, expected graduation, Spring 2023
- Current GPA: 4.0
- Area of Research: liquid break-up phenomena and mechanical erosion in the solid rocket motor c-d nozzle (Multi-phase, Experimental, Numerical using Star-CCM+).

Cairo University Faculty of Engineering, Giza, Egypt
Master of Science-Mechanical Engineering, Mar. 2017
- GPA: A^+ [4]
- Area of Research: Numerical investigation for heat transfer enhancement in parabolic trough absorption tube using twisted tape inserts. (Numerical using Ansys Fluent)

Cairo University Faculty of Engineering, Giza, Egypt
Bachelor of Science-Mechanical Engineering, May. 2014
- GPA: 4.0 (Distinction with Honor Degree), **Ranked as the first on my batch**
- Graduation Project: Dual fuel fire tube boiler design for a hospital & air conditioning system design for surgery and patient's rooms in a hospital. (Numerical - Ansys Fluent)

PUBLICATIONS

- Abousabae, M., Amano, R. S., "Propellant Aluminum Content and Alumina agglomerates Initial Velocity Impacts on the Mechanical Erosion in Solid Rocket Motor Nozzle", Submitted Draft

- Abousabae, M., Amano, R. S., "Mechanical Erosion Investigation in Solid Rocket Motor Nozzle Through Droplet Breakup and Surface Tension Influence", Submitted Draft to ASME. J. Energy Resour. Technol. (Under Review)
- Hasan, A. S., Abousabae, M., Al Hamad, S., and Amano, R. S. (July 11, 2022). "Experimental and Numerical Investigation of Tubercles and Winglets Horizontal Axis Wind Turbine Blade Design." ASME. J. Energy Resour. Technol. January 2023; 145(1): 011302.
- Hasan, A. S., Abousabae, M., Al Hamad, S., and Amano, R. S. (July 11, 2022). "Experimental and Numerical Investigation of Vortex Generators and Winglets in Horizontal Axis Wind Turbine Blade Design." ASME. J. Energy Resour. Technol. January 2023; 145(1): 011301.
- Abousabae, M., and Amano, R. S. (December 8, 2021). "Air Flow Acceleration Effect on Water Droplet Flow Behavior in Solid Rocket Motor." ASME. J. Energy Resour. Technol. August 2022; 144(8): 082305.
- Abousabae, M., Amano, R. S., and Casper, C. (January 27, 2021). "Investigation of Liquid Droplet Flow Behavior in a Vertical Nozzle Chamber." ASME. J. Energy Resour. Technol. May 2021; 143(5): 052108.
- Hasan, A., Selim, O. M., Abousabae, M., Amano, R. S., and Otieno, W. (April 19, 2021). "Economic, Exergy, and Environmental Analyses of the Energy Assessments for U.S. Industries." ASME. J. Energy Resour. Technol. November 2021; 143(11): 112107.
- Qandil, M. D., Abbas, A. I., Salem, A. R., Abdelhadi, A. I., Hasan, A., Nourin, F. N., Abousabae, M., Selim, O. M., Espindola, J., and Amano, R. S. (March 4, 2021). "Net Zero Energy Model for Wastewater Treatment Plants." ASME. J. Energy Resour. Technol. December 2021; 143(12): 122101.
- Selim, O. M., Abousabae, M., Hasan, A., and Amano, R. S. (November 19, 2020). "Analysis of Energy Savings and CO2 Emission Reduction Contribution for Industrial Facilities in USA." ASME. J. Energy Resour. Technol. August 2021; 143(8): 082303.
- Hasan, A. S., Abousabae, M., Salem, A. R., and Amano, R. S. (July 29, 2020). "Study of Aerodynamic Performance and Power Output for Residential-Scale Wind Turbines." ASME. J. Energy Resour. Technol. January 2021; 143(1): 011302.
- Salem, A. R., Nourin, F. N., Abousabae, M., and Amano, R. S. (July 29, 2020). "Experimental and Numerical Study of Jet Impingement Cooling for Improved Gas Turbine Blade Internal Cooling With In-Line and Staggered Nozzle Arrays." ASME. J. Energy Resour. Technol. January 2021; 143(1): 012103.
- Khalil, E.E, Alhariry, G., Eldegwy, A., Abousabae, M., "Heat Transfer Enhancement in Parabolic Trough Absorption Tube Using Twisted Tape Inserts", 2018 Joint Thermophysics and Heat Transfer Conference, AIAA AVIATION Forum, (AIAA 2018-3910).

SOFTWARE SKILLS

- STAR-CCM+
- ANSYS Fluent software
- Microsoft office
- MATLAB
- Solid Works
- AutoCAD 2-D
- Hourly Analysis Program (HAP)
- Good command of using ion exchange systems sizing and selection programs.
- Good command of using RO systems sizing programs.
- AutoVue Professional
- ProjectWise
- Pipenet for piping pressure drop calculation

AWARDS AND CERTIFICATES

- Michael Krauski Memorial Award - UWM 2022 Student Research Poster Competition · May 2022.
- Student Choice Award - UWM 2022 Student Research Poster Competition · May 2022.

- University of Wisconsin-Milwaukee, ME Department Chancellor Award for the outstanding research productivity in 2021.
- University of Wisconsin-Milwaukee, ME Department Chancellor Award for the outstanding research productivity in 2020.
- University of Wisconsin-Milwaukee, Student research poster competition, 4th place among 57 graduate students. (Spring. 2020).
- University of Wisconsin-Milwaukee Chancellors' Graduate Student Award (Fall 2019).
- US DOE certified energy auditor for completing 9 energy auditing visits to manufacturing companies.
- International Reverse Osmosis Certification, International Desalination Association. (Sep. 2018)
- Advanced power plant cycle chemistry by David Addison, Thermal chemistry (Feb. 2016)
- Ranked as the first on my class in my both undergraduate studies, and master's degree.
- Certificate of excellence from Schlumberger.
- Letter of Recommendation from DR. Daniel Schurzig (my supervisor in Hannover, Germany) for fulfilling my tasks to his full satisfaction, also for helping my colleagues in their tasks.